RYDBERG ATOM DIAMAGNETISM

by

MICHAEL MASON KASH

B.A., Lake Forest College

(1977)

Submitted to the Department of Physics in
partial fulfillment of the requirements
for the degree of

DOCTOR OF PHILOSOPHY

at the

MASSACHUSETTS INSTITUTE OF TECHNOLOGY

July, 1988

Signature of Author _____
Department of Physics

Certified by _____
Daniel Kleppner
Lester Wolfe Professor of Physics
Thesis Supervisor

Accepted by _____
George F. Koster
Professor of Physics
Chairman, Department Committee

RYDBERG ATOM DIAMAGNETISM

by

MICHAEL MASON KASH

Submitted to the Department of Physics
in July of 1988 in partial fulfillment
of the requirements for the degree of
Doctor of Philosophy

Abstract

This thesis contains a description of an experimental investigation about highly excited lithium atoms in a strong magnetic field. Under these conditions, the atom experiences a diamagnetic energy shift which can be comparable to its binding energy. The high resolution spectra, including level anticrossings, are collected in regimes of energy and field where current theoretical analyses are viable.

Thesis Supervisor: Daniel Kleppner
Lester Wolfe Professor of Physics

This thesis is dedicated to my parents

Robert and Shirley Kash

and to my sister and brother-in-law

Barbara and Jeffrey Joyce.

TABLE OF CONTENTS

Chapter 1. INTRODUCTION

Elucidating the behavior of atoms in strong fields is a central goal of modern atomic physics. The subject encompasses a wide variety of situations, such as rf ionization of atoms, and atomic structure in large electric and magnetic fields. The unifying theme is that the atom-field interaction dominates the system dynamics. This thesis presents an experimental investigation of highly excited atoms in a strong magnetic field with high resolution laser spectroscopy.

Early interest in this problem arose from the recognition that astrophysical magnetic fields could be large on the atomic scale, and that one could expect drastic changes in atomic structure. The atomic unit of field is 2.35×10^5 T. Absorption features due to hydrogen have been observed in the spectra of white dwarf stars with magnetic fields in the range of 10^2 to 10^4 T. On neutron stars, fields have been observed in the range of 10^7 to 10^9 T, though atomic spectra have not been seen [WZW87].

Although magnetic fields that are strong on the atomic scale are far larger than the largest fields yet made in the laboratory, the laboratory study of atomic structure in the strong field regime has emerged as an active area of atomic physics. This development followed the realization that highly excited atoms — Rydberg atoms — enter the strong field regime at fields which are quite modest.

1.1 The Problem

The approximate Hamiltonian which describes a hydrogen atom in a uniform magnetic field in the z-direction is

$$H_o(B) = \frac{1}{2} p^2 - \frac{1}{r} + \frac{1}{2} BL_z + \frac{1}{8} B^2\rho^2 , \tag{1.1.1}$$

where atomic units are used. (Here r is the distance from the stationary proton to the electron, L_z is the component of angular momentum along the magnetic field, and ρ is the distance from the z-axis to the electron.) Roughly speaking, the first two terms are those associated with the field-free atom. The third term represents the interaction of the atom's permanent magnetic dipole moment with the magnetic field. This factor is called the paramagnetic Hamiltonian and causes the Zeeman effect. The fourth term can be viewed as the magnetic field interacting with the magnetic moment induced in the atom by changing the magnetic field from zero to some finite value. This quantity is referred to here as the diamagnetic Hamiltonian. Equation (1.1.1) can be broken into three parts:

$$H_o = \frac{1}{2} p^2 - \frac{1}{r} \qquad \text{(field–free atom)} , \tag{1.1.2a}$$

$$H_p = \frac{1}{2} BL_z \qquad \text{(paramagnetism)} , \tag{1.1.2b}$$

$$H_d = \frac{1}{8} B^2 \rho^2 \qquad \text{(diamagnetism)} . \tag{1.1.2c}$$

The eigenstates of H_o are well known. The set of states which are simultaneous

eigenstates of L^2 and L_z are the familiar spherical states:

$$H_o \mid nlm > = E_n \mid nlm > , E_n = -\frac{1}{2n^2}, n = 1, 2, \cdots , \tag{1.1.3a}$$

$$L^2 \mid nlm > = l(l+1) \mid nlm > , l = 0, 1, \cdots , n-1 , \tag{1.1.3b}$$

$$L_z \mid nlm > = m \mid nlm > , m = -l, \cdots , 1, 0, 1, \cdots , l . \tag{1.1.3c}$$

Note that each energy E_n has a degeneracy of n^2 . In the presence of a magnetic field, this degeneracy is broken.

The contribution to the energy from the paramagnetic term, H_p, is easy to calculate, because the spherical states are also eigenstates of H_p :

$$H_p \mid nlm > = \frac{1}{2} Bm \mid nlm > . \tag{1.1.4}$$

This energy change, in spectroscopists' units, is $0.47 \frac{\text{cm}^{-1}}{\text{T}} mB$.

The contribution to the energy shift of H_d is difficult to calculate because the total Hamiltonian is not separable in any orthogonal coordinate system. The order of magnitude can be estimated by noting that the size of the atom is about n^2. So

$$< H_d > = \frac{1}{8} B^2 < \rho^2 > \sim \frac{1}{8} B^2 n^4 , \tag{1.1.5}$$

which is nearly $5.0\times10^{-7} \frac{\text{cm}^{-1}}{\text{T}^2} B^2 n^4$.

The atomic unit of field is so large, about 10^4 times the largest laboratory magnetic field, that diamagnetism is usually negligible compared with paramagnetism.

However, when the field or atom is very large, diamagnetism dominates. Rydberg atoms, or atoms with large n, exhibit huge diamagnetism. In terms of the atomic binding energy, the diamagnetic energy is

$$\frac{< H_d >}{|< H_o >|} \sim \frac{1}{4} (Bn^3)^2 . \tag{1.1.6}$$

For B=10 T and n=40, this ratio is about 2. How can the energy levels of this system be calculated?

This is the main problem in the thesis: *The effect of diamagnetism need not be small and cannot be easily calculated.*

Roughly speaking, the strength of the diamagnetic Hamiltonian can be divided into three regions. These may be visualized on an energy versus field diagram, and possess distinctive spectral features. See Fig. 1.1.1.

1. The l-mixing regime is that region of energy and field where the magnetic field mixes the (degenerate) zero-field angular momentum states, but does not mix states from different n's. Degenerate perturbation theory may be used here. The spacings between the levels *from a fixed n* are nearly constant for the low energy levels, and are nearly proportional to successive even integers for the high energy levels. This effect is the result of the special dynamical symmetry of the hydrogen atom and the cylindrical symmetry of the magnetic field.

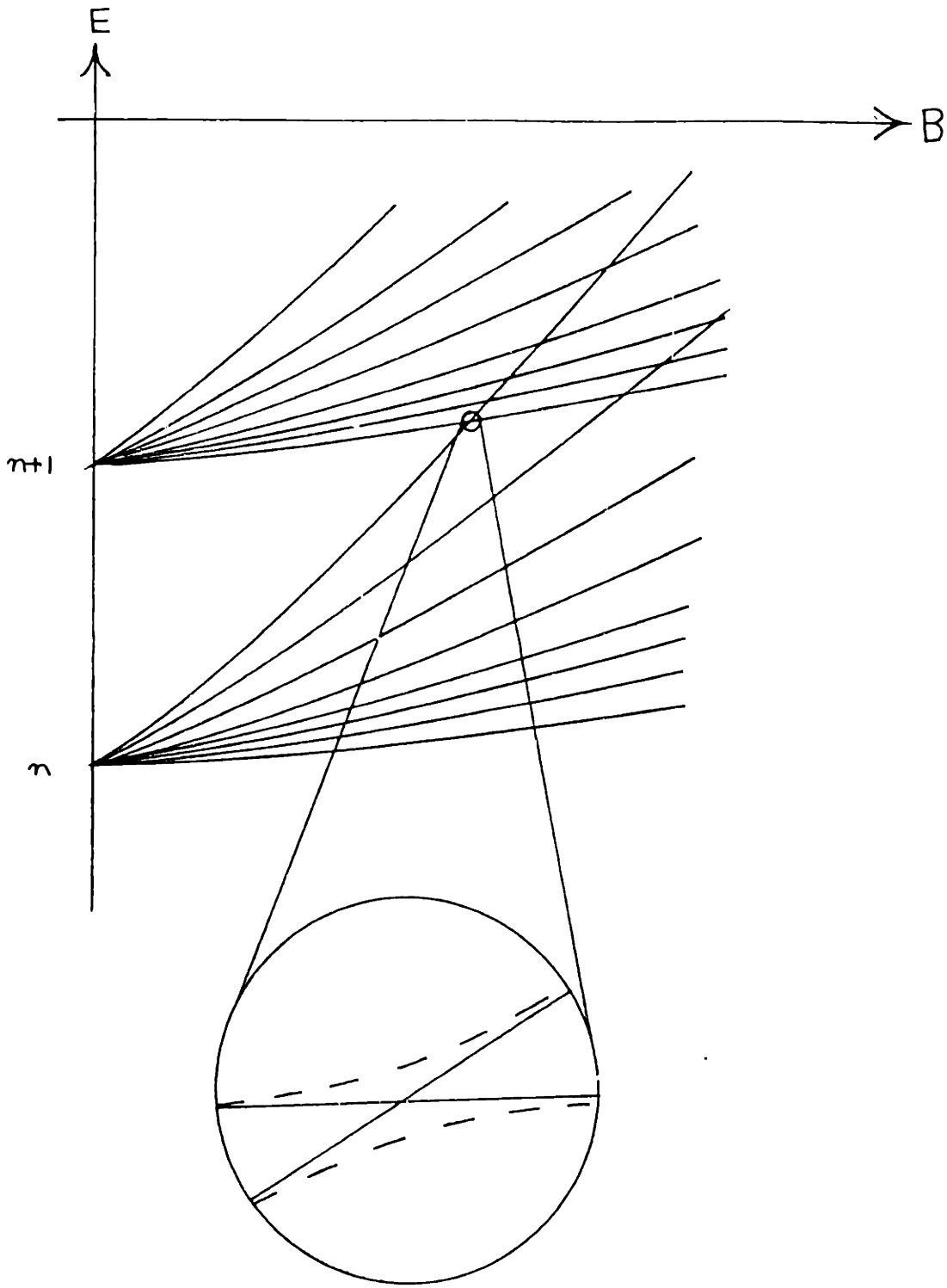

Figure 1.1.1 A schematic representation of Rydberg atom energy levels in a magnetic field, showing the l-mixing and part of the n-mixing regimes. The inset shows a very sharp hydrogen anticrossing (solid lines) and a typical alkali-metal anticrossing (dashed lines). See Fig. 2.2.1 for an accurate plot of hydrogen energy levels as a function of magnetic field.

2. The n-mixing regime extends from the l-mixing regime to where levels from several n's have crossed. Although n's have been mixed, it is still possible to say to which n a particular level belongs. Actually, levels with the same m (and parity) never cross. In hydrogen Rydberg atoms, the levels very nearly cross, but in other alkali-metal Rydberg atoms, the level anticrossings can be significant. These anticrossings are measurable features of the spectra which reflect the valence electron's wave function at the core of the atom.

3. In the strong-mixing regime, levels from so many n's have crossed that it is not possible to say to which n a particular state belongs. The region extends above the zero field ionization limit, where the states and energies are dominated by the magnetic field. This region is sometimes called the quasi-Landau regime.

This thesis discusses the spectra of hydrogen (theoretically) and lithium (theoretically and experimentally) in the l- and n-mixing regimes. It is an experiment in high resolution laser spectroscopy. "High resolution" is a relative term: our typical resolution, 0.0005 cm^{-1}, is low by today's standards. Nevertheless, it represents close to a 100-fold increase over previous work.

1.2 The Machinery

The experiment described in this thesis is designed to measure accurately the energy levels of Rydberg atoms in a uniform magnetic field. The apparatus consists of a source of atoms, a magnet, an excitation mechanism, and a Rydberg atom detector. The idea is to perform laser spectroscopy on the atoms while they are in the magnet.

Lithium is used rather than hydrogen because narrow-linewidth lasers are not readily available with the ultraviolet wavelengths needed to excite hydrogen to Rydberg states. Lithium possesses many features similar to those of hydrogen, and can be excited by the scheme shown in Fig. 1.2.1. Two photons from the first laser drive the 2s $\rightarrow$ 3s transition, and one photon from the second laser drives the 3s $\rightarrow$ Rydberg state transition. The 2s and 3s states have no paramagnetic shifts and very small diamagnetic shifts, so the first transition is field-independent. Thus the binding energy of the Rydberg state can be determined from the binding energy of the 3s state and the frequency of the second laser.

A schematic diagram of the apparatus is displayed in Fig. 1.2.2. The velocity of the atoms is parallel to the magnetic field direction, so there is no motional electric field in the atom's rest frame. (Rydberg atoms are sensitive to electric fields.) The lasers cross the atomic beam at right angles so there is no Doppler shift or broadening.

Rydberg states are detected by electric field ionization. After crossing the laser beams, the atoms enter a region containing an electric field large enough to ionize

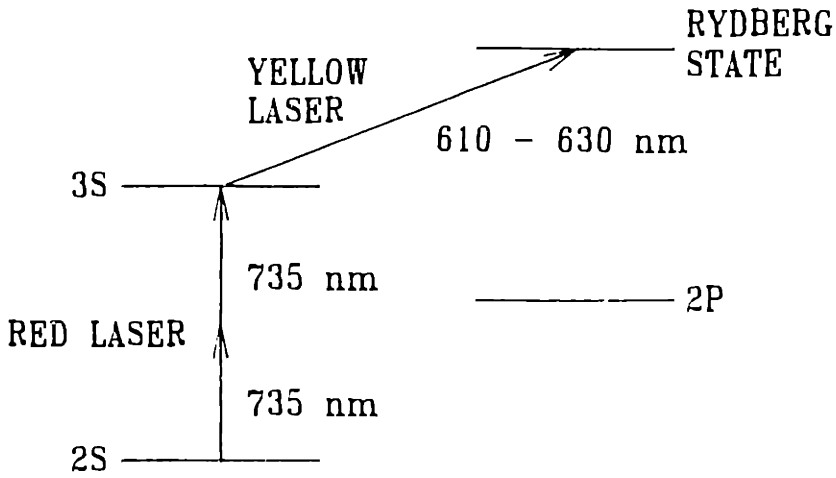

Figure 1.2.1. Laser excitation scheme of atomic lithium.

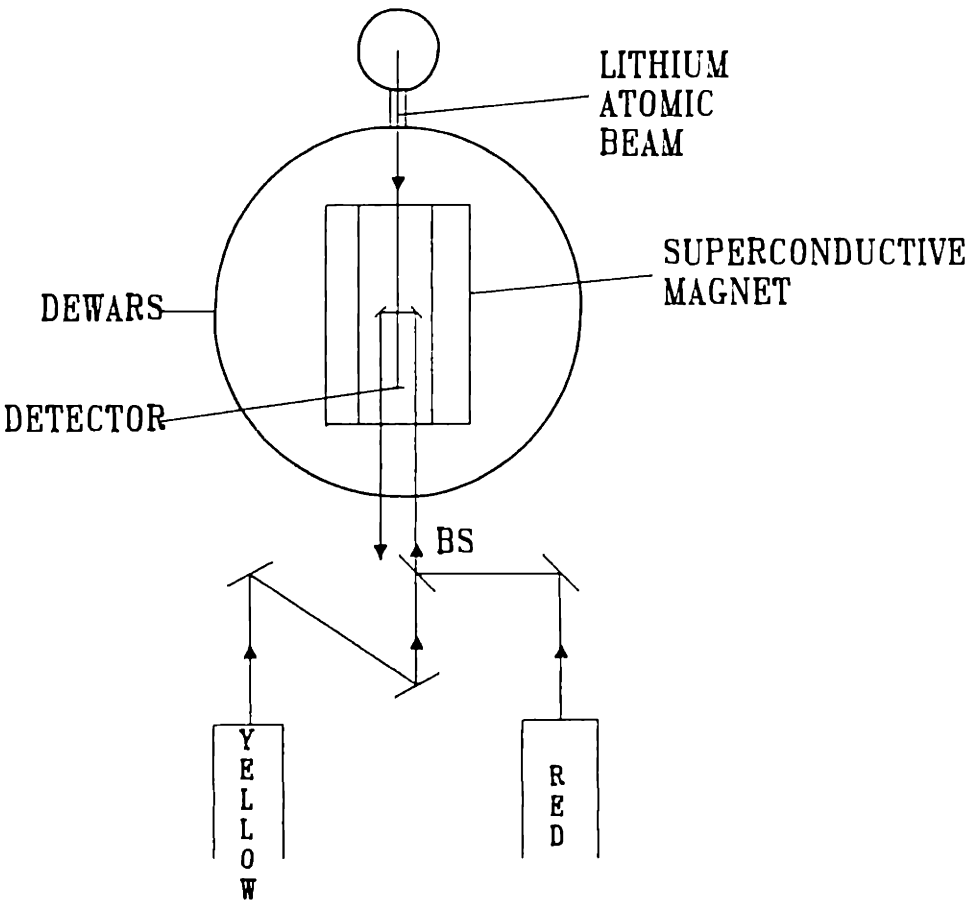

Figure 1.2.2. Schematic diagram of the apparatus.

rapidly those in a Rydberg state. The resulting electrons are counted by a charged particle detector.

Spectra are obtained by setting the magnetic field at a fixed value and recording the electron current as a function of laser frequency. The laser is reset to its initial frequency, the field is changed, and the process is repeated. In this way, the levels are mapped out as a function of field.

1.3 The Reason

Despite the difficulty of finding the eigenvalues and eigenstates of the Hamiltonian in Eq. (1.1.1), impressive theoretical progress toward a solution has been made during the last ten years or so. The techniques are somewhat complicated, involving the dynamical symmetry of the hydrogen atom, and to make detailed predictions about the position of energy levels, a computer is needed to diagonalize a large matrix which represents the Hamiltonian. This representation is finite and therefore is only an approximation to the real situation. Accurate measurements are needed to compare with these calculations. No calculations are presently available in the regime $Bn^3 \gg 1$, where there is much speculation about the quantal connection with instabilities in the corresponding classical motion [GAD87]. High resolution spectra may provide insight.

There is also the desire to see new elementary physical phenomena demonstrated. Basically the system under study is *one* electron in a Coulomb electric field and a uniform magnetic field — it is easy to visualize. The solution is complicated in general, but there are some features which can be explained in reasonably simple ways, such as anticrossings, or the distribution of levels before different n's have crossed. It is satisfying to obtain these insights.

None of these reasons is totally compelling. The fundamental form of the electromagnetic interaction in Eq. (1.1.1) is not being tested. If there is good

agreement between calculation and measurement, fine; if not, the calculation was done incorrectly, or the wrong experiment was done. (The last clause means that some effect was inadvertently disturbing the system.) Neither outcome changes what is believed to be the way electromagnetic fields interact with electrons. Also, "the problem is simple but the solution is complicated" isn't unique to this situation. There are lots of systems with a simple Hamiltonian that can't be generally solved in detail, such as the lithium atom itself!

On the other hand, the reasons cited above for undertaking this study are substantial and defensible. Many people are interested in the problem: about sixty papers have been written on this topic during the last decade. Much of this interest has been generated by the thesis advisor, conveying his enthusiasm and insight to others. And this *is* a very nice problem, illustrating basic physical principles pushed and tested in new regimes. As discussed in the next section, the general problem of atoms in a magnetic field has played an essential role in the development of quantum mechanics.

1.4 The History

Possibly the first person to inquire into the effect of a magnetic field on atoms was Michael Faraday. In 1845, Lord Kelvin suggested that Faraday investigate the action of electricity on the polarization of light. Faraday found that the polarization rotated when light traveled through an atomic vapor parallel to a magnetic field. He also found that certain materials were weakly affected by a magnetic field; those attracted to the field, he called paramagnetic, while those repelled by the field, he called diamagnetic. Pieter Zeeman (1865-1943) observed the field-induced broadening in the principal transition of sodium in a flame (1896) and resolved the field-induced splitting of cadmium fluorescence in a discharge (1897), confirming the earlier (classical) prediction of his thesis advisor, Hendrik Lorentz. They shared the 1902 Nobel Prize in physics. Refinements of such studies eventually led Uhlenbeck and Goudsmit to the concept of electron spin (1925) [ABB84, pp. 54-56, 177-178, GAY84].

Armed with the formalism of quantum mechanics, Landau (1930) predicted the spectrum of a charge in a uniform magnetic field. This was probably the first calculation involving the diamagnetic Hamiltonian. (It is interesting to note that the Hamiltonian has terms proportional to B and B^2, while the eigenenergies, the Landau levels, are proportional to B. [LAL77, pp. 456-459])

The effect of diamagnetism on atomic energy levels was demonstrated by Jenkins and Segrè in 1939. They studied n=10-35 in sodium with a field of 2.7T [JES39]. These results were immediately interpreted by Schiff and Snider, using perturbation theory and an "adiabatic" calculation. The division of the spectrum into l- and n-mixing regimes was made [SCS39]. Here the unfortunate name "quadratic Zeeman effect" was born.

Using a grating spectrograph, Garton and Tompkins (1969) presented the barium spectrum with B=2.407(5)T through the zero field ionization limit. The absorption maxima revealed an unexpected uniform spacing — "quasi-Landau levels", 1.5 times the cyclotron frequency [GAT69]. This totally unexpected observation stimulated much of the modern interest in the problem.

Tunable dye lasers pushed the experimental effort into new frontiers. With higher spectral intensity, atomic beam methods could be used, reducing the motional electric field and producing less distorted spectra. Pulsed laser experiments in the Kleppner group clearly resolved the l- and n-mixing of sodium levels [ZCK78], and the evolution of levels from l-mixing through the strong-mixing regimes [CZH80].

Notable among the current experimental studies is work by Welge and his colleagues, who have studied the spectrum of hydrogen in fields around 6 T [HWM86]. Laser spectroscopy of hydrogen presents a great challenge even without the added complication of a magnetic field, because of the lack of narrow ultraviolet

laser sources. Pulsed lasers are required, and the resolution is consequently limited. Because many interesting features of the excitation spectrum turn out to manifest themselves in global variations of the transition strength, data with limited resolution still hold considerable interest. Cacciani has carried out a number of studies on the diamagnetic structure of lithium using an ultraviolet pulsed laser which excites Rydberg states with one photon [CLP86a,b].

Theoretical developments have been dominated by Gay and Delande [GAY86], employing the powerful techniques of dynamical group theory. (They have also published fine experimental work on cesium and rubidium in cells in magnetic fields.) Wunner and his associates have extended their numerical expertise from astrophysical-sized field into the laboratory-sized field regime, using very large basis diagonalization to predict hydrogenic spectra [WWZ86].

High resolution spectroscopy is required if theory is to be tested critically, and is in any case desirable in the exploration of areas not yet accessible to theory. The goal of the present work is to develop a workable system capable of producing high resolution spectra of lithium in a magnetic field, and to study spectral details such as level anticrossings. In October of 1982, George Robert Welch and I descended into the MIT Spectroscopy Laboratory to make Rydberg states in an atomic beam of lithium inside of a superconductive magnet with actively stabilized cw dye lasers. There were *many* technical problems to overcome.

Chapter 2. DIAMAGNETISM IN HYDROGEN

Hydrogen is the quintessential testing ground for a great variety of theoretical and experimental atomic physics. It often provides the starting point for calculations about multielectron atoms, and because of the remarkable symmetry of the Coulomb potential, many hydrogenic derivations can be carried out analytically. Most theory of diamagnetism has been developed for hydrogen.

Henry Cavendish (1731-1810) is credited as being the first to distinguish hydrogen from other gases by the description "inflammable air from the metals." However, Cavendish did not claim to be the discoverer of hydrogen. Early observations of the gas were made by van Helmont, Boyle, Mayow, and Hales. Paracelsus (1493-1541) described a gas as "air rises and breaks forth like a wind," which has been erroneously cited as an allusion to hydrogen [WEL68, pp.177-185].

This chapter presents the development of the Hamiltonian for hydrogen in a magnetic field, and discusses the terms, their interpretation, and their consequences. A numerical method for predicting the spectrum is considered, followed by a comparison of useful representations of the hydrogen atom. Finally, the effects of nuclear motion are evaluated.

2.1 The Hamiltonian and Elementary Considerations

We begin by considering the Hamiltonian for hydrogen in a magnetic field, and discuss the meaning of the terms. The immediate consequences of these terms are presented, followed by an application of perturbation theory.

The Hamiltonian

In zero magnetic field, the Hamiltonian for an electron in a Coulomb potential is the sum of the kinetic and potential energies:

$$H_o = \frac{1}{2}p^2 - \frac{1}{r} \ . \tag{2.1.1}$$

Within the context of a Hamiltonian formalism, a magnetic field must be introduced via a (non-unique) vector potential $\vec{A}$ such that $\vec{B} = \vec{\nabla} \times \vec{A}$. The prescription for which Hamilton's (classical) equations of motion reproduce Newton's equations of motion is

$$H_o(B) = \frac{1}{2}(\vec{p}+\vec{A}(\vec{r}))^2 - \frac{1}{r} \ . \tag{2.1.2}$$

Here, $\vec{p}$ is the canonical momentum of the system, which in quantum mechanics has the usual commutation relation with $\vec{r}$. In configuration space, the canonical momentum operator is given by $\vec{p} = -i\vec{\nabla}$. It is generally *not* the mechanical, or kinetic, momentum of the electron, as it was in zero-magnetic field. In classical physics, the kinetic momentum is

$$\dot{\vec{r}} = \vec{\nabla}_p H_o(B) = \vec{p} + \vec{A} \ . \tag{2.1.3}$$

The quantity $\dot{\vec{r}}$ is physically measurable and therefore gauge invariant. Hence $\vec{p}$ depends on the choice of gauge, and the Hamiltonian of Eq. (2.1.2) is still the sum of the kinetic and potential energies.

To make further progress we choose a specific gauge. The gauge which is universally selected in the theory of diamagnetism is the (static) symmetric gauge $\vec{A} = (\vec{B}\times\vec{r})/2$. For a *uniform* magnetic field, then $\vec{\nabla} \cdot \vec{A} = 0$ (a Coulomb gauge) and thus $\vec{p} \cdot \vec{A} = \vec{A} \cdot \vec{p}$. This vector potential is also cylindrically symmetric about the magnetic field. The Hamiltonian may be written in the form

$$H_o(B) = \frac{1}{2}p^2 + \frac{1}{2}\vec{p} \cdot (\vec{B}\times\vec{r}) + \frac{1}{8}(\vec{B}\times\vec{r})^2 - \frac{1}{r}$$

$$= \frac{1}{2}p^2 - \frac{1}{r} + \frac{1}{2}\vec{B} \cdot \vec{L} + \frac{1}{8}(\vec{B}\times\vec{r})^2 \ , \tag{2.1.4}$$

where the (canonical) angular momentum, $\vec{L} = \vec{r} \times \vec{p}$, has been introduced. The terms are grouped in the following way:

$$H_o(B) = H_o + H_p + H_d \ , \tag{2.1.5a}$$

where

$$H_o = \frac{1}{2}p^2 - \frac{1}{r} \qquad \text{(hydrogen atom)} \ , \tag{2.1.5b}$$

$$H_p = \frac{1}{2}\vec{B} \cdot \vec{L} \qquad \text{(paramagnetism)} , \tag{2.1.5c}$$

and

$$H_d = \frac{1}{8}(\vec{B}\times\vec{r})^2 \qquad \text{(diamagnetism)} . \tag{2.1.5d}$$

Traditionally, paramagnetism is interpreted as the interaction of the atom's permanent magnetic dipole moment with the magnetic field, while diamagnetism is considered as the interaction of the atom's induced magnetic dipole moment with the magnetic field. This picturesque language suggests that paramagnetism and diamagnetism are part of the atom's pctential energy. However, the above derivation shows that they are really part of the electron's kinetic energy.

Constants of Motion

The Hamiltonian in Eq. (2.1.4) is rotationally invariant about the field axis: if $\vec{B} = B\hat{z}$, then

$$[H_o(B), L_z] = 0 . \tag{2.1.6a}$$

Quantum theory allows us to construct, in principle, simultaneous eigenstates of $H_o(B)$ and L_z. Let the eigenvalues of L_z be m. The (normalized) wave functions may be written as

$$\psi(\vec{r}) = F(\rho, z)e^{im\phi} \tag{2.1.6b}$$

where ρ, z, and ϕ define the usual cylindrical coordinates, and F is a real-valued function of ρ, z .

To say "what the electron is doing", we evaluate the (gauge invariant) probability current density [LAL77 pp. 470-471]:

$$\vec{j} = Re\,\psi^{*}(\vec{p}+\vec{A})\psi = F^{2}(\frac{m}{\rho} + \frac{B\rho}{2})\hat{\phi} \; . \tag{2.1.6c}$$

The z-component of the total kinetic angular momentum about the origin is

$$L_{mz} = \int d^{3}r \; \vec{r} \times \vec{j} \cdot \hat{z} = m + \frac{B}{2}<\rho^{2}> \; , \tag{2.1.6d}$$

which shows that L_z is the kinetic angular momentum only for zero magnetic field. We also see that difference between the canonical and kinetic angular momenta is the average induced magnetic moment.

Internal parity is also a constant of the motion. We define the parity operator by its action on the coordinates of the wave function:

$$\pi\psi(\vec{r}) = \psi(-\vec{r}) \; . \tag{2.1.7a}$$

Then we can show that

$$[H_{o}(B), \pi] = 0 \; . \tag{2.1.7b}$$

Note that we do *not* change the sources of magnetic field under this operation: $\pi\vec{B} = \vec{B}$. Again the implication is that it is possible to find simultaneous

eigenfunctions of $H_o(B)$ and π. We also have

$$[\pi, L_z] = 0 \ , \tag{2.1.7c}$$

so the energy, azimuthal (canonical) angular momentum, and parity of a state may be specified.

Qualitative Features of the Energy Shift

Our goal is to find the solution to the eigenvalue equation

$$H_o(B) \mid \psi > = E \mid \psi > \ . \tag{2.1.8a}$$

Unfortunately, no analytic solution is known. Before discussing methods for obtaining approximate solutions, we use the Feynman-Hellman theorem [CDL77 p. 1192-1193] to characterize the general behavior of the eigenvalues. In an eigenstate of $H_o(B)$, again with $\vec{B} = B\hat{z}$, we have

$$E = < H_o(B) > \tag{2.1.8b}$$

and

$$\frac{\partial E}{\partial B} = < \frac{\partial H_o(B)}{\partial B} > = \frac{1}{2} m + \frac{1}{4} B < \rho^2 > \ . \tag{2.1.8c}$$

Because $< \rho^2 >$ is positive-definite, if $m \geq 0$, then the slope of energy with field is strictly positive. Therefore, the energy can *never* decrease. This points out possible computation errors of eigenvalues [WWZ86], and also that some authors calculate

quantities other than E in Eq. (2.1.8a) yet call it the energy [WUR82].

Atomic size may be estimated from Eq. (2.1.8c). Solving for $< \rho^2 >$ yields

$$< \rho^2 > = \frac{4}{B} \left[\frac{\partial E}{\partial B} - \frac{m}{2} \right] . \tag{2.1.8d}$$

Roughly speaking, we find that the energy shift is proportional to B^2 at low fields and proportional to B^x, $1 < x < 2$, at high fields. Thus the atom stays rather constant in size when the field is small, but shrinks when the field is large.

The Ground State

As a first attempt toward a solution of Eq. (2.1.8), we apply perturbation theory to the ground state of hydrogen. Here H_o (Eq. (2.1.5a)) is the unperturbed Hamiltonian, while H_d (Eq. (2.1.5c)) is the perturbation. (Since m is a good quantum number, and $m = 0$ for the ground state, the contribution of H_p to the energy is zero.) The order of perturbation is indicated inside of parentheses.

We use the usual spherical states for the unperturbed, or zeroth order, states. For the ground state, the energy and the configuration-space wave function are

$$E_0^{(0)} = - \frac{1}{2} , \tag{2.1.9a}$$

and

$$< \vec{r} \mid 0\ (0) > = \psi_0^{(0)}(\vec{r}) = R_{10}(r) Y_{00}(\Omega) = 2e^{-r} \frac{1}{\sqrt{4\pi}} \ . \tag{2.1.9b}$$

The first-order correction to the energy is given by

$$E_0^{(1)} = < 0\ (0) \mid H_d \mid 0\ (0) > = 2\ \frac{B^2}{8} \ . \tag{2.1.10}$$

The second-order correction to the energy is given by

$$E_0^{(2)} = \left[\frac{B^2}{8} \right]^2 \sum_{nlm}{}' \frac{| < nlm\ (0) \mid \rho^2 \mid 0\ (0) > |^2}{E_{nlm}^{(0)} - E_0^{(0)}} \tag{2.1.11}$$

where the sum extends over all states, including those in the (positive energy) continuum, but excluding the ground state. The technique for formally evaluating this sum was developed by Dalgarno and Lewis [DAL55], and amounts to solving an inhomogeneous differential equation for the first-order correction to the ground-state wave function. Non-degenerate perturbation theory assumes that the energy and wave function may be expanded in a power series. The first terms in that series are related by [SCH68]

$$(H_o - E_0^{(0)}) \mid 0\ (0) > = 0 \ , \tag{2.1.12a}$$

$$(H_o - E_0^{(0)}) \mid 0\ (1) > = (E_0^{(1)} - H_d) \mid 0\ (0) > \ , \tag{2.1.12b}$$

and

$$E_0^{(1)} = < 0\ (0) \mid H_d \mid 0\ (0) > \ , \tag{2.1.12c}$$

$$E_0^{(2)} = < 0\ (0) \mid H_d \mid 0\ (1) > . \qquad (2.1.12d)$$

In the derivation of these equations, it is assumed that the unperturbed state is normalized and the first-order correction is orthogonal to that state. The latter is accomplished by adding an appropriate multiple of the unperturbed state to any solution of Eq. (2.1.12b). Working with configuration-space wave functions, so that $< \vec{r} \mid 0\ (1) > = \psi_0^{(1)}(\vec{r})$, Eq. (2.1.12b) may be written as

$$(-\frac{1}{2}\nabla^2 - \frac{1}{r} + \frac{1}{2})\psi_0^{(1)} = \frac{B^2}{4}(1 - \frac{r^2}{2}\sin^2\theta)\psi_0^{(0)}$$

$$= \frac{B^2}{2}(1 - \frac{r^2}{3})e^{-r}Y_{00} + \frac{B^2}{6}\frac{r^2}{\sqrt{5}}e^{-r}Y_{20} . \qquad (2.1.13a)$$

Generally, the first-order correction to the wave function may be written as

$$\psi_0^{(1)}(\vec{r}) = \sum_{l=0}^{\infty}\sum_{m=-l}^{l} f_l(r)Y_{lm}(\Omega) . \qquad (2.1.13b)$$

However, since the spherical harmonics are orthonormal, and the operator $H_o - E_0^{(0)}$ is diagonal in l and m, only terms proportional to Y_{00} and Y_{20} will satisfy Eq. (2.1.13a). Thus the correction is

$$\psi_0^{(1)} = f_0(r)Y_{00}(\Omega) + f_2(r)Y_{20}(\Omega) , \qquad (2.1.13c)$$

where Eq. (2.1.13a) implies that f_0 and f_2 must satisfy

$$-\frac{1}{2r}(rf_0)'' + (\frac{1}{2} - \frac{1}{r})f_0 = \frac{B^2}{2}(1 - \frac{r^2}{3})e^{-r} , \qquad (2.1.13d)$$

and

$$-\frac{1}{2r}(rf_2)'' + (\frac{3}{r^2} + \frac{1}{2} - \frac{1}{r})f_2 = \frac{B^2}{6}\frac{r^2}{\sqrt{5}}e^{-r} \ . \tag{2.1.13e}$$

Particular solutions for both of these ordinary, linear, second-order, inhomogeneous, differential equations may be found by assuming that the solution is a power series times an exponential:

$$f_k(r) = (a_0 + a_1 r + a_2 r^2 + a_3 r^3 + \cdots)e^{-r} \ , \ k = 1, 2 \ . \tag{2.1.13f}$$

In both cases, the series terminates. We find

$$f_0(r) = \frac{B^2}{6}(C - r^2 - \frac{r^3}{3})e^{-r} \ , \tag{2.1.13g}$$

$$f_2(r) = \frac{B^2}{6\sqrt{5}}(\frac{r^2}{2} - \frac{r^3}{3})e^{-r} \ . \tag{2.1.13h}$$

The constant C is selected to make $\psi_0^{(1)}$ orthogonal to $\psi_0^{(0)}$. The result is $C = 11/2$. Now that the first-order correction to the ground-state wave function has been obtained, Eq. (2.1.12d) provides us with the second-order correction to the ground-state energy. It is

$$E_0^{(2)} = -\frac{53}{3}\left[\frac{B^2}{8}\right]^2 \ . \tag{2.1.13i}$$

This method was pushed further by Galindo and Pascual [GAP76]. They determined the shift analytically to fifth order in the diamagnetic operator. Their result

is

$$E_0(B) = -\frac{1}{2} + \frac{1}{4}B^2 - \frac{53}{192}B^4 + \frac{5581}{4608}B^6$$

$$- \frac{21,577,397}{2,211,840}B^8 + \frac{31,283,298,283}{265,420,800}B^{10} + O(B^{12}) \,. \qquad (2.1.14)$$

This series, in their words, "is at most asymptotic." Cizek and Vrscay [CIV82] use algebraic methods and compute ("exact") numerical values to 36^{th} order in B^2. The perturbation series has zero radius of convergence for any non-zero field, even in the ground state.

We have investigated how much of the second-order shift comes from the (positive energy) continuum by *numerically* summing the terms of Eq. (2.1.11) over bound states. The result is

$$E_0^{(2)} \simeq -1.15\left[\frac{B^2}{8}\right]^2 . \qquad (2.1.15)$$

Therefore, about 35% of the second-order diamagnetic shift of the ground state comes from the continuum. As will be discussed in the next section, however, we do not believe that the continuum plays such an important role in the diamagnetic structure of some Rydberg states.

2.2 The Spherical Basis

The Schroedinger equation for hydrogen in a magnetic field, Eq. (2.1.8a), is not separable in any (orthogonal) coordinate system. This is known because Eisenhart [EIS48] has listed all Hamiltonians and their corresponding coordinate systems for which the one-particle Schroedinger equation is separable. Unfortunately, Eq. (2.1.4) is not among the enumeration.

Perturbation theory is difficult to apply because an energy level with principal quantum number n is n^2-fold degenerate, and there is no known, useful basis in which the diamagnetic Hamiltonian, Eq. (2.1.5d), is analytically diagonal. As discussed in Sec. 2.1, there is no reason to believe that perturbation theory will produce a convergent series for the energy. However, a simple analytical expression for the first-order diamagnetic shift and the correct zeroth-order eigenstates would be desirable for making predictions in the l–mixing regime; that is, when $< H_d > \ll n^{-3}$ and n–mixing may be ignored.

This situation is distinct from that of the hydrogen atom in a uniform *electric* field [LAL77, pp. 287-291]. There, the total Hamiltonian is separable in parabolic coordinates, and for any n the atom-field interaction is diagonal in the basis of parabolic states. Thus calculating the first-order effect of the electric field on hydrogen is straightforward, and perturbations up to twenty-fifth order in the electric field have been found [SIL78]. Each of these terms include the contribution of the continuum.

Again, the series is divergent for all non-zero values of the electric field.

In this section, the representation of $H_o(B)$ in a spherical basis is discussed. The selection rules and some matrix elements are presented, followed by some numerical results. Finally, the implication of level "crossings" among states with the same parity and azimuthal quantum numbers is studied.

Selection Rules and Some Matrix Elements

Our goal is to represent $H_o(B)$ as a matrix in a basis of spherical hydrogenic states, and then diagonalize the matrix to find the new energies and states. We should include the complete set of all bound and continuum states with a given m and π, but that is not practical. Referring to Eqs. (2.1.5), we have

$$< n'l'm' \mid H_o \mid nlm > = -\frac{1}{2n^2}\delta_K(n', n)\delta_K(l', l)\delta_K(m', m) , \qquad (2.2.1a)$$

and

$$< n'l'm' \mid H_p \mid nlm > = \frac{1}{2}Bm\,\delta_K(n', n)\delta_K(l', l)\delta_K(m', m) , \qquad (2.2.1b)$$

where δ_K is the Kronecker delta, which takes the value one if the arguments are equal, and zero otherwise. The atomic and paramagnetic Hamiltonians are diagonal in this basis. Furthermore, for fixed m, the paramagnetic Hamiltonian is proportional to the unit matrix, which means that we need only represent $H_o + H_d$ in the basis, then diagonalize, and finally add $Bm/2$ to each resulting diagonal matrix element.

Matrix elements of the diamagnetic operator may be written as

$$< n'l'm' \mid H_d \mid nlm > = \frac{1}{8}B^2 < n'l' \mid r^2 \mid nl >< l'm' \mid \sin^2\theta \mid lm > . \qquad (2.2.1c)$$

The radial and angular factors are considered separately.

The angular matrix element is evaluated by developing $\sin^2\theta$ in terms of spherical harmonics:

$$\sin^2\theta = \frac{2}{3}\sqrt{4\pi}Y_{00}(\Omega) - \frac{2}{3}\sqrt{\frac{4\pi}{5}}Y_{20}(\Omega) . \qquad (2.2.2a)$$

Then the matrix element may be evaluated using the Gaunt formula [WEI78, pp. 10-33]. This shows that the matrix elements vanish unless

$$m' = m \text{ and } l' = l \text{ or } l \pm 2 . \qquad (2.2.2b)$$

The value is

$$< l'm' \mid \sin^2\theta \mid lm > = \frac{2(l^2+l-1+m^2)}{(2l-1)(2l+3)} \delta_K(m',m)\delta_K(l',l)$$

$$- \left[\frac{(l_<+m+2)(l_<+m+1)(l_<-m+2)(l_<-m+1)}{(2l_<+5)(2l_<+3)^2(2l_<+1)}\right]^{1/2} \delta_K(m',m)\delta_K(l',l\pm 2) . \qquad (2.2.2c)$$

The radial matrix elements are more difficult to evaluate. Here we outline a snazzy technique. Baym [BAY73] presents a transformation of the radial Schroedinger equation due to Schwinger. (We have not found the original reference.) In configuration space, the radial equation for hydrogen (in zero field) is

$$\frac{d^2R}{dr^2} + \frac{2}{r}\frac{dR}{dr} + \left[2E + \frac{2}{r} - \frac{l(l+1)}{r^2}\right]R = 0 . \tag{2.2.3a}$$

Let

$$r = \frac{\lambda}{2}\rho^2 , \tag{2.2.3b}$$

and

$$R(r) = \frac{F(\rho)}{\rho} . \tag{2.2.3c}$$

Then Eq. (2.2.3a) becomes

$$\frac{d^2F}{d\rho^2} + \frac{1}{\rho}\frac{dF}{d\rho} + \left[2\lambda^2 E\rho^2 + 4\lambda - \frac{(2l+1)^2}{\rho^2}\right]F = 0 \tag{2.2.3d}$$

which is the radial equation of a two-dimensional isotropic harmonic oscillator (!) with energy, frequency, and angular momentum given by

$$E_{os} = 2\lambda , \tag{2.2.3e}$$

$$\omega_{os} = \sqrt{-2\lambda^2 E} , \tag{2.2.3f}$$

and

$$m_{os} = 2l+1 . \tag{2.2.3g}$$

The harmonic oscillator may be solved by well-known algebraic methods [CDL77, pp. 727-741]. Therefore, given the energies and normalized wave functions of the two-dimensional harmonic oscillator, we can immediately write the energies and wave

functions of the radial equation for hydrogen, using Eqs. (2.2.3b-c, e-g). If the hydrogenic radial wave functions are to be normalized, we find that

$$\lambda = \frac{\sqrt{2}}{n} , \tag{2.2.3h}$$

and

$$\omega_{os} = \frac{\sqrt{2}}{n^2} \tag{2.2.3i}$$

where n is the usual principal quantum number for hydrogen.

A very useful property of harmonic oscillators is that the dynamical operators may be written in terms of the raising and lowering operators. This can be used to evaluate matrix elements for the harmonic oscillator, and thus hydrogenic radial matrix elements. Here we present some of the latter:

$$< nl \mid r^g \mid nl > = \frac{n^{g-1}}{2^{g+1}} \sum_{s=0}^{g+1}{}' \binom{g+1}{s}^2 \frac{(n+l+1+g-s)!}{(n+l)!} \frac{(n-l-1)!}{(n-l-1-s)!} , \tag{2.2.4a}$$

where g is a non-negative integer, the sum extends over terms with non-negative factorial arguments, and the first factor in the sum is the standard binomial coefficient:

$$\binom{r}{s} = \frac{r!}{s!(r-s)!} . \tag{2.2.4b}$$

Specifically, we have

$$< nl \mid nl > = 1 , \tag{2.2.4c}$$

$$< nl \mid r \mid nl > = \frac{1}{2}[3n^2 - l(l+1)] , \tag{2.2.4d}$$

$$< nl \mid r^2 \mid nl > = \frac{n^2}{2}[5n^2 + 1 - 3l(l+1)] . \tag{2.2.4e}$$

Now, a few less common ones:

$$< n\ l-1 \mid nl > = \frac{1}{n}\sqrt{n^2 - l^2} , \tag{2.2.5a}$$

$$< n\ l-1 \mid r \mid nl > = \frac{3}{2} n \sqrt{n^2 - l^2} , \tag{2.2.5b}$$

$$< n\ l-2 \mid r^2 \mid nl > = \frac{5}{2} n^2 \sqrt{(n^2 - l^2)[n^2 - (l-1)^2]} . \tag{2.2.5c}$$

Most of theses results have appeared elsewhere, though the derivation is novel. (Equations (2.2.4e) and (2.2.5c) are in the review article by Garstang [GAR77]; Eqs. (2.2.4d), (2.2.4e), and (2.2.5b) appear in Condon and Shortley [COS51, p. 117, p. 132].)

In view of the angular momentum selection rules (Eq. (2.2.2b)), only Eqs. (2.2.4e) and (2.2.5c) are needed to evaluate the matrix elements of H_d within a given n. However, matrix elements between states of *different* n present a formidable challenge. The oscillator representation can be used, but it involves two oscillators with different frequencies. Such calculations usually *result* in hypergeometric functions which are difficult to evaluate accurately. For matrix elements

$< nl \mid r \mid n' l-1 >$, the reader is referred to Condon and Shortley [COS51, pp. 131-133]. No references have been found for r^2 off-diagonal matrix elements. The lack of selection rules on n illustrates a serious drawback to the spherical basis for analytical work. However, it readily generalizes to alkali-metal atoms as discussed below.

Though degenerate, there are some states which are not coupled by H_d to any other state with the same n, and hence, the first-order diamagnetic shift is given by Eq. (2.2.1c). These states are

$$| n \; l=n-1 \; m=\pm(n-1) > , \tag{2.2.6a}$$

$$| n \; l=n-1 \; m=\pm(n-2) > , \tag{2.2.6b}$$

$$| n \; l=n-2 \; m=\pm(n-2) > , \tag{2.2.6c}$$

$$| n \; l=n-2 \; m=\pm(n-3) > . \tag{2.2.6d}$$

For $n \geq 4$, there are 8 such states at a given n; for $n=2$ and 3, the number of these "effectively non-degenerate" states is 4 and 7. These states have large values of m, and are difficult to access experimentally [HUK83].

The $n=3$ level is the lowest level for which degeneracy is relevant. States $| 3\ 0\ 0 >$ and $| 3\ 2\ 0 >$ are coupled by H_d, and degenerate perturbation theory requires the construction of linear combinations of these state which diagonalize H_d. In the ordered basis $\{ | 3\ 0\ 0 >, | 3\ 2\ 0 > \}$, we have

$$H_d = \frac{1}{8}B^2 \begin{bmatrix} 138 & -30\sqrt{2} \\ -30\sqrt{2} & 60 \end{bmatrix} . \qquad (2.2.7a)$$

The (first-order) eigenvalues and the (zeroth-order) eigenstates are

$$E^{(1)}_{3+0}(B) = 156.628,148,2 \left[\frac{1}{8}B^2\right] , \qquad (2.2.7b)$$

$$E^{(1)}_{3-0}(B) = 41.371,881,85 \left[\frac{1}{8}B^2\right] , \qquad (2.2.7c)$$

$$| 3 + 0 (0) > = 0.915,629,010 | 3\ 0\ 0 > - 0.402,024,273 | 3\ 2\ 0 > , \qquad (2.2.7d)$$

$$| 3 - 0 (0) > = 0.402,024,273 | 3\ 0\ 0 > + 0.915,629,010 | 3\ 2\ 0 > . \qquad (2.2.7e)$$

Silverstone and Moats [SIM81] have computed numerically the ("exact") perturbation series to 87^{th} order for each of these states.

Numerical Results

We now have constructed an analytic matrix representation of $H_o(B)$ using the hydrogenic spherical basis, for a given n. Therefore, we can find the eigenvalues and eigenstates, neglecting n-mixing, by diagonalizing the matrix. These are the first-order energies and the zeroth-order ("right linear combination of") states for the perturbation H_d. These *states* are field independent, because within a fixed n, the atomic Hamiltonian, H_o, is proportional to the unit matrix, and therefore unaffected by diagonalization. Thus, the only matrix elements of $H_o(B)$ which are not part of a unit

matrix are those of H_d, and all of those are proportional to B^2.

However, finding eigenvalues and eigenvectors of a matrix *analytically* is not generally possible if the dimension of the matrix is greater then four. (It is often quite difficult if the dimension of the matrix is greater than two!) Also, n-mixing can be important, and we do not have matrix elements of r^2 between states with different n's. Therefore, it is necessary to implement numerical methods first to create the (finite) representation of $H_o(B)$ in the spherical basis, and second to diagonalize the resulting matrix. (We do use the analytic results for the angular matrix elements, Eq. (2.2.2c).)

The technique we employ is quite flexible and may also be applied to alkali-metal atoms. Since hydrogen may be considered as an alkali-metal atom, the method is discussed later, in Sec. 3.2. Here we only present the results for hydrogen, displayed in the standard form of energy levels as a function of magnetic field.

Because of the memory limitation imposed by the compiler on our computer, the basis size is (usually) limited to approximately 150 states. For a given m and π, we select n's which are closest to the energy range under study, since these states are likely to have the largest diamagnetic matrix elements and the smallest energy differences. We also neglect the contribution of the continuum. The difference in energy between states n and $n+1$ is nearly n^{-3}, while the difference in energy between a state n and the zero-field ionization limit is $1/2n^2$. On the other hand, the ground state's nearest neighbor ($|2\,0\,0>$) differs in energy by 3/8, while the zero-field

ionization limit differs in energy by 1/2. Fractionally speaking, Rydberg states are closer to each other than to the continuum. Therefore, although we know that a large part of the ground-state second-order diamagnetic shift comes from the continuum, we feel justified in neglecting the continuum in many calculations of Rydberg states. An important motivation of our experiment is to check the reliability of these calculations.

Figure 2.2.1 shows the energy levels of $m=0$, $\pi=-1$ states of hydrogen in a magnetic field ranging from 0 to 2.5 T. The displayed energy range encompasses states around $n=40$. Evidently, the energies depend quadratically on the field. Also apparent is the change in spacing of levels of the same n at a fixed field, about one-fifth of the way up the manifold.

A labeling scheme is needed to identify the states. We use the so-called Castro convention, after Jarbas Castro [CAS81]. States are named by the principal quantum number n from which they come, the azimuthal quantum number m, and a non-negative integer k, which ranges from 0 (highest energy) to $n-|m|-1$ (lowest energy), and takes on odd values for odd parity states, and even values for even parity states. Each line of Fig. 2.2.1 can be associated with a state $|nkm>$. For $n=40$, $m=0$, $\pi=-1$, we have $k=1, 3, 5, \cdots, 37, 39$. The number k is not the eigenvalue of some operator which commutes with $H_o(B)$. The only physical significance is that higher values of k indicate lower diamagnetic shifts, among states of a fixed n. This scheme does not work if it is not possible to say from which n a

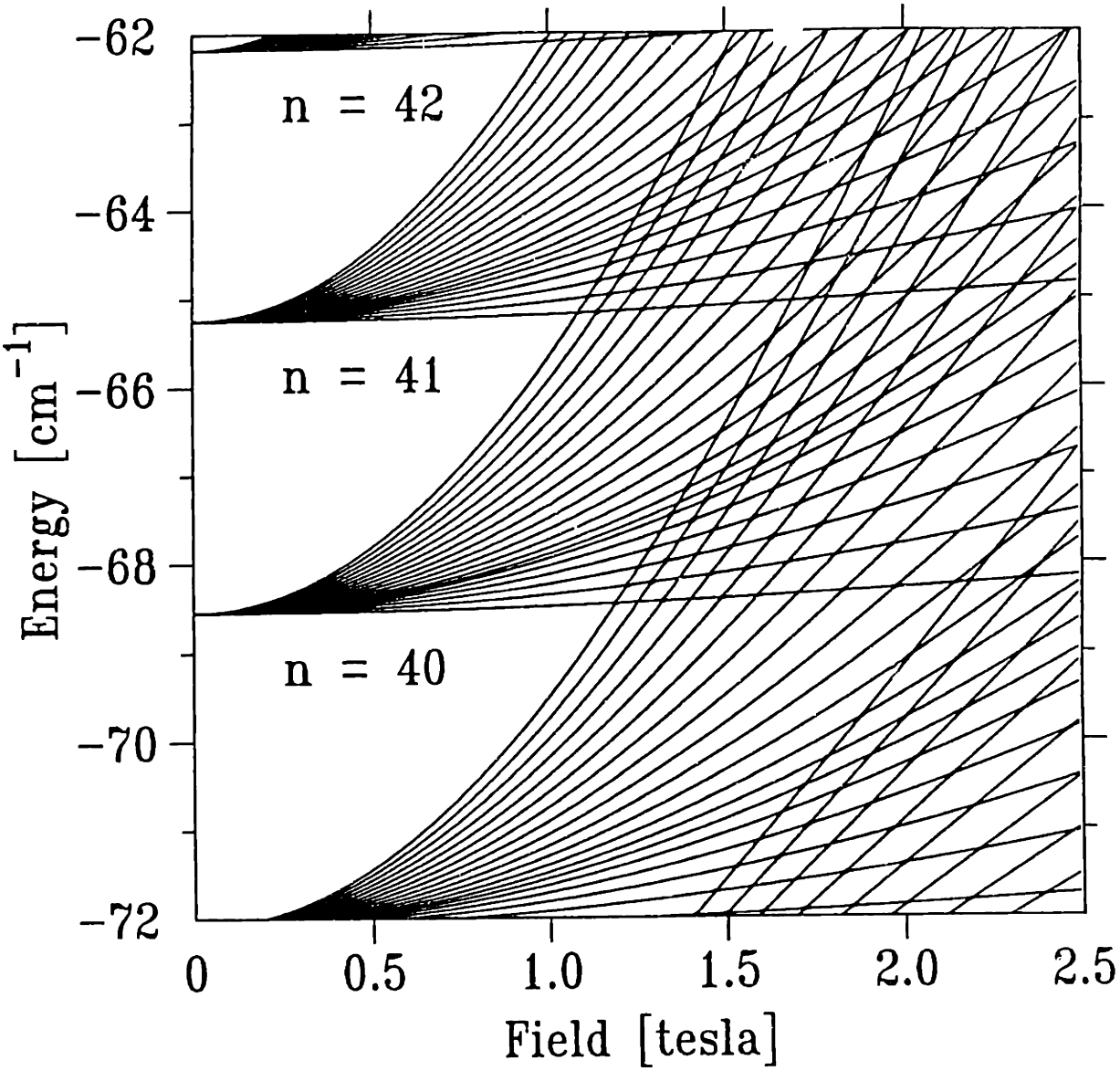

Figure 2.2.1. Hydrogen energy levels in a magnetic field. The basis contained 120 m=0, π=−1 states: n=38→43. The plot shows the quadratic dependence of energy on magnetic field, the interesting spacing between levels of a given n at a fixed field, and the close crossing of levels from different n's.

state has come.

Level Crossing and Symmetry

In Fig. 2.2.1, levels from different n's very nearly cross each other. The energies are degenerate to well within our computational precision, about 0.0001 cm^{-1}. Any levels which appear not to cross are the result of the plotting program's method of interpolation between field points.

The levels do not cross exactly. That is inferred by looking at the energy levels from lower values of n [ZKK80], where levels from different values of n look like they are going to cross, but repel when they get close. We call these features "anticrossings." The minimum separation between the lowest energy state from $n+1$ and the highest state of n is plotted in Fig. 2.2.2. We see that the anticrossing size decreases exponentially with n. A fit to these calculations yields for the anticrossing size, a,

$$a \sim (9\times10^{6}\mathrm{cm}^{-1})e^{-2.10\sqrt{n(n+1)}}, \qquad (2.2.8)$$

so the lowest-field anticrossing size between n=39 and n=40 (states $|\,39\ 0\ 0\,>$ and $|\,40\ 38\ 0\,>$) is about 2 Hz.

Degeneracy is always associated with some symmetry, for states with the same energy must be distinguishable by some observable (Hermitian operator which commutes with the Hamiltonian) in order to be meaningfully different states.

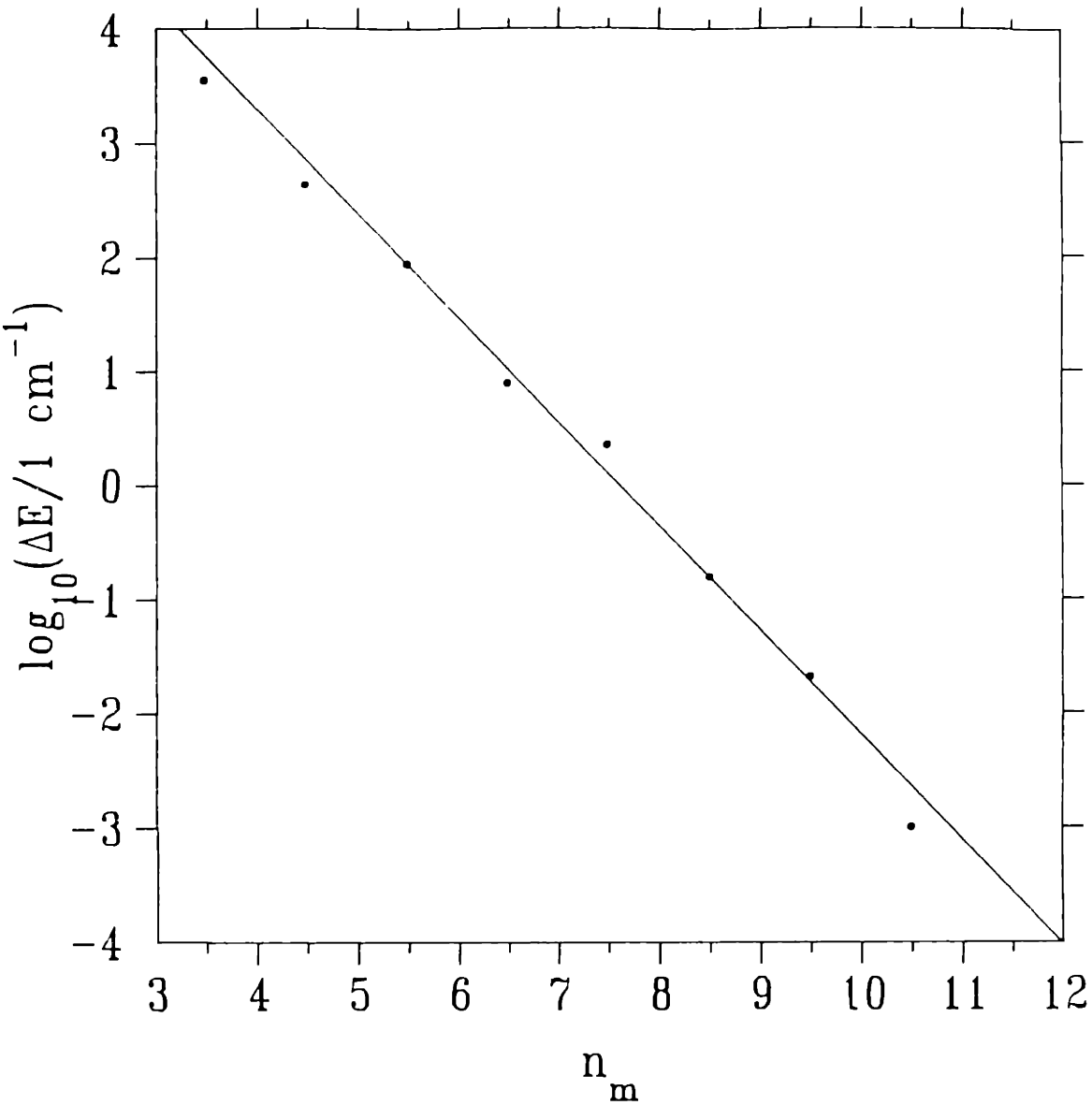

Figure 2.2.2. Anticrossing size as a function of n_m. The minimum separation of the lowest-field anticrossing between n and $n+1$ is plotted as a function of the geometric mean of n and $n+1$: $n_m = \sqrt{n(n+1)}$. The calculations here are for states with $m=0,\pi=+1$.

Sometimes the symmetry is geometrically evident, such as the rotational invariance of $H_o(B)$ about the field axis. Other times, the symmetry depends on the detailed nature of the potential, such as the l-degeneracy for states of fixed n in the zero-field hydrogen atom. The latter degeneracy is often called "accidental," but in 1935 V. Fock found that the hydrogen atom could be represented by "hyperspherical" harmonics in a four-dimensional momentum space [FOC35]. In that representation, the n^2-fold degeneracy is evident.

The study of level crossings reveals degeneracies in the atom-field system. The "no-crossing rule" [MER70] shows that level crossings indicate the existence of some symmetry. Let us consider this rule in the context of the hydrogen atom in a magnetic field. The reasoning is indirect.

Let $| 1; B >$ and $| 2; B >$ be simultaneous eigenstates of $H_o(B)$, L_z, and π. That means

$$H_o(B) | 1; B > = E_1(B) | 1; B > , \tag{2.2.9a}$$

$$H_o(B) | 2; B > = E_2(B) | 2; B > , \tag{2.2.9b}$$

$$L_z | 1; B > = m_1 | 1; B > , \tag{2.2.9c}$$

$$L_z | 2; B > = m_2 | 2; B > , \tag{2.2.9d}$$

$$\pi \mid 1; B > = \pi_1 \mid 1; B > , \tag{2.2.9e}$$

and

$$\pi \mid 2; B > = \pi_2 \mid 2; B > . \tag{2.2.9f}$$

We tentatively *assume* that these states becomes degenerate at some value of the field, $B = B_c$:

$$E_1(B_c) = E_2(B_c) . \tag{2.2.9g}$$

In a neighborhood of B_c, the Hamiltonian may be expanded as

$$H_o(B) \simeq H_o(B_c) + (B - B_c)W \tag{2.2.10a}$$

where, if the magnetic field is in the z-direction, we have

$$W = \left[\frac{\partial H_o(B)}{\partial B}\right]_{B=B_c} = \frac{1}{2}L_z + \frac{1}{4}B_c\rho^2 . \tag{2.2.10b}$$

Now consider matrix elements of W:

$$W_{11}(B) = \frac{1}{2}m_1 + \frac{1}{4}B_c < 1; B \mid \rho^2 \mid 1; B > , \tag{2.2.10c}$$

$$W_{22}(B) = \frac{1}{2}m_2 + \frac{1}{4}B_c < 2; B \mid \rho^2 \mid 2; B > , \tag{2.2.10d}$$

and

$$W_{12}(B) = \frac{1}{4}B_c < 1; B \mid \rho^2 \mid 2; B > . \tag{2.2.10e}$$

From degenerate perturbation theory, we must have

$$\mathrm{Re}[W_{12}(B_c)] = 0 \,, \tag{2.2.11a}$$

and

$$\mathrm{Im}[W_{12}(B_c)] = 0 \,, \tag{2.2.11b}$$

if the states are to be degenerate at $B = B_c$. Equations (2.2.9g), (2.2.11a), and (2.2.11b) are three algebraic equations in one unknown. Generally, it is not possible to satisfy these equations simultaneously, and hence the assumption of degenerate eigenstates is false. Unless $W_{12}(B_c)$ is identically zero for all B_c, or unless Eqs. (2.2.9g), (2.2.11a), and (2.2.11b) are dependent, then the levels must not cross.

As an example, assume states $|\,1; B>$ and $|\,2; B>$ have different values of m: $m_1 \neq m_2$. Then $W_{12}(B_c) = 0$, because ρ^2 does not couple states of different m. Therefore, states with different m's may cross exactly. An identical argument shows that states with different π's may cross exactly.

Constants of motion are associated with separation constants in the "separation of variables" technique for solving partial differential equations. For example, the fact L_z commutes with $H_o(B)$ implies that the wave function may be factored as in Eq. (2.1.6b).

Figure 2.2.2 shows that some states with the same m and π very nearly cross. We feel this suggests the existence of an *approximate* symmetry. By that we mean the

Hamiltonian may be written as

$$H_o(B) = H_{SYM}(B) + H_{SB}(B) \ . \tag{2.2.12}$$

The operator $H_{SYM}(B)$ has three independent constants of motion (an additional one to L_z and π), exactly crossing levels, and a coordinate system in which $H_{SYM}(B)$ separates. The operator $H_{SB}(B)$ breaks the symmetry, and causes (vanishingly) small anticrossings between some Rydberg states. It might cause large anticrossings between other Rydberg states, indicating a breakdown of the symmetry.

Such a division is speculative, because we have not found a way to do it. Other authors believe our conjecture is incorrect. Derek Richards considers the small anticrossings to reflect the fact that the states we studied in Fig. 2.2.2 have wave functions which occupy completely different regions of configuration space, and do not indicate the presence of another constant of motion [RIC83]. He claims that a Hamiltonian either is separable or not, and therefore energy levels either cross or not. We think that the size of an anticrossing is the measure of the *degree* of non-separability. Jean-Claude Gay feels that our conclusion is correct, but that our reasoning is wrong, because anticrossing sizes depend on the basis used [GAY86]. However, we find that anticrossing *sizes* away from the "edges" of the basis are very insensitive to the particular basis used, though the field location of the anticrossing may change somewhat.

Although the observation of the very small anticrossings among Rydberg diamagnetic levels has stimulated much work on the symmetry of the problem, no such division of the Hamiltonian has been found. Perhaps it never will be.

2.3 Alternate Representations of Hydrogen

In the last section we found that the basis of hydrogenic spherical states is quite cumbersome for analytic calculations. However, the numerical "observation" of very small anticrossings among diamagnetic Rydberg levels inspired real theoretical physicists to study the problem. Exploiting the special symmetries of the Coulomb potential, substantial results have been produced. These include an understanding of the spacing of levels in the l–mixing regime, "exact" perturbation series for diamagnetic Rydberg states, and optimal bases for representing the Hamiltonian prior to diagonalization. Here we discuss some of these.

The Angular Momentum Representation

We begin with a review of the angular momentum representation of the (zero-field) hydrogen atom. The subject is discussed in many quantum mechanics books, especially in one by Englefield [ENG72]. The summation convention for the components of vector operators is used throughout this discussion.

Consider a Hermitian operator defined on Cartesian coordinates:

$$\vec{O} = (O_x, O_y, O_z) = (O_1, O_2, O_3) \; . \tag{2.3.1}$$

The operator is an angular momentum if the following commutation relations hold among its coordinates:

$$[O_i, O_j] = i\epsilon_{ijk} O_k \ . \tag{2.3.2a}$$

The eigenvalues and eigenstates follow immediately:

$$O^2 \mid a \ b > = a(a+1) \mid a \ b > , \tag{2.3.2b}$$

and

$$O_3 \mid a \ b > = b \mid a \ b > , \tag{2.3.2c}$$

where

$$a = 0, \ 1/2, \ 1, \ 3/2, \ \cdots \ , \tag{2.3.2d}$$

and

$$b = -a, -a+1, \ \cdots \ , a-1, a \ . \tag{2.3.2e}$$

The eigenstates are related by the operators

$$O_\pm = O_1 \pm iO_2 \tag{2.3.2f}$$

by

$$O_\pm \mid a \ b > = \sqrt{a(a+1) - b(b\pm1)} \mid a \ b\pm1 > . \tag{2.3.2g}$$

The Hamiltonian for the (field-free) hydrogen atom is

$$H_o = \frac{1}{2}p^2 - \frac{1}{r} \ , \tag{2.3.3}$$

and since the potential is spherically symmetric, commutes with all components of the

orbital angular momentum $\vec{L} = \vec{r} \times \vec{p}$:

$$[H_o, L_i] = 0, \text{ for } i = 1,2,3 . \tag{2.3.4a}$$

We know that simultaneous eigenstates of H_o, L^2, and L_3 may be constructed:

$$H_o \mid Elm > = E \mid Elm > , \tag{2.3.4b}$$

$$L^2 \mid Elm > = l(l+1) \mid Elm > , \tag{2.3.4c}$$

and

$$L_3 \mid Elm > = m \mid Elm > . \tag{2.3.4d}$$

We expect that states with the same l but different m's will be $(2l+1)$-fold degenerate. This is because Eqs. (2.3.2f) and (2.3.4a) imply that

$$[H_o, L_\pm] = 0 . \tag{2.3.4e}$$

Therefore, if we have a state $\mid Elm >$ which satisfies Eq. (2.3.4b), we can construct two other states, $\mid Elm \pm 1 >$, with the same energy:

$$H_o L_\pm \mid Elm > = L_\pm H_o \mid Elm > = L_\pm E \mid Elm > = E L_\pm \mid Elm > , \tag{2.3.4f}$$

and by Eq. (2.3.2g),

$$H_o \mid Elm \pm 1 > = E \mid Elm \pm 1 > . \tag{2.3.4g}$$

This process may be extended to construct all $2l+1$ degenerate sublevels.

For the *Coulomb* potential there is another constant of motion:

$$\vec{A}' = \frac{1}{2}(\vec{p}\times\vec{L} - \vec{L}\times\vec{p}) - \frac{\vec{r}}{r} . \tag{2.3.5a}$$

This operator was discovered in classical mechanics, and first used to find the quantal solutions of H_o by Pauli [PAU26]. It can be shown [ENG72, pp. 109-111] that $\vec{A}'$ possesses the following properties:

$$[H_o, A_i'] = 0 , \tag{2.3.5b}$$

$$\vec{A}'\cdot\vec{L} = \vec{L}\cdot\vec{A}' = 0 , \tag{2.3.5c}$$

$$A'^2 = 1 + 2H_o(L^2+1) , \tag{2.3.5d}$$

$$[A_i', L_j] = i\varepsilon_{ijk}A_k' , \tag{2.3.5e}$$

and

$$[A_i', A_j'] = -2iH_o\varepsilon_{ijk}L_k . \tag{2.3.5f}$$

Equation (2.3.5b) shows that $\vec{A}'$ is a constant of motion; Eq. (2.3.5e) shows that $\vec{A}'$ is a vector, but Eq. (2.3.5f) shows that $\vec{A}'$ is not an angular momentum. The other relations will be computationally useful below.

In the present discourse, we wish to consider only states with the same energy. We introduce a new operator defined by

$$\vec{A} = \sqrt{-\frac{1}{2H_o}}\,\vec{A}' \,, \tag{2.3.6a}$$

which is Hermitian if $E<0$. Useful properties of $\vec{A}$ are now enumerated:

$$[H_o, A_i] = 0 \,, \tag{2.3.6b}$$

$$[A_i, A_j] = i\varepsilon_{ijk}L_k \,, \tag{2.3.6c}$$

$$[A_i, L_j] = i\varepsilon_{ijk}A_k \,, \tag{2.3.6d}$$

$$\vec{A}\cdot\vec{L} = \vec{L}\cdot\vec{A} = 0 \,, \tag{2.3.6e}$$

and

$$H_o = -\frac{1}{2(A^2+L^2+1)} \,. \tag{2.3.6f}$$

Finally, we introduce two more operators:

$$\vec{J}_1 = \frac{1}{2}(\vec{L}+\vec{A}) \,, \tag{2.3.7a}$$

and

$$\vec{J}_2 = \frac{1}{2}(\vec{L}-\vec{A}) \,. \tag{2.3.7b}$$

These operators have even more exciting properties:

$$[J_{1i}, J_{1j}] = i\varepsilon_{ijk}J_{1k} \,, \tag{2.3.7c}$$

$$[J_{2i}, J_{2j}] = i\varepsilon_{ijk}J_{2k} \ , \tag{2.3.7d}$$

$$[J_{1i}, J_{2j}] = 0 \ , \tag{2.3.7e}$$

$$J_1^2 = J_2^2 = \frac{1}{4}(L^2+A^2) \ , \tag{2.3.7f}$$

and

$$H_o = -\frac{1}{2[2(J_1^2+J_2^2)+1]} \ . \tag{2.3.7g}$$

Thus, we have represented the Hamiltonian for hydrogen in terms of two independent angular momenta of equal magnitude. The basis states are product angular momentum states:

$$|j_1m_1j_2m_2> = |j_1m_1> \times |j_2m_2> \ , \tag{2.3.8a}$$

and the quantum numbers are determined by

$$J_1^2 \ |j_1m_1j_2m_2> = j_1(j_1+1)\,|j_1m_1j_2m_2> \ , \tag{2.3.8b}$$

$$J_2^2 \ |j_1m_1j_2m_2> = j_2(j_2+1)\,|j_1m_1j_2m_2> \ , \tag{2.3.8c}$$

$$J_{1z} \ |j_1m_1j_2m_2> = m_1\,|j_1m_1j_2m_2> \ , \tag{2.3.8d}$$

and

$$J_{2z} \ |j_1m_1j_2m_2> = m_2\,|j_1m_1j_2m_2> \ . \tag{2.3.8e}$$

The eigenvalues of H_o may be found immediately:

$$E = -\frac{1}{2[4j_1(j_1+1)+1]} = -\frac{1}{2(2j_1+1)^2} = -\frac{1}{2n^2} \tag{2.3.9a}$$

where

$$n = 2j_1+1 = 1, 2, 3, \cdots . \tag{2.3.9b}$$

The degeneracy of a hydrogenic level is clearly n^2, for the energy is independent of m_1 and m_2, and m_1 takes on $2j_1+1 = n$ values while m_2 takes on $2j_2+1 = n$ values.

The utility of this representation comes from the ability to represent dynamical operators in terms of the angular momenta, $\vec{J}_1$ and $\vec{J}_2$. Let us introduce another operator

$$\vec{B} = -2\vec{r} - i[\vec{r}(\vec{r}\cdot\vec{p})-2r^2\vec{p}] . \tag{2.3.10a}$$

Its commutation relation with the Hamiltonian is [ENG72, p. 57]

$$[\vec{B}, H_o] = 3\sqrt{-2H_o}\,\vec{A} - 4\vec{r}H_o . \tag{2.3.10b}$$

The matrix element of the commutator between *any* two states with the same energy is zero, because

$$< E\alpha | [\vec{B}, H_o] | E\alpha' > = (E-E)< E\alpha | \vec{B} | E\alpha' > = 0 , \tag{2.3.10c}$$

where α refers to any complete set of quantum numbers. Then Eq. (2.3.10b) gives

$$0 = 3(\frac{1}{n})< E\alpha \mid \vec{A} \mid E\alpha' > - 4< E\alpha \mid \vec{r} \mid E\alpha' >(- \frac{1}{2n^2}) , \tag{2.3.10d}$$

or,

$$\vec{r} \rightarrow - \frac{3}{2} n\vec{A} . \tag{2.3.10e}$$

The arrow means "$\vec{r}$ is replaced as an operator by $- \frac{3}{2} n\vec{A}$ in any matrix element between states of the same energy."

This operator makes the Stark effect easy to evaluate in first order. The perturbing Hamiltonian is

$$H_S = \vec{F} \cdot \vec{r} \rightarrow - \frac{3}{2} n\vec{F} \cdot \vec{A} . \tag{2.3.11a}$$

We quantize both $\vec{J}_1$ and $\vec{J}_2$ along the field axis $\vec{F}=F\hat{z}$. Equations (2.3.7a) and (2.3.7b) imply that

$$\vec{A} = \vec{J}_1 - \vec{J}_2 , \tag{2.3.11b}$$

and therefore

$$H_S \rightarrow - \frac{3}{2} n (J_{1z} - J_{2z})F \tag{2.3.11c}$$

which is obviously diagonal in the product angular momentum basis. Thus the first-order energy shift is

$$E_S^{(1)} = -\frac{3}{2} n (m_1 - m_2) F \ . \tag{2.3.11d}$$

This suggests that when these two angular momenta are quantized along the same axis, that we may identify the product states as the well-known parabolic states [LAL77, pp. 128-132, 287-291].

The spherical states may be recovered by adding these two angular momenta when they are quantized along the same axis. This follows from Eqs. (2.3.7a) and (2.3.7b):

$$\vec{L} = \vec{J}_1 + \vec{J}_2 \ . \tag{2.3.12a}$$

The machinery of Clebsch-Gordan coefficients then provides the transformation between spherical and parabolic states:

$$| nlm > = \sum_{m_1 m_2} < j_1 m_1 j_2 m_2 | lm > | j_1 m_1 j_2 m_2 > \tag{2.3.12b}$$

where $j_1 = j_2 = (n-1)/2$. The coefficients vanish unless $m = m_1 + m_2$. This is in agreement with the z-component of Eq. (2.3.12a). This relation was first derived by David Park [PAR60] in the seminal paper on this methodology.

If both electric and magnetic fields are present, and the magnetic field is sufficiently weak so that the diamagnetic interaction may be neglected, the perturbing Hamiltonian may be written as

$$H_{Sp} = \vec{F}\cdot\vec{r} + \frac{1}{2}\vec{B}\cdot\vec{L} \rightarrow -\frac{3}{2}n\vec{F}\cdot\vec{A} + \frac{1}{2}\vec{B}\cdot\vec{L}\ , \tag{2.3.13a}$$

or,

$$H_{Sp} \rightarrow \vec{\omega}_1\cdot\vec{J}_1 + \vec{\omega}_2\cdot\vec{J}_2 \tag{2.3.13b}$$

where

$$\vec{\omega}_1 = -\frac{3}{2}n\vec{F} + \frac{1}{2}\vec{B}\ , \tag{2.3.13c}$$

and

$$\vec{\omega}_2 = +\frac{3}{2}n\vec{F} + \frac{1}{2}\vec{B}\ . \tag{2.3.13d}$$

If $\vec{J}_1$ is quantized along $\vec{\omega}_1$ and $\vec{J}_2$ is quantized along $\vec{\omega}_2$, then the product angular momentum states diagonalize H_{Sp}, and the first-order energy shift is

$$E_{Sp}^{(1)} = \omega_1 m_1 + \omega_2 m_2\ . \tag{2.3.13e}$$

Transformations between different bases may require rotations of the quantization axes, which is accomplished with the Wigner "D" matrices [WEI78, pp.104-107]. Degeneracies arise when $\omega_1 = \omega_2$; that is, when the fields are perpendicular, or one is zero. This was first pointed out by Demkov, Monozon, and Ostrovskii [DMO69], though Pauli noted that H_{Sp} could be diagonalized in this manner [PAU26].

Returning to diamagnetism, let $\vec{B} = B\hat{z}$ define the quantization axes of $\vec{J}_1$ and $\vec{J}_2$. Among the many important papers of Delande and Gay, one contains a rigorous

derivation of the operator replacernent for the diamagnetic Hamiltonian [DEG84]. Their result is

$$H_d = \frac{1}{8}B^2\rho^2$$

$$\rightarrow \frac{1}{16}B^2n^2(3n^2+1-4J_{1z}^2-4J_{2z}^2+4J_{1z}J_{2z}-4J_{1+}J_{2-}-4J_{1-}J_{2+}) \ . \qquad (2.3.14a)$$

This operator may be easily represented in the basis of product angular momenta. Unfortunately, no coupling of the angular momenta has been found that leads to a basis in which this operator is diagonal. This would have given the first-order diamagnetic energy shift and the zeroth-order states. That was the goal of this entire development, and it remains unachieved.

The diamagnetic operator replacement may be expressed in terms of $\vec{L}$ and $\vec{A}$ using Eqs. (2.3.7a), (2.3.7b), and (2.3.6f). The result is

$$H_d \rightarrow \frac{1}{16}B^2n^2(n^2+3+L_z^2+4A^2-5A_z^2) \ . \qquad (2.3.14b)$$

The last two factors in the parentheses express the essence of the symmetry of the (zeroth-order) diamagnetic states. They are often designated by the operator Λ:

$$\Lambda = 4A^2 - 5A_z^2 \ . \qquad (2.3.14c)$$

This operator was first derived in the quantal framework by David Herrick [HER82] using a different method. The zeroth-order diamagnetic eigenstates are eigenstates of

Λ. Using the Castro labeling scheme, we have

$$\Lambda \mid nkm > = \lambda_k \mid nkm > , \tag{2.3.14d}$$

where λ_k is an irrational number which (generally) can only be found numerically. The diamagnetic energy shift is given by

$$E_d^{(1)} = \frac{1}{16} B^2 n^2 (n^2+3+m^2+\lambda_k) . \tag{2.3.14e}$$

See Table 2.3.1 for an evaluation of λ_k for both parities in $n=40$, $m=0$.

k	$E^{(1)}$ (cm^{-1})	λ_k	γ	$E^{(\Gamma)}$ (cm^{-1})	$4m_l^2$	$E^{(V)}$ (cm^{-1})
0	3.10776	6220.2	39	3.11563	1	0.63639
1	2.96897	5870.8	38	2.99169	1	0.63639
2	2.83458	5532.5	37	2.87093	9	0.63322
3	2.70285	5200.9	36	2.75334	9	0.63322
4	2.57515	4879.4	35	2.63893	25	0.62686
5	2.45120	4567.4	34	2.52770	25	0.62686
6	2.33033	4263.2	33	2.41965	49	0.61733
7	2.21341	3968.8	32	2.31478	49	0.61733
8	2.09999	3683.3	31	2.21308	81	0.60461
9	1.98971	3405.7	30	2.11456	81	0.60461
10	1.88396	3139.5	29	2.01922	121	0.58872
11	1.78103	2880.4	28	1.92706	121	0.58872
12	1.68204	2631.2	27	1.83808	169	0.56966
13	1.58679	2391.4	26	1.75227	169	0.56966
14	1.49519	2160.9	25	1.66964	225	0.54741
15	1.40577	1938.3	24	1.59019	225	0.54741
16	1.32270	1726.6	23	1.51392	289	0.52199
17	1.24185	1523.1	22	1.44083	289	0.52199
18	1.16513	1330.0	21	1.37091	361	0.49338
19	1.09172	1145.2	20	1.30417	361	0.49338
20	1.02237	970.6	19	1.24061	441	0.46160
21	0.95712	806.4	18	1.18023	441	0.46160
22	0.89557	651.4	17	1.12303	529	0.42665
23	0.83826	507.2	16	1.06900	529	0.42665
24	0.78528	373.8	15	1.01815	625	0.38851
25	0.73693	252.1	14	0.97048	625	0.38851
26	0.69291	141.3	13	0.92599	729	0.34720
27	0.65991	58.2	12	0.88468	729	0.34720
28	0.61466	-55.7	11	0.84654	841	0.30270
29	0.60812	-72.2	10	0.81158	841	0.30270
30	0.53176	-264.4	9	0.77980	961	0.25503
31	0.53172	-264.5	8	0.75120	961	0.25503
32	0.43491	-508.2	7	0.72578	1089	0.20419
33	0.43431	-509.7	6	0.70353	1089	0.20419
34	0.32418	-786.9	5	0.68446	1225	0.15016
35	0.32409	-787.2	4	0.66857	1225	0.15016
36	0.20243	-1093.4	3	0.65586	1369	0.09296
37	0.20209	-1094.3	2	0.64633	1369	0.09296
38	0.06988	-1427.1	1	0.63997	1521	0.03257
39	0.06983	-1427.2	0	0.63679	1521	0.03257

Table 2.3.1. Diamagnetic shifts for $n=40$, $m=0$ at $B=1$ T. Diagonalization with only $n=40$ produced $E^{(1)}$. The factors λ_k, $E^{(\Gamma)}$, and $E^{(V)}$ were computed from Eqs. (2.3.14e), (2.3.15h), and (2.3.16e) respectively.

We see that λ_k changes sign where the spacings between different k's change in Fig. 2.2.1.

In the language of the approximate symmetry and the anticrossing of levels with the same m and π discussed in Sec. 2.2, we say that states with very different λ_k's are expected to exhibit very near crossings, while states with very similar λ_k's should have large anticrossings. This is different from an exact symmetry, where the eigenvalues of the symmetry operator need only be different to allow the exact crossing of levels.

Two limiting symmetries may be identified which correspond to the two types of spacings seen in Fig. 2.2.1. The trick is to find an approximation to H_d which can be easily diagonalized.

The first symmetry is associated with the low k states, which have the greatest diamagnetic shifts. We will call this the Γ regime. These states are localized in the xy-plane, without much extent along the z-axis, something like a disk. We expect that

$$< A_z^2 > \ll < A^2 > , \tag{2.3.15a}$$

so that

$$\Lambda \approx 4(A_x^2+A_y^2) , \tag{2.3.15b}$$

and then we have

$$H_d^{(\Gamma)} \rightarrow \frac{1}{16} B^2 n^2 (n^2+3+L_z^2+4A_x^2+4A_y^2) \ , \tag{2.3.15c}$$

which may be expressed in terms of the angular momenta as

$$H_d^{(\Gamma)} \rightarrow \frac{1}{16} B^2 n^2 [n^2+3+(J_{1z}+J_{2z})^2+4(J_{1x}-J_{2x})^2+4(J_{1y}-J_{2y})^2] \ . \tag{2.3.15d}$$

This is diagonal in the basis formed by coupling the angular momenta in the following way:

$$\vec{\Gamma} = (J_{1x}-J_{2x}, J_{1y}-J_{2y}, J_{1z}+J_{2z})$$

$$= (A_x, A_y, L_z) \ . \tag{2.3.15e}$$

Using Eqs. (2.3.7c), (2.3.7d), and (2.3.7e) we can show that

$$[\Gamma_i, \Gamma_j] = i \varepsilon_{ijk} \Gamma_k \ ; \tag{2.3.15f}$$

that is, $\vec{\Gamma}$ is an angular momentum. We know its eigenvalues and eigenstates. The "diamagnetic" operator is

$$H_d^{(\Gamma)} \rightarrow \frac{1}{16} B^2 n^2 (n^2+3+4\Gamma^2-3\Gamma_z^2) \ , \tag{2.3.15g}$$

which is diagonal in the $\vec{\Gamma}$ angular momentum basis. The matrix elements of $H_d^{(\Gamma)}$ are

$$E_d^{(\Gamma)} = \frac{1}{16} B^2 n^2 [n^2+3+4\gamma(\gamma+1)-3m^2] \ . \tag{2.3.15h}$$

Here, m is used as the eigenvalue of Γ_z, since $\Gamma_z = L_z$. Given n and m, we have

$$\gamma = n-1,\ n-2,\ \cdots\ ,|m|+1,|m|\ . \tag{2.3.15i}$$

Considering all possible m's for a given n, there are n^2 states. Equation (2.3.15h) should approximate well the diamagnetic energy shift of hydrogen for states with large γ (or small k). For $m=0$, $\gamma=n-1$ is an even parity state while $\gamma=n-2$ is an odd parity state. Equation (2.3.15h) is evaluated and displayed in Table 2.3.1. The agreement between Eq. (2.3.15h) and numerical diagonalization is quite good for small k's, but Eq. (2.3.15h) is an order of magnitude too large for large k's. Finally, Eq. (2.3.15h) predicts that the largest diamagnetic shift should be approximately $5B^2n^4/16$, which is a bit larger than $B^2n^4/8$. This coupling was tentatively suggested by J. J. Labarthe [LAB81], though his evaluation of H_d was not correct. The states of this symmetry type are sometimes called "rotators," for they have the symmetry of an angular momentum.

The second symmetry goes with the high k states, which have very small diamagnetic shifts. We call this the V regime. These states are localized along the z-axis, without much extent into the xy-plane, something like a tube. We expect

$$< A^2 > \approx < A_z^2 >\ , \tag{2.3.16a}$$

so that

$$\Lambda \approx -\ A_z^2\ , \tag{2.3.16b}$$

and

$$H_d^{(V)} \rightarrow \frac{1}{16}B^2n^2(n^2+3+L_z^2-A_z^2) , \tag{2.3.16c}$$

or

$$H_d^{(V)} \rightarrow \frac{1}{16}B^2n^2(n^2+3+4J_{1z}J_{2z}) . \tag{2.3.16d}$$

This is diagonal in the product angular momentum basis, or the parabolic basis. The matrix elements of $H_d^{(V)}$ are

$$E_d^{(V)} = \frac{1}{16}B^2n^2(n^2+3+4m_1m_2) . \tag{2.3.16e}$$

The range of m_1 and m_2 is

$$m_1, m_2 = -(\frac{n-1}{2}), -(\frac{n-1}{2})+1, \cdots, (\frac{n-1}{2})-1, (\frac{n-1}{2}) . \tag{2.3.16f}$$

If we are only interested in states with fixed m, then m_1 and m_2 are constrained by

$$m = m_1 + m_2 . \tag{2.3.16g}$$

The product angular momentum states are not states of good parity. However, since each state is two-fold degenerate, symmetric and antisymmetric combinations of the degenerate product angular momentum states yield states of good parity which still diagonalize $H_d^{(V)}$. (Exception: if n is odd and $m=0$, the state with $m_1=m_2=0$ is non-degenerate, but is already a state of good parity.) This model suggests that the high-k states should be parity-degenerate. This is found to be the case in hydrogen. (See also Clark [CLA81].) Predictions of Eq. (2.3.16e) are compared with numerical

diagonalization in Table 2.3.1. We see that Eq. (2.3.16e) is nearly a factor of two too small at the highest k's, where the agreement should be best. Evidently, the approximation of Eq. (2.3.16b) is too crude. However, when H_d is represented in this basis (Eq. (2.3.14a)), numerical diagonalization efficiently produces eigenvalues for the high-k states. This symmetry was first recognized by David Herrick [HER82]. The states of this symmetry type are sometimes called "vibrators," because they have the symmetry of two independent harmonic oscillators.

Further Developments

Delande and Gay used another representation that is not restricted to a particular n [DEG86]. The transformation uses *semi-parabolic* coordinates [FLU74], defined by

$$r = \frac{1}{2}(\xi^2+\eta^2) , \tag{2.3.17a}$$

$$\xi^2 = r + z , \tag{2.3.17b}$$

$$\eta^2 = r - z , \tag{2.3.17c}$$

and

$$\rho = \xi\eta . \tag{2.3.17d}$$

If we let

$$\psi(\vec{r}) = f_1(\xi)f_2(\eta)e^{im\phi} \tag{2.3.17e}$$

in the Schroedinger equation for the field-free hydrogen atom,

$$\nabla^2\psi + \frac{2}{r}\psi + 2E\psi = 0 , \tag{2.3.17f}$$

then we get

$$\frac{d^2f_1}{d\xi^2} + \frac{1}{\xi}\frac{df_1}{d\xi} + \left[2E\xi^2 - \frac{m^2}{\xi^2} + \alpha_1\right]f_1 = 0 , \tag{2.3.17g}$$

$$\frac{d^2f_2}{d\eta^2} + \frac{1}{\eta}\frac{df_2}{d\eta} + \left[2E\eta^2 - \frac{m^2}{\eta^2} + \alpha_2\right]f_2 = 0 , \tag{2.3.17h}$$

where the separation constants obey

$$\alpha_1 + \alpha_2 = 4 . \tag{2.3.17i}$$

Equations (2.3.17g) and (2.3.17h) are the radial equations of two two-dimensional oscillators with energy, frequency, and angular momentum given by

$$E_{os} = \frac{1}{2}\alpha , \tag{2.3.17j}$$

$$\omega_{os} = \sqrt{-2E} , \tag{2.3.17k}$$

and

$$m_{os} = m . \tag{2.3.17l}$$

The diamagnetic Hamiltonian in these coordinates is

$$H_d = \frac{1}{8} B^2 \xi^2 \eta^2 \,. \qquad (2.3.17m)$$

Representing the field-free hydrogen atom as two isotropic harmonic oscillators allows us to represent the diamagnetic Hamiltonian in terms of raising and lowering operators. Although no coupling of these oscillators leads to a diagonal representation of the total Hamiltonian $H_o(B)$, couplings do exist which reproduce the limiting symmetries discussed above. Important selection rules reduce the complexity of the representation.

This careful choice of basis allows Delande and Gay to produce tremendous results. In Rydberg states with n=30–60, they have developed perturbation series up to 60^{th} order in B^2. (The radius of convergence is zero.) Using 100 states, they calculate energies in the regime defined by Bn^3=1.2 (for n=33) which are in agreement with other calculations with basis sizes in the thousands. They have truly developed and exploited the special symmetry of the Coulomb potential.

At present, Delande and Gay feel that their approach is not satisfactory for $Bn^3 \gg 1$. There, they find their eigenvalues are sensitive to the particular basis used, and so "do not converge." We await their future results.

2.4 Two-Body and Motional Effects

The preceding sections have contained discussions about the dynamics of a spinless electron in Coulomb and uniform magnetic fields. This model roughly corresponds to the hydrogen atom. However, the nucleus of the real hydrogen atom is not infinitely massive, and the motion of the nucleus requires some consideration. Two important effects come out of this analysis: the atomic units, including that of the magnetic field, must be changed to account for the finite nuclear mass, and a "motional Stark effect" shifts the energy levels.

Classical Model

Some insight into the problem may be obtained by considering a classical description. Figure 2.4.1 shows the vectors describing the position of an electron and a proton in a uniform, and constant magnetic field. The vectors $\vec{r}_e$ and $\vec{r}_p$ are defined with respect to an inertial coordinate system; the standard two-body vectors are also introduced:

$$\vec{R} = (m_e \vec{r}_e + m_p \vec{r}_p)/M \ , \tag{2.4.1a}$$

$$\vec{r} = \vec{r}_e - \vec{r}_p \ , \tag{2.4.1b}$$

where

$$M = m_e + m_p \tag{2.4.2a}$$

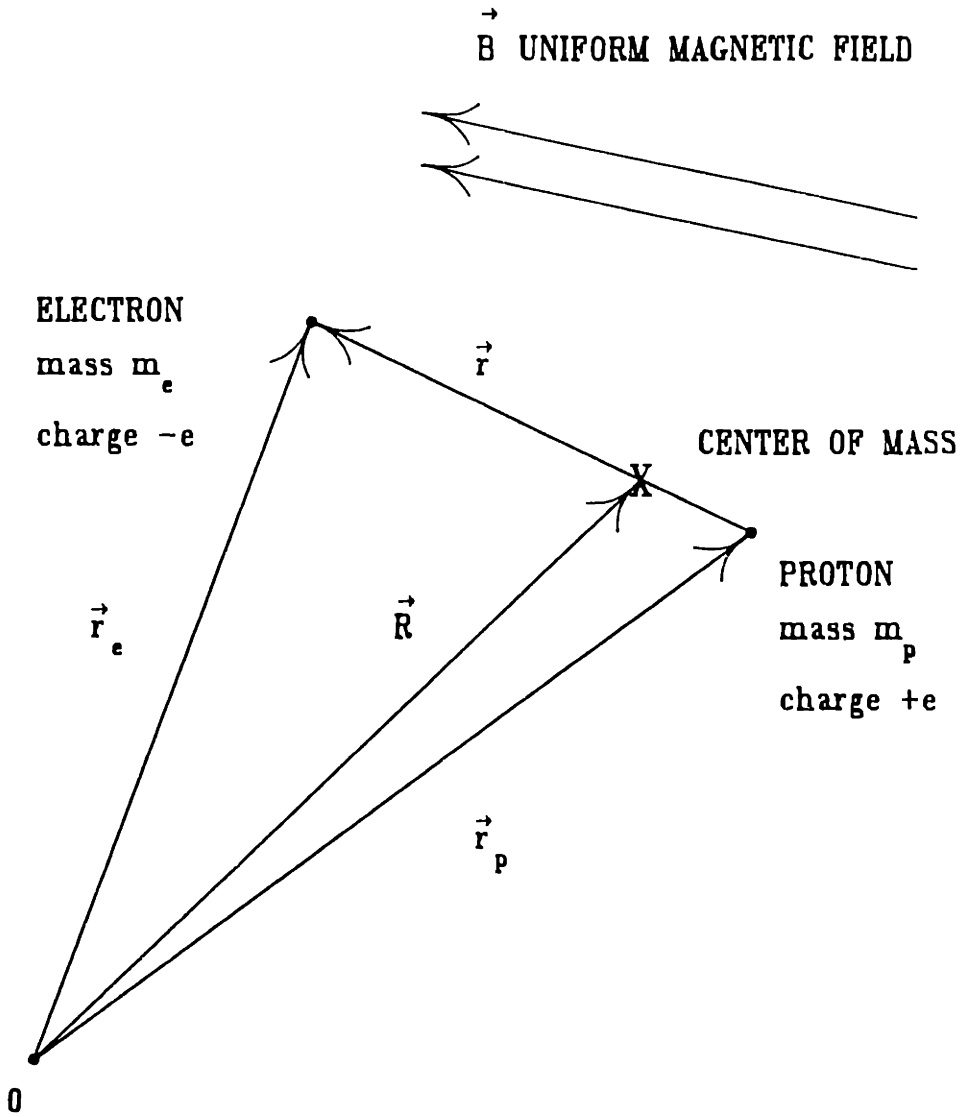

Figure 2.4.1. The conventional coordinates of a two-body system.

is the total mass of the system. It is also convenient to introduce the reduced mass

$$\mu = (m_e^{-1} + m_p^{-1})^{-1} \tag{2.4.2b}$$

although this won't be used until later. Newton's laws give:

$$m_e \ddot{\vec{r}}_e = \frac{-e^2}{4\pi\varepsilon_o} \frac{(\vec{r}_e - \vec{r}_p)}{|\vec{r}_e - \vec{r}_p|^3} + (-e)\dot{\vec{r}}_e \times \vec{B} , \tag{2.4.3a}$$

$$m_p \ddot{\vec{r}}_p = \frac{e^2}{4\pi\varepsilon_o} \frac{(\vec{r}_e - \vec{r}_p)}{|\vec{r}_e - \vec{r}_p|^3} + e\dot{\vec{r}}_p \times \vec{B} . \tag{2.4.3b}$$

The careful reader will observe that SI units are now being used. This is necessary since eventually new "atomic" units will be defined. Adding Eqs. (2.4.3) yields

$$m_e \ddot{\vec{r}}_e + m_p \ddot{\vec{r}}_p = e\vec{B} \times (\dot{\vec{r}}_e - \dot{\vec{r}}_p) \tag{2.4.4a}$$

or, using Eqs. (2.4.1) and (2.4.2a),

$$M\ddot{\vec{R}} = e\vec{B} \times \dot{\vec{r}} . \tag{2.4.4b}$$

As expected, the motion of the center of mass is governed by the net external force; the particular force between the two particles doesn't matter. However, since $\vec{B}$ is constant, then the last equation can be re-written as

$$\frac{d}{dt} (M\dot{\vec{R}} - e\vec{B} \times \vec{r}) = 0 , \tag{2.4.5a}$$

or

$$\vec{P}_o = M\dot{\vec{R}} - e\vec{B} \times \vec{r} \tag{2.4.5b}$$

is a constant of motion. Clearly the mechanical momentum of the center of mass is *not* constant, although for most atoms in laboratory-size fields, $|\, M\dot{\vec{R}}\,| >> |\, e\vec{B} \times \vec{r}\,|$. The quantity $\vec{P}_o$ is the generalized momentum of the system. As an illustration, consider the electron and the proton each interacting with a constant, uniform field $\vec{B} = B\hat{z}$ but *not* interacting with each other. This means that there's no Coulomb force in Eqs. (2.4.3), but $\vec{P}_o$ is still constant. The motion of the non-interacting particles is described by helices with axes parallel to the field. The paths are

$$\begin{aligned} \vec{r}_e &= [x_{ec} + \sigma_e \cos(\omega_e t - \phi_e)]\hat{x} \\ &\quad + [y_{ec} + \sigma_e \sin(\omega_e t - \phi_e)]\hat{y} \\ &\quad + [z_{eo} + v_e t]\hat{z} \end{aligned} \tag{2.4.6a}$$

$$\begin{aligned} \vec{r}_p &= [x_{pc} - \sigma_p \cos(\omega_p t - \phi_p)]\hat{x} \\ &\quad + [y_{pc} + \sigma_p \sin(\omega_p t - \phi_p)]\hat{y} \\ &\quad + [z_{po} + v_p t]\hat{z} \end{aligned} \tag{2.4.6b}$$

where (x_{ec}, y_{ec}) determines the axis of the electron's helix, σ_e is the radius of the electron's path projected onto the xy-plane, v_e is the electron's velocity along the field, and $\omega_e = eB/m_e$ is the electron cyclotron frequency. The corresponding quantities for the proton are similarly defined. Figure 2.4.2 shows the projection onto the xy-plane. The generalized momentum is

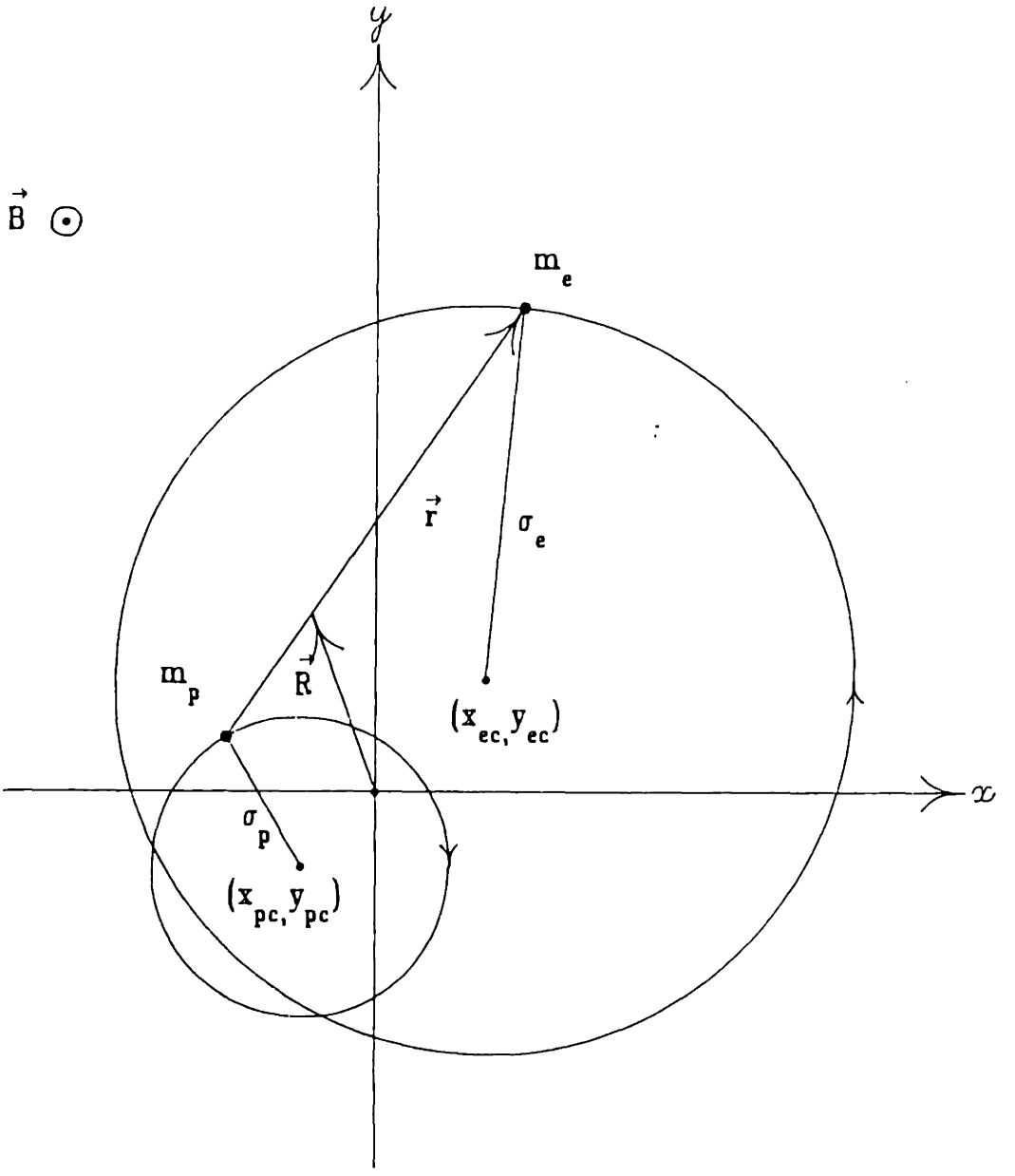

Figure 2.4.2. Projection of paths for the non-interacting proton and electron onto the *xy*-plane. Clearly $\vec{R}$ moves around so that its time derivative is *not* constant.

$$\vec{P}_o = (m_e v_e + m_p v_p)\hat{z} - e\vec{B} \times [(x_{ec} - x_{pc})\hat{x} + (y_{ec} - y_{pc})\hat{y}] \; . \qquad (2.4.7)$$

The first term is the total kinetic momentum along the field, and the second term is eB times the distance between the axes. Since the magnetic field exerts no force along itself, it's quite reasonable that the total kinetic momentum in this direction is constant. Because the field is uniform translations along the field leave the system unchanged. Indeed, Eq. (2.4.5b) indicates that the component of $\vec{P}_o$ along $\vec{B}$ is always just the (constant) total kinetic momentum along $\vec{B}$:

$$\vec{P}_o \cdot \vec{B}/B = M\dot{\vec{R}} \cdot \vec{B}/B \; . \qquad (2.4.7)$$

The second term involves the distance between the axes of the helices, which is unchanged in time or with translations perpendicular to the field. It also has the dimensions of momentum. Beyond that, however, I can give no interpretation.

In order to make a connection with the forthcoming quantal discussion, $\vec{P}_o$ must be expressed in terms of the canonical momenta of the system:

$$M\dot{\vec{R}} = m_e\dot{\vec{r}}_e + m_p\dot{\vec{r}}_p = \vec{p}_e + e\vec{A}(\vec{r}_e) + \vec{p}_p - e\vec{A}(\vec{r}_p) \; , \qquad (2.4.8)$$

where $\vec{p}_e$ and $\vec{p}_p$ are the canonical momenta of the electron and proton, and $\vec{A}(\vec{r}_e)$ and $\vec{A}(\vec{r}_p)$ represent a vector potential associated with the magnetic field, evaluated at the location of the electron and proton. If the (static) symmetric gauge of a constant, uniform field is used,

$$\vec{A} = \frac{1}{2}\,\vec{B} \times \vec{r}\,, \tag{2.4.9a}$$

then

$$\vec{P}_o = \vec{P} - \frac{e}{2}\,\vec{B} \times \vec{r}\,, \tag{2.4.9b}$$

where

$$\vec{P} = \vec{p}_e + \vec{p}_p \tag{2.4.10}$$

is the total canonical momentum of the charges.

Quantum Description

A quantal formulation begins by guessing a Hamiltonian for the system:

$$H_H(B) = \frac{\pi_e^2}{2m_e} + \frac{\pi_p^2}{2m_p} + V(r)\,, \tag{2.4.11a}$$

where the kinetic momenta, those associated with the kinetic energies of the particles, and potential energy are given by

$$\vec{\pi}_e = \vec{p}_e + e\vec{A}(\vec{r}_e)\,, \tag{2.4.11b}$$

$$\vec{\pi}_p = \vec{p}_p - e\vec{A}(\vec{r}_p)\,, \tag{2.4.11c}$$

$$V(r) = \frac{-e^2}{4\pi\varepsilon_o}\,\frac{1}{|\vec{r}_e - \vec{r}_p|}\,, \tag{2.4.11d}$$

and the canonical momenta, in the configuration representation, are defined as

$$\vec{p}_e = -i\hbar\vec{\nabla}_{r_e} , \tag{2.4.11e}$$

$$\vec{p}_p = -i\hbar\vec{\nabla}_{r_p} . \tag{2.4.11f}$$

Using the coordinate transformations of Eqs. (2.4.1), the total and relative canonical momenta may be introduced:

$$\vec{p}_e = \vec{p} + \frac{m_e}{M}\vec{P} , \tag{2.4.12a}$$

$$\vec{p}_p = -\vec{p} + \frac{m_p}{M}\vec{P} , \tag{2.4.12b}$$

where

$$\vec{P} = -i\hbar\vec{\nabla}_R , \tag{2.4.12c}$$

$$\vec{p} = -i\hbar\vec{\nabla}_r . \tag{2.4.12d}$$

Herold, Ruder, and Wunner [HRW81] have demonstrated that

$$\vec{P}_o = \vec{P} - \frac{e}{2}\vec{B}\times\vec{r} \tag{2.4.9}$$

is the quantal generalized momentum by considering the quantity conjugate to an infinitesimal translation of the system described by the Hamiltonian in Eq. (2.4.11a). Translational invariance assures that the generalized momentum is constant. When a magnetic field is present, however, a displacement of origin changes the vector potential: a gauge transformation is required to preserve the invariance of the

Hamiltonian. More directly, one can verify that $\vec{P}_o$ is a constant of motion by showing that

$$[H_H(B), P_{oi}] = 0 \qquad \text{for } i = 1, 2, 3 . \tag{2.4.13}$$

Further, for neutral systems such as the proton-electron system, it is also true that

$$[P_{oi}, P_{oj}] = 0 \quad \text{for } i, j = 1, 2, 3 \tag{2.4.14}$$

so all components of the vector $\vec{P}_o$ may be specified simultaneously. Now the particle kinetic momenta can be expressed in terms of $\vec{p}$, $\vec{P}_o$, $\vec{r}$, and $\vec{R}$:

$$\vec{\pi}_e = \vec{p} + \frac{m_e}{M}\vec{P}_o + \frac{e}{2}\vec{B} \times (\vec{r}+\vec{R}) , \tag{2.4.15a}$$

$$\vec{\pi}_p = -\vec{p} + \frac{m_p}{M}\vec{P}_o + \frac{e}{2}\vec{B} \times (\vec{r}-\vec{R}) . \tag{2.4.15b}$$

The Hamiltonian becomes a bit messy, but evaluating such things builds character:

$$H_H(B) = \frac{p^2}{2\mu} + \frac{P_o^2}{2M} + \frac{e^2}{8\mu}[(\vec{B}\times\vec{r})^2 + (\vec{B}\times\vec{R})^2] + \frac{e}{2}\left[\frac{1}{m_e} - \frac{1}{m_p}\right]\vec{p} \cdot \vec{B} \times \vec{r}$$

$$+ \frac{e}{2}\left[\frac{1}{m_e} + \frac{1}{m_p}\right]\vec{p} \cdot \vec{B} \times \vec{R} + \frac{e}{M}\vec{P}_o \cdot \vec{B} \times \vec{r} \tag{2.4.16}$$

$$+ \frac{e^2}{4}\left[\frac{1}{m_e} - \frac{1}{m_p}\right](\vec{B}\times\vec{r}) \cdot (\vec{B}\times\vec{R}) + V(r) .$$

This is easier to interpret if we try a partial separation of the wave function, using the

fact that the wave function can be an eigenfunction of $\vec{P}_o$. The form of $\psi(\vec{R}, \vec{r})$ which is suggested by the form of $\vec{P}_o$ is

$$\psi(\vec{R}, \vec{r}) = \exp[\frac{i}{\hbar}(\hbar\vec{K} + \frac{e}{2}\vec{B} \times \vec{r}) \cdot \vec{R}]\phi(\vec{r}) , \tag{2.4.17}$$

where $\vec{K}$ is a constant vector. It's not difficult to show that

$$\vec{P}_o \psi = \hbar\vec{K}\psi . \tag{2.4.18}$$

Denoting the argument of the exponential in Eq. (2.4.17) by $\alpha(\vec{R}, \vec{r})$, we find (after much algebra) that

$$H_H(B)\psi = e^{\alpha}H_{rel}(B)\phi = Ee^{\alpha}\phi , \tag{2.4.19a}$$

$$H_{rel}(B) = H_M + H_m + H_i(B) , \tag{2.4.19b}$$

$$H_M = \frac{(\hbar K)^2}{2M} , \tag{2.4.19c}$$

$$H_m = \frac{e}{M}\hbar\vec{K} \times \vec{B} \cdot \vec{r} , \tag{2.4.19d}$$

$$H_i(B) = \frac{p^2}{2\mu} + V(r) + \frac{e}{2\mu}\beta\vec{L} \cdot \vec{B} + \frac{e^2}{8\mu}(\vec{B} \times \vec{r})^2 , \tag{2.4.19e}$$

$$\beta = \mu\left[\frac{1}{m_e} - \frac{1}{m_p}\right] = \frac{m_p - m_e}{m_p + m_e} , \tag{2.4.19f}$$

$$\vec{L} = \vec{r} \times \vec{p} \ . \tag{2.4.19g}$$

This is the sort of thing that we wanted to see. Crudely speaking, H_M is the translational energy of the center of mass, and simply shifts E by an additive constant. The term $H_i(B)$ is the Hamiltonian of a particle with charge $-e$ and mass μ in a uniform magnetic field, except that the paramagnetic term is multiplied by the factor β. Unlike the usual two-body problem, however, the term H_m couples the system motion to the internal coordinate; generally the eigenfunctions and eigenenergies of H_{rel} depend on $\vec{K}$. How is $\vec{K}$ determined? To make an estimate, we go back to the classical form, Eq. (2.4.5b). Then

$$\frac{\hbar\vec{K}}{M} \approx \dot{\vec{R}} - \frac{e}{M}\vec{B} \times \vec{r} \ . \tag{2.4.20}$$

For thermal atoms, the speed is around 2×10^{3}m/sec. For a field of 10T, and taking r as the Bohr radius, the second term is about 5×10^{-2}m/sec; the atomic velocity dominates. So now we can see that

$$H_m = \frac{e}{M}\hbar\vec{K}\times\vec{B} \cdot \vec{r} \approx \dot{\vec{R}}\times\vec{B} \cdot (e\vec{r}) = -\vec{F}_m \cdot (-e\vec{r}) \ , \tag{2.4.21}$$

where $\vec{F}_m = \dot{\vec{R}}\times\vec{B}$ is the motional electric field, that is, the electric field the atom "sees" in its rest frame. This field interacts with the atomic electric dipole operator, $-e\vec{r}$, and produces the motional Stark effect.

To evaluate $\vec{K}$ within the quantal framework, note that the (gauge-invariant,

physically measurable) total kinetic momentum may be formed by adding Eqs. (2.4.15a) and (2.4.15b):

$$\vec{\pi} = \vec{\pi}_e + \vec{\pi}_p = \vec{P}_o + e\vec{B} \times \vec{r} \tag{2.4.22a}$$

or

$$\vec{P}_o = \vec{\pi} - e\vec{B} \times \vec{r} \,. \tag{2.4.22b}$$

Consider the expectation value of all of these operators in a state given by Eq. (2.4.17):

$$\hbar\vec{K} = <\vec{\pi}> - e<\vec{B}\times\vec{r}> \,. \tag{2.4.22c}$$

The expectation value of the kinetic momentum may be measured. The expectation value of $\vec{B}\times\vec{r}$ is

$$< \psi \mid \vec{B}\times\vec{r} \mid \psi > = < \phi \mid \vec{B}\times\vec{r} \mid \phi > \tag{2.4.22d}$$

where generally ϕ depends on $\vec{K}$ because of H_m. Then Eq. (2.4.22c) is an implicit equation for $\vec{K}$, which may require a numerical solution. However, if we regard H_m as a perturbation to $H_i(B)$ and therefore ϕ as an eigenfunction of $H_i(B)$, then

$$H_i(B)\phi = [E - (\hbar K)^2/2M]\phi \tag{2.4.23}$$

and ϕ is independent of $\vec{K}$. Moreover, $H_i(B)$ is cylindrically symmetric about an axis defined by $\vec{B}$, so we may construct simultaneous eigenfunctions of $H_i(B)$ and the component of angular momentum along $\vec{B}$. In that case, the expectation value of

$\vec{B} \times \vec{r}$ vanishes, and $\vec{K}$ is completely determined by the expectation value of the kinetic momentum. Then the action of H_m is just the motional Stark effect discussed above. From Eq. (2.4.19d), we have

$$H_m = \frac{e}{M} \langle \vec{\pi} \rangle \times \vec{B} \cdot \vec{r} = - \vec{F}_m \cdot (-e\vec{r}) \tag{2.4.24}$$

with $\vec{F}_m = \frac{\langle \vec{\pi} \rangle}{M} \times \vec{B}$.

Our goal is to study the atom-field interaction, $H_i(B)$. The eigenstates of $H_i(B)$ can be specified by parity (π), and the projection of angular momentum along the magnetic field (m). The effect of H_m may be viewed as a perturbation. Because $\vec{F}_m$ is always perpendicular to $\vec{B}$, H_m couples states with $\Delta m = \pm 1$ and opposite parity. The effect is usually second order in $\vec{F}_m$ since nondegenerate states with definite parity have vanishing electric dipole moments. However, should the field and energy be such that a state with $m = 0$, $\pi = -1$ is crossing another state with $m = \pm 1$, $\pi = +1$, the motional field will act in first order producing an anticrossing of the levels with a size proportional to F_m. Clearly the atomic velocity should be made parallel to the magnetic field so that $H_m = 0$.

Armed with $H_i(B)$, the appropriate units for energy, length, and field which reduce $H_i(B)$ to a scaled, dimensionless form may be determined. Let quantities with underscores be dimensionless, while those with subscript H represent the defining unit:

$$\vec{r} = a_H \underline{\vec{r}}, \quad \vec{L} = \hbar \underline{\vec{L}}, \quad \vec{B} = B_H \underline{\vec{B}}, \quad E = E_H \underline{E} \ . \tag{2.4.25}$$

We substitute these relations into Eq. (2.4.19e) and group the units together. If we take

$$\frac{\hbar^2}{\mu a_H^2} = \frac{e^2}{4\pi\varepsilon_o a_H} = \frac{e\hbar B_H}{\mu} = \frac{e^2 B_H^2 a_H^2}{\mu} = E_H \tag{2.4.26a}$$

or

$$a_H = \frac{\hbar^2 4\pi\varepsilon_o}{\mu e^2}, \quad E_H = \frac{\mu}{\hbar^2}\left[\frac{e^2}{4\pi\varepsilon_o}\right]^2, \quad B_H = \left[\frac{\mu}{4\pi\varepsilon_o}\right]^2 \left[\frac{e}{\hbar}\right]^3 \tag{2.4.26b}$$

and let the direction of $\vec{B}$ define the z-axis, then we can divide Eq. (2.4.17e) by E_H and obtain

$$\underline{H}_i(B) = -\frac{1}{2}\nabla_{\underline{r}}^2 - \frac{1}{\underline{r}} + \frac{\beta}{2}\underline{B}\underline{L}_z + \frac{1}{8}\underline{B}^2\rho^2 \ . \tag{2.4.27}$$

The reason Eqs. (2.4.21a) are not overdetermined is that both the paramagnetic and diamagnetic terms come from the same vector potential. The standard practice of dropping the underscores yields the Hamiltonian derived near the beginning of this chapter, except for the factor β in the paramagnetic term. The units for length, energy and field are similar to the standard ones except that the reduced mass replaces the electron mass. Let us refer to the "atom" which consists of an electron in a (stationary) Coulomb field as "heavium". In the following table, the "atomic" units for heavium and hydrogen are compared.

Atom:	Heavium	Hydrogen
Unit:		
Energy (cm^{-1})	$2.194,746,306(2)\times10^{5}$	$2.193,551,660(2)\times10^{5}$
Length (cm)	$5.291,772,49(24)\times10^{-9}$	$5.294,6545(2)\times10^{-9}$
Magnetic Field (T)	$2.350,518(3)\times10^{5}$	$2.347,960(3)\times10^{5}$
Electric Field (V/cm)	$5.142,208(1)\times10^{9}$	$5.136,611(1)\times10^{9}$
β	1	0.998,911,3(8)
Rydberg Constant (cm^{-1})	109,737.315,34(13)	109,677.5830(1)
Zeeman splitting: $E_p(m=+1) - E_p(m=-1)$ for 1T (cm^{-1})	0.933,728,7(2)	0.933,220,2(2)

Table 2.4.1 Comparison of heavium and hydrogen scaled units. All constants are from Cohen and Giacomo [COG87]. The energy units are twice the appropriate Rydberg constant. The Zeeman splitting is β times the energy unit divided by the magnetic field unit for each atom.

Of course, the heavium units are the conventional atomic units. (Some older references use a magnetic field unit which is this one times the fine structure constant. Then the fine structure constant appears in their reduced equations.) The electric field unit is defined to make H_m consistent with $H_i(B)$. Specifically,

$$F_H = \frac{e^5\mu^2}{(4\pi\varepsilon_o)^3\hbar^4} \,. \tag{2.4.28}$$

The finite mass connection is important in precision experiments where numerical predictions are tested stringently. For example, if a computer calculation put a state at $\underline{E} = -1\times10^{-3}$ and $\underline{B} = 3\times10^{-5}$ ($E \approx -200$ cm^{-1}, $B \approx 7T$), the difference between hydrogen and heavium would be $\Delta E = 0.12$ cm^{-1} and $\Delta B = -77$ gauss. If

the Zeeman separation of corresponding $m = +1$ and $m = -1$ states is used to measure the magnetic field, and has a value of 10 cm^{-1} ($B \approx 10T$), the difference between hydrogen and heavium would be $\Delta B = 58$ gauss.

Chapter 3. DIAMAGNETISM IN LITHIUM

The last chapter discussed methods for predicting the diamagnetic spectrum of hydrogen (in the infinite mass approximation). However, the hydrogen ground state is so tightly bound that there are no suitable lasers for performing high resolution spectroscopy. Although one group [HWM86] developed *pulsed* lasers which are blue enough to create hydrogen Rydberg states in a magnetic field, the decision here was to gain the advantages of high resolution at the expense of theoretical simplicity. Lithium is similar to hydrogen in many respects, and has several experimental advantages. (See Fig. 5.1.1 for a comparison between the energy levels of hydrogen and lithium.) One of the significant differences is in the nature of the anticrossing of levels from different principle quantum numbers, but the same azimuthal and parity quantum numbers. The measurement of these anticrossings is a central goal of this work. To make detailed comparisons between theory and experiment, predictions for the diamagnetic spectrum of lithium must be made.

There are two strategies for calculating the effect of diamagnetism on lithium Rydberg states. The first is to represent an approximate Hamiltonian for lithium in a magnetic field with a finite matrix, and to diagonalize that matrix numerically for each value of magnetic field. The second is to treat the difference between the lithium and hydrogen Hamiltonians as a perturbation to be applied after the hydrogen problem has been solved. The latter approach facilitates the interpretation of the lithium results in

terms of the concepts developed for hydrogen in Sec 2.3. However, since those concepts are not particularly simple, the advantage is questionable. The former approach is easy to implement, gives testable and accurate results, but does not reveal much insight into the problem.

The main difference between the diamagnetic Rydberg spectra of hydrogen and lithium is that levels with the same azimuthal and parity quantum numbers but different principle quantum numbers exhibit anticrossings. Away from these features, the energy levels look quite similar, except at zero field, where lithium does not have degenerate angular momentum states. Both of these properties attest to the non-Coulomb potential of the valence electron, and provide somewhat complementary information about the ionic core.

This chapter presents the approximate Hamiltonian and the numerical methods which are used to make detailed spectral predictions. Eigenvectors may also be computed and used to estimate transition probabilities. Perturbation theory provides a detailed description of anticrossings. Finally, the effect of small electric fields is considered.

3.1 The Hamiltonian and Numerical Methods

Let us begin by considering an approximate Hamiltonian for lithium *without* a magnetic field. If we ignore the spins of the electrons and nucleus and the motion of the nucleus, then the Hamiltonian may be written in atomic units as

$$H_{Li} = \sum_{i=1}^{3} \left[\frac{p_i^2}{2} - \frac{3}{r_i} \right] + \sum_{j>i=1}^{3} \frac{1}{r_{ij}} , \tag{3.1.1}$$

where we have taken the nuclear charge as +3. The eigenfunctions of this Hamiltonian are of the form $\psi(\vec{r}_1, \vec{r}_2, \vec{r}_3)$. The ground state configuration is $(1s^2, 2s)$, while other states in the "optical spectrum" have configurations $(1s^2, nl)$. Douglas Rayner Hartree (1897-1958) laid the groundwork for finding numerical wave functions and energies of polyelectronic atoms [GIL74, Vol. XII, pp. 613-616] and for a rigorous derivation of quantum defect theory. Since we are interested in the valence electron, we follow the method of Hartree [HAR28] and consider an approximate Hamiltonian for the outer electron

$$H_A = \frac{1}{2} p^2 + V(r) \tag{3.1.2a}$$

where $V(r)$ is a spherical potential such that

$$V(r) \approx -\frac{1}{r} \text{ for } r > r_c \ . \tag{3.1.2b}$$

Here, r_c is that radius beyond which the difference between the true and Coulomb

potentials is negligible. For radii smaller than r_c, the potential is determined by the self-consistent field method. The goal is to find a solution of Eq. (3.1.2a) which is finite at the origin and zero at infinity.

Since the potential is spherical, the wave function may be separated in the usual manner:

$$\psi(\vec{r}) = R(r)Y_{lm}(\Omega) \tag{3.1.3a}$$

where Y_{lm} is a spherical harmonic and the radial wave function satisfies the Schroedinger equation

$$-\frac{1}{2r}\frac{d^2}{dr^2}(rR) + \frac{l(l+1)}{2r^2}R + V(r)R = ER \tag{3.1.3b}$$

with boundary conditions

$$r = 0: \qquad rR = 0\,, \tag{3.1.3c}$$

$$r \to \infty: \qquad rR = 0\,. \tag{3.1.3d}$$

Hartree proposed integration outward from the origin to r_c, and integration inward from infinity to r_c. The eigenvalue is determined by requiring that at r_c,

$$\frac{\frac{d}{dr}(rR_{out})}{rR_{out}} = \frac{\frac{d}{dr}(rR_{in})}{rR_{in}}\,. \tag{3.1.3e}$$

For finite r larger than r_c, Hartree has shown that the radial wave function may be written as

$$rR_{out}(r) = G_l(2r, t)\cos\pi n^* + H_l(2r, t)\sin\pi n^* \qquad (3.1.4a)$$

where

$$n^* = n - \delta_l, \quad t = (n^*)^{-2} = -2E \ , \qquad (3.1.4b,c,d)$$

and the detailed form of G_l and H_l is not important. Here δ_l is the (total) quantum defect, n is the principal quantum number, and n^* is the effective principal quantum number. For fixed r, both G_l and H_l may be expanded in a power series of t, with no terms proportional to $t^{1/2}$. This is also true of the inner radial wave function. (See Eq. (3.2.5d).) Then condition (3.1.3e) implies that, for each l,

$$\delta_l = \delta_l^{(0)} + \delta_l^{(1)}t + \delta_l^{(2)}t^2 + \ \ldots \qquad (3.1.5a)$$

The term $\delta_l^{(0)}$ is the quantum defect of the series limit; the higher order terms are the small change in quantum defect expressed as a power series in energy. For all alkali-metal atoms, the total quantum defect is positive. This is the quantum mechanical derivation of the Ritz formula,

$$E = -\frac{1}{2}\,(n - \delta_l^{(0)} - \delta_l^{(1)}t - \delta_l^{(2)}t^2 \ldots)^{-2} \ . \qquad (3.1.5b)$$

All of this suggests two important results. The first is that if enough energies of states in a series are known, then all of the energies of that series can be predicted. For lithium, the quantum defects are determined accurately from experimental measurements as discussed in Sec. 5.1. The second is that outside of r_c, the potential

energy of the valence electron may be assumed to be $-1/r$. Thus, given the energy, the radial Schroedinger equation may be integrated inward from ∞ to r_c to get an accurate approximation to the radial wave function of the valence electron.

The Hamiltonian for lithium in a magnetic field is obtained by the same reasoning as for hydrogen, by introducing the vector potential:

$$H_A(B) = \frac{1}{2}\,(\vec{p} + \vec{A})^2 + V(r)\,. \tag{3.1.6a}$$

If we use the symmetric Coulomb gauge for a uniform magnetic field, $\vec{A} = \frac{1}{2}\,\vec{B}\times\vec{r}$, the Hamiltonian becomes

$$H_A(B) = \frac{1}{2}\,p^2 + V(r) + \frac{1}{2}\,\vec{B}\cdot\vec{L} + \frac{1}{8}\,(\vec{B}\times\vec{r})^2\,. \tag{3.1.6b}$$

The identification of the atomic, paramagnetic, and diamagnetic Hamiltonians is clear. We solve Schroedinger's (time independent) equation approximately by representing the Hamiltonian as a matrix in a spherical basis, and diagonalizing the matrix for magnetic field values of interest.

Nuclear motion plays a role in the precision spectroscopy of lithium, though not as great as in that of hydrogen. A simple description regards lithium as a two-body system, with the valence electron as one body, and the ionic core as the other. Then the results of Sec. 2.4 may be adapted. The paramagnetic term must be multiplied by β:

$$H_A(B) = \frac{1}{2}\, p^2 + V(r) + \frac{\beta}{2}\vec{B} \cdot \vec{L} + \frac{1}{8}\,(\vec{B}\times\vec{r})^2 \,. \qquad (3.1.6c)$$

The units for lithium -6 and -7 which reduce the Hamiltonian to dimensionless form are displayed in the following table. See Eq. (2.4.26) and (2.4.28) for the definitions of these units.

Atom:	lithium-6	lithium-7
Unit:		
Energy (cm^{-1})	$2.194,546,146(2)\times10^{5}$	$2.194,574,700(2)\times10^{5}$
Length (cm)	$5.292,2551(2)\times10^{-9}$	$5.292,1863(2)\times10^{-9}$
Magnetic Fields (T)	$2.350,089(3)\times10^{5}$	$2.350,150(3)\times10^{5}$
Electric Field (V/cm)	$5.141,2703(5)\times10^{9}$	$5.141,4041(5)\times10^{9}$
β	0.999,818(1)	0.999,844(1)
Rydberg Constant (cm^{-1})	109,727.3073(1)	109,728.7350(1)
Zeeman Splitting: $E_p(m=+1) - E_p(m=+1)$ for 1T (cm^{-1})	0.933,6442(2)	0.933,6562(2)

Table 3.1.1 Comparison of lithium-6 and lithium-7 scaled units. All constants are from Cohen and Giacomo [COG87] and Mattuch *et al.* [MTW65]. The energy units are twice the appropriate Rydberg constant. The Zeeman splitting is β times the energy unit divided by the magnetic field unit for each atom.

The difference between the units for lithium and those for hydrogen (with infinite nuclear mass) is important for precision spectroscopy. For example, if a computer calculation put a state at $\underline{E} = -1\times10^{-3}$ and $\underline{B} = 3\times10^{-5}$ ($E \approx$ -200 cm^{-1}, $B \approx$ 7T), the difference between lithium-7 and hydrogen would be $\Delta E = 0.017$ cm^{-1} and ΔB = -11 gauss. If the Zeeman separation of corresponding m = +1 and m = -1

states is used to measure the magnetic field, and has a value of 10 cm^{-1} ($B \simeq 10T$), the difference between lithium-7 and hydrogen would be $\Delta B = 8.3$ gauss. As discussed in Secs. 4.3 and 4.2, the energy difference is at the limit of our experimental resolution; the field difference is just beyond it.

Matrix Elements

The basis used to represent the Hamiltonian shown in Eq. (3.1.6b) is selected to make the calculation of the matrix elements straightforward. Both the atomic and paramagnetic Hamiltonians are diagonal in a spherical basis, that is, one where the wave functions are written in the form of Eq. (3.1.3a). The atomic energies are determined from quantum defects, which are known accurately from spectroscopy. Since the total Hamiltonian commutes with L_z (defining the z-axis by the magnetic field), states with different azimuthal quantum numbers m have vanishing diamagnetic matrix elements. The same is true of parity. Therefore, the basis need contain only one m, and even or odd (but not both) angular momentum quantum numbers (l's). Here, the paramagnetic Hamiltonian is proportional to the unit matrix. Therefore, we need only set up the matrix of atomic and diamagnetic Hamiltonians to be diagonalized; the paramagnetic energy may be added after the diagonalization.

A matrix representation of the Hamiltonian must be finite. Therefore, this mode of description only approximates the true system. The success of the method depends on an intelligent choice of basis states. It is reasonable to choose states which are

close in energy to the region of interest. The energies of the basis states and the magnetic fields considered are converted to reduced values using the parameters of Table 3.1.1. This table also converts the results of the computation back to measurable quantities.

Computation of matrix elements is discussed by Zimmerman *et al.* [ZLK79]. For diamagnetism, we need to evaluate

$$< n'l'm' \mid \rho^2 \mid nlm > = < n'l' \mid r^2 \mid nl >< l'm' \mid \sin^2\theta \mid lm > \qquad (3.1.7)$$

The angular matrix element was discussed in Sec 2.2. The result is [GAR77]

$$< l'm' \mid \sin^2\theta \mid lm > = \frac{2(l^2+l-1+m^2)}{(2l-1)(2l+3)}\,\delta_K(m',m)\delta_K(l',l)$$

$$- \left[\frac{(l_<+m+2)(l_<+m+1)(l_<-m+2)(l_<-m+1)}{(2l_<+5)(2l_<+3)^2(2l_<+1)}\right]^{1/2} \delta_K(m',m)\delta_K(l',l\pm 2)\,. \qquad (3.1.8)$$

Here δ_K is the Kronecker delta function, which is one of its two arguments are equal, and zero otherwise.

The radial matrix element must be evaluated numerically. The technique we use was developed by Myron Zimmerman and relies on Hartree's observation that outside of some radius r_c the potential of the valence electron is Coulombic. The energy of a state specified by (n,l) is found using the Ritz formula, Eq. (3.1.5b), with spectroscopically determined quantum defects. Given the energy, the Schroedinger

equation is integrated inward from infinity. Because we are evaluating r^2 matrix elements of Rydberg states, the wave function inside of r_c — crudely speaking the ionic core radius — does not contribute significantly to the integral and may be ignored.

Two schemes are used to scale the radial coordinate so as to give approximately the same number of integration points between nodes of the radial wave function. The first is logarithmic. In Eq. (3.1.3b), let

$$r = e^x \ , \tag{3.1.9a}$$

$$R = r^{-1/2}X \ . \tag{3.1.9b}$$

Then the radial equation becomes

$$X'' = g(e^x)X \tag{3.1.9c}$$

with

$$g(e^x) = g(r) = -2r - 2Er^2 + (l+1/2)^2 \ . \tag{3.1.9d}$$

The second change of variable is a power law substitution. In Eq. (3.1.3b), let

$$r = x^2 \ , \tag{3.1.10a}$$

$$R = x^{-3/2}X \ . \tag{3.1.10b}$$

This time the radial equation becomes

$$X'' = g(x^2)X \tag{3.1.10c}$$

with

$$g(x^2) = g(r) = [\frac{3}{4} + 4l(l+1)]\ \frac{1}{r} - 8(1+Er)\ . \tag{3.1.10d}$$

In numerical applications, the quadratic scaling leads to a nearly constant number of integration points per oscillation of the radial wave function. Historically, our programs have used the logarithmic scaling, which seems to be a reasonable compromise between speed and accuracy. The logarithmic scaling is assumed in the subsequent discussion.

The integration algorithm comes from Numerov [NUM33]. Boris Vasilievich Numerov (1981-1943) was a Russian astronomer who refined the calculation of asteroid trajectories by developing a method for integrating Newton's laws [GIL74, Vol. X, pp. 158-160]. The method is very efficient for ordinary, second order, linear differential equations *without* a first order term. It requires two initial values and is $O(h^6)$ in local accuracy, where h is the step size of x. The formula is [HAR58]:

$$X_{i+1} = [(24/h^2+10g_i)X_i + (g_{i-1}-12/h^2)X_{i-1}]/(12/h^2-g_{i+1}) \tag{3.1.11a}$$

where

$$g_i = g(x_i)\ , \tag{3.1.11b}$$

$$X_i = X(x_i) \ . \tag{3.1.11c}$$

The initial point "at infinity" is taken to be far enough outside of the outer classical turning point that the wave function is nearly exponential; we use $r_o = 2n(n+15)$. This defines x_o. Then the initial values are

$$X_o = 10^{-10} \ , \tag{3.1.12a}$$

$$X_1 = X(x_o - h) = X_o[1 + h(g_o)^{1/2}] \ . \tag{3.1.12b}$$

Normally we use h=0.005. We take the radius of the ionic core as

$$r_c = (\alpha_{cd})^{1/3} \tag{3.1.12c}$$

where α_{cd} is the dipole polarizability of the core. For lithium, α_c = 0.1907 [LIT70], so $r_c \approx 0.576$. If the integration crosses the inner classical turning point before reaching r_c, the integration terminates if R begins to diverge faster than r^{-l-1}. Otherwise, the integration is stopped at r_c .

Radial matrix elements require the integration of the product of two normalized radial wave functions and the radial operator. A simple trapezoidal integration method is used, and the sums are computed simultaneously with the wave function, so that the wave function need not be stored. The integration begins at the higher $n's$ r_o, and terminates when either wave function starts to diverge inside of the centrifugal barrier, or at r_c. The formula is

$$<1 \mid r^k \mid 2> \approx \frac{\Sigma X_{1i} X_{2i} (r_i)^{2+k}}{[\Sigma X_{1i}^2 r_i^2]^{1/2} [\Sigma X_{2i}^2 r_i^2]^{1/2}} , \tag{3.1.13}$$

where each sum ranges from $i=0$ to the termination value.

This procedure generates radial wave functions which do not have the standard phase convention. All of these wave functions are positive at infinity, while the usual practice is to require that the radial wave function (for $l=0$), or its derivative (for $l>0$) be positive at zero. (Our method does not even evaluate the wave function at the origin.) This means that these matrix elements may not have the standard sign. No observable depends on this, because changing the sign of a state amounts to a unitary transformation of the basis. However, one must be careful not to mix the sign conventions.

The conventional sign convention may be achieved as follows. In hydrogen, the number of radial nodes is $n-l-1$. This is the number of sign *changes*, and does not include (possible) zeros at the origin or infinity. For alkali-metal atoms, the number of nodes is $n-l-1-[\delta_l]$ where the last term is the greatest integer part of the quantum defect of the state in question. In lithium, the greatest integer part of all quantum defects is zero. To get the standard phase convention, multiply the wave function obtained here by $(-1)^{n-l-1}$.

Matrix Diagonalization

Consider a definite basis of lithium states with definite m, π, and a range of $n's$. After the matrix of ρ^2 has been computed for all of the states in the basis, it is multiplied by $B^2/8$ for a given B and added to the diagonal matrix containing the atomic energies of all of the states. The resultant matrix is diagonalized, and the energies and sometimes the states are stored. If desired, the paramagnetic energy may be added to all of the energies.

Two algorithms have been used to diagonalize the matrix. The first is the Jacobi method [PFT88, pp. 360-367]. This is an iterative procedure, which consists of a sequence of transformations each of which sets one off-diagonal matrix element to zero. This is achieved by diagonalizing the corresponding 2×2 submatrix. The transformations proceed until the magnitude of off-diagonal elements is below some predetermined value. Accumulating the product of the transformations yields the eigenvectors. The second method, which is faster for large matrices, is that of Givens-Householder [PFT88, pp. 367-381, ORT67]. It proceeds in a multistep process. The matrix is reduced to tri-diagonal form with a definite number of operations. Then this matrix is diagonalized. Eigenvectors may be found as a third step. For large matrices, the first step takes much longer than the second.

Our calculations are performed using the VENIX/11 V.2 operating system on our SMS 11/73 computer. This 16-bit machine presently has two megabytes (2×2^{20}

bytes) of memory. The compiler limits each program to 256 kbytes (2^{16}) bytes for itself and the same for its data. For an N×N matrix representation of the Hamiltonian, only $(N^2+N)/2$ data locations are needed because the matrix is symmetric. If eigenvectors are desired, an additional N^2 locations must be provided. Floating point operations have been found to give a precision corresponding to 0.0001 cm^{-1} for n's around 30, so each matrix element (data location) requires 4 bytes. The largest basis which can be used has about 150 states if no eigenvectors are stored, and about 80 states if eigenvectors are stored.

Recently George Welch implemented a memory management system that allows a full megabyte to be used, allowing us to diagonalize a 700×700 matrix. The diagonalization time for an N×N matrix is $3.1\times10^{-5}N^3$ seconds, so with a basis consisting of 700 states, each field point requires about 3 hours. This also means we can represent lithium m=0, π=-1 states with n's ranging from 2 to about 50. However, increasing the basis size much more will make the computation time impractically long.

Results

The most convenient way to present the numerical results is in an energy versus field diagram, such as that shown in Fig. 3.1.1. This figure differs from those in hydrogen (see Fig. 2.2.1) in that the levels clearly anticross. This will be discussed more in the next section. Detailed comparisons between the numerical predictions and

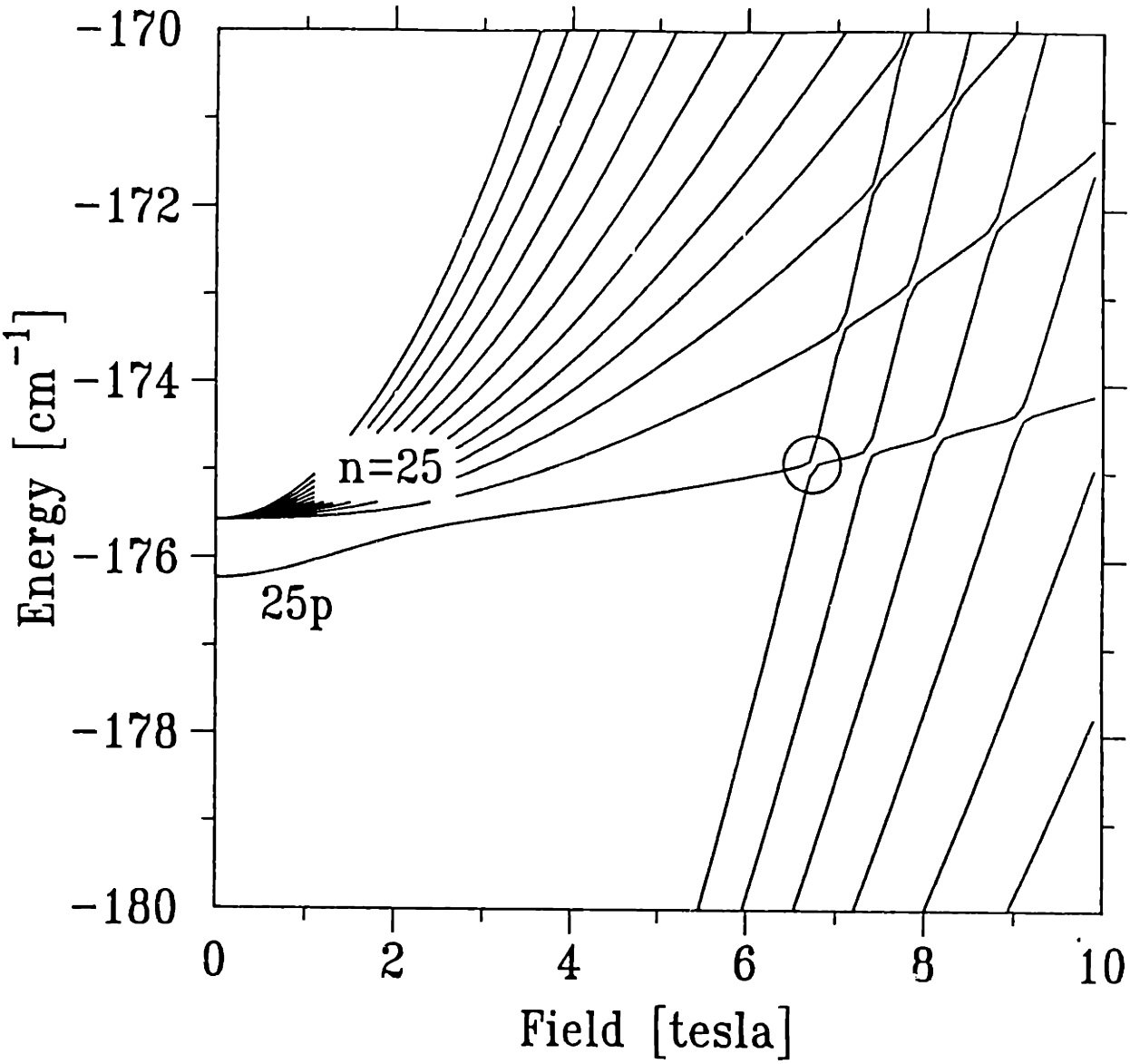

Figure 3.1.1 Lithium energy levels as a function of magnetic field, with m=0, π=-1, and n's near n=25.

the experimental results are presented in Chap. 6.

The relation between even and odd parity states is different in lithium and hydrogen. As may be seen in Fig. 3.1.2, the highest energy (low k) states of n=25, m=0, π=±1 are nearly degenerate, while the lowest energy (high k) states are interlaced. This is opposite to the behavior in hydrogen (see Sec. 2.3), and is apparently related to the large s-state quantum defect. When m=±1, the parity degeneracies of hydrogen and lithium are the same, as long as the field is sufficiently high that the p-state is mixed into the manifold. The degeneracy of parity has implications in our experimental determination of magnetic field which are discussed in Sec. 4.2.

On the other hand, the global energy level behavior of lithium is similar to that of hydrogen. This is the underlying justification for the use of lithium instead of hydrogen in our experiment.

Diamagnetism of Low-Lying States and the Core

We now discuss the diamagnetic shifts of the lithium 2s and 3s states and their impact on our two-photon transition. In Sec. 5.4, it will be shown that the diamagnetic shift of the 3s state does not significantly affect our determination of the Rydberg state energy. The numerical integration routine described is least reliable for calculating matrix elements of low-lying states, because the integration stops at approximately the

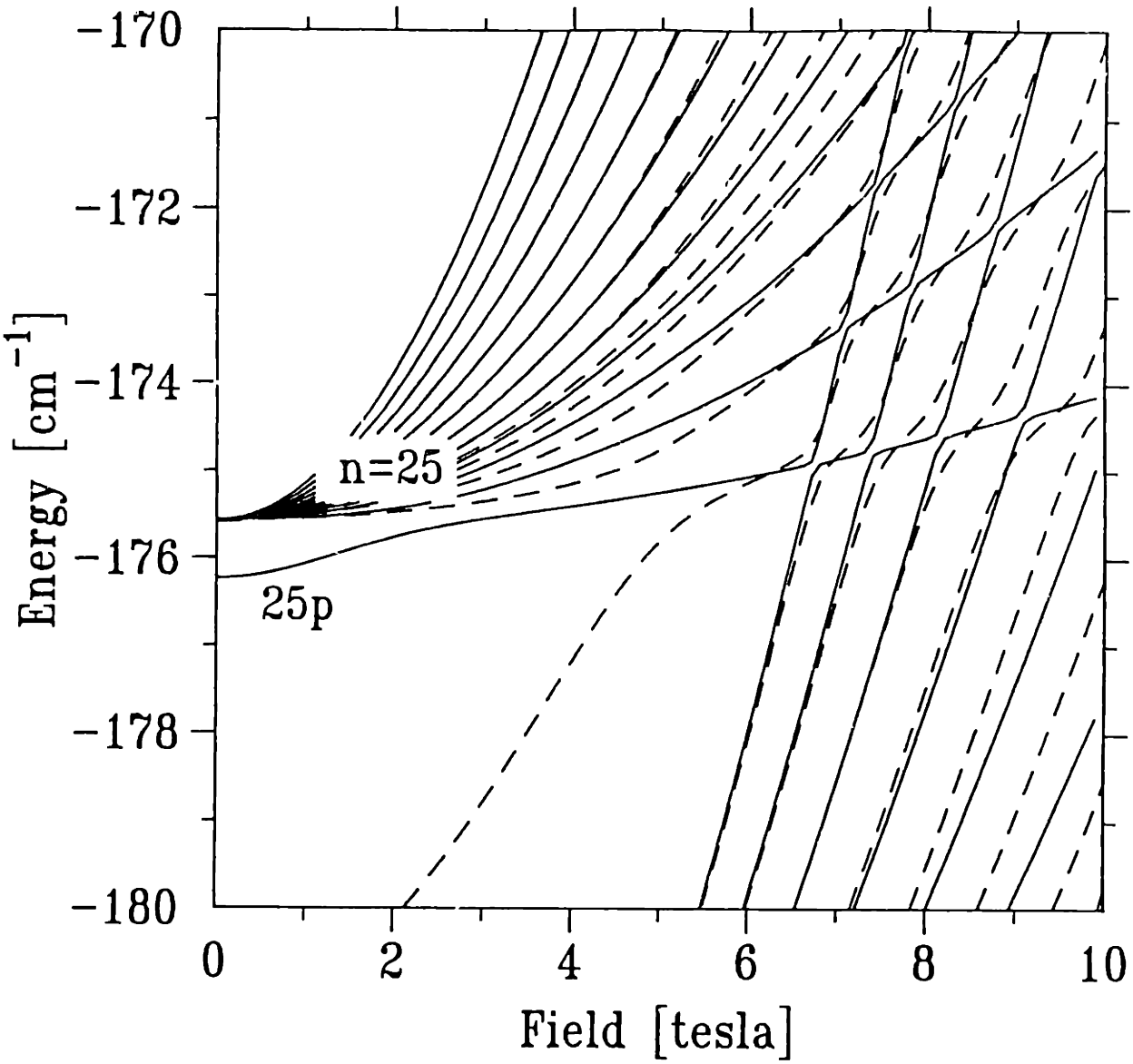

Figure 3.1.2 Lithium energy levels as a function of magnetic field, with m=0, π=±1, and n's near n=25. The solid lines show odd parity states, while the dashed lines show even parity states. Note the near degeneracy of the different parity high energy (low k) states of n=25.

core radius. Fortunately, a number of matrix elements for lithium have been calculated using the method of Hartree-Fock [CFF77]. These are compared with our calculations in the following table. Also presented are some matrix elements of the core electrons in the 1s orbitals, which our method does not give.

Matrix Element	Present Method	Hartree Fock
$\langle r \rangle_{1s}$		0.573,125
$\langle r \rangle_{2s}$	3.876,790	3.873,663
$\langle r \rangle_{3s}$	10.166,56	
$\langle r^2 \rangle_{1s}$		0.446,803
$\langle r^2 \rangle_{2s}$	17.709,89	17.738,455
$\langle r^2 \rangle_{3s}$	117.6068	

Table 3.1.2 Comparison of r and r^2 expectation values using two methods. In our method, 10,000 (quadratically spaced) points were used. The Hartree-Fock value is from Fischer [CFF77]. For both expectation values in the 2s state the deviation is less than 1%.

Notice that the value of $\langle r \rangle_{1s}$ is very close to the core radius estimated from the dipole core polarizability (see Eq. (3.1.12c)).

The ground state is non-degenerate and the diamagnetic shift may be easily calculated using (non-degenerate) perturbation theory:

$$\Delta E(2s) = \frac{1}{8} B^2 (\langle \rho^2 \rangle_{2s} + \langle \rho_1^2 + \rho_2^2 \rangle_{1s}) . \qquad (3.1.14a)$$

The 2s and 1s states are spherically symmetric; the core matrix element is symmetric

with respect to exchange [BES57]. Therefore

$$\Delta E\,(2s)/B^2 = \frac{1}{12}\,\langle r^2\rangle_{2s} + \frac{1}{6}\,\langle r^2\rangle_{1s}$$

$$= 0.176\ \text{MHz/T}^2 + 8.93\ \text{kHZ/T}^2$$

$$= 0.185\ \text{MHz/T}^2\ . \qquad (3.1.14b)$$

We also need to know the diamagnetic shift of the $3s$ state. *Assuming* the core matrix element is unchanged, the shift is

$$\Delta E\,(3s)/B^2 = \frac{1}{12}\,\langle r^2\rangle_{3s} + \frac{1}{6}\,\langle r^2\rangle_{1s}$$

$$= 1.176\ \text{MHz/T}^2 + 8.93\ \text{kHz/T}^2$$

$$= 1.185\ \text{MHz/T}^2\ . \qquad (3.1.15)$$

The shift in the laser frequency for driving the two-photon transition $2s \rightarrow 3s$ is

$$\Delta\nu/B^2 = 0.500\ \text{MHz/T}^2\ . \qquad (3.1.16)$$

The diamagnetic shift due to the core alone is quite small, and below our experimental precision.

3.2 Anticrossings and the Ionic Core

The circled feature in Fig. 3.1.1 is one of the most fascinating aspects of the lithium diamagnetic spectrum. The levels look like they're going to cross with increasing energy, but veer off at the last moment. This is a general property of the eigenvalues of non-separable Hamiltonians; the size of the anticrossing is a measure of the non-separability.

Figure 3.2.1 shows a blow-up of the circled feature of Fig. 3.1.1. The energy levels look like a hyperbola. The model discussed below supports that observation. The size of an anticrossing is the minimum separation between the levels; the anticrossing field is the location of this minimum.

Many people refer to these objects as "avoided crossings." We prefer "anticrossing." "Avoided" functions as an adjective of "crossing": therefore, an avoided crossing is a type of crossing. But it is not a crossing at all. The word "anticrossing" means levels that do not cross.

The Two-State Model

The essence of this model is that lithium may be considered as hydrogen perturbed by the lithium core. Then the anticrossings in the diamagnetic spectrum of lithium are the result of the crossing of two hydrogenic levels coupled by the lithium core. This model was conceived as a parallel theory to that of Komarov [KGJ80],

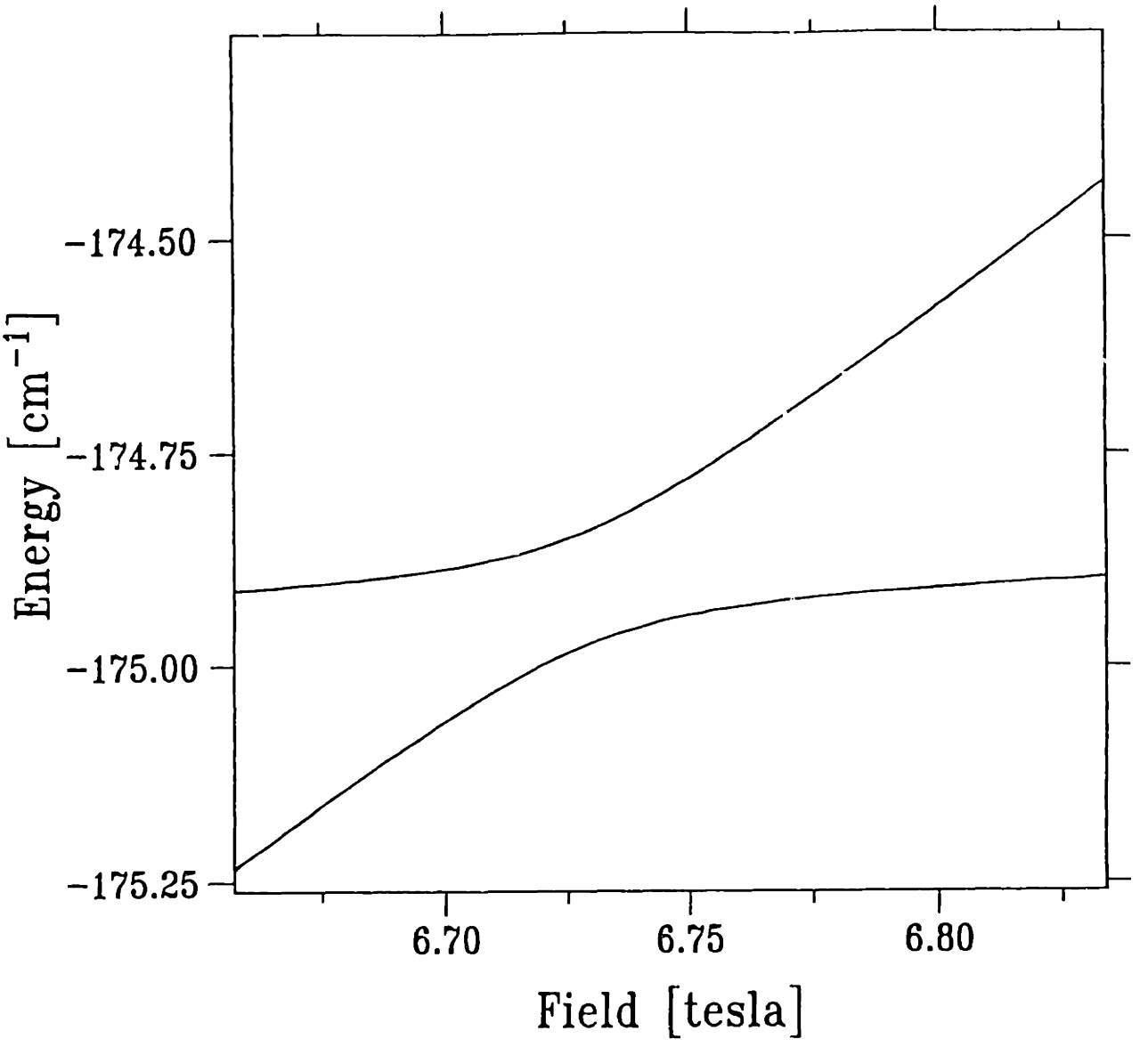

Figure 3.2.1 Lithium anticrossing. This is the first anticrossing between n=24, m=0, π=-1 and n=25, m=0, π=-1, and is shown circled in Fig. 3.1.1.

which interprets similarly the anticrossings in the Stark spectrum of alkalis [ZKW82]. Of course, there is a difference: in the Stark effect of hydrogen, the levels actually cross, where as in the Rydberg diamagnetic spectrum of hydrogen, the levels have small anticrossings. (See Fig. 2.2.2.)

Two crossing levels whose states are coupled by a constant perturbation yield new levels which look like hyperbolae. Both numerical predictions and experimental data may be fit by the hyperbola, so that the anticrossing size and the anticrossing field may be extracted. Relative transition strengths can be explained in terms of this model.

The first ingredient of the model is the form of the Hamiltonian for the valence electron of lithium. It is the sum of the hydrogen Hamiltonian and a core operator:

$$H_A = H_o + V_c \ , \tag{3.2.1a}$$

where

$$H_o = \frac{1}{2} p^2 - \frac{1}{r} \tag{3.2.1b}$$

and

$$V_c = \sum_{l=0}^{\infty} \mathrm{v}_l(r) P_l \ . \tag{3.2.1c}$$

Here, $\mathrm{v}_l(r)$ is a short range spherical potential which vanishes as l gets large, and P_l is the projector operator into the l^{th} subspace of the valence electron. The appearance

of l in $v_l(r)$ allows for possible changes in the core caused by different amounts of penetration of the valence electron into the core. A (less general) specific example of a model core potential is given by the static polarization model. The operator is

$$V_c(r) = -\frac{1}{2}\,\alpha_{cd}\,\frac{1}{r^4} \tag{3.2.2}$$

where α_{cd} is the dipole polarizability of the core. Here, the form of the operator is independent of l; of course, matrix elements of this operator do depend on l.

Let $| nlm >$ represent the spherical states of hydrogen. The most general (bound state) matrix element of the core operator defined by Eq. (3.2.1) is

$$< nlm \mid V_c \mid n'l'm' > = < nl \mid v_l(r) \mid n'l > \; \delta_K(l,l')\delta_K(m,m') \,, \tag{3.2.3}$$

since the angular wave functions are normalized spherical harmonics.

The second component of the model is a useful form of the radial wave functions of hydrogen which clearly separates the dependence on energy and angular momentum near the origin. The procedure for obtaining this merits some discussion. To evaluate the matrix element, the representation must be properly normalized. We shall find a series expansion about zero for the solution to the radial Schroedinger equation:

$$\frac{d^2R}{dr^2} + \frac{dR}{dr} + \left[2E + \frac{2}{r} - \frac{l(l+1)}{r^2}\right]R = 0 \,. \tag{3.2.4}$$

Because of the removable singularity at the origin, a Frobenius expansion is required:

$$R(r) = r^s \sum_{k=0}^{\infty} a_k r^k \ . \tag{3.2.5a}$$

If $a_o \neq 0$, then the coefficients of r^{-2} require that $s = l$ or $-(l+1)$; the former is selected so that the function is regular at the origin. The coefficients of r^{-1} show that

$$a_1 = - \frac{1}{l+1} a_o \ . \tag{3.2.5b}$$

The recursion relation among subsequent coefficients is

$$a_{k+2} = \frac{a_{k+1} + E a_k}{(k+2)l + 3} \ , \ k \geq 0 \ . \tag{3.2.5c}$$

This is *not* the usual series for the hydrogen radial wave function because the exponential behavior at large r has not been factored out: this series will not terminate. However, because all of the coefficients are proportional to a_o, a_o may be taken as the normalization constant. It also shows that the a_k's are polynomials in E (not $E^{1/2}$) as well as being functions of l. Therefore it is possible to group the powers of E together, and write

$$R(r) = a_o r^l \sum_{k=0}^{\infty} F_l^{(k)}(r) E^k \ . \tag{3.2.5d}$$

Using Eqs. (3.2.5b) and (3.2.5c), the initial terms in the series may be constructed:

$$R(r) = a_o r^l \left[\left(1 - \frac{r}{l+1} + \frac{r^2}{(2l+3)(l+1)} + \ldots\right) + \left(-\frac{r^2}{2l+3} + \ldots\right) E + \ldots \right] . \tag{3.2.5e}$$

Of course, the wave functions and energies are well known. The energy is $E = -1/2n^2$. One standard form of the wave function is [LAL77, pp. 117-120]:

$$R_{nl}(r) = A r^l e^{-r/n} F(-n+l+1,\ 2l+2,\ 2r/n) \tag{3.2.6a}$$

where the normalization constant is

$$A = \frac{2^{l+1}}{n^{l+2}(2l+1)!} \left[\frac{(n+l)!}{(n-l-1)!}\right]^{1/2} \tag{3.2.6b}$$

and $F(a, b, x)$ is the confluent hypergeometric function

$$F(a, b, x) = 1 + \frac{a}{b}\frac{x}{1!} + \frac{a(a+1)}{b(b+1)}\frac{x^2}{2!} + \ldots \tag{3.2.6c}$$

which terminates when a is a negative integer. For $l=0$, Eq. (3.2.5e) gives $R(0) = a_o$ while Eq. (3.2.6a) give $R_{no}(0) = A$, which establishes that $a_o = A$. Then it is clear that the bracketed term in Eq. (3.2.5e) must be equal to the product of the exponential and confluent hypergeometric function in (3.2.6a). The first few terms may be verified by the industrious reader.

There is an expansion of the confluent hypergeometric function in terms of Bessel functions (of the first kind) which puts the above discussion on a somewhat more formal basis. If you're good, if you're *really* good, you can show that the radial

wave function may be expressed as [ABS70]

$$R_{nl}(r) = \frac{1}{n^{l+2}} \left[\frac{(n+l)!}{(n-l-1)!}\right]^{1/2} \left[\frac{2}{r}\right]^{1/2} \sum_{k=o}^{\infty} A_k \left[\frac{r}{2n^2}\right]^{k/2} J_{2l+1+k}(\sqrt{8r}) \qquad (3.2.7a)$$

with

$$A_o = 1,\ A_1 = 0,\ A_2 = l+1,\ A_3 = -\frac{2}{3}n,\ A_4 = \frac{1}{2}(l+2)(l+1), \qquad (3.2.7b)$$

or generally

$$(k+1)A_{k+1} = (k+2l+1)A_{k-1} - 2nA_{k-2}\ . \qquad (3.2.7c)$$

The first two factors may be expanded in a power series of n^{-2}:

$$\frac{1}{n^{l+2}} \left[\frac{(n+l)!}{(n-l-1)!}\right]^{1/2} = \frac{1}{n^{3/2}} \left[1 - \frac{l(l+1)(2l+1)}{12n^2} + O(n^{-4})\right]. \qquad (3.2.7d)$$

Therefore, near the origin the normalized radial wave function has the form

$$R_{nl}(r) = \frac{1}{n^{3/2}} \sum_{k=0}^{\infty} f_l^{(k)}(r)\left(\frac{1}{n^2}\right)^k\ . \qquad (3.2.8)$$

Using Eqs. (3.2.7a) and (3.2.7d), we could explicitly construct $f_l^{(k)}(r)$, but that is not necessary in what follows.

The matrix element of the core operator in Eq. (3.2.3) may now be expressed in terms of $f_l^{(k)}(r)$:

$$< nl \mid v_l(r) \mid n'l > = - \frac{1}{(nn')^{3/2}} \left[\tilde{\delta}_l^{(0)} + \left[\frac{1}{n^2} + \frac{1}{n'^2} \right] \frac{\tilde{\delta}_l^{(1)}}{2} + O(n^{-4}) \right] \quad (3.2.9a)$$

where

$$\tilde{\delta}_l^{(0)} = - \int_0^\infty (r^2 dr) v_l(r) [f_l^{(0)}(r)]^2 \quad (3.2.9b)$$

and

$$\tilde{\delta}_l^{(1)} = - 2 \int_0^\infty (r^2 dr) v_l(r) f_l^{(0)}(r) f_l^{(1)}(r) \, . \quad (3.2.9c)$$

The symbols selected to represent these integrals suggest a connection with quantum defects. Identifying these integrals as quantum defects may be justified by considering the diagonal matrix element. Perturbation theory gives the shift to a hydrogen energy level caused by the core. In first order, the shift is

$$\Delta E = < nlm \mid V_c \mid nlm > = - \frac{1}{n^3} [\tilde{\delta}_l^{(0)} + \frac{1}{n^2} \tilde{\delta}_l^{(1)} + O(n^{-4})] \quad (3.2.10)$$

From quantum defect theory, the energy of a lithium state

$$E = - \frac{1}{2(n-\delta_l)^2} = - \frac{1}{2n^2} [1 + 2 \frac{\delta_l}{n} + 3(\frac{\delta_l}{n})^2 + O(\frac{\delta_l}{n})^3] \, , \quad (3.2.11a)$$

so the first order (in quantum defect) shift is

$$\Delta E = -\frac{\delta_l}{n^3} \ . \tag{3.2.11b}$$

The Ritz expansion of the quantum defect, Eq. (3.1.5a), may be expanded in powers of n^{-1}, rather than powers of $(n^*)^{-2}$. The result is

$$\delta_l = \delta_l^{(0)} + \frac{1}{n^2}\delta_l^{(1)} + \frac{1}{n^3}\, 2\delta_l^{(1)}\delta_l^{(0)} + \frac{1}{n^4}\,[\delta_l^{(2)}+3\delta_l^{(1)}(\delta_l^{(0)})^2] + O(n^{-5}) \ . \tag{3.2.11c}$$

In the spirit of considering the first order (in quantum defect) shift in energy, Eqs. (3.2.11b) and (3.2.11c) yield

$$\Delta E = -\frac{1}{n^3}\,[\delta_l^{(0)} + \frac{1}{n^2}\,\delta_l^{(1)} + O(n^{-4})] \tag{3.2.11d}$$

in agreement with the first order perturbation calculation of Eq. (3.2.10). The higher order terms of Eqs. (3.2.11c) and (3.2.11a) may be considered as higher-order perturbation-theory corrections of the core operator. Alternatively, the constants $\tilde{\delta}_l^{(0)}$ and $\delta_l^{(1)}$ may be fit to a set of $\delta_l(n)$ using the formula

$$\delta_l(n) = \tilde{\delta}_l^{(0)} + \frac{1}{n^2}\,\tilde{\delta}_l^{(1)} \ . \tag{3.2.11e}$$

The point of this discussion is that since quantum defects may be determined from experimental spectra, off-diagonal matrix elements of the core may be calculated using Eq. (3.2.9a). We do not need to do integrals such as those of Eqs. (3.2.9b) and (3.2.9c).

The third piece of the model considers the effect of the magnetic field on the lithium valence electron. The total Hamiltonian is

$$H_A(B) = H_A + H_p + H_d \ , \tag{3.2.12a}$$

where

$$H_A = H_o + V_c \ , \tag{3.2.12b}$$

$$H_p = \frac{1}{2} \vec{B} \cdot \vec{L} \ , \tag{3.2.12c}$$

$$H_d = \frac{1}{8} (\vec{B} \times \vec{r})^2 \ . \tag{3.2.12d}$$

If we define the Hamiltonian of hydrogen in a magnetic field as

$$H_o(B) = H_o + H_p + H_d \ , \tag{3.2.12e}$$

then for lithium in a magnetic field, the Hamiltonian is

$$H_A(B) = H_o(B) + V_c \ . \tag{3.2.12f}$$

The procedure is to find the eigenstates of $H_o(B)$ and then consider the effect of V_c perturbatively.

Now we assert that the diamagnetic states of hydrogen, that is the eigenstates of $H_o(B)$, may be expressed as linear combinations of the (bound) spherical states of hydrogen, or the eigenstates of H_o. In the simplest form of this statement, we assume that there is no n-mixing so that the states are field-independent. These states are the "right linear combination" of states discussed in Chap. 2 which diagonalize the

diamagnetic Hamiltonian with a given n. Although there is no analytic transformation between the spherical states and these states, there are some approximate expressions. (See the Γ and V regimes discussed in Sec. 2.3.) Also, the transformation can be generated numerically: because the states are field-independent, this transformation need be generated only once. A more complicated form of the model uses the n-mixed, field-dependent states of hydrogen, which must be generated numerically. Both versions of our model neglect the effect of the hydrogen continuum. Furthermore, it is assumed that the anticrossings considered are *not* in the strong mixing regime, so that the hydrogen states may be meaningfully labeled by the appropriate principal quantum number and another quantum number associated with the diamagnetic energy. As discussed in Sec. 2.1, this also insures that the hydrogen states (very nearly) cross. Given the transformation between bases of hydrogen, the effect of the core may be calculated using the core matrix element of Eq. (3.2.3).

Anticrossing Size and Shape

Beginning with the simpler version of our model, we neglect the n-mixing induced by the diamagnetic operator H_d. Then the eigenstates of $H_o(B)$ may be labeled and expanded as

$$| nkm > = \sum_{l=|m|}^{n-1}{}' < nlm \mid nkm > | nlm > \qquad (3.2.13)$$

where the prime on the sum indicates only odd (even) l's if the parity is π=-1 (+1).

The Castro labeling convention for k is used, as discussed in Sec 2.2: odd (even) k's indicate $\pi = -1(+1)$. Now we consider the energy of two "crossing" hydrogen states, both with the same m and π. The quotes around the word "crossing" mean that we know that the levels really anticross, but that the size of the anticrossing is very small. In a neighborhood of the field at which the crossing occurs, the energies of the two states may be expanded in a Taylor series about the crossing field B_c. For the two states we have

$$| 1 > = | nkm > ; \; E_1(B) = E_1(B_c) + c_1 (B - B_c) + \ldots \tag{3.2.14a}$$

$$| 2 > = | n'k'm > ; \; E_2(B) = E_2(B_c) + c_2 (B - B_c) + \ldots \tag{3.2.14b}$$

The crossing energy is defined to be the eigenvalue of $H_o(B)$ for both states at the crossing field: $E_c = E_1(B_c) = E_2(B_c)$. From the discussion of the Feynman-Hellman theorem presented in Sec. 2.2, the slopes are

$$c_1 = \frac{\partial E_1}{\partial B}\Big|_{B_c} = \frac{1}{2} m + \frac{1}{4} B_c < 1 | \rho^2 | 1 > , \tag{3.2.14c}$$

$$c_2 = \frac{\partial E_2}{\partial B}\Big|_{B_c} = \frac{1}{2} m + \frac{1}{4} B_c < 2 | \rho^2 | 2 > . \tag{3.2.14d}$$

We use degenerate perturbation theory to express the action of the core. In the two-state basis $\{| 1 >, | 2 >\}$, the total Hamiltonian is represented as

$$H_A(B) = \begin{bmatrix} (H_A(B))_{11} & (H_A(B))_{12} \\ (H_A(B))_{21} & (H_A(B))_{22} \end{bmatrix} \tag{3.2.15a}$$

where

$$(H_A(B))_{11} = E_1(B) + < 1 \mid V_c \mid 1 > , \tag{3.2.15b}$$

$$(H_A(B))_{22} = E_2(B) + < 2 \mid V_c \mid 2 > , \tag{3.2.15c}$$

and

$$(H_A(B))_{12} = < 1 \mid V_c \mid 2 > . \tag{3.2.15d}$$

The eigenvalues of this representation are well known:

$$E_{\pm} = \frac{1}{2} [(H_A(B))_{11}+(H_A(B))_{22}] \pm \frac{1}{2} \{[(H_A(B))_{11}-(H_A(B))_{22}]^2 + 4 \mid (H_A(B))_{12} \mid^2\}^{1/2} \tag{3.2.15e}$$

The parameters of this formula may be expressed as

$$\frac{1}{2} [(H_A(B))_{11}+(H_A(B))_{22}] = E_a + \frac{1}{2} (c_1+c_2)(B-B_a) , \tag{3.2.15f}$$

$$(H_A(B))_{11} - (H_A(B))_{22} = (c_1-c_2)(B-B_a) , \tag{3.2.15g}$$

where the *anticrossing* energy and field have been introduced:

$$E_a = E_c + \frac{1}{2}\left[< 1 \mid V_c \mid 1 > + < 2 \mid V_c \mid 2 > \right.$$

$$\left. - \frac{c_1 + c_2}{c_1 + c_2} \left(< 1 \mid V_c \mid 1 > - < 2 \mid V_c \mid 2 >\right)\right] \qquad (3.2.15h)$$

$$B_a = B_c - \frac{< 1 \mid V_c \mid 1 > - < 2 \mid V_c \mid 2 >}{c_1 - c_2} \qquad (3.2.15i)$$

It is evident that the eigenvalues form a hyperbola as a function of $B - B_a$. When the field is far from B_a, the energies of hydrogen are simply shifted by the (diagonal matrix elements of the) core. See Fig. 3.2.2 for a summary of these ideas.

The separation of the eigenvalues may be expressed as a function of $B - B_a$:

$$\Delta E = E_+ - E_- = a\left[1 + \left[\frac{B - B_a}{b}\right]^2\right]^{1/2} \qquad (3.2.16a)$$

where the minimum separation, or anticrossing size, is

$$a = 2\left|< 1 \mid V_c \mid 2 >\right|, \qquad (3.2.16b)$$

and the scale length, is

$$b = \frac{2\left|< 1 \mid V_c \mid 2 >\right|}{c_1 - c_2} . \qquad (3.2.16c)$$

The scale length is the change in B from B_a which increases the separation to $\Delta E = a\sqrt{2}$. Now the parameters a, b, and B_a may be determined by fitting Eq. (3.2.16a) to either theory or experiment. As an example, the separation between the

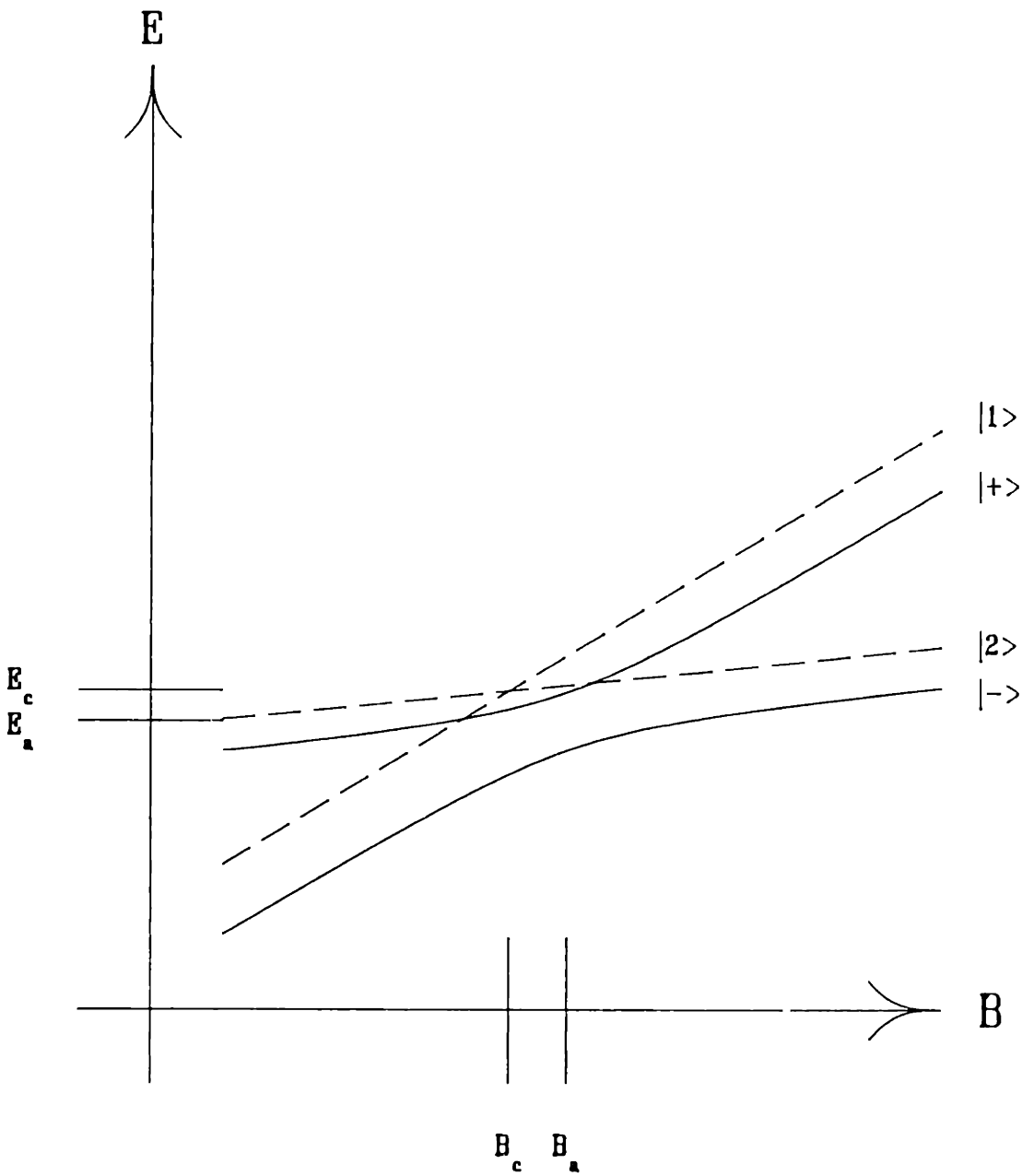

Figure 3.2.2 The effect of the lithium core on a hydrogen "crossing". The dashed lines show the eigenenergies of $H_o(B)$, while the solid lines illustrate the lithium energy levels in the context of the two-state model.

levels of the anticrossing of Fig. 3.2.1 is presented in Fig. 3.2.3. Equation (3.2.16a) is fit to it, and the parameters are presented in Table 3.2.1.

size:	a = 0.1335(2) cm^{-1}
position:	B_c = 6.722,14(3) T
scale length:	b = 0.031,89(5) T

Table 3.2.1 Parameters of the "first" anticrossing between n=24 and n=25, m=0, π=-1, based on fitting Eq. (3.2.16a) to the calculation of Fig. 3.2.3.

The deviation between the calculated and fit energy separation is plotted in Fig. 3.2.4. The fit is quite good, although clearly the true level separation is more complicated than Eq. (3.2.16a). One factor not incorporated into the model is the effect of other nearby anticrossings. These certainly change the separation at the asymptotes of the anticrossing under consideration.

The model also provides a means for calculating the anticrossing parameters based on our knowledge of hydrogen. From Eqs. (3.2.16b), (3.2.13), (3.2.9a), and (3.2.3), the anticrossing size may be written as

$$a = 2|\langle 1 \mid V_c \mid 2 \rangle| = 2|\langle nkm \mid V_c \mid n'k'm \rangle| \tag{3.2.17a}$$

or

$$a = 2\Big| \sum_{l=|m|}^{\min(n-1,\, n'-1)}{}' \langle nlm \mid nkm \rangle^{*} \langle n'lm \mid n'k'm \rangle \times$$

$$\frac{1}{(nn')^{3/2}} \left[\tilde{\delta}_l^{(0)} + \left(\frac{1}{n^2} + \frac{1}{n'^2}\right)\tilde{\delta}_l^{(1)} + O(n^{-4})\right]\Big| . \tag{3.2.17b}$$

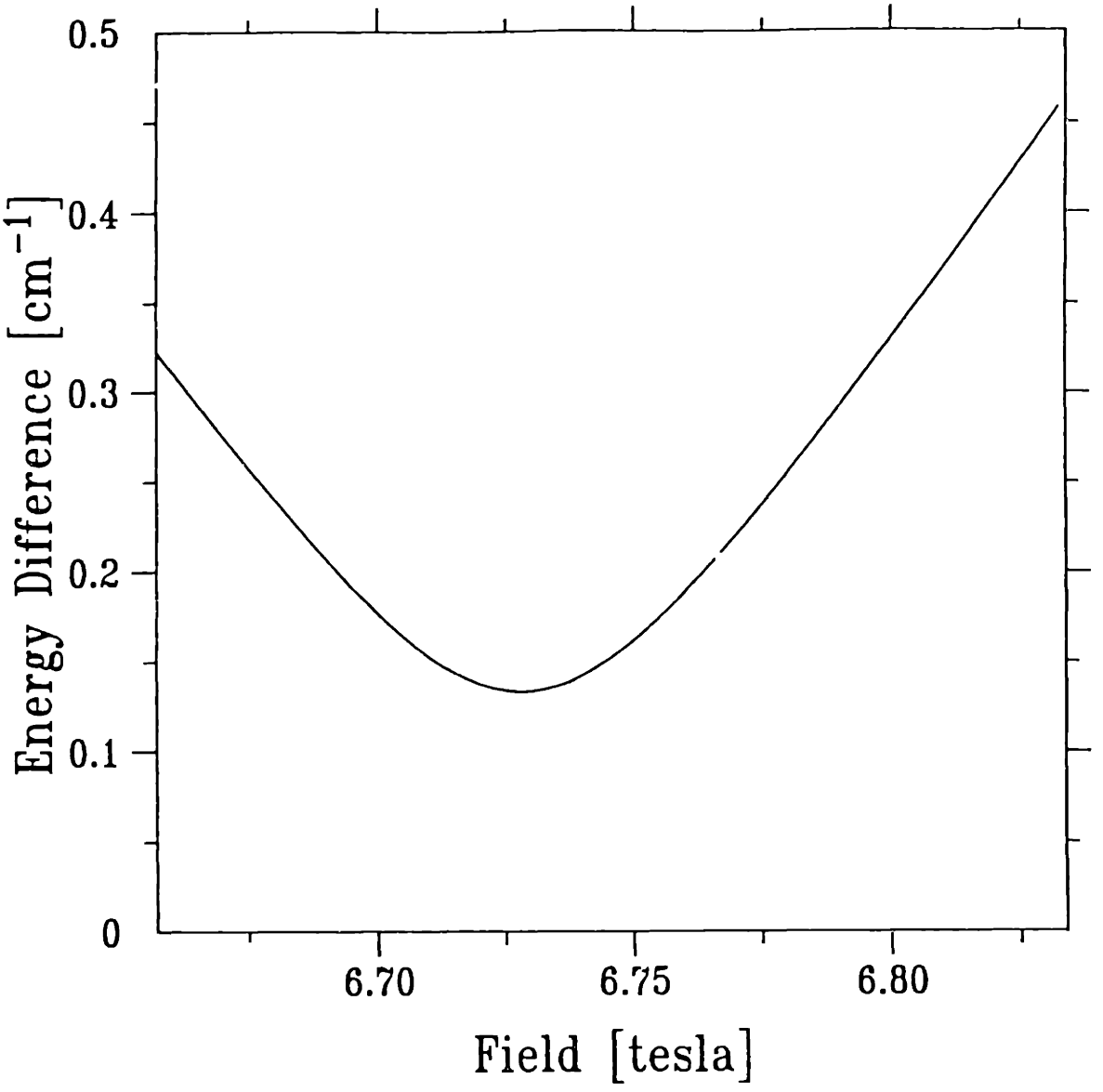

Figure 3.2.3 Anticrossing separation. This curve is the difference between the energy levels in Fig. 3.2.1.

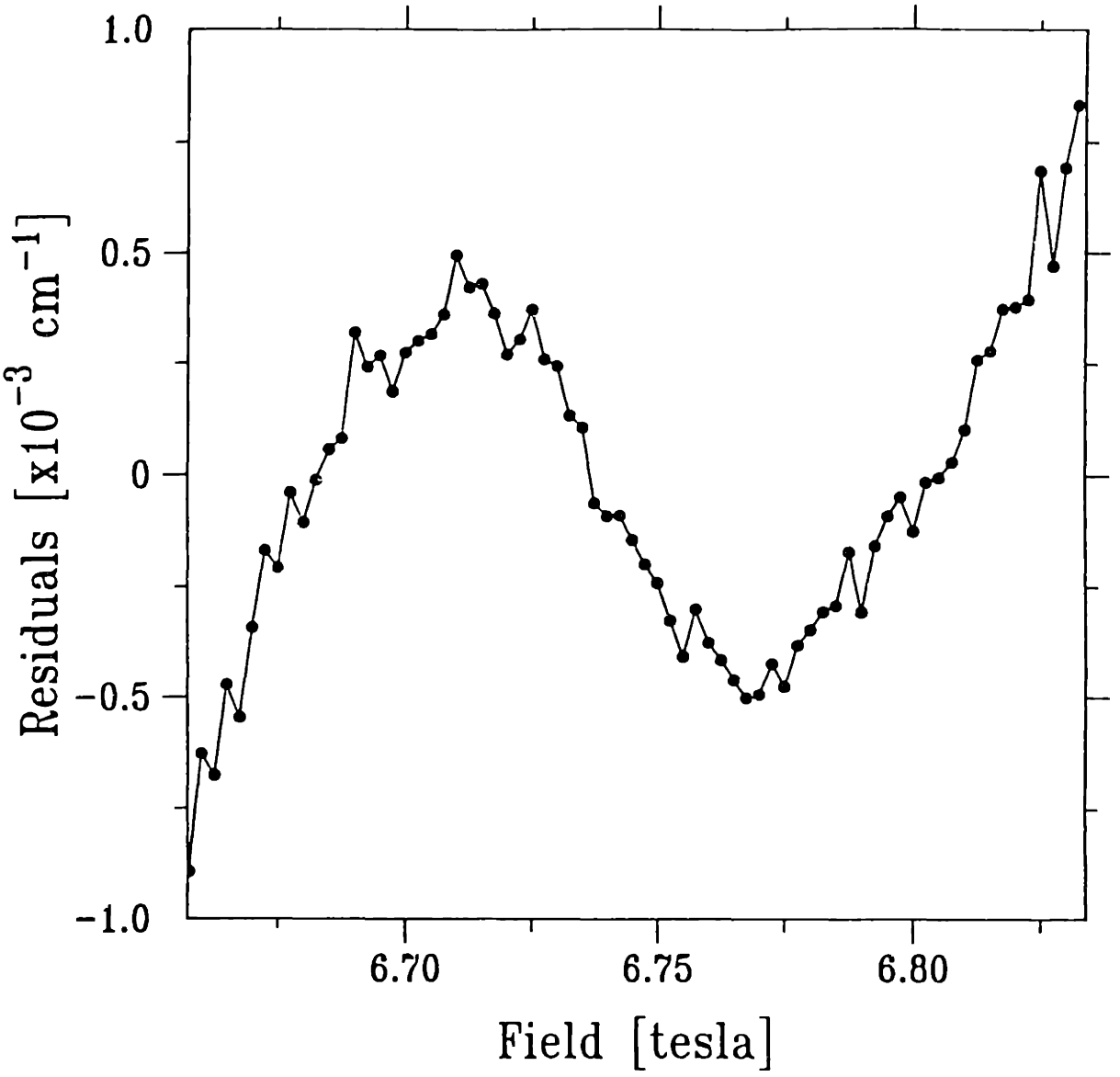

Figure 3.2.4 Deviation between the energy separation for the anticrossing of Fig. 3.2.1 and its fit by Eq. (3.2.16a). The gross structure of the curve looks like a third-order polynomial, and is caused by neglecting nearby anticrossings in the two state model. The "noise" is caused by the finite convergence criterion of the diagonalization program, and shows our typical numerical precision.

Note that there is not a double sum because the core matrix element is diagonal in l. For a given n, m, and π, the transformation coefficients may be generated numerically. They are the eigenvectors of the hydrogen diamagnetic Hamiltonian, $H_o(B)$, projected on to the spherical states of hydrogen. For the anticrossing presented in Fig. 3.2.1, the result of Eq. (3.2.17b) is $a = 0.117\ \mathrm{cm}^{-1}$. This is 12% smaller than the value predicted by the lithium matrix diagonalization, reported in Table 3.2.1. It is quite likely that neglecting n-mixing is responsible for this difference.

The expression for anticrossing size may be simplified on the basis of the following observations. If there is only one significant quantum defect for a given parity, then the sum in Eq. (3.2.17b) may be eliminated. For instance, for the odd (even) parity states of lithium, only the p (s) state quantum defect is very different from zero. Furthermore, the energy dependence of quantum defects is generally small for Rydberg states because $|\delta_l^{(0)}| >> |\delta_l^{(1)}/n^2|$. Finally, the transformation coefficients have a magnitude which is *of order* the reciprocal square root of the number of states with the given n, m, and π. This follows from the fact that the transformation must be unitary, and the coefficients are all roughly the same size. Most often we have $|m| << n$, so for a particular parity

$$|< nlm \mid nkm >| \sim (n/2)^{-1/2} . \qquad (3.2.17c)$$

A crude estimate of the anticrossing size is then given by

$$a \sim \frac{4\tilde{\delta}_l^{(0)}}{(nn')^2} \ . \tag{3.2.17d}$$

Again for the anticrossing of Fig. 3.2.1, this estimate predicts a ~0.12 cm^{-1}, which agrees fortuitously well with the more careful evaluation of Eq. (3.2.17b). Here $\tilde{\delta}_1^{(0)} \simeq 0.05$ is used as the p state quantum defect. The estimate predicts that between a given n and n', the anticrossings are all roughly the same size.

To correct the model for the n-mixing induced by diamagnetism, the transformation between diamagnetic and spherical states must be augmented. The transformation which replaces Eq. (3.2.13) is

$$| nkm; B > = \sum_{\bar{n}=1}^{\infty} \sum_{l=|m|}^{\bar{n}-1}{}' < \bar{n}lm \mid nkm; B > | \bar{n}lm > . \tag{3.2.18}$$

The remainder of the model is the same. The anticrossing size is

$$a = 2\Big| \sum_{\bar{n}=1}^{\infty} \sum_{\bar{n}'=1}^{\infty} \sum_{l=|m|}^{\min(\bar{n}-1,\, \bar{n}'-1)}{}' < \bar{n}lm \mid nkm; B >^* < \bar{n}'lm \mid n'k'm; B > \times$$

$$\frac{1}{(nn')^{3/2}} [\tilde{\delta}_l^{(0)} + (\frac{1}{n^2} + \frac{1}{n'^2}) \frac{\tilde{\delta}_l^{(1)}}{2} + O(n^{-4})]\Big| \tag{3.2.19}$$

This expression was evaluated for the anticrossing of Fig. 3.2.1 using n=22-27 and B=6.7T. The hydrogen transformation coefficients for n~25 are rather insensitive to field changes ~1T, at least for fields ≤10T, so the particular value of B used in Eq. (3.2.19) is not critical. The result is a=0.131 cm^{-1}, just 2% lower than the result of

the lithium matrix diagonalization. Using more n's may improve the result.

The necessity of having to perform large basis diagonalizations for hydrogen at many fields in order to find the transformation coefficients and the crossing fields rather limits the practical usefulness of this more complete model. It is easier just to diagonalize the approximate lithium Hamiltonian as discussed in Sec. 3.1. However, the simple model provides insight into the nature of anticrossings, and then useful parameters may be extracted from the lithium calculations. The difference between the simple and more complex model is n-mixing. This indicates that anticrossing sizes depend strongly on the details of the wave function.

Relative Transition Strengths

The two-state model for core-induced anticrossings also predicts the relative transition strength to the two coupled states from some initial state. For electric dipole transitions, the transition operator is $T = -\vec{r} \cdot \hat{\epsilon}$, where $\hat{\epsilon}$ is the polarization unit vector of the radiation causing the transition. For our experiment, the initial state is the lithium 3s state, and the final state is a lithium Rydberg state with odd parity and m=0 or ±1. The transition matrix element is $< 0 \mid T \mid nkm; B >$, where $\mid 0 >$ is the 3s state of lithium. The 3s state is not strongly affected by a magnetic field ≤10 T because is not degenerate with 3d in lithium. Its diamagnetic shift is

$$E_d = \langle H_d \rangle_{3s} \approx (1.19 \text{ MHz/T}^2) B^2 . \qquad (3.2.20)$$

(See Sec. 3.1.) The transition matrix element may be evaluated using the lithium matrix diagonalization with eigenvector storage. The basis includes odd parity spherical Rydberg states in the energy range of interest. The final value of m depends on the polarization: if $\hat{\epsilon}$ is parallel to $\vec{B}$, $m=0$; if $\hat{\epsilon}$ is perpendicular to $\vec{B}$, $|m|=1$. The eigenvectors are expressed as a linear combination of the spherical states:

$$|nkm;B> = \sum_{\bar{n}'s} \sum_{l=|m|}^{\bar{n}-1}{}' <\bar{n}lm|nkm;B>|\bar{n}lm> \qquad (3.2.21a)$$

where the sum over $\bar{n}$ includes all of the principal quantum numbers in the basis. Then the transition matrix element is

$$<0|T|nkm;B> = \sum_{\bar{n}'s} <\bar{n}1m|nkm;B><0|T|\bar{n}1m> \qquad (3.2.21b)$$

where only $l=1$ appears because electric dipole transitions must change l by 1. The transition strength is proportional to the magnitude squared of the transition matrix element. Figure 3.2.5 displays a "sequence plot" of the relative strength of the transitions to the anticrossing of Fig. 3.2.1 for ten different values of magnetic field. Clearly the transition probability to the upper state of the anticrossing becomes quite small near the center of the anticrossing. The same type of calculation for a wider field and energy range is shown in Fig. 3.2.6. This figure demonstrates that the change in transition strength is local to the anticrossing. Sufficiently far away from the anticrossing field on either side, the transition strength is unchanged.

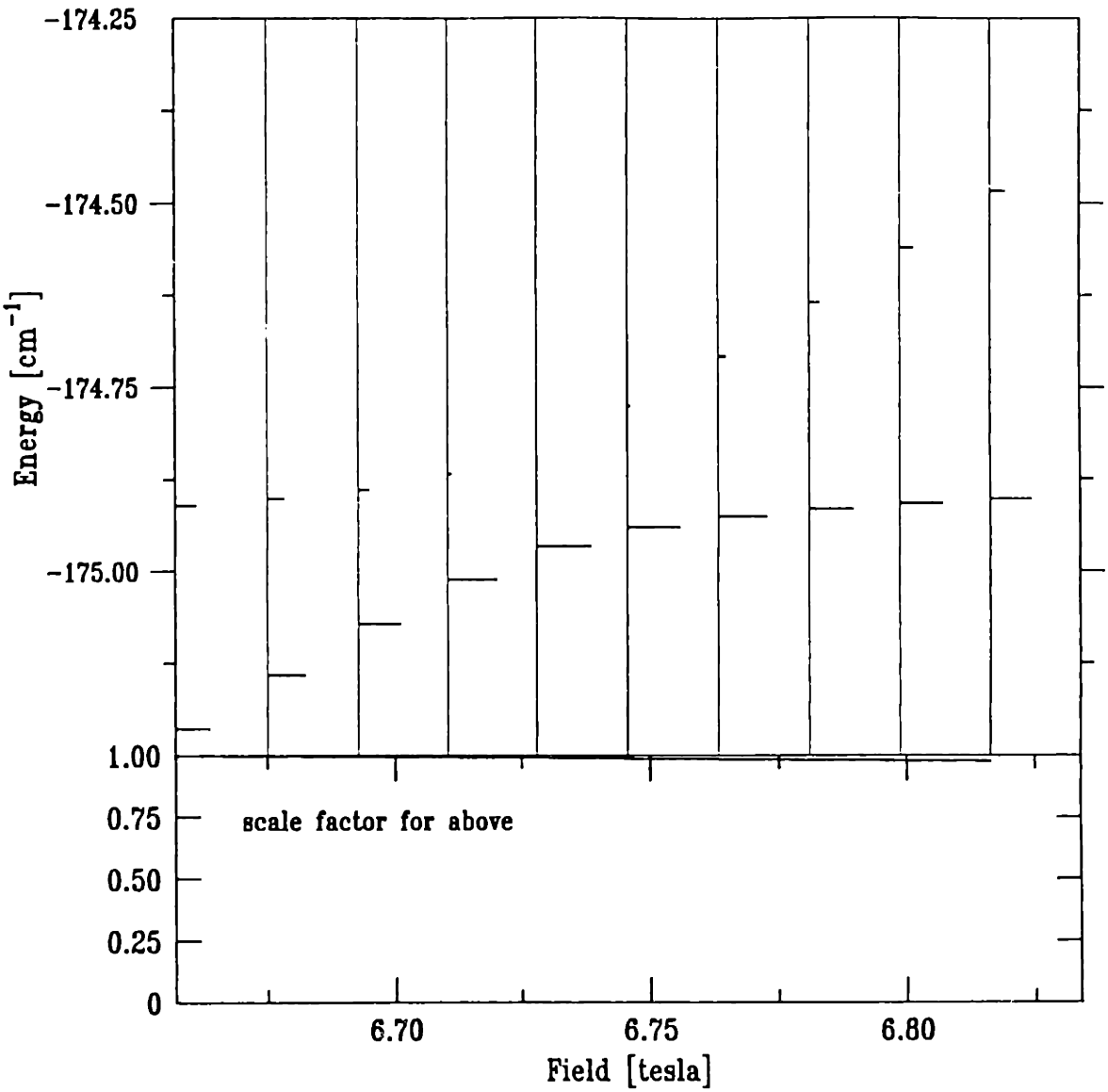

Figure 3.2.5 Relative transition strengths for the lithium anticrossing of Fig. 3.2.1. The strength to the upper level decreases while the strength to the lower level increases.

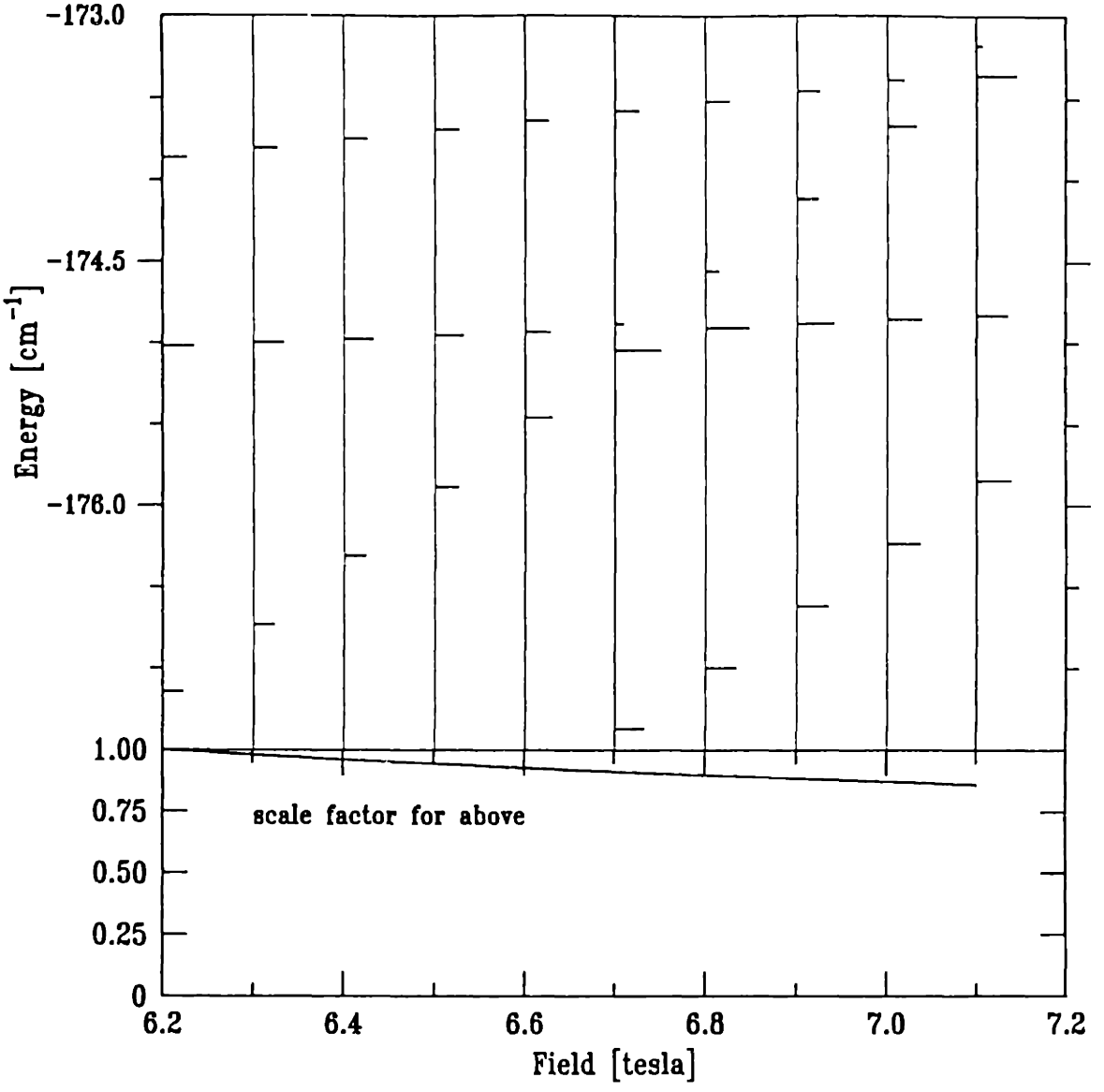

Figure 3.2.6 Relative transition strengths for the lithium anticrossing of Fig. 3.2.1, with a larger field and energy range than that of Fig. 3.2.5. The local nature of the change in transition strength is evident.

To explain this phenomenon in terms of the two-state model, we let $|+>$ represent the upper state of the lithium diamagnetic anticrossing, and $|->$ represent the lower, as in Fig. 3.2.2. The relative transition strength to these two states is the magnitude squared of

$$r = \frac{<0|T|+>}{<0|T|->} . \tag{3.2.22}$$

The eigenvectors of the 2×2 Hamiltonian in Eq. (3.2.15a) corresponding to the eigenvalues in Eq. (3.2.15e) are [CDL77, pp. 420-423]

$$|+> = \cos\frac{\theta}{2}\, e^{-i\phi/2}|1> + \sin\frac{\theta}{2}\, e^{i\phi/2}|2> \tag{3.2.23a}$$

$$|-> = -\sin\frac{\theta}{2}\, e^{-i\phi/2}|1> + \cos\frac{\theta}{2} e^{i\phi/2}|2> \tag{3.2.23b}$$

where states $|1>$ and $|2>$ are the (uncoupled) hydrogen states, and

$$\cot\theta = \frac{(H_A(B))_{11} - (H_A(B))_{22}}{2|(H_A(B))_{21}|} = \frac{1}{b}(B - B_a)\ ,\ 0 \le \theta < \pi\ , \tag{3.2.23c}$$

$$(H_A(B))_{21} = |(H_A(B))_{21}|e^{i\phi} = \frac{1}{2}\, ae^{i\phi}\ ,\ 0 \le \phi < 2\pi\ . \tag{3.2.23d}$$

Now r in Eq. (3.2.22) may be evaluated in terms of hydrogenic transition matrix elements. Let

$$x = e^{-i\phi}\frac{<0|T|1>}{<0|T|2>} = \frac{<1|V_c|2>}{|<1|V_c|2>|}\cdot\frac{<0|T|1>}{<0|T|2>} \tag{3.2.24a}$$

The magnitude squared of x is the relative transition strength to the crossing diamagnetic states of hydrogen. Relative transition strengths for hydrogen are plotted in Fig. 3.2.7, which shows that this ratio does not change in the vicinity of the crossing; the states are only weakly field dependent. (Note to the careful and thoughtful reader: To apply the model carefully, $|0>$ should be the 3s state of lithium, not hydrogen. However, since we are dealing with dipole matrix elements to Rydberg states, the *ratio* x is independent which atom's 3s state is used.) Generally the wave functions may be selected so that all of the matrix elements in Eq. (3.2.24a) are real, so x is real, but it may be positive or negative. Then let

$$x = \cot \alpha, \; 0 \le \alpha < \pi \; . \tag{3.2.24b}$$

The ratio of transition amplitudes to the coupled states is

$$r = \cot (\alpha - \frac{\theta}{2}) \; . \tag{3.2.24c}$$

If x is positive so that $0 \le \alpha < \pi/2$, then $r \rightarrow \infty$ at $\theta = 2\alpha$. If x is negative, so that $\pi/2 < \alpha \le \pi$, then $r=0$ at $\theta=2\alpha-\pi$. This explains the vanishing of one of the states: it is a destructive interference of the uncoupled transition amplitudes. Note that a state vanishes at $B = B_a$ ($\theta = \frac{\pi}{2}$) only if $x=1$ (-1), or $\alpha=\pi/4$ ($3\pi/4$). Alternatively, if $x=0$ ($\pm\infty$), meaning that transition to state $|1>$ ($|2>$) is forbidden, then $r=-1$ (1) when $\theta = \pi/2$. This predicts the appearance of "forbidden" transitions near anticrossings. We also see that when $(B-B_a)/b >> 1$, then $\theta \rightarrow 0$ and $r \rightarrow x$.

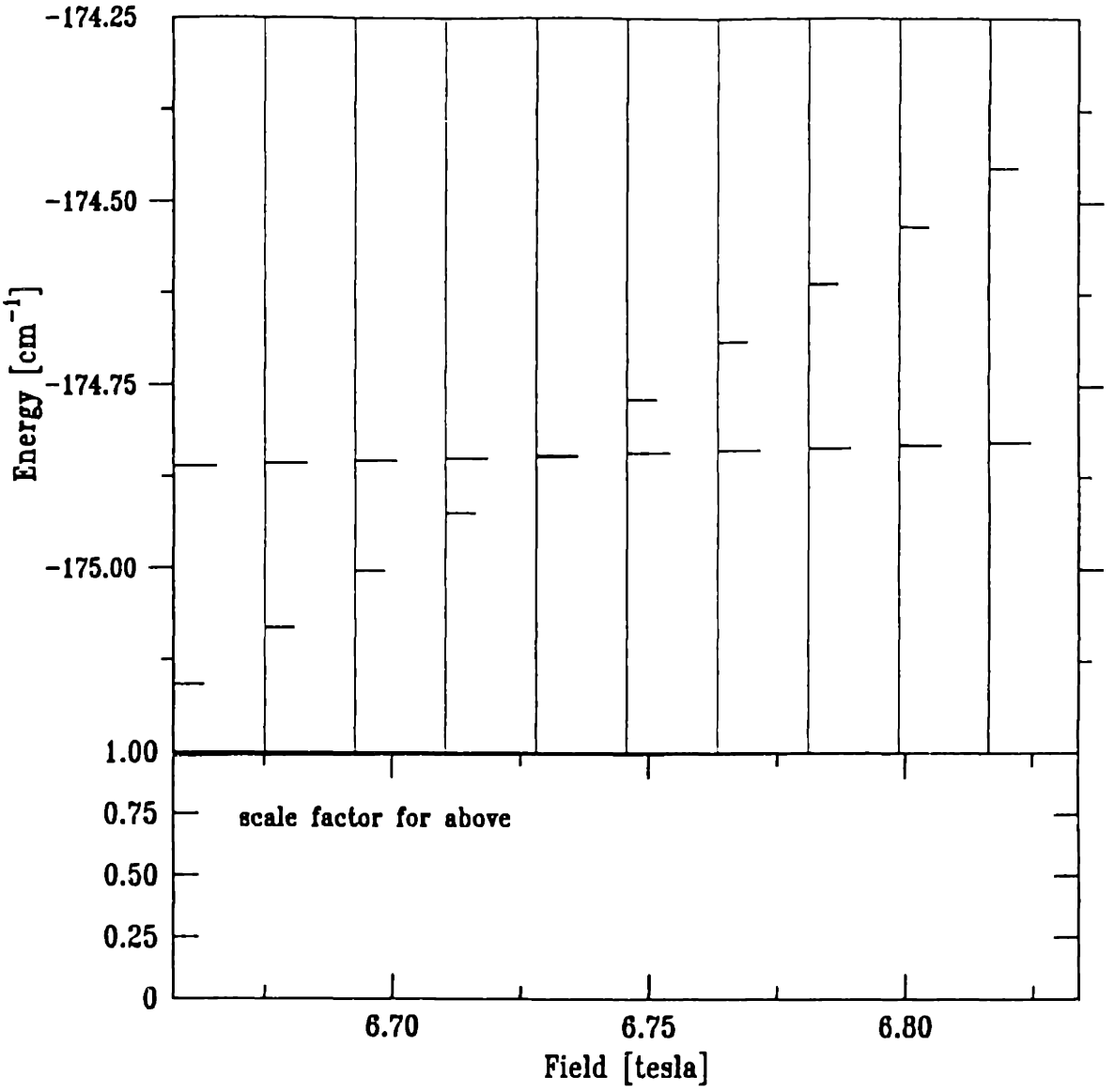

Figure 3.2.7 Relative transition strengths in hydrogen in the vicinity of the lithium anticrossing of Fig. 3.2.1. The strengths remain constant throughout the crossing.

Similarly, when $(B-B_a)/b << -1$, then $\theta \rightarrow \pi$ and $r \rightarrow -x$. This justifies the local nature of the anticrossing. If x were complex, then r would never become zero or infinity.

Using the value of x computed from the hydrogen diagonalization, the prediction of Eq. (3.2.24e) may be compared with relative transition strengths computed from the lithium diagonalization. The results are displayed in Fig. 3.2.8.

The sign of x, or the sign of $< 1 \mid V_c \mid 2 >< 0 \mid T \mid 1 >/< 0 \mid T \mid 2 >$, determines which of the two states vanishes. If x is negative (positive), then the upper (lower) state disappears. All of the $m=0$, odd parity, core-induced anticrossings of lithium that we have studied have $x<0$: the upper state vanishes.

The following argument provides some justification of this, in terms of the simple (no n-mixing) version of the two-state model. Because we are considering electric dipole transitions from the 3s state ($\mid 0 >$), the transition matrix element may be computed from Eq. (3.2.13). Only the $l=1$ state contributes:

$$< 0 \mid T \mid 1 > = < n\,1m \mid 1 >< 0 \mid T \mid n\,1m >, \tag{3.2.25a}$$

$$< 0 \mid T \mid 2 > = < n'1m \mid 2 >< 0 \mid T \mid n'1m > . \tag{3.2.25b}$$

The core matrix element may be approximately evaluated by assuming that the only significant odd parity contribution comes from the $l=1$ set of states:

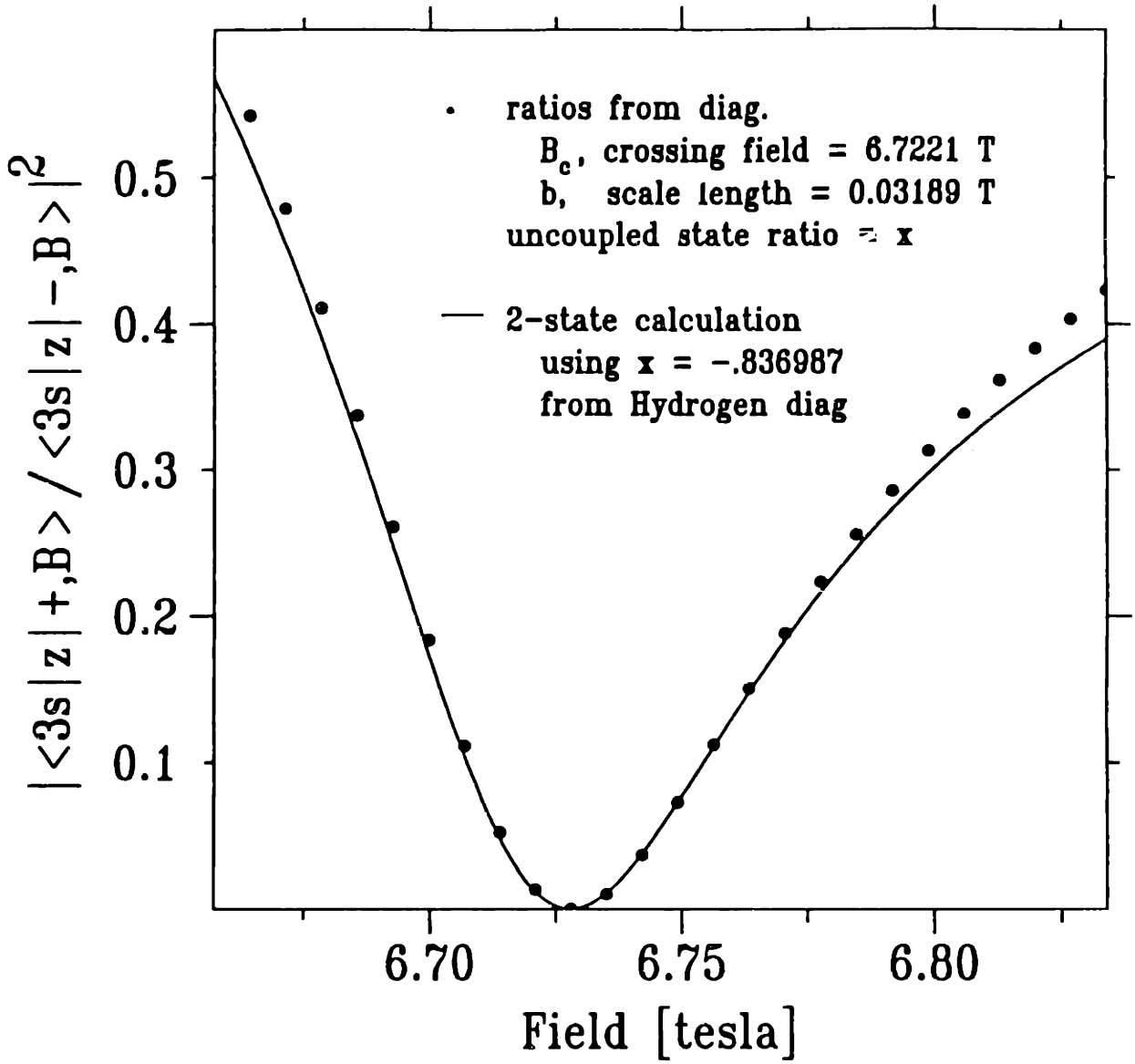

Figure 3.2.8 Comparison of relative transition strengths. The solid curve is Eq. (3.2.24e) using x from the hydrogen calculation. The dots are the relative strengths computed from the lithium diagonalization.

$$< 1 \mid V_c \mid 2 > \approx < n\,1m \mid 1 >^{*} < n'1m \mid 2 >< n\,1m \mid V_c \mid n'1m > \qquad (3.2.25c)$$

Now the appropriate product may be estimated as

$$\frac{< 1 \mid V_c \mid 2 >< 0 \mid T \mid 1 >}{< 0 \mid T \mid 2 >} \approx$$

$$|< n\,1m \mid 1 >|^2 \frac{< 0 \mid T \mid n\,1m >}{< 0 \mid T \mid n'1m >} < n\,1m \mid V_c \mid n'1m > \qquad (3.2.25d)$$

In this form, the signs of the mixing coefficients are irrelevant. The core matrix element $< n\,1m \mid V_c \mid n'1m >$ is negative, as may be seen from Eqs. (3.2.3) and (3.2.9). The signs of the transition matrix elements between the spherical states are the same, because the angular parts are the same, and the extent of the 3s radial wave functions, $<r>_{3s} \approx 10$, is within the first node of Rydberg state radial wave functions with $n > 10$. That is, the Rydberg state radial wave functions do not change sign over a region where the 3s radial wave function is significantly different from zero. Therefore, x is negative, and the upper state should lose oscillator strength near the anticrossing field.

3.3 Electric Field Effects

There are two sources of electric field in our experiment. The first is the motional electric field caused by the atom's movement through the magnetic field, as discussed in Sec. 2.4. The second is a stray electric field apparently caused by contamination of surfaces near where the lasers excite the atoms. This will be considered in Sec. 4.4. The Stark effect can be extremely large in Rydberg atoms, and detailed studies have been presented in earlier papers of the Kleppner group [ZLK79]. Here we present a brief review of the Stark effect and its application to lithium, and some discussion of how small electric fields affect diamagnetic energy levels and anticrossings.

The Stark Effect

During October, 1913, at the Technical College of Aachen, Germany, Johannes Stark (1874-1957) observed splittings of the spectral lines of hydrogen and helium in electric fields ranging from 10 to 31 kvolt/cm. Apparently, Woldeman Voigt had suggested that Stark undertake the study of this electrical analogy of the Zeeman effect. Stark's preliminary experiments began in early 1906 [GIL74, Vol. XII, pp. 613-616]. Clearly, some very significant experiments take a long time.

As with diamagnetism, the Stark effect of lithium may be calculated by two methods. The first method uses an approximate Hamiltonian for lithium to construct a

finite basis of wave functions and matrix elements of the atom-field interaction and then diagonalizes the matrix for each value of field. The second method starts with the analytic results for hydrogen and adds the effect of the core perturbatively. Only the first view will be presented here.

The approximate Hamiltonian for lithium was displayed in Eq. (3.1.2). Using the energies based on experimentally determined quantum defects, radial wave functions are constructed using the numerical techniques mentioned in Sec. 3.1. The total (approximate) Hamiltonian for the valence electron of lithium in an electric field is

$$H_E = H_A + H_S \ , \tag{3.3.1a}$$

where

$$H_S = \vec{F} \cdot \vec{r} \ . \tag{3.3.1b}$$

and H_A is given by Eq. (3.1.2). Here, $\vec{F}$ is the static electric field. Because H_S is an odd operator, spherical states with $\Delta l = 1$ are coupled. Therefore, the basis must include both parities (both even and odd l's). If $\vec{F} = F\hat{z}$ defines the quantization axis, then only states with $\Delta m = 0$ are coupled by H_S, so only one value of m is needed in the basis. If $\vec{F} = F\hat{x}$, then states with $\Delta m = \pm 1$ are coupled. These selection rules follow from the angular matrix elements. Let $\vec{F} = F_x\hat{x} + F_z\hat{z}$. Then the spherical matrix elements of H_S are

$$< nlm \mid H_S \mid n'l'm' > = < nl \mid r \mid n'l' > \times$$

$$[F_x < lm \mid \sin\theta\cos\phi \mid l'm' > + F_z < lm \mid \cos\theta \mid l'm' >] , \qquad (3.3.2a)$$

where the angular matrix elements may be shown to be

$$< lm \mid \sin\theta\cos\phi \mid l+1 \; m+1 > = -\frac{1}{2}\left[\frac{(l+m+1)(l+m+2)}{(2l+1)(2l+3)}\right]^{1/2} , \qquad (3.3.2b)$$

$$< lm \mid \sin\theta\cos\phi \mid l+1 \; m-1 > = \frac{1}{2}\left[\frac{(l-m+1)(l-m+2)}{(2l+1)(2l+3)}\right]^{1/2} , \qquad (3.3.2c)$$

and

$$< lm \mid \cos\theta \mid l+1 \; m > = \left[\frac{(l+1)^2 - m^2}{(2l+1)(2l+3)}\right]^{1/2} . \qquad (3.3.2d)$$

All other matrix elements are zero. The diagonalization proceeds as described in Sec. 3.1.

Energy levels may be plotted as a function of electric field, similar to the plots of energy levels as a function of magnetic field in Figs. 3.1.1 and 3.1.2. More useful are "sequence plots" which indicate the relative strength of the transitions from the 3s state to the Rydberg state. Figures 3.3.1 and 3.3.2 show how the n=65 levels shift and distribute oscillator strength, for m=0 and m=1, where here the quantization axis is along the electric field. The polarization of the radiation which drives the transition determines the final value of m. If the polarization is parallel to the electric field, then

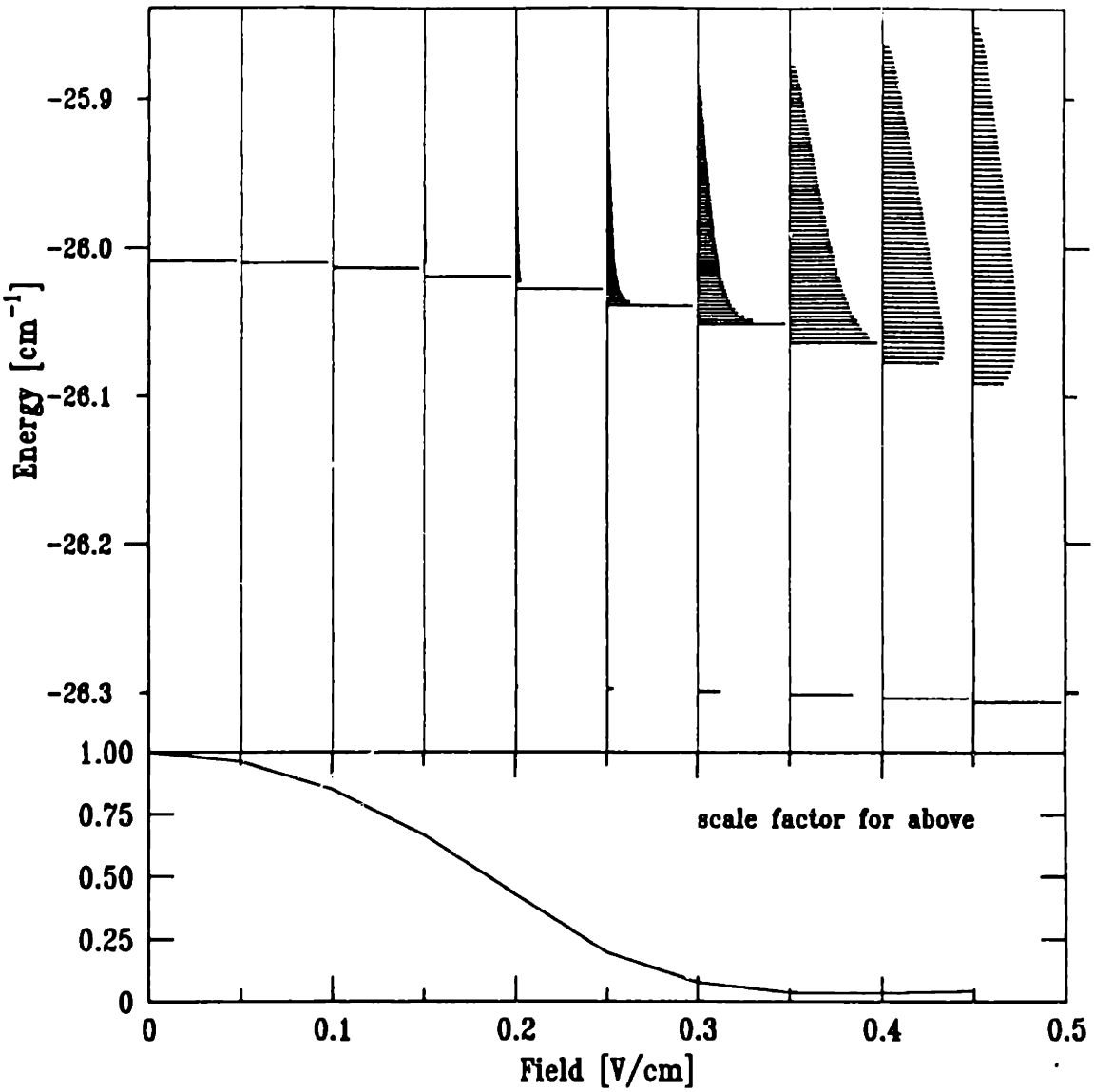

Figure 3.3.1 Sequence plot for the n=65, m=0 Stark effect in lithium. No n-mixing is included. Fields greater than 0.25 V/cm exhibit significant excitation of the "s state".

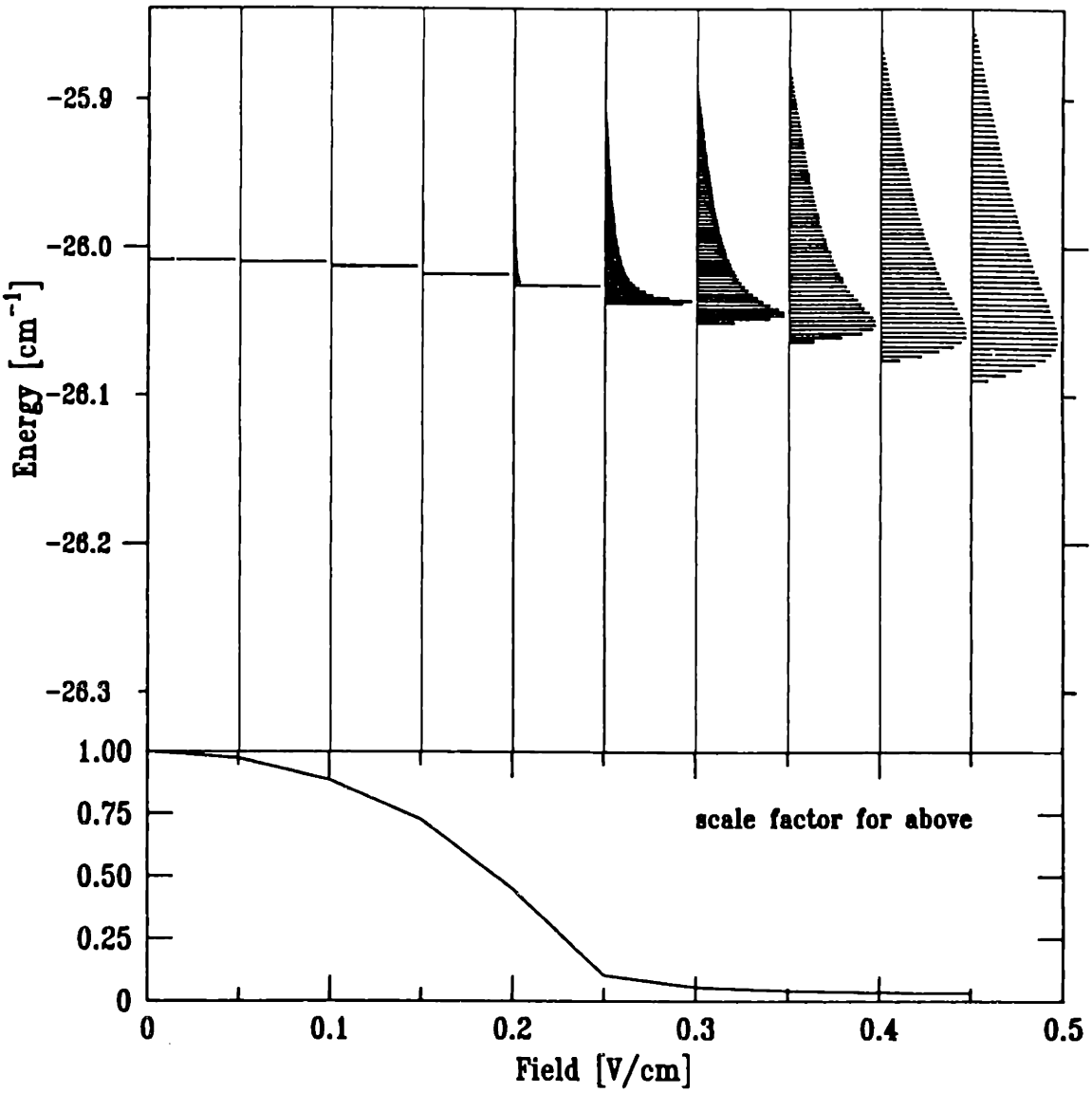

Figure 3.3.2 Sequence plot for the n=65, m=1 state in lithium. No n-mixing is included.

the final m=0; if the polarization is perpendicular to the field, then the final m=±1. (Because H_E is invariant under time reversal, states with m=+1 and -1 are degenerate.)

The purpose of studying the Stark effect in our experiment is to measure the stray electric field. As discussed in Sec. 4.4, the procedure is to observe a sufficiently large n such that the p state is well-mixed into the manifold. For example, n=65 would be appropriate if the field were approximately 0.25 V/cm. The manifold width is proportional to the field magnitude. This can be seen from the Stark effect for hydrogen, where the first order shift is given by [LAL77, pp. 287-288]

$$E_S^{(1)} = \frac{3}{2}\, n(n_1 - n_2)F \ . \tag{3.3.3a}$$

The parabolic quantum numbers n_1 and n_2 are constrained by

$$n = n_1 + n_2 + |m| + 1, \ \ n_1 \ , \ \ n_2 \geq 0 \ . \tag{3.3.3b}$$

The width of the manifold is the difference between the maximum and minimum shifts:

$$\Delta E^{(1)} = 3n(n - |m| - 1)F \approx 3n^2F \tag{3.3.3c}$$

where the approximation holds for $n >> |m|$ and $n >> 1$. In practical units,

$$\Delta E^{(1)} = (3.84 \text{ MHz/V/cm})n^2F \ . \tag{3.3.3d}$$

This may be verified for n=65 using Fig. 3.3.1 or 3.3.2 and a ruler.

The stray field's direction may be determined by rotating the laser polarization until the s-state vanishes. (Actually, it is the state that becomes the s-state at zero field. There really is no excitation of even parity states.) Then the polarization is perpendicular to the stray field, because $m=\pm 1$ does not have an s-state.

Stark Shifts of Diamagnetic Levels

The problem is to calculate the shift in the lithium diamagnetic levels caused by an electric field. The diamagnetic states of lithium are eigenstates of the Hamiltonian given in Eq. (3.1.7b). The total Hamiltonian for the valence electron of lithium in both magnetic and electric fields is

$$H_T = H_A(B) + H_S \tag{3.3.4}$$

where $H_A(B)$ is given by Eq. (3.1.6b) and H_S is given by Eq. (3.3.1b).

We begin by considering H_S as a perturbation to $H_A(B)$. Then the eigenstates of $H_A(B)$, assumed to be specified by $|nkm; B>$, are coupled by H_S. In our experiment, odd parity diamagnetic states are excited, so we need to consider the shift caused by the electric field and even parity states. If the odd parity state is not degenerate with any even parity state, then the shift is given by

$$\Delta E = < nkm; B \mid H_S \mid nkm; B > +$$

$$\sum_{n'} \sum_{k'}{}' \sum_{m'} \frac{|< nkm; B \mid H_S \mid n'k'm'; B >|^2}{E(nkm; B) - E(n'k'm'; B)} \tag{3.3.5a}$$

where the sum over k' is restricted to even parity values. The first term vanishes because H_S is an odd operator. Thus the shift is second order in electric field. To evaluate the odd-even matrix element of H_S, the diamagnetic states may be expressed in terms of the spherical states (see Eq. (3.2.18)) using the diagonalization program discussed in Sec. 3.1:

$$< nkm; B \mid H_S \mid n'k'm'; B > = \sum_{\bar{n}} \sum_{l=\pm|m|}^{\bar{n}-1}{}' \sum_{\bar{n}'} \sum_{l'=\pm|m|}^{\bar{n}'-1}{}' < nkm; B \mid \bar{n}lm >^* \times$$

$$< n'k'm; B \mid \bar{n}'l'm' >< nlm \mid H_S \mid n'l'm' > \tag{3.3.5b}$$

where the sum over $l(l')$ is restricted to odd (even) parity values. Many terms in the sum vanish because of the angular selection rules discussed above. For instance, if the electric field is parallel to the magnetic field (which defines the quantization axis), then $< nkm; B \mid H_S \mid n'k'm'; B >$ vanishes unless $m' = m$. Also, the terms in Eq. (3.3.5b) always vanish unless $l' = l \pm 1$. Nevertheless, evaluating Eqs. (3.3.5) on a computer is a bookkeeping nightmare A table of relevant spherical matrix elements and energies is first created using the technique described in Sec. 3.1. Then these values are retrieved as needed for evaluating the nested sums in Eqs. (3.3.5).

The order of magnitude of the shift is given by assuming that the largest term in the sum of Eq. (3.3.5a) comes from the even parity state which is closest in energy to the given odd parity state. If that even parity state is from the same n, then the energy denominator is roughly the spacing of the diamagnetic manifold, or the maximum diamagnetic energy, $B^2n^4/8$, divided by the number of (even and odd parity) states, n:

$$|E(nkm; B) - E(nk'm'; B)| \sim \frac{1}{8} B^2n^3 . \tag{3.3.6a}$$

The mixing coefficients in Eq. (3.3.5b) are of order the reciprocal square root of the number of states with given n, m, and parity, or $\sqrt{2/n}$. This is because the transformation must be unitary, and the coefficients within the same n are roughly the same size. The spherical matrix element is crudely given by the size of the atom, or n^2F. The number of terms in the sums of Eq. (3.3.5b) is about n, because we are only considering contributions from $\bar{n} = \bar{n}' = n$, and there are about $n/2$ different l's. Since $l' = l \pm 1$, there are nearly $2l$''s for each l. Finally,

$$|\Delta E| \sim (\frac{1}{8} B^2n^3)^{-1} |n(\frac{2}{n})n^2F|^2 = 64n(\frac{F}{B})^2 , \tag{3.3.6b}$$

or in practical units,

$$|\Delta E| \sim 1 \text{ GHz(T/V/cm)}^2 \, n(\frac{F}{B})^2 . \tag{3.3.6c}$$

The sign of the shift depends on the relative positions of the odd and even parity

states. This expression diverges as $B \rightarrow 0$ because the even and odd parity states from the same n become nearly degenerate.

The (unnormalized) correction to the odd parity diamagnetic state is given by

$$| nkm; B\ (1) > =$$

$$\sum_{n'} \sum_{k'}{}' \sum_{m'} \frac{< n'k'm'; B \mid H_S \mid nkm; B >}{E(nkm; B) - E(n'k'm'; B)} \mid n'k'm'; B >, \tag{3.3.7}$$

where the sum over k' is restricted to even parity values. This shows that the first order correction to the odd parity diamagnetic state consists of a linear combination of even parity diamagnetic states. Therefore, electric dipole transition matrix elements from even parity states (such as 3s) to odd parity diamagnetic states are unaffected in first order. However, the reverse is true for the even parity diamagnetic states: their first order correction is a linear combination of odd parity states, which will allow transitions from even parity states. Therefore, a small electric field makes the "wrong" parity states visible in a spectrum. The fact can be particularly devastating if one experimentally studies a region of the spectrum where calculations are difficult, because it is not always possible to distinguish "wrong" states from "right" ones.

Equation (3.3.4a) is not valid if the even and odd parity states are degenerate. Then degenerate perturbation theory may be used. Fortunately, the discussion of the two-state model in Sec. 3.2 readily carries over here. We consider states which are opposite parity, crossing eigenstates of $H_A(B)$, coupled by H_S, rather than nearly

crossing eigenstates of $H_o(B)$, coupled by V_c. Let

$$| 1 > = | nkm; B >, \quad \pi = -1 \tag{3.3.8a}$$

$$| 2 > = | n'k'm'; B >, \quad \pi = +1 \tag{3.3.8b}$$

In the basis $\{| 1 >, | 2 >\}$, the matrix elements of H_T are

$$(H_T)_{11} = E_1(B) = E(nkm; B) \tag{3.3.9a}$$

$$(H_T)_{22} = E_2(B) = E(n'k'm'; B) \tag{3.3.9b}$$

and

$$(H_T)_{12} = < 1 | H_S | 2 > = < nkm; B | H_S | n'k'm'; B > \tag{3.3.9c}$$

In contrast to the core interaction, the electric field does not contribute to the diagonal matrix elements. Therefore, the anticrossing energy and field are the same as the crossing energy and field (cf. Eqs. (3.2.15h) and (3.2.15i)). The anticrossing size is proportional to F:

$$a = 2|< 1 | H_S | 2 >| = 2|< nkm; B_c | \vec{r} | n'k'm'; B_c > \cdot \vec{F}| \tag{3.3.10}$$

where the matrix element is given by Eq. (3.3.5b). The order of magnitude was estimated above. The anticrossing size is roughly

$$a \sim 2|n(\frac{2}{n})n^2F| = 4n^2F , \tag{3.3.11a}$$

or in practical units

$$a \sim 5(\text{MHz/V/cm})n^2F \ . \qquad (3.3.11b)$$

While this estimate appears independent of B, the approximate value of the mixing coefficients in Eq. (3.3.5b) assumes that the states are well-mixed by the magnetic field.

The relative transition strengths to an electric-field induced anticrossing follow from the two state model. In Eq. (3.2.24a) we have $< 0 \mid T \mid 2 > = 0$ so $x = \infty$. Therefore, the transition strengths are equal at the crossing field, whereas far away from the crossing field, only the odd parity state is excited.

The most straight forward approach is to represent the entire Hamiltonian H_T (see Eq. (3.3.4)) in a basis of odd and even parity states, and diagonalize it for desired values of magnetic and electric fields. The computation is considerably simplified if the electric and magnetic fields are parallel, for then only one value of m need be included in the basis. If the electric and magnetic fields are perpendicular, at least two m's must be included in the basis, and the paramagnetic term must be included in the representation before diagonalization because different m's have different paramagnetic shifts.

Although this method predicts useful eigenvalues and eigenvectors, it is difficult to identify "where the levels come from". We often diagonalize the two parities separately and overlay them on the result from the larger diagonalization of the total Hamiltonian. This helps pick out which states are "even", or present because of the

electric field.

In the discussion so far, it has been assumed that a state can be labeled meaningfully by n and k. Computationally, this restriction may be removed by replacing n and k with a new number, kk, which simply orders the diagonalized states' energies for a given m, π, and B. (The number kk labels the highest energy state by 1, and counts up to the lowest energy state.) Though not physical in the sense of being the eigenvalue of a Hermitian operator, this labeling scheme makes the problem computationally tractable whether or not n and k are meaningful.

Figure 3.3.3 presents the relative transition strengths to the $n=25$, $m=0$ states in parallel magnetic and electric fields. The "odd" parity states are much stronger than the "even" ones, though the states were sorted by referring to Fig. 3.1.2.

Changes in Core Anticrossings

Electric fields cause the core anticrossing size, energy, and field to shift. The most important contributions to these changes in odd parity core anticrossings come from the nearest even parity diamagnetic states. For example, consider the circled anticrossing in Fig. 3.1.1. Figure 3.1.2 shows that there is an even parity core anticrossing surrounding the odd parity core anticrossing. (The even parity one is bigger because $m=0$ states contain the s-state, which has a large quantum defect. See Eq. (3.2.17d).)

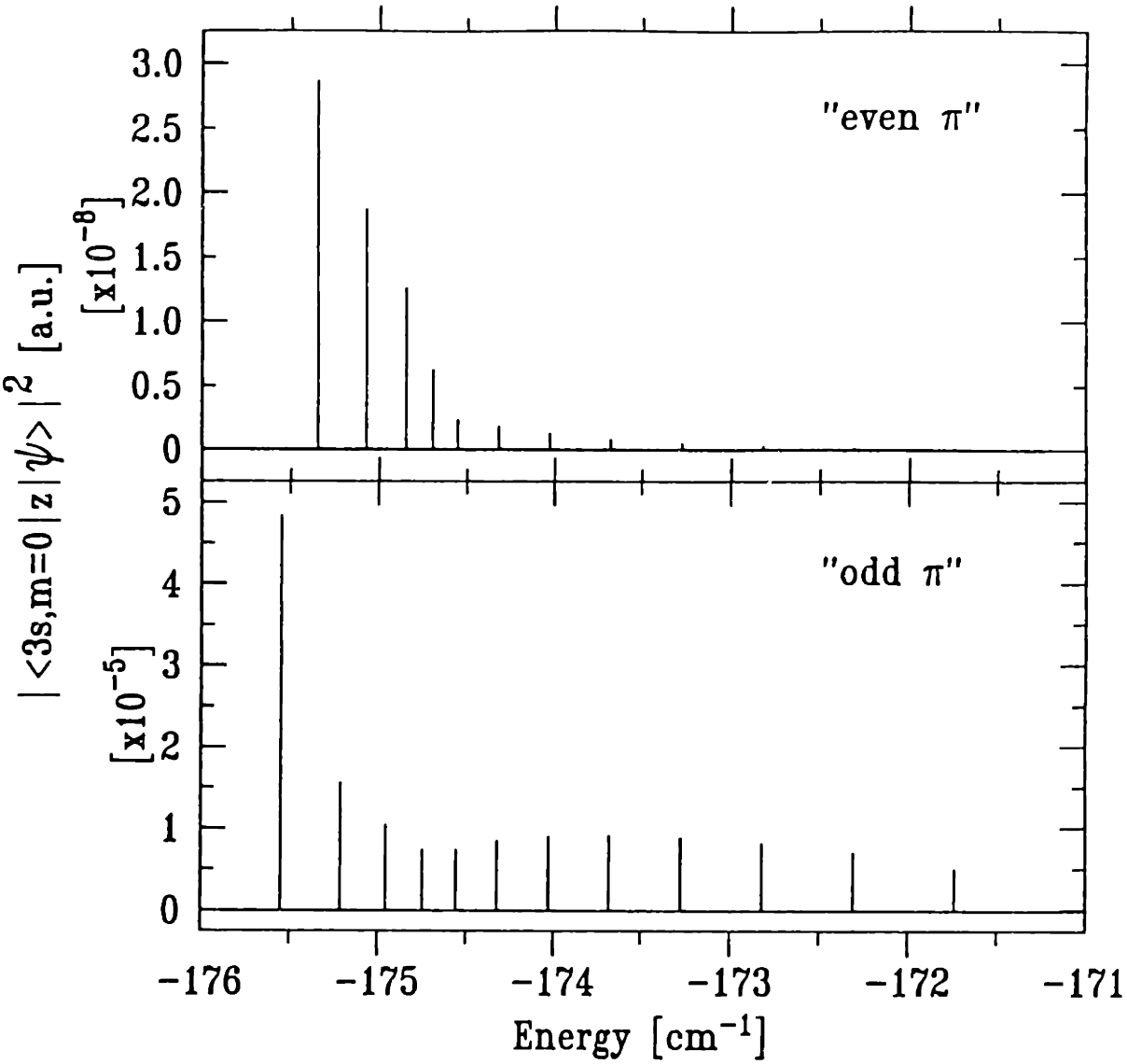

Figure 3.3.3 Transition strengths to levels around n=25, with B=3.0 T, F=0.1 V/cm, the fields parallel, and m=0. Compare this with Fig. 3.1.2. The basis is n=24–26, m=0. The 25s state is not in this energy range.

The shift in levels may be calculated using Eqs. (3.3.5). Unfortunately, because we are considering competing shifts, a reliable and simple order of magnitude estimate is not possible. The results of Eqs. (3.3.5) are presented in Fig. 3.3.4. Our experiment has enough resolution to see a shift of this magnitude.

Alternatively, diagonalization of H_T may be performed. In a sense, it is an easier calculation than evaluating Eqs. (3.3.5) two times (one for each state), but does require the larger basis. As usual, it is difficult to distinguish "odd" and "even" parity states without also calculating separate odd and even parity energy level diagrams.

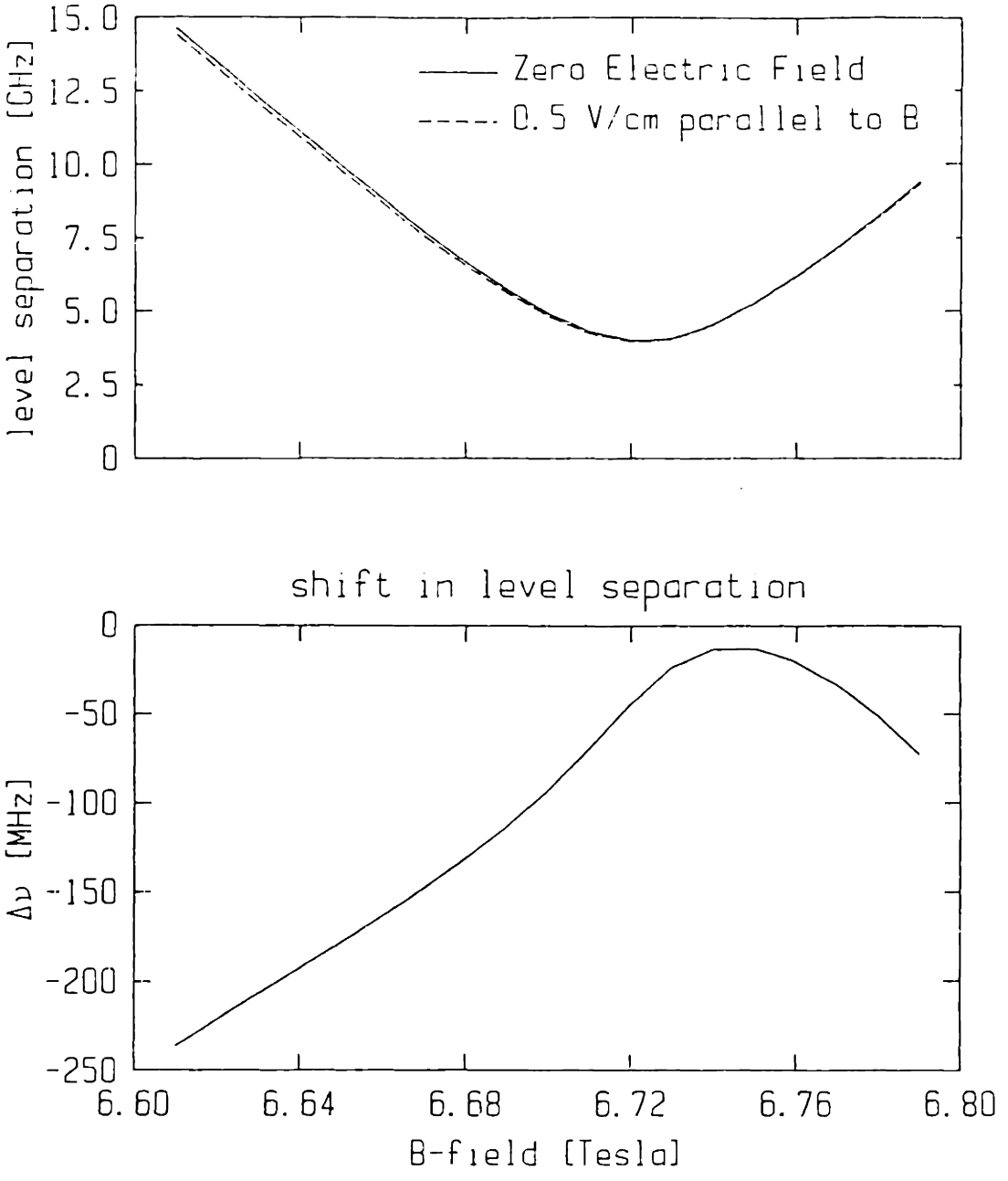

Figure 3.3.4 Electric field effects on a core anticrossing. The separation of the anticrossing circled in Fig. 3.1.1 is shown with and without a parallel electric field. Equations (3.3.5) were used.

Chapter 4. EXPERIMENTAL DESIGN

The experimental goal is to measure accurately and precisely the energy levels of lithium atoms in a strong magnetic field. The experiment employs an atomic beam which travels along the axis of a superconductive solenoid. The atomic velocity is parallel to the magnetic field direction to minimize the motional electric field, and the intersection of the atomic and laser beams is at right angles to reduce the Doppler width and shift. Two laser beams excite the atom in a two-step process. The first step is a two-photon transition from the 2s state to the 3s state. The second step is a one-photon transition from 3s to Rydberg states. Cascade fluorescence and electric field ionization provide the signature of these atomic excitations. Stabilized c.w. lasers create narrow bandwidth radiation that reveals spectra with linewidths of approximately 25 MHz. This figure represents a one hundred-fold increase over previous studies [CLP86a,b]. Finally, the laser wavelength is measured accurately to determine the binding energy of the excited states. A schematic diagram is shown in Fig. 1.2.2. The details of these experimental parts are discussed in this chapter.

4.1 The Atomic Beam

The goal of the atomic beam design is to produce a well collimated gas of atoms traveling parallel to the axis of a superconductive solenoid. The beam must also have enough flux and current in the interaction chamber to give sufficiently large signals. These goals are achieved using a "tube oven" atomic beam source and a collimator tube. Figure 4.1.1 presents an overview of the atomic beam.

Tube Oven Construction

Our tube ovens are constructed by placing about 1.1 gram of lithium metal wire into a 304 stainless steel tube with 1/2" nominal O.D. and 0.028" wall thickness. The tube is 8" long, and each end has a 2 1/2" long crimp. The oven hole is 0.040" diameter and is located 4" from either end. The construction procedure is listed below:

1. Cut Tube. Use a circular saw with a 1/32"-thick "stone blade" to give sharp edges. Deburr as needed.

2. Clean Tube. Use Alconox soap with a bottle brush, and rinse several times with acetone.

3. Crimp one end. Use a hydraulic press or vise, and then hammer the end to flatness.

4. Drill atomic beam hole. The surface is prepared by milling a flat region parallel to the crimp. This is most easily accomplished by holding the tube in the "oven assembly jig," a clamp we made for this purpose. Use a #40 bit which is in good condition.

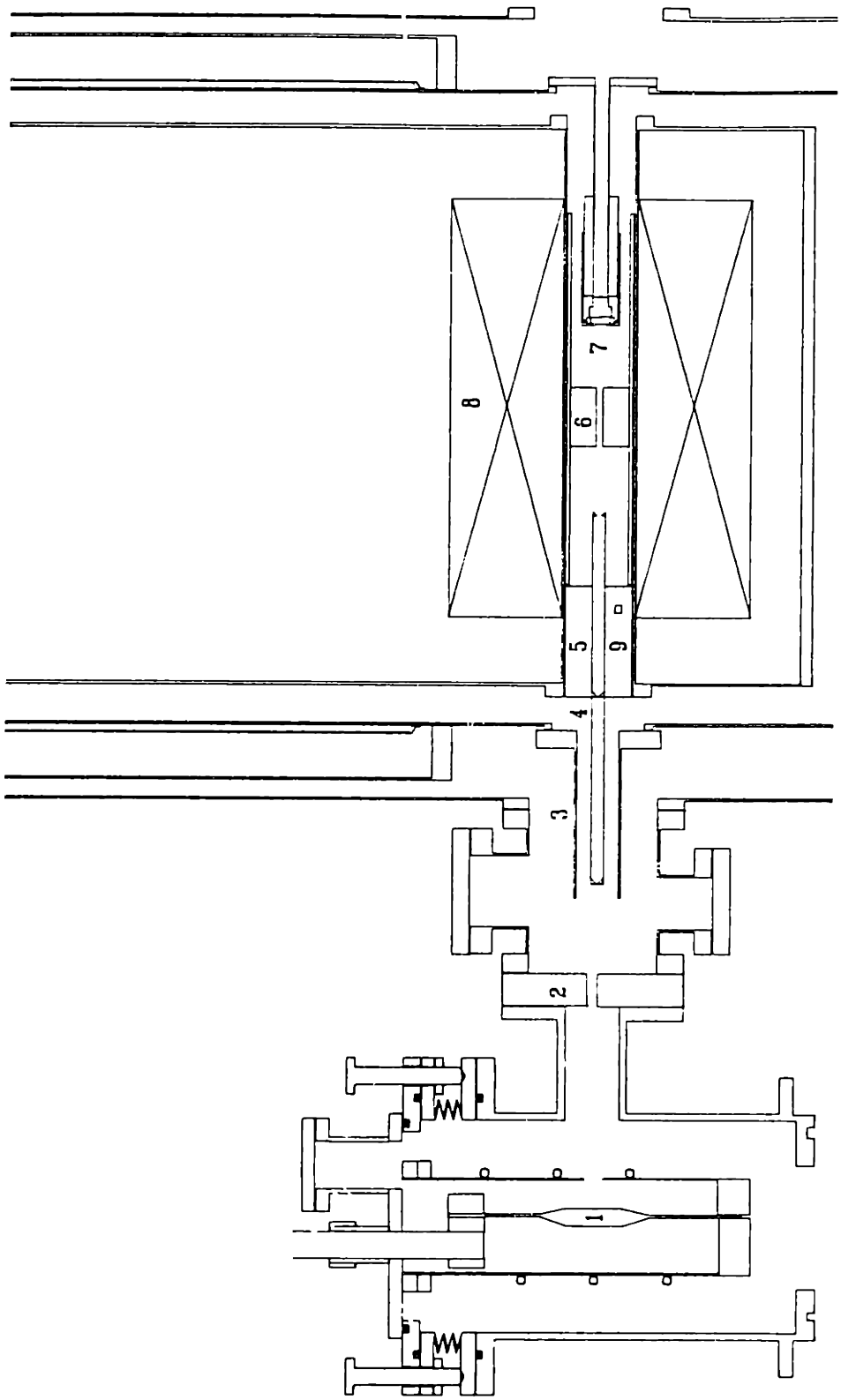

Figure 4.1.1 Atomic beam path. Atoms travel from the tube oven (1), through the atomic beam gate valve (2) and are collimated by the three concentric apertures in the tube (4) before entering the interaction chamber (6) and finally stop on the carbon foil in front of the charged particle detector (7). The collimator-tube holder (5) is concentric with the magnet (8) bore, and also houses the Hall probe (9). Radiation heating of the collimator tube (4) is minimized by a shield (3).

5. Load lithium. Roll out 10" of 1/8" diameter wire and cut with diagonal cutting pliers. Clean the wire with a double rinse in petroleum ether to remove the mineral oil. (Note: Lower oven manifold pressure seems to be obtained if the wire is not black on the surface.) Fold the wire to fit into the tube and compress the wire with a rod. This procedure is carried out in a fume hood. We handle the lithium with gloves.

6. Crimp other end. This crimp should be reasonably parallel to the first one.

7. Attach thermocouple. We spot weld a chromel-alumel (type K) thermocouple to the tube just above the lower (lithium side) crimp.

The construction takes 1-2 hours. We have tried to make ovens in advance, but it seems that fresh ovens give better performance.

Oven Operation

The oven is clamped with water cooled copper blocks. These clamps also deliver a.c. current to the oven for resistive heating. The crimp length was formally 2", but we found that keeping the lithium farther from the clamps lengthened the oven life since all of the lithium can be vaporized. The current comes from a current step-up transformer with a turns ratio of 50. The primary is powered by an autotransformer. Lithium is a far better electrical conductor than stainless steel, so most of the current goes through the alkali metal rather than the tube walls. When the temperature is greater than 600°C, the top of the tube oven glows while the bottom is dark: the boundary is an indication of the lithium level. The oven hole glows more brightly than the stainless steel since the hole approximates a blackbody with perfect

emissivity. This feature is useful for optical oven alignment. Roughly speaking, the oven at 740°C has a voltage drop of 1.4 V with 210 A going through it; the delivered power is 290 W and the resistance is about 6.7 mΩ. (The resistance is around 4 mΩ at 100°C.)

As shown in Fig. 4.1.2, the tube is surrounded by a water cooled cold shield. This is the first collimator and condenses most of the lithium except that which gets out through a 1/2" diameter hole. This hole is rather large, but when it was 1/4" diameter it often became clogged with lithium. In our oven, the lower clamp is part of the cold shield. The idea was to minimize the (alternating) magnetic field (from the heating current) outside of the oven. On the other hand, the fringing field of the superconductive solenoid caused alternating forces on the molten alkali metal. This disturbed the normal oven operation and resulted in very short oven lifetimes. We put mu-metal inside of the cold shield to reduce the fringing field at the tube oven.

The cold shield and tube oven are attached to a flange at the top of the oven manifold. This part of the the manifold is adjustable by means of a large diameter bellows, allowing on-line optimization of the oven position.

Vacuum Equipment

The vacuum in the source manifold is maintained by a 2" diffusion pump (Varian M2) using Dow-Corning DC-705 silicone pump oil. It is backed by a Welch

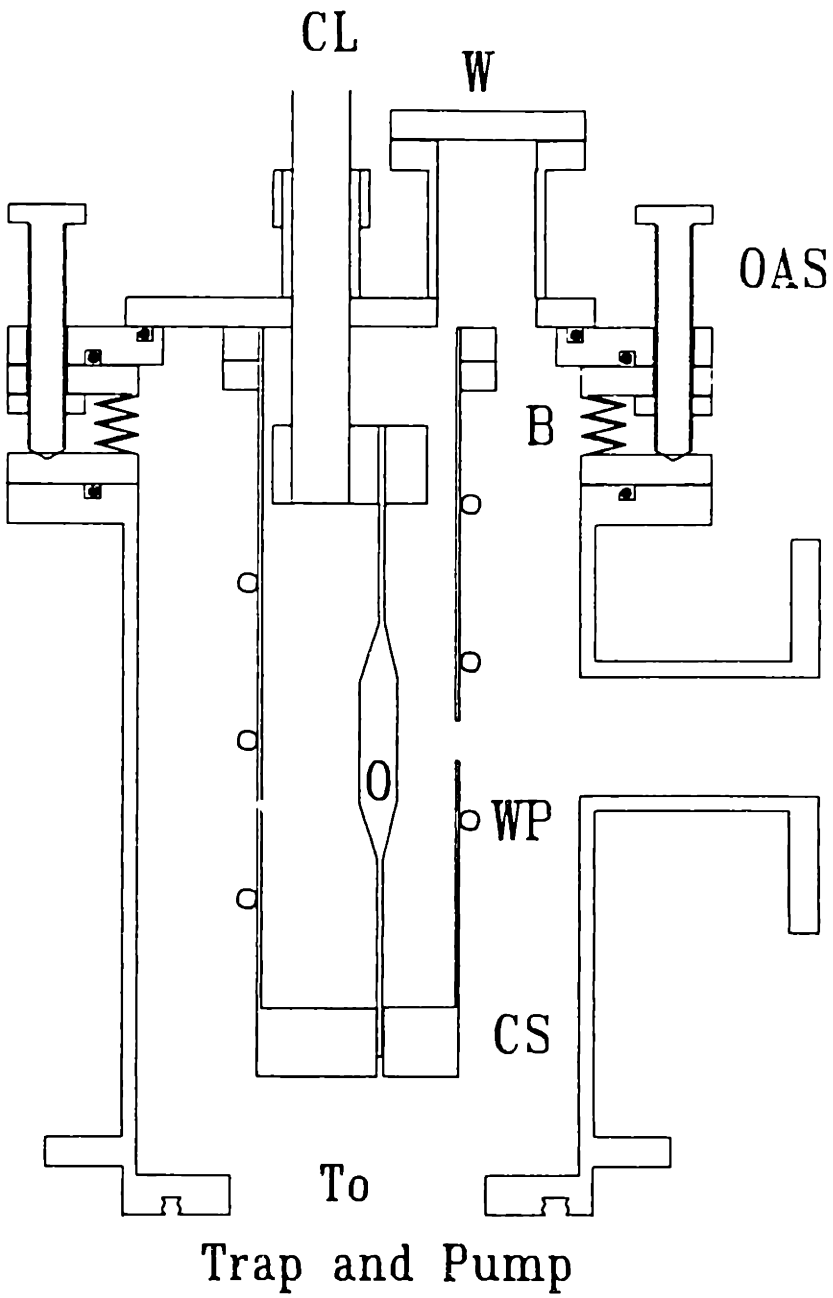

Figure 4.1.2 Oven manifold. Four 3/8 -24 oven adjustment screws (OAS) adjust the tube oven (O) position by altering the bellows (B) extension. Heating current is supplied through an insulated current lead (CL) and returned through the grounded cold shield (CS), which is cooled by water pipes (WP). The cold shield condenses most of the lithium.

Duo-Seal Model 1402 mechanical pump filled with Convoil hydrocarbon oil. The foreline contains a Mass Vac "Visi-Trap" foreline trap with a copper gauge filter to reduce backstreaming. This foreline also backs the diffusion pump on the dewar vacuum manifold. There is a valve between each diffusion pump and the foreline, each with its own thermocouple gauge, so that either chamber can be vented and pumped down while the other is under high vacuum. All demountable fixtures on the high vacuum side are sealed with viton O-rings.

Backstreaming into the oven manifold is reduced with a water cooled baffle (Varian 322), and water pumping is increased with a liquid nitrogen cryotrap (Varian 325). The last element was added to reduce contamination of the interaction chamber and thus reduce stray electric fields, but there's no definite evidence that the trap affected this field. Heating tape bakes the oven manifold to about 140°C. The tube oven and cold shield bake by operating the oven without cooling water. Running the oven near 400°C raises the cold shield temperature to about 100°C. (The cold shield temperature should be less than the lithium melting point.) Baking for ~1 day leads to low manifold pressure, about 3×10^{-7} Torr when the components are all at room temperature. The manifold pressure while running the oven at beam temperature depends strongly on the temperature and some poorly controlled parameter such as lithium cleanliness. On a good day, after baking and with LN_2 in the trap, an oven temperature is 650°C yields a manifold pressure of around 1×10^{-6} Torr. Manifold

pressures near 10^{-5} Torr seem to reduce the beam flux at the interaction chamber. (Note: Except for the tube oven, all temperatures are measured with copper-constantan (type T) thermocouples.) Pressures are measured with a Penning gauge (CVC GPH-320B) – at the limit of its sensitivity.

An atomic beam gate valve isolates the oven manifold from the dewar manifold. The gate is driven by a bellows-sealed shaft. The motion is perpendicular to the beam. The gate moves in a ball-bearing track slightly angled toward an O-ring which is concentric with the beam. It is rather amazing that either side of the valve may be vented while the other remains under vacuum. The open clear aperture is 1/4" diameter; it keeps most of the lithium in the oven manifold.

Beam Collimation

Most of the beam collimation occurs in the collimator tube. The tube is concentric with the magnet bore and contains three knife-edge baffles to align the atomic velocity with the magnetic field and reduce the scattering of atoms and molecules onto the inner surfaces of the interaction chamber. Possible atomic trajectories can be worked out using the data contained in Fig. 4.1.3. The oven hole and the two smaller diameter baffles define the beam: in the center of the interaction chamber, the beam diameter is 2 mm and the divergence angle is 3 mrad. The third baffle is designed to stop molecules scattered off the other two baffles from getting into the interaction chamber.

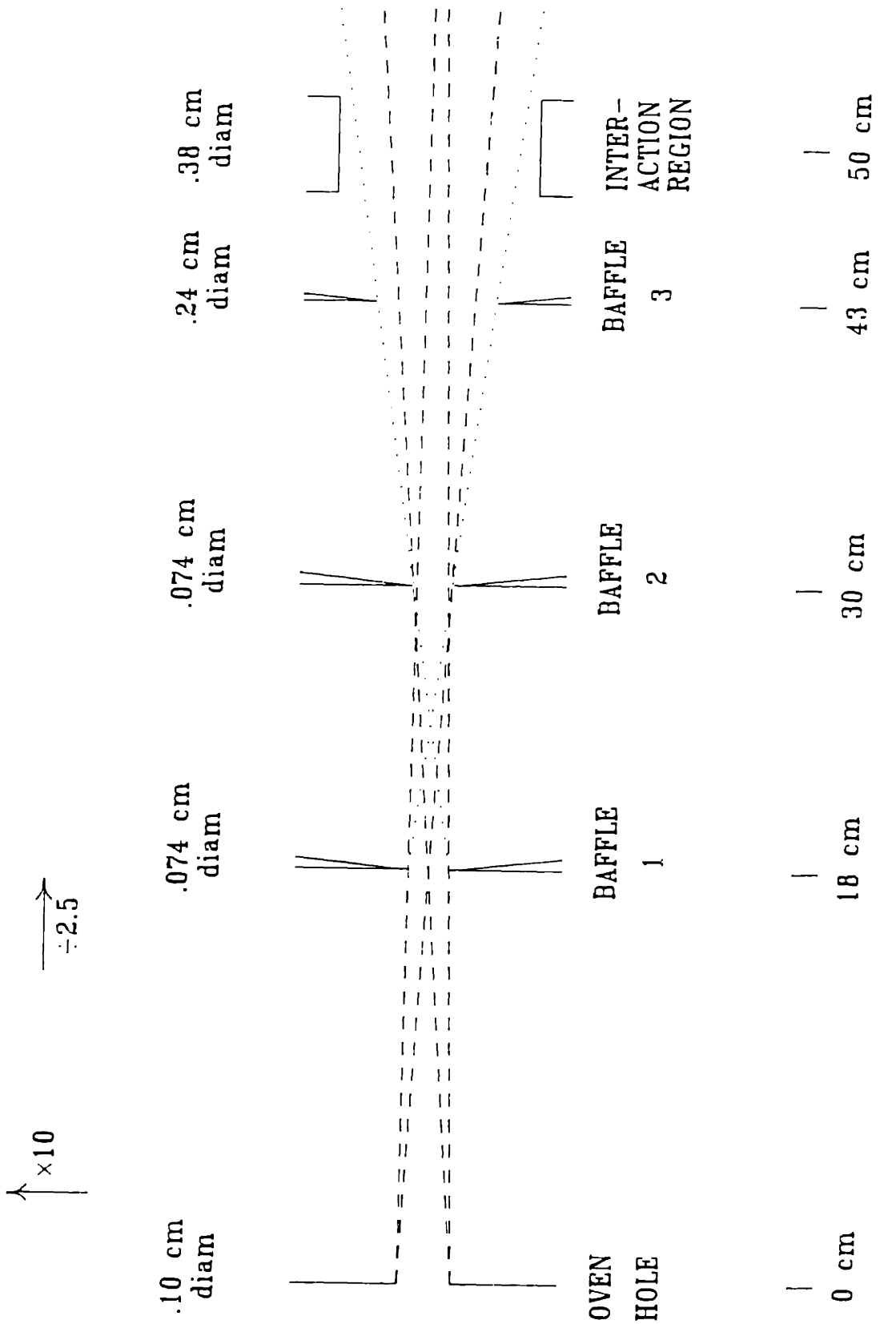

Figure 4.1.3 Scale drawing of the principal apertures in the atomic beam.

As described in Sec. 4.4, the biggest experimental problem we have is a stray electric field inside of the interaction chamber. It distorts the high resolution spectra. One cause of this field might be water molecules which stick to the inner surfaces of the interaction chamber. Possibly these water molecules are dislodged by atoms hitting one of the first two baffles. We know that the rate of increase of the stray electric field is proportional to the atomic beam current through the interaction chamber, but the mechanism is not definite. Since the field may be reduced by a low temperature bake, water seems a likely candidate.

Vapor Pressure of Lithium

To predict the characteristics of the atomic beam, the vapor pressure of the beam material is needed. The lithium vapor pressure is taken from the reference tables of Nesmeyanov [NES63]. The data are reduced to a semi-empirical formula. For the vapor pressure in torr and the temperature in kelvin, the *atomic* vapor pressure above liquid lithium is

$$\log p = 10.345{,}40 - 8491.378/T - 0.000{,}088{,}40*T - 0.681{,}06 \log T \ . \qquad (4.1.1)$$

The common (base 10) logarithm is used; the formula is valid in the range 181°C (the melting point) to about 1000°C, but the uncertainty is not specified. The atomic density may be estimated from the ideal gas law:

$$p = nkT \ . \tag{4.1.2}$$

Note that 1 torr = 1333.32 dyne/cm^2 = 133.32 Pa. The following small table gives the atomic vapor pressure and density over a useful range of temperatures.

T(°C)	p(torr)	n(atoms/cm^3)
600	5.1×10^{-2}	5.6×10^{14}
620	8.2×10^{-2}	8.8×10^{14}
640	1.3×10^{-1}	1.4×10^{15}
660	2.0×10^{-1}	2.0×10^{15}
680	3.0×10^{-1}	3.0×10^{15}
700	4.5×10^{-1}	4.4×10^{15}
720	6.5×10^{-1}	6.3×10^{15}
740	9.4×10^{-1}	8.9×10^{15}
760	1.3	1.2×10^{16}
780	1.9	1.7×10^{16}
800	2.6	2.3×10^{16}
820	3.5	3.1×10^{16}
840	4.7	4.1×10^{16}
860	6.3	5.4×10^{16}
880	8.3	7.0×10^{16}
900	1.1×10^{1}	9.0×10^{16}

Table 4.1.1. Atomic lithium vapor pressure and density.

Thermal Beam Properties

Many estimates of atomic beam characteristics are based on the oven operating in the effusive regime. For this to be valid, the mean free path of the source gas must be larger than the characteristic size of the oven hole. The mean free path is given by [RAM56, p. 12],

$$\lambda = (\sqrt{2} n_s \sigma)^{-1} \tag{4.1.3}$$

where n_s is the source density and σ is the collision cross section. The latter is crudely approximated by using the geometric cross-section area:

$$\sigma = \pi[(n^*)^2 a_B]^2 \tag{4.1.4}$$

where a_B is the Bohr radius. For the lithium ground state, $n^* = 1.6$ and $\sigma = 6\times10^{-16}$ cm^2. At 700°C, we find $\lambda = 0.3$ cm which is greater than the oven hole diameter (0.1 cm). However, if the cross-section is really larger by an order of magnitude or more, then the effusive condition is not met.

The beam parameters may be estimated by assuming that the collimation is determined mostly by the second baffle and the oven hole. The atomic beam current through the second baffle is [RAM56, pp. 11-21]

$$I_B = \frac{n_s \bar{v}_s A_s}{4\pi l_B^2} A_B \tag{4.1.5}$$

where n_s is the atomic density in the source, $\bar{v}_s$ is the mean atomic speed in the source,

$$\bar{v}_s = 2\left[\frac{2kT}{\pi m}\right]^{1/2}, \tag{4.1.6}$$

A_s is the source area, l_B is the distance from the source to the second baffle, and A_B is the area of this baffle. In Eq. (4.1.6), m is the atomic mass. If nothing scatters the

beam after this baffle, the current through the interaction chamber is also I_B. The flux scales inversely with the distance squared:

$$F_I = \frac{I_B}{A_B} \left[\frac{l_B}{l_I}\right]^2 \tag{4.1.7}$$

where l_I is the distance from the source to the interaction chamber center. The mean speed in the beam is given by

$$\bar{v}_B = \frac{3}{4} \left[\frac{2\pi kT}{m}\right]^{1/2} . \tag{4.1.8}$$

Over the temperature range in Table 4.1.1, the mean speed in the beam ranges from 1.9 to 2.2 $\times 10^5$ cm/sec. The following table contains some typical values for these properties, assuming the parameters shown in Fig. 4.1.3.

T(°C)	I_B (atoms/sec)	F_I (atoms/cm^2/sec)	n_I (atoms/cm^3)
600	2.7×10^{11}	2.3×10^{13}	1.2×10^{8}
620	4.3×10^{11}	3.6×10^{13}	1.9×10^{8}
640	7.0×10^{11}	5.8×10^{13}	3.0×10^{8}
660	1.0×10^{12}	8.4×10^{13}	4.2×10^{8}
680	1.5×10^{12}	1.3×10^{14}	6.4×10^{8}
700	2.3×10^{12}	1.9×10^{14}	9.3×10^{8}
720	3.3×10^{12}	2.7×10^{14}	1.3×10^{9}
740	4.7×10^{12}	3.9×10^{14}	1.9×10^{9}
760	6.4×10^{12}	5.3×10^{14}	2.5×10^{9}
780	9.1×10^{12}	7.6×10^{14}	3.6×10^{9}
800	1.2×10^{13}	1.0×10^{15}	4.9×10^{9}
820	1.7×10^{13}	1.4×10^{15}	6.6×10^{9}
840	2.3×10^{13}	1.9×10^{15}	8.7×10^{9}
860	3.0×10^{13}	2.5×10^{15}	1.1×10^{10}
880	3.9×10^{13}	3.3×10^{15}	1.5×10^{10}
900	5.1×10^{13}	4.2×10^{15}	1.9×10^{10}

Table 4.1.2 Atomic beam properties in the interaction chamber, based on kinetic theory [RAM56, pp. 11-21].

We measured the atomic beam density in the interaction chamber by looking for absorption of laser light tuned to the 2s→2p transition when the oven was very hot: 860°C. (At that time we had a laser filled with DCM laser dye which could operate at 6708 Å.) We attenuated the laser beam with crossed dichroic sheet polarizers, and reduced focusing by not using a telescope – see Sec. 4.3. The intensity of laser light was ≈ 2 mW/cm^2; less than the saturation intensity but not *much* less, so we probably did not get exactly linear absorption. But since we only need an estimate of the density, then we can assume Beer's law is close:

$$I_T = I_o \exp(-n\sigma_o l) , \tag{4.1.9}$$

where I_T and I_o are the transmitted and initial intensities on resonance, n is the atomic density, σ_o is the absorption cross section on resonance, and l is the width of the atomic beam which the laser traverses. The (unsaturated) cross section for the larger line displayed in Fig. 4.1.4 may be shown to be $(3\lambda^2/2\pi)(5/12)$; the smaller is $(3\lambda^2/2\pi)(1/4)$. Both lines predict a density 9×10^8 atoms/cm^3, about an order of magnitude smaller than that indicated in Table 4.1.2. Perhaps the temperature of the molten lithium isn't as high as the thermocouple reading; perhaps the oven is not in the effusive regime and there are substantial collisions near the hole in the tube oven. An indication that the former may be more likely is given by considering the oven lifetime. The total emission rate of atoms from the oven is

$$Q = \frac{1}{4} n_s \bar{v}_s A_s \tag{4.1.10}$$

so the oven lifetime is

$$\tau = \frac{N}{Q} \tag{4.1.11}$$

where N is the total number of lithium atoms in the oven. At 700°C we expect τ = 14 hours. We see at least a factor of two more than this. Also, note that kinetic theory predicts the *total* atomic density of both lithium isotopes but only ^{7}Li is excited. This is a small error since ^{6}Li makes up less than 6% of naturally occurring lithium.

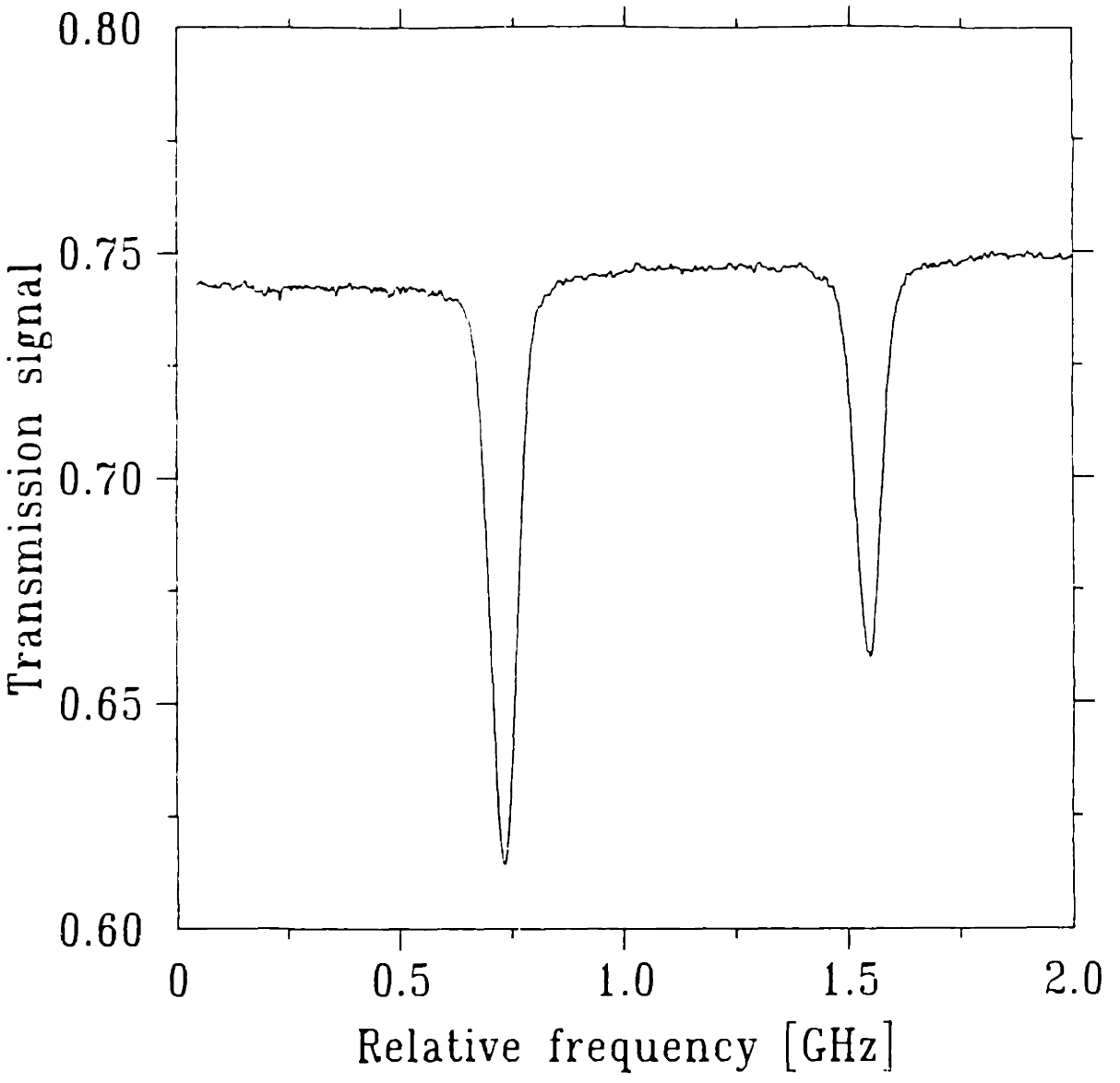

Figure 4.1.4 Atomic beam absorption of the principal transition of ^{7}Li. The larger peak is the transition $2S_{1/2}F=2 \rightarrow 2P_{3/2}$ $F=1, 2, 3$; the smaller is $2S_{1/2}F=1 \rightarrow 2P_{3/2}$ $F=0, 1, 2$. The oven temperature was 860°C. (Data file 1985: aug 6.5)

Sources of Lithium

For commercial purposes, lithium is presently extracted from brines of the Great Salt Lake, Utah, Searles Lake, California and from large deposits in Nevada and North Carolina [HAM75]. All lithium used in this experiment was obtained from

Lithium Corporation of America: LITHCO
449 North Cox Road
Gastonia, NC 28054
(704) 867-8371

The metal is available in several forms, but we usually used 1/8" diameter wire wrapped on a spool and stored under mineral oil. A pound of the "low sodium (<.007%)" wire (#455) costs about $100. Future buyers should note that the inner shipping can does not contain sufficient mineral oil to cover the entire spool; additional oil must be added immediately upon opening the sealed can and releasing the argon gas inside. Also, the spool floats in mineral oil, so a weight must be used to keep the spool submerged.

At one point we were concerned that the mineral oil was contaminating the atomic beam and vacuum system, leading to a stray electric field in the interaction chamber. Robert Kosak of Lithco was quite helpful by providing high purity (>99.96%) lithium foil (0.008"×1.6") packed under argon only. Working in an argon-filled glove box, the foil was carefully transferred to the tube oven. As described in later sections, this procedure did not help the stray field problem. The oven manifold pressure remains low during oven operation if the foil is used, or if clean wire is used.

as the wire isn't black, and the mineral oil is cleaned off with petroleum ether, the time-consuming glove box technique seems unnecessary.

Isotopically pure lithium is available from

Oak Ridge National Laboratory
Isotope Distribution Office
Post Office Box X
Oak Ridge, TN 37831-6015
(615) 574-6984

Gregory Potter ((615) 574-6507) is the person in charge of lithium. Either ^{6}Li or ^{7}Li is available at purities of >99.9%. The normal form is randomly shaped 1-3 gm pieces stored in mineral oil. The cost is $0.50/gm up to 50 grams plus a $250 chemical conversion charge (from LiOH to Li metal), and takes 8-10 weeks to receive. Special orders take 12-14 weeks. All orders require a previously submitted "end use statement". Fortunately our two-step excitation scheme allows laser selection of the desired isotope, so this expense seems unwarranted. However, ^{6}Li makes up about 6% of the material from Lithco. If there were a desire to study ^{6}Li, an isotopically pure sample would eliminate the need to run the oven at an unusually high temperature.

Safety Precautions

Lithium is a corrosive material, whose vapor can etch to opacity the windows of cells and improperly operated heat pipe ovens. We have found that our thermal atomic beam presents little difficulty except for the rather high operating temperature required for adequate beam flux.

Like all alkali metals, lithium reacts with water and liberates hydrogen. However, the reaction is least vigorous in lithium. The metal can be handled with gloves in a fume hood, although after removing the mineral oil, the silvery metal surface quickly turns black, apparently the signature of lithium nitride, Li_3N. There is sufficient time to prepare a tube oven.

After operating the oven, the vacuum manifold must be cleaned. We normally vent to 1 atmosphere of argon, and find the lithium as a black powder on all geometrically accessible surfaces *except* on the mu-metal shield surrounding the tube oven. There we see shiny crystals. After exposure to air, the black powder turns gray-white, indicating lithium hydroxide, LiOH. This latter material cleans off easily with water; the black powder reacts somewhat vigorously with water. We usually use a tissue saturated with water held in a hemostat to remove the powder, and then we rinse with acetone to remove the water. The cold shield and mu-metal insert are cleaned by placing them in a large beaker and flooding with water. It is possible, though not probable, to ignite the hydrogen gas with this technique, so caution must be used. Often we take the cold shield outdoors and drop it into a bucket of water.

Excess lithium metal should be stored under mineral oil and collected by the MIT Safety Office. Old tube ovens are cut open and flooded with water in a beaker before disposal. Finally, while we have tried to conduct ourselves with safety in mind, it's useful to remember that generally less than 1 gram of lithium must be removed

during a cleanup.

4.2 The Magnet

In January, 1976, Myron Zimmerman inherited a superconductive magnet, power supply, and cryostat from the laboratory of Aram Mooradian at MIT Lincoln Labs. The cryostat was of the "foot" design, with the solenoid bore vertical. Myron Zimmerman employed a vertical-traveling atomic beam to achieve the goal of spectral measurements without the complications of the motional Stark effect. Although this effort paid off in producing a publishable spectrum of the diamagnetic l- and n-mixing of sodium Rydberg states [ZCK78], numerous problems with the dewar, the atomic beam, and the detector made running the experiment quite unsatisfactory. Jarbas Castro, Myron Zimmerman's successor, developed a new cryostat in association with Alan M. Taylor of Andonian Cryogenics, Inc. during October and November of 1978. The new dewar system used the same magnet oriented with its bore horizontal, so the difficulty of a vertical atomic beam was eliminated. The machine produced the important observation of the evolution of quasi-Landau levels from the l-mixing regime [CZH80].

Materials and Specifications

The magnet is a "high-field" type, made in the distant past by General Electric. The windings are made of niobium tin (Nb_3Sn) tape, wound into pancakes like recorder tape on a reel. The tape is laminated with layers of polyester film for insulation, and copper sheet for dynamic stability [WIL83, pp. 317-318]. These

pancakes are stacked into a solenoid. In between the pancakes are copper disks to dissipate heat during quenching and to provide space to allow good thermal contact between the superconductor and the liquid helium. The magnet leads are shorted by a copper shield, which looks open electrically in parallel with a superconductor. The overall dimensions of the solenoid are

Inner (bore) diameter	2"
Outer diameter	8 1/4"
Length	11 1/4"

The field at the center of the magnet is about 10 T when 90 A flow through the windings. When the current is swept at 100 A/2500 sec, the back emf is about 0.8 volt, so the inductance is nearly 20 H. Jarbas Castro reported that the homogeneity of the field was about 1×10^{-3} over a volume of 1 cm^3, which seems quite reasonable based on the shape and size of the magnet [CAS81]. Our interaction volume is a cylinder only about 2 mm long and 0.1 mm in diameter. The linewidths we see are about the same whether or not the magnet is on; field homogeneity does not seem to be a major limit to our resolution.

Electrical Operation

The power supply and sweep controller system is a General Electric model GEK-31512, actually constructed by Hewlett-Packard. The major operating component in the sweep controller is a 10-turn, 200 Ω, linear potentiometer, which is motor driven. The potentiometer seems to degrade with time, and must be replaced

occasionally to give smooth current sweeps. The current is monitored by measuring differentially the voltage drop across a 0.0096 Ω (nominal) resistor in series with the magnet. A Kikusui PAB18-3 power supply, connected in parallel with the GE, provides trimming current from 0 to 3 A for fine adjustment of the field under computer control. The connection is a little tricky since neither magnet lead operates at ground. A floating output difference amplifier (gain=1) interfaces the Kikusui remote current control to the computer digital-to-analog output. The trimming current is monitored by measuring differentially the voltage drop across a parallel combination of three one-ohm resistors, so that the maximum voltage drop is about 1 volt. The Kikusui current supply does not seem to affect the operation of the GE current supply except when the GE current is zero, when the GE device will indicate an overload condition. The back emf caused by rapid changes of the Kikusui current through the magnet's inductance is registered on the GE supply's panel meter and may in fact cause a slight change in the GE current.

Field Determination

Measuring the magnetic field at the atoms presents a formidable problem. As is often the case, it is best to use the atoms themselves. We measure the optical frequency difference between the $k=21$, $m=+1$ and $m=-1$ states of the $n=21$ manifold. This difference, about 1 cm^{-1}/T, is due entirely to the paramagnetic interaction. The separation is the electron cyclotron frequency (or twice the Bohr magnetron, $2\mu_B/hc$)

modified slightly (for us, imperceptibly) by the finite nuclear mass (see Secs. 2.4 and 3.1). The manifold n=21 is selected because the iodine molecule has many tabulated absorptions in the frequency region around 16,031 cm^{-1} corresponding to the 3s→21p transition in lithium, and because the diamagnetic spectrum is *relatively* uncomplicated, say by levels from lower n. See Figs. 4.2.1 and 4.2.2 for the m=1, 0, -1 odd and even diamagnetic states of n=21. One complication with this technique is that a stray electric field parallel to the magnetic field (the axis which defines m) will couple states with opposite parity and the same m. The resulting Stark shift should be largest in the lowest energy states with given n and m; however, the *shift* should be the same to first order in the electric field, so the *difference* in m=+1 and m=-1 paramagnetic energies should be effected only in second order in the usually small electric field. The uncertainty in our determination of the magnetic field is about 20 gauss, limited by the frequency difference measurement.

The above method is accurate but awkward. If one is making measurements at n=76 for example, the laser must be tuned approximately 231 cm^{-1} to n=21 to make a field measurement. Ideally we would use a Hall effect probe located somewhere near the atoms that puts out a voltage proportional to the magnetic field, which could be calibrated using the n=21 level. This assumes that the relationship between the magnetic field at two different spatial (and temporal) points is constant, and that is simply *not* true. In older superconductive magnets such as ours, the phenomenon of

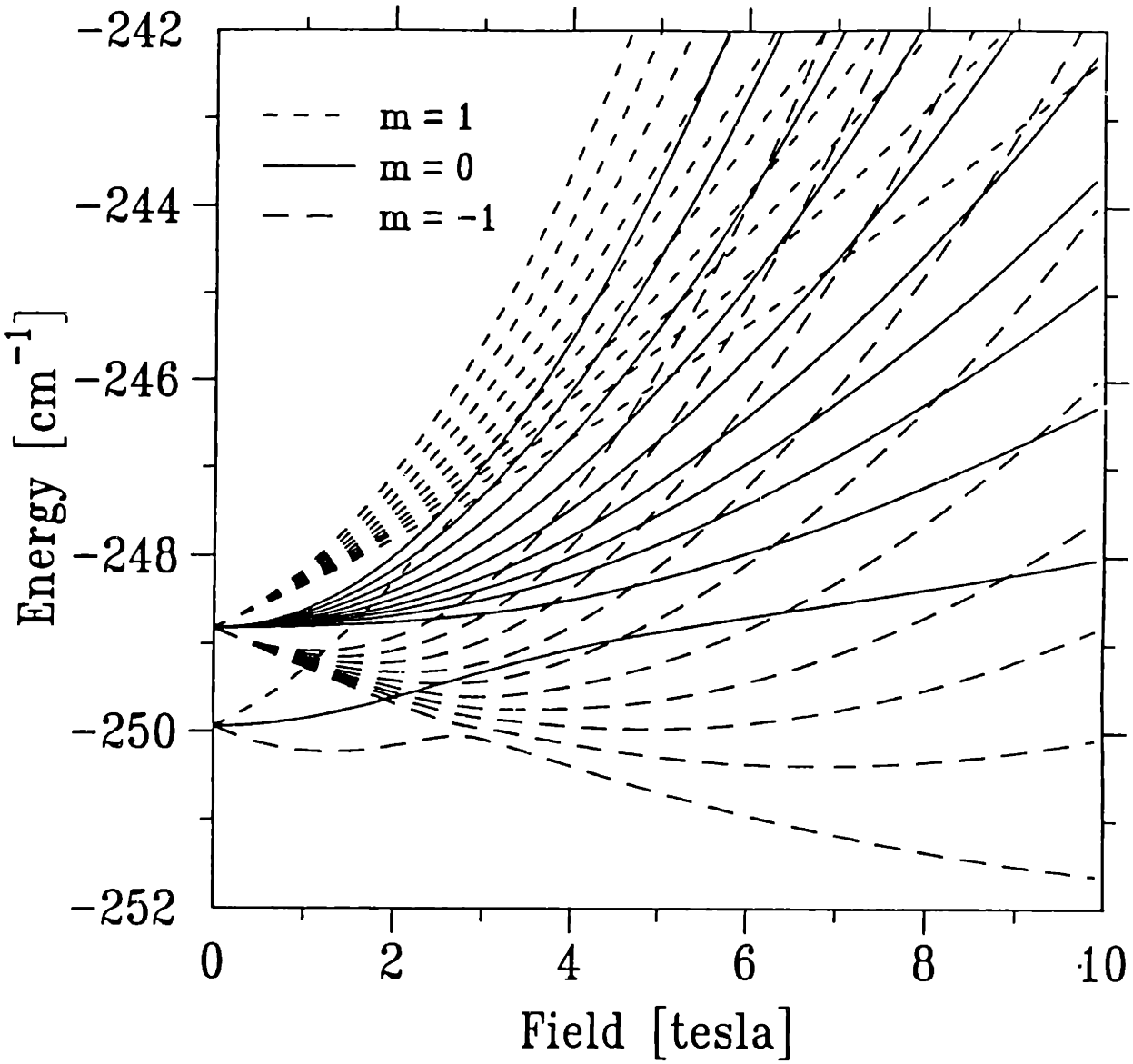

Figure 4.2.1 Energy levels of lithium n=21 in a magnetic field. Here m=1, 0, -1, and π = -1.

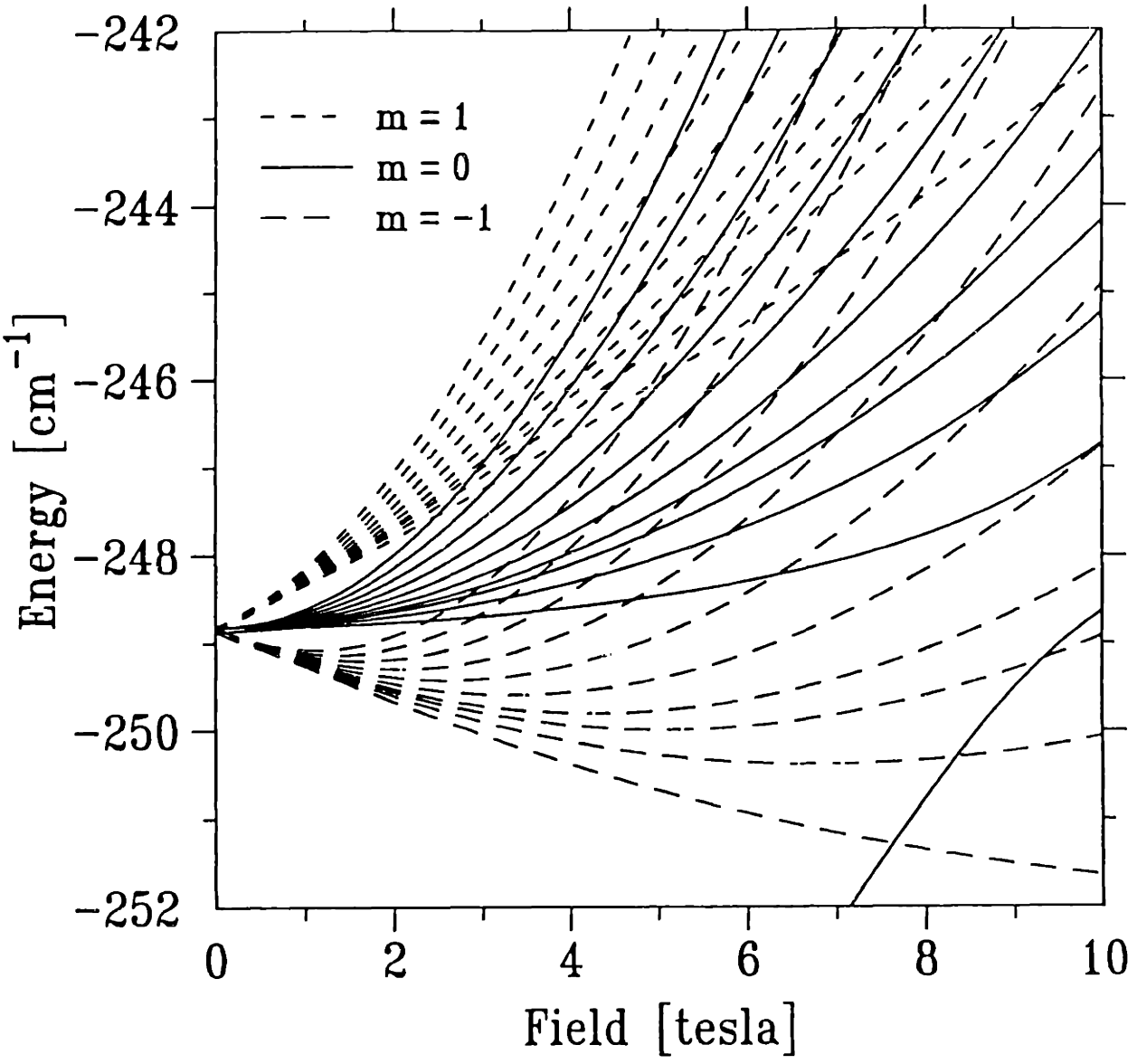

Figure 4.2.2 Energy levels of lithium n=21 in a magnetic field. Here m=1, 0, -1, and π = +1.

"flux pinning" (the trapping of flux quanta ($\approx 2\times10^{-7}$ gauss cm^2) which penetrate a type II superconductor on material defects in Ni_3Sn [AMI81, WIL83, pp. 294-297]) makes the value of the magnetic field at a point a rather random number. A careful study was made of the magnetic field at the atoms, using the $n=21$ manifold, the value of the magnet current (see Fig. 4.2.3), and the voltage across a Hall generator (see Fig. 4.2.4) placed close to the magnet's outer edge. The current measurement indicates substantial hysteresis; the Hall generator measurement demonstrates spatial inconsistency. Modern twisted multifilament wire largely eliminates the problem. Magnet current calibration now gives accurate field determination [JIR87].

We spent a great deal of time trying to make a good magnetic field probe. (The magneto-resistor probe used by our predecessors is completely inadequate for our needs. It is not linear, reproducible, nor stable.) See Fig. 4.2.5 for a description. The Hall generator is a Bell BHA-921 cryogenic semiconductor probe. The constant current source uses an Analog Devices AD584 voltage reference, an OP-07 precision op-amp, and 16 TRW metal oxide resistors in series-parallel (to average out the temperature coefficient) in a standard constant-current configuration [HOH80]. The temperature of these components is regulated to 0.1°C. The current is about 250 mA, stable to better than 1×10^{-5}. Hall voltages are measured using a bridge-type circuit, suggested by Larry Rubin of the MIT Magnet Lab [RNS75], and a Keithley 197 DMM. The Hall coefficient is temperature dependent and somewhat (±0.2%) cycle

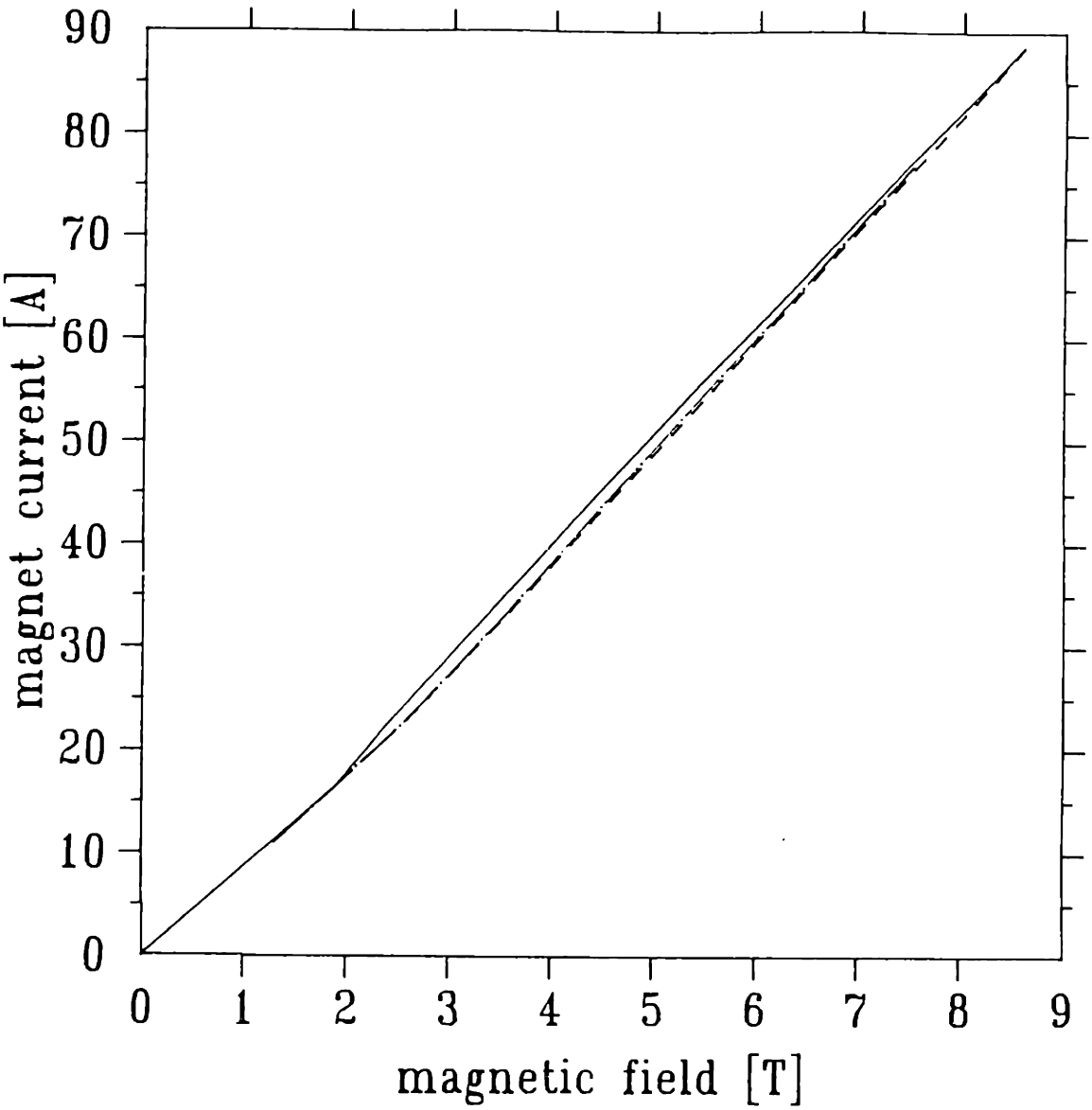

Figure 4.2.3 Magnet current calibration. Solid line: increasing field. Dashed line: decreasing field. Dashed-dotted line: increasing field again. (Data files 1988: jan 21.11-85)

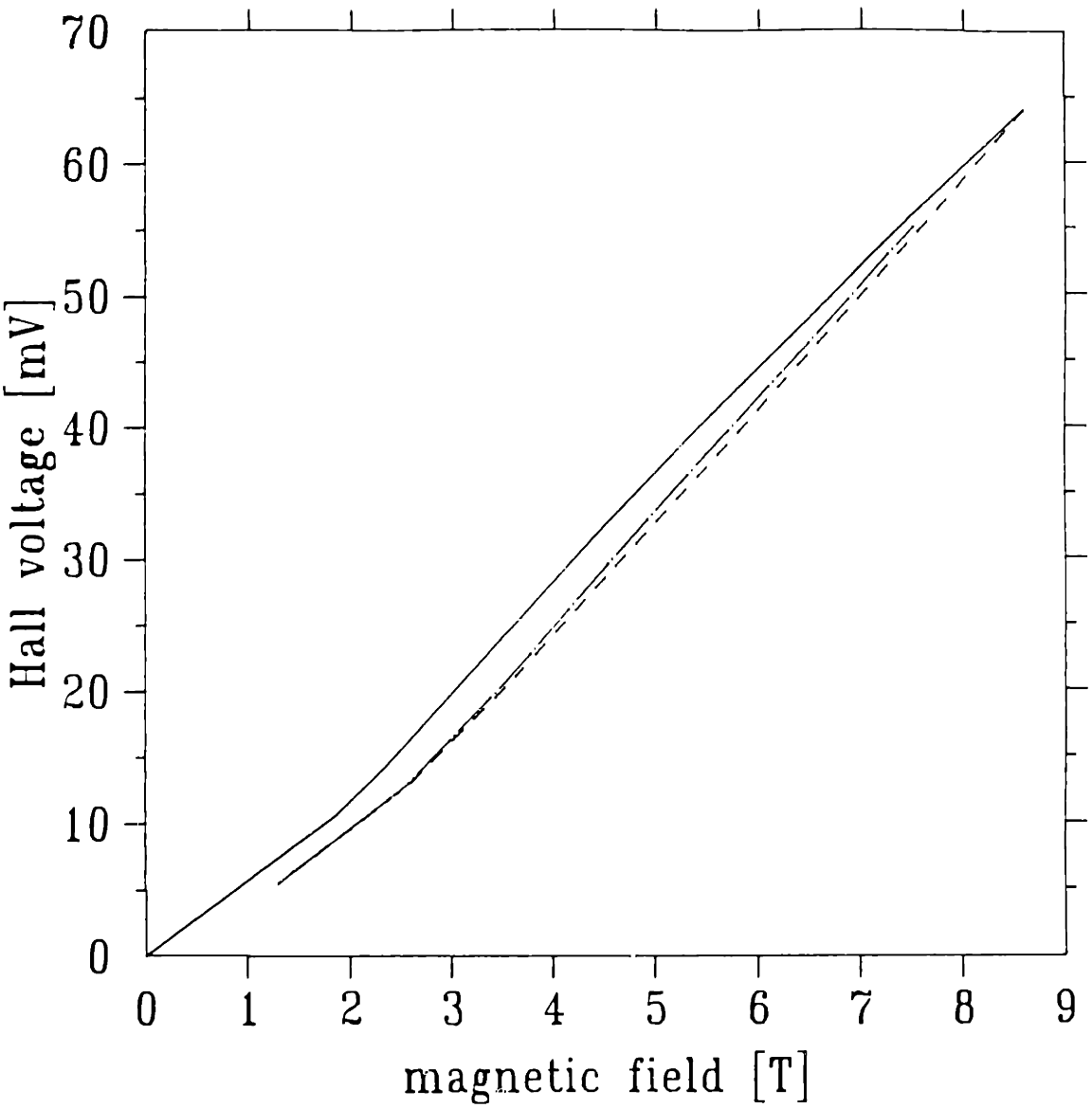

Figure 4.2.4 Hall generator calibration. Solid line: increasing field Dashed line: decreasing field. Dashed-dotted line: increasing field again. (Data files 1988: jan 21.11-85)

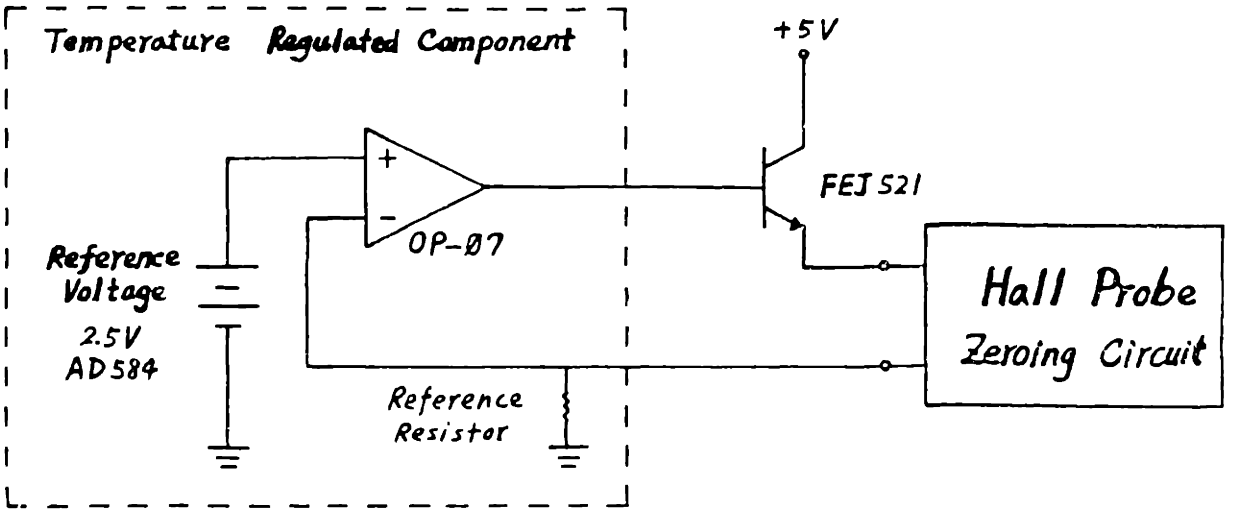

(a) Constant Current Source

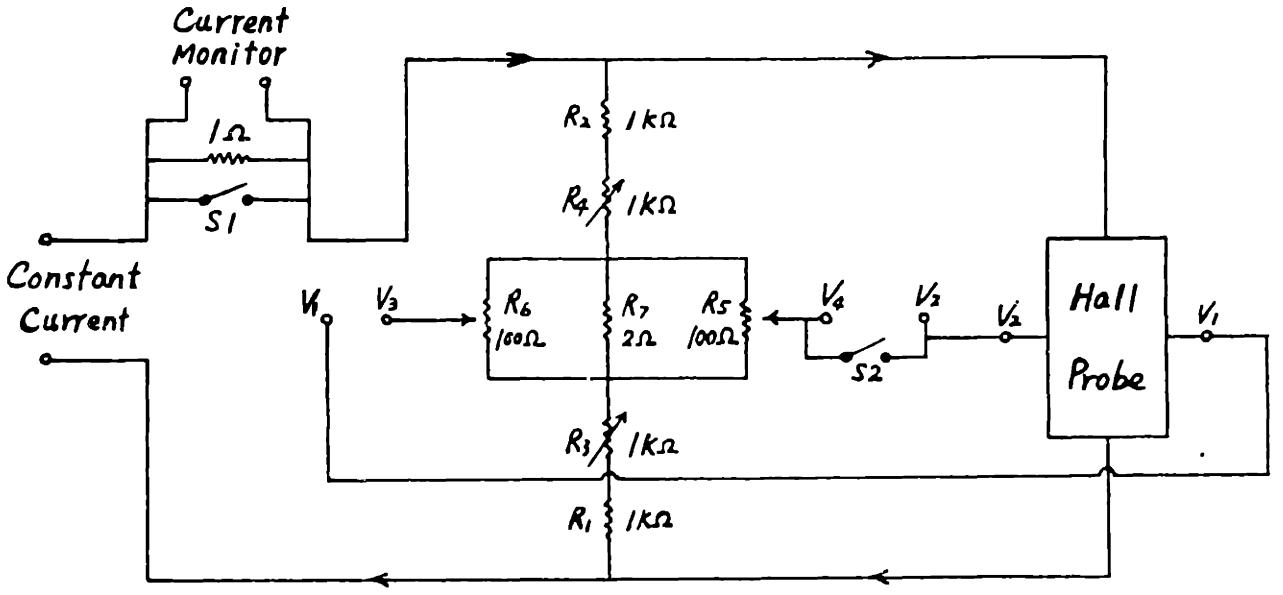

(b) Hall Probe Bridge Zeroing Circuit

Figure 4.2.5 Hall Generator Circuitry. Both the constant current source (a) and the bridge circuit (b) are shown. The bridge circuit is operated in the following manner: make V_2=V_4 by adjusting R_3, R_4, and R_5; close S_2; make V_1=V_3 by adjusting R_6 in zero magnetic field. The field is monitored by measuring the potential difference V_1 - V_3.

dependent.

Although the Hall probe cannot be used to measure the field accurately *absoiutely*, it can be used differentially over small changes in field. For example, we can set the magnetic field to some value, scan over n=21 for later field determination, then set the laser to the desired transition and increase the field by small increments (50-100 gauss) while recording the Hall voltage during each laser scan. When the final field is reached, we then scan over n=21. The first and last scans give us $\Delta B/\Delta V_H$ (~0.11 T/mV). Assuming this is constant over the change in field, then V_H specifies the field at each scan. This technique is used when studying anticrossings. The field assigned to each scan has an uncertainty of about 20 gauss.

Cryogenic Considerations

The vacuum jacket of the cryostat has a volume of 104 liters and is normally pumped by a water-baffled 2" oil diffusion pump, just like the oven manifold. The poor conductance between the pump and the dewar limits the pumping speed to ~ 1 liter/sec, and the pressure ultimately reaches $1\text{-}2\times10^{-5}$ Torr when the dewars are at room temperature. The liquid nitrogen dewar holds about 36 liters; the available volume of the helium dewar is nearly 72 liters. Liquid helium costs about $6 per liter, and the loss rate is about 1 liter/hour so operating the magnet is expensive. The heat of vaporization of liquid helium is about 0.7 watt-hour/liter; that of liquid nitrogen is around 45 watt-hour/liter [ROS73]. (The heat of vaporization for water is about 630

watt-hour/liter.) Pre-cooling the magnet with LN_2 is prudent. When liquid nitrogen is placed in either dewar, the jacket pressure becomes $1\text{-}2\times10^{-6}$ Torr. When liquid helium is collected in the helium dewar, the diffusion pump is valved off and pressure drops below 1×10^{-7}Torr, out of range of the Penning gauge.

Jarbas Castro left some instructions for transferring liquid helium to the research dewar. Basically, we follow his advice, which seems to be fairly standard cryogenic practice. Here are the major guidelines:

1. Pump out the LHe transfer tube to $<1\times10^{-4}$ Torr before each transfer. We attach it to our oven manifold to accomplish this.

2. The dewar vacuum manifold should be pumped out until the pressure reaches $1\text{–}2\times10^{-5}$ Torr before adding liquefied gases to the dewars. This may take several days.

3. Completely fill the LN_2 dewar with LN_2. When either the LN_2 or LHe dewar is filled with LN_2, the dewar is vented with an inverted "U" tube to reduce water condensation.

4. Pre-cool the LHe dewar and magnet by filling the LHe dewar with at least 10 inches of LN_2. The magnet must be covered. The magneto-resistor probe is used as a thermometer, and reads 14.419(1) mV.

5. Wait at least two hours and blow out the LN_2 from the LHe dewar with He gas. (We usually run HV and stray field tests on the system with LN_2 in the helium dewar for several days before adding LHe.) We place a flexible 0.5" diam tube through the fill port down to about 0.1" away from the bottom of the LHe dewar. Try to get as much LN_2 out as possible.

6. Close all ports and flowmeters and rough pump the LHe dewar. The magneto-resistor probe ultimately drops to about 11.45(1) mV and the pressure falls to about 1 Torr in approximately one-half hour.

7. When the magneto-resistor probe begins to rise, stop pumping and back fill the LHe dewar with He gas at approximately 2 psi regulator pressure. When full, stop the gas flow and then open the dewar. The gas is very cold, so use the gas fill valve to release the pressure gradually.

8. An extension tip must be placed on the research dewar side of the LHe transfer tube to reach the dewar bottom. The low lab ceiling forces us to insert the transfer tube into the research dewar before placing the other end into the storage dewar. The former is sealed with electrical tape. The latter is sealed with red-vacuum hose, and the tube slides through the O-ring seal of the pressure bonnet. All valves should be open to reduce the pressure build up when the transfer tube first touches the LHe.

9. Apply 15(2) oz/in^2 of He gas to the pressure bonnet, now with all valves closed except for the flowmeters on the magnet leads. The settling time for the pressure gauge on the transfer tube is ~3 minutes because the total volume is so large. The magneto-resistor probe voltage continues to rise for about 15 minutes after starting the gas flow. In another hour, some LHe begins to collect in the research dewar. The magneto-resistor probe voltage drops to less than 2 mV when LHe collects. It ultimately reaches 1.661 mV.

10. The LHe level in the storage dewar is monitored by an American Magnetics 20" LHe level probe. It takes about one hour to reach 20" (≈50 liters) after some LHe has collected. The dewar holds a maximum of 72 liters.

Recently, our procedure has been to fill the LHe research dewar with as much LHe as possible on the night before the scheduled run. The helium seems to boil less vigorously after eight hours, and we get enough sleep to run for the next twenty hours.

We like the new 100 liter "superdewar" storage dewars, since they are quite light and maneuverable, and don't have a liquid nitrogen jacket, although the loss rate is higher than in traditional storage vessels, about 2 liter/day.

4.3 Lasers and Optics

Two tunable laser light sources excite the lithium atoms to Rydberg states, as described in Fig. 1.2.1. Since the najor goal of the work is high resolution laser spectroscopy, the lasers must have narrow bandwidth. To minimize Doppler broadening, the lasers cross the atomic beam at right angles, as displayed in Fig. 1.2.2. The constraints of the magnet-bore size, and the critical focusing requirement for non-linear excitation, dictate a rather elaborate optical system. Accurate wavelength determination, essential for useful spectroscopy, also presents a challenge.

Laser Equipment and Operation

Actively stabilized ring dye lasers produce the required optical radiation. Although commercially manufactured, these devices are difficult to operate. The instruction manuals are complete, but they make sense after a long period of vast confusion. For me, several years of frustration yielded reasonable competence in the art of ring laser alignment. The major rules of engagement for dye lasers are to keep them clean, and not to move the optics very much. Gentleness and restraint are important. If a problem develops, ask a local expert for some suggestions. When large problems arise, the manufacturer's field service engineers will come and fix the lasers for mere money. Ring dye lasers cost about $60K, and a service cost of $100/hour can seem like a real bargain. Michael Feld, Professor of Physics and Director of the MIT Spectroscopy Laboratory, once said that the state of a society can

be judged by the sophistication of its dye lasers. Our society may be in terrible trouble.

An organic dye dissolved in solution has essentially a continuum of quantum states over a ~100 nm range. In a continuous wave (cw) dye laser, the dye is pumped by a powerful ion laser; a cavity built around the fluorescing dye produces tunable coherent radiation. A ring cavity has traveling wave eigenmodes, while a linear cavity configuration supports standing waves. See Fig. 4.3.1. The approximate resonance condition for radiation in the ring is that the cavity perimeter equals an integral number of wavelengths; in a linear laser, the cavity length is an integral number of half-wavelengths. Ring lasers are preferred because they can be operated at high power in a single cavity mode, whereas a phenomenon called spatial hole burning causes linear lasers to be intrinsically multimode at high power [PIK74]. We have used Coherent, Inc. Model 699 and 599 dye lasers in this work. Both linear and ring lasers use a birefringent filter for coarse tuning, and two etalons (with free spectral ranges of 10 and 225 GHz) for selecting a particular cavity mode. The lasers can be frequency stabilized to an external cavity using standard techniques [JHR79]. See Fig. 4.3.2. The optimum performance of ring lasers is nicely described by Johnston, Brady, and Proffitt [JBP82]. Some of the other useful specifications are listed in the following table.

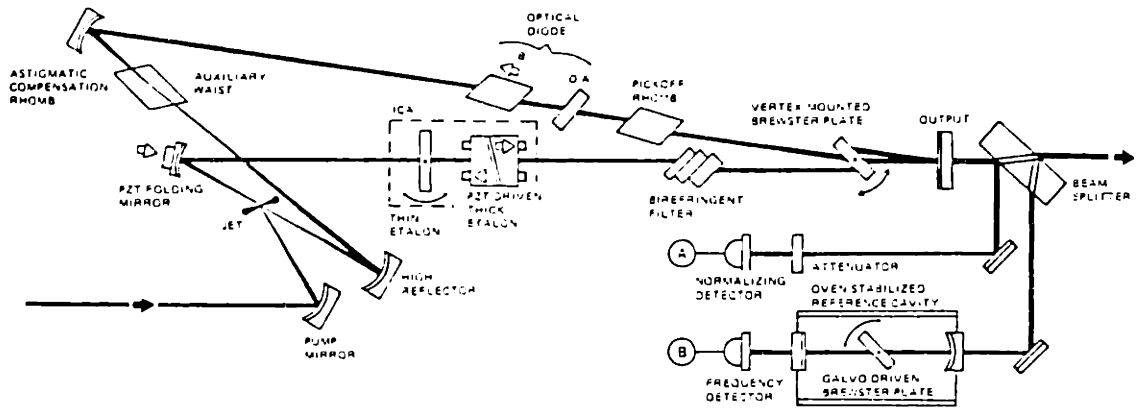

(a)

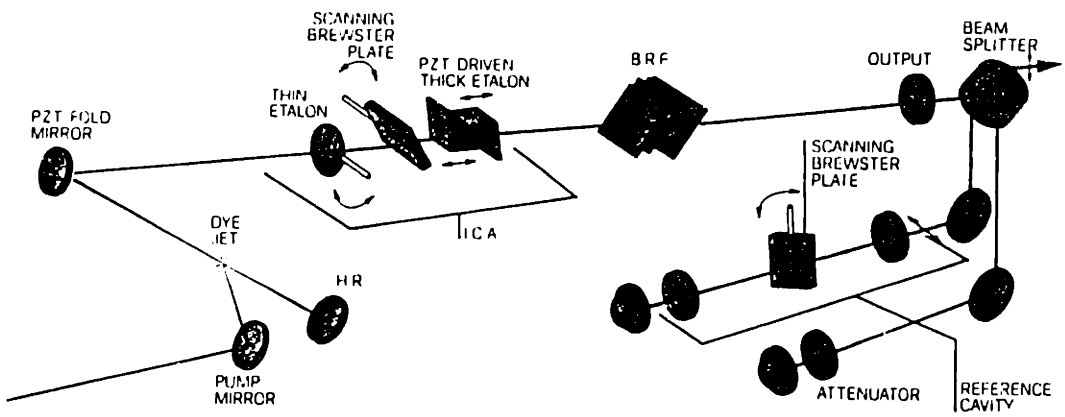

(b)

Figure 4.3.1 (a) Ring laser cavity schematic [COH82, p. 7]. (b) Linear laser cavity schematic [COH84].

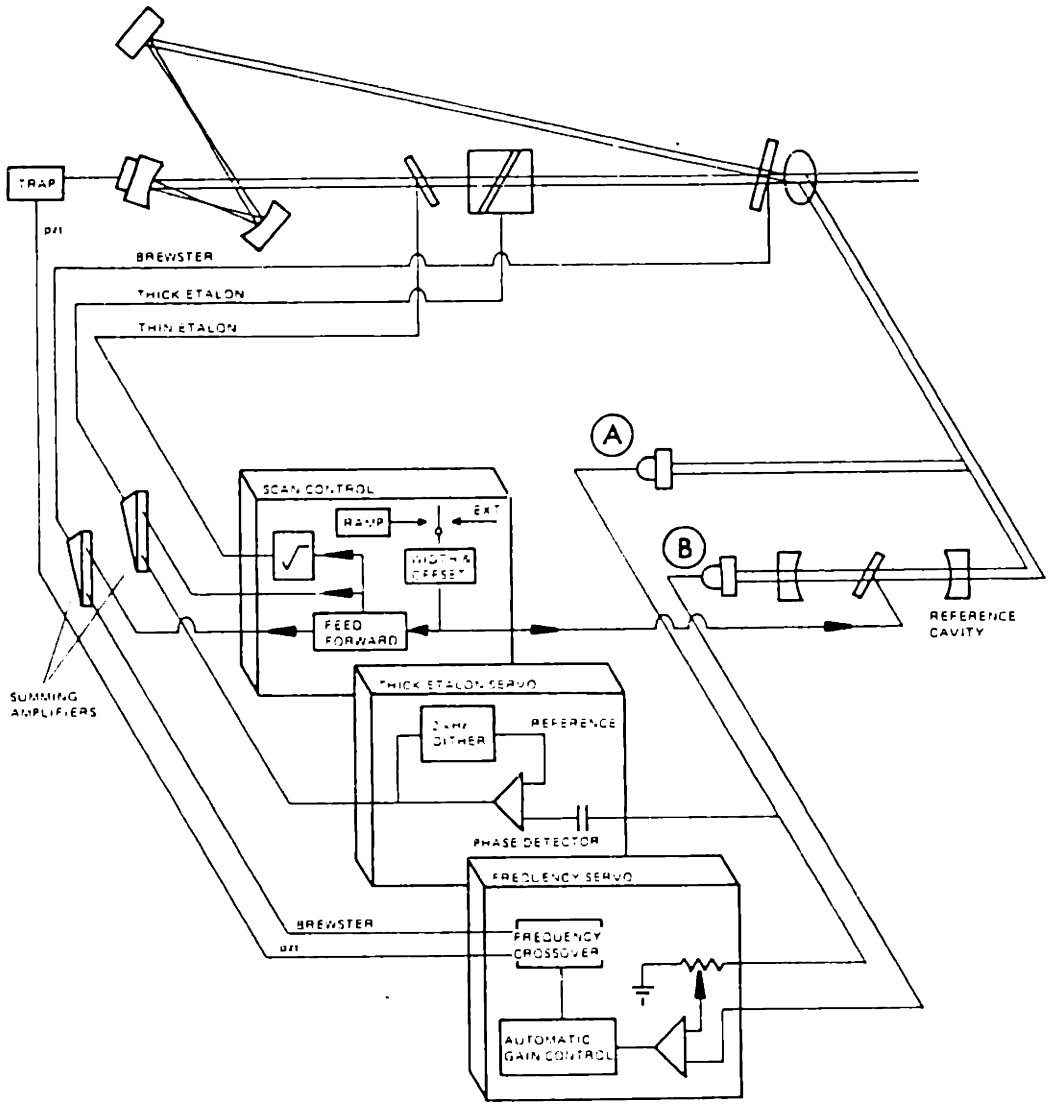

Figure 4.3.2 Stabilization schematic for the Coherent 699-21 [COH82, p. 10].

Frequency Jitter:	<1 MHz(in 10 kHz BW, when locked to the reference cavity.)
Frequency Drift:	<100 MHz/hour
Continuous Scan Width:	30 GHz
Scan Linearity:	2%

Table 4.3.1 Some specifications of the Coherent CR699-21 ring dye laser.

The frequency jitter depends on environmental noise; the frequency drift rate depends on the stability of air temperature and pressure. The scan linearity may be better than is specified. We studied the red laser frequency (as measured by the passively stabilized 300 MHz spectrum analyzer – see below) as a function of the scanning voltage applied to the laser. See Fig. 4.3.3. The largest deviation from a straight line correspond to 75 MHz out of the 10 GHz scan width; about 0.8%. Nevertheless, scan linearity is an important consideration in precision spectroscopy. To compensate for non-linearity, the absolute frequency is found from nearby iodine absorption lines using a stable cavity to provide interpolating frequency markers. This method is discussed later in this section.

The red laser, which drives the 2s→3s transition, is a Coherent CR699-21 actively stabilized ring dye laser. The dye solution is made by dissolving 1.5 gm of Exciton LD700 in 100 ml of reagent grade methanol, adding this to 1 liter of reagent grade ethylene glycol, and stirring for ~12 hours. The dye circulator with this ring laser is a Coherent 5920, in which all surfaces in contact with the dye solution are

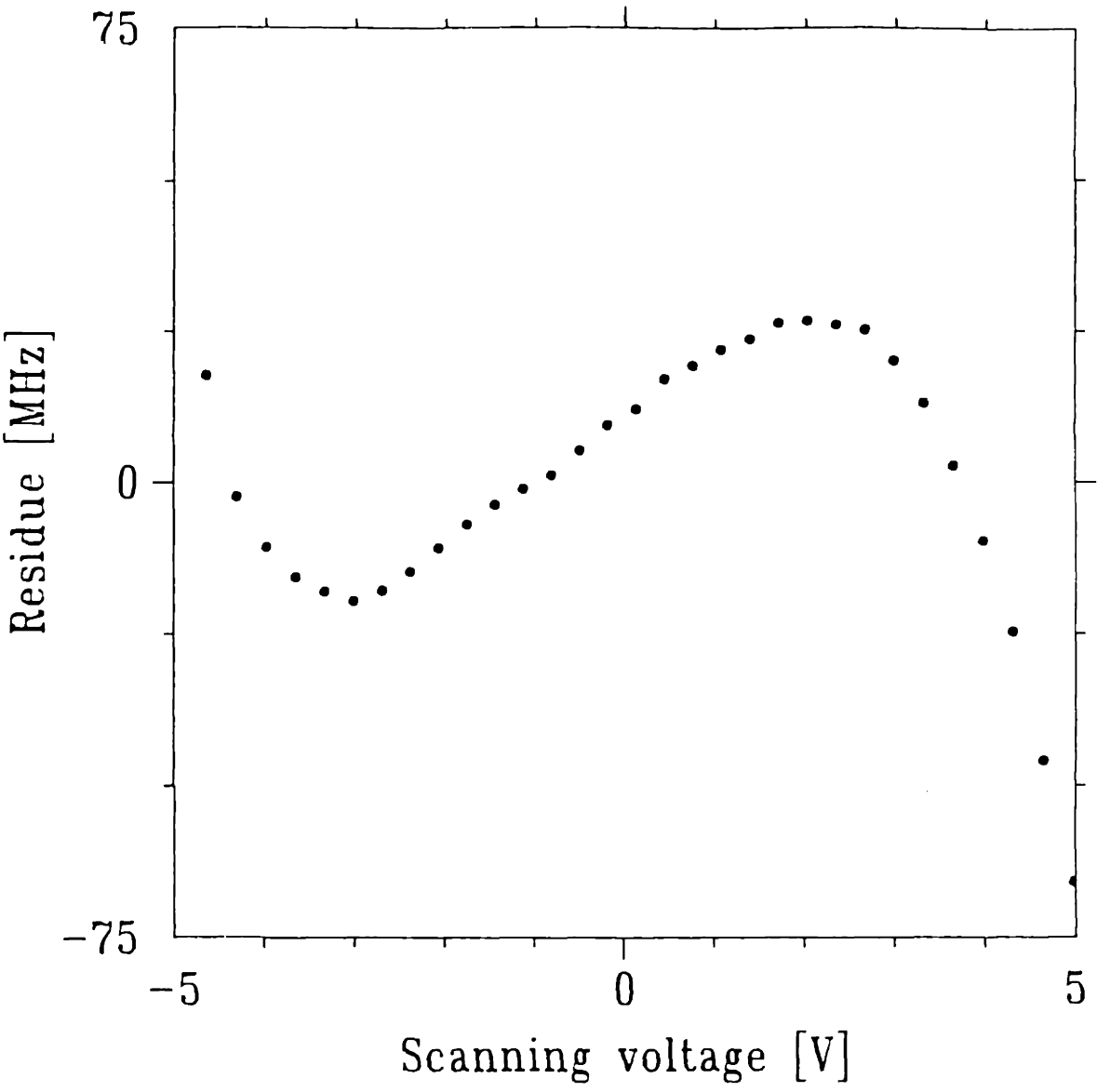

Figure 4.3.3 Scan Linearity of the Red Ring Laser. The relative laser frequency (as determined from the 300 MHz etalon) as a function of the external scanning voltage was fit by a straight line. The deviation from fit as a function of voltage is plotted here. (Data file 1987: apr 21.29)

plastic (except for the jet nozzle and catcher tube in the laser). This strongly increases the lifetime of LD700; we generally change this dye only once per year. The gain of this dye is one of the largest known: with a circulator pressure of 40 psi, and the pump laser power at 5.4 W, the dye absorption is 87-93%, and the single-mode output power is 1.2–1.4 W, depending on the cleanliness of the (standard LD700) laser optics. Dye lasers operating in the red seem more sensitive to dirt than those operating in the yellow or blue. Recently, a nitrogen gas purge was added to this ring laser to help reduce the contamination rate on the optics. (When the laser is off, the gas flow rate is 0.5 SCFH (standard cubic feet per minute); when on, 1.5 SCFH.) The preliminary results are promising, although careful cleaning of the optics with reagent grade acetone and lens tissue is still necessary. The peak of the dye gain is very near 735 nm, just where we need it.

The yellow laser, which drives the 3s→np transition, is also a Coherent CR699-21 actively stabilized ring dye laser. The dye solution is made by dissolving 2.0 gm of Lamdachrome (or Exciton) Kiton Red dye in 1.2 liter of reagent grade ethylene glycol and stirring for ~2 hours. (Only ~1 liter of solution is needed.) This ring's circulation pump is a Coherent 591, made with standard brass and stainless steel fittings. However, the Kiton Red lifetime is quite long, nearly a year. This dye has rather low gain, but has a very useful tuning range: it is in between Rhodamine 6G and DCM. With a circulator pressure of 51 psi, and the pump power set to 6.1 W, the

dye absorption is 80-85%, and the single-mode output power is 300-350 mW in the central wavelength region of the dye gain. We use standard (Rhodamine 6G) laser optics. The following table shows the wavelength range of the yellow ring laser.

λ_{air} (nm)	Use	Output Power (mW)	Birefringent Filter Setting
601.7	Bluest	100	624
614.76	3s→76p	360	685
623.62	3s→21p	320	725
633.13	3s→15p	320	769
647.8	Reddest	100	837

Table 4.3.2 Useful operating parameters of the yellow ring laser.

As always, careful cleaning of the dye laser optics with acetone and lens tissue helps maintain the performance.

When a spectrum with a frequency range larger than 30 GHz is required, we usually scan the laser 15 GHz, then hop the laser 10 GHz by changing thick etalon modes, and scan 15 GHz again. These scans are later overlapped using iodine absorptions which are common to both sets of data. This process may be repeated to produce a spectrum with a width equal to that of the dye gain. We have made scans up to 100 cm^{-1}.

Large frame ion lasers are needed to pump the ring dye lasers. The system combines high voltage (≈480 VDC), high current (≈40-60 ADC), and water (6 gallons/minute) in a plasma tube which contains the discharge. This discharge makes

noble gas ions in metastable states which function as the gain medium. The typical output power is about 10 W, and the "wall power" required is 480 VAC, 3ϕ at 100 A. The conversion efficiency is about 2×10^{-4}, with the remaining power taken away by the cooling water. The plasma tubes have a lifetime of 2-5 years, and cost $15-20K; a new laser costs generally more than $50K. The lasers require skill in service: for example, the internal power supply chassis is floated to −300 VDC, and neither the anode nor the cathode of the plasma tube are at ground.

The red ring is pumped by a Coherent CR3000K krypton-ion laser with a Coherent Innova K3000 retrofit plasma tube. This tube was installed on December 12, 1985, and has been quite stable. Like dye lasers, large frame ion lasers require cleanliness and gentleness, as described in their manuals. We operate this laser in multiline configuration (no intra-cavity prism) with red optics, so the active wavelengths are 676.4 and 647.1 nm. At present, a plasma tube current of 47A produces 5.4–5.6 W of output power. This laser has a nitrogen gas purge which effectively reduces the contamination rate on the plasma tube's Brewster windows. (Flow rates are 0.5 SCFH when the laser is off, and 1.5 SCFH when the laser is on.) Cleaning the Brewster windows with reagent grade methanol is required every 2-3 months.

The yellow ring is pumped by a Coherent Innova I100-10 argon ion laser, with a 10 W (nominal blue green power) plasma tube. This tube was installed on August 21,

1987. We operate the laser in the single line configuration, by using an intracavity prism. Presently the laser output power is 6.1 W at 514.5 nm when the plasma tube current is 39 A. The Brewster windows are protected by "dust shields" which contain a proprietary "dirt reducing" material. They work sometimes, but quality control appears to be a problem. Cleaning with methanol and lens tissue is required about once per month. The newer Innova tubes have two unusual properties compared with the older supergraphite or early Innova tubes. First, the plasma tube pressure seems to rise only. Since installation, this argon-ion tube has not taken a fill from its argon reservoir, yet the pressure continues to rise very slowly. The manufacturer says not to worry. Second, the spatial mode structure is not completely clean: there are some rings in it. We use the intracavity aperture set to #11 to achieve a clean circular mode. The I100 power supply and current control are very reliable, and the resonator assembly is quite stable: both large frame lasers have fairly constant power after about one hour of operation.

Input Optics for Lasers

Figure 1.2.2 shows the basic path of the laser beams. The goal is to place a beam waist from both lasers at the center of the interaction region. The laser beams must be overlapped and have their propagation direction perpendicular to the atomic beam velocity. The power and frequency of each laser must be monitored.

A more detailed description of the optical set up is contained in Fig. 4.3.4. The fundamental ideas are to expand the laser beams with telescopes, to combine them with a dichroic mirror beam splitter, and to focus the beams down to a waist inside of the interaction region with one lens. Alignment is quite complicated and requires great skill and dexterity. It is useful to have two mirrors between the laser and the telescope, so the beam can always be made to go through the telescope parallel to the laser table. This allows for simple telescope adjustment. It is also important to use thick or wedge-shaped beam splitters to avoid interference of the reflected beams. All mirrors in the main beam paths are CVI laser-quality dielectric coated mirrors, optimized for the appropriate wavelength range; the lenses are Melles Griot BK-7 glass with HEBBAR broadband antireflection coating. This coating is adequate because no tight beam foci touch their surfaces. The mirror mounts are all standard Newport 2-inch holders, except for the final pointing mirrors which are Aerotech 3-inch mounts with differential screw adjustments. The main beams are about 6 inches above the laser table; most wavelength monitoring beams are 10 inches above the table, mounted on 2-inch diameter posts.

The main red laser beam is deflected by two mirrors before entering a telescope with +5 magnification. This telescope is formed with -20 mm and +100 mm focal length lenses, the second of which is mounted on a linear translator. The telescope can be adjusted to give a nearly parallel output beam. Next, the large beam is

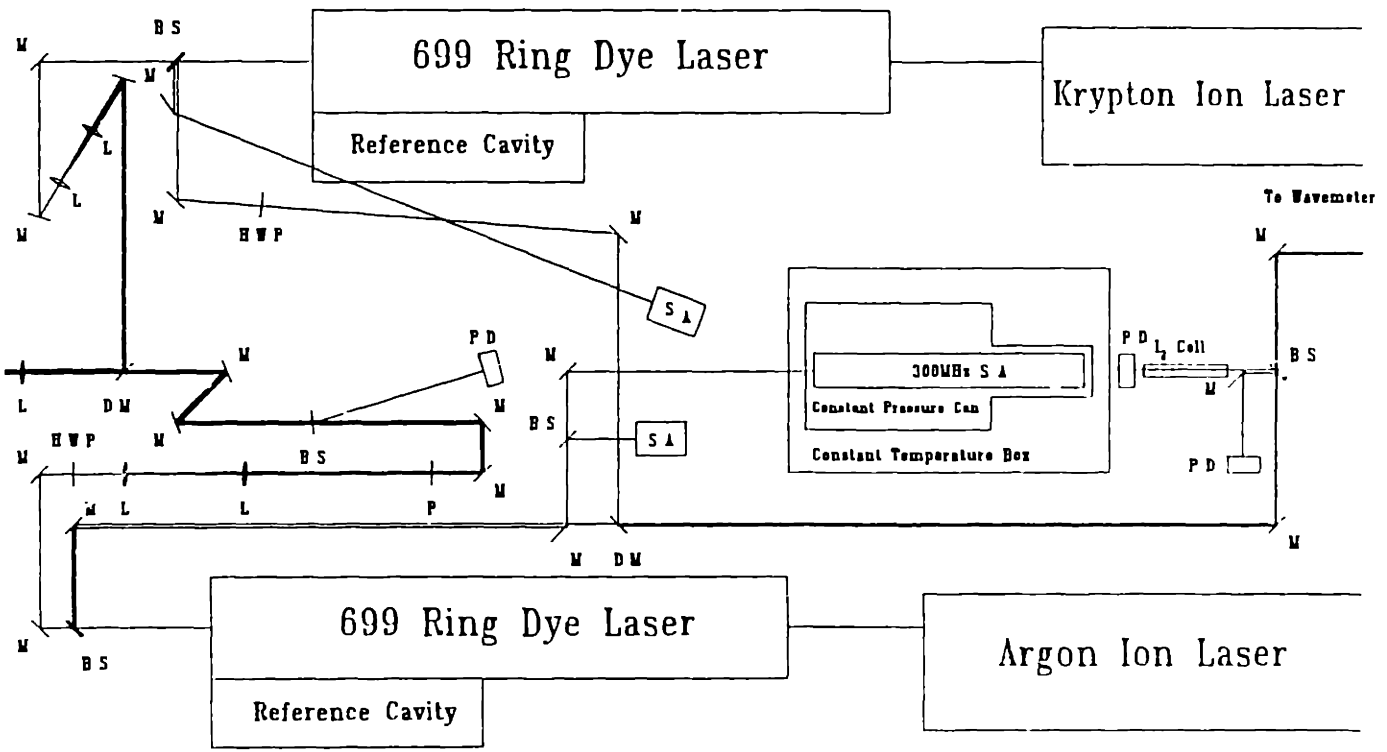

Figure 4.3.4 Detailed optical layout. The following abbreviations are used: BS-beam splitter, M-mirror, DM-dichroic mirror, L-lens, HWP-half-wave plate, PD-photodiode, SA-spectrum analyzer, P-polarizer. The different lasers are joined with dichroic mirror beam splitters, which reflect red and pass yellow. Not shown are several iris apertures which help in alignment, the overlap pinhole and mirrors, and holders for neutral density filters in the yellow beam.

deflected by another mirror onto the CVI dichroic beam splitter, which reflects ≈99% of the red light. The dichroic element sits in an Aerotech mount with differential screws, and also on a linear translator whose motion is parallel to the incident red beam. This adjusts the angle between the laser and atomic beams in the interaction region, and thus can minimize the Doppler effect. (Note: Moving the dichroic beam splitter toward the yellow ring produces a blue shift in the frequency of the two-photon resonance peak. Because of the atomic beam divergence, the linewidth and line asymmetry are minimized when the doppler shift is zero.) The laser beam then is focused by a 400 mm focal length lens into the cryostat through a CVI broadband antireflection coated window. The focus is set by maximizing the two-photon cascade fluorescence, while keeping the scattered red laser light at a minimum. The latter is checked by blocking the atomic beam. The beam waist (the radius of a Gaussian beam where the intensity is e^{-2} of that in the center) is determined by measuring the maximum power transmission through a 100(4) μ diam pinhole neglecting diffraction. The waist is about 51(3) μ. The system is reasonably efficient: the losses from just after the first beam splitter past the laser to just after the final focusing lens amount to about 4%, while losses going into the cryostat and coming back out (through two windows and two prisms) amount to about 10%.

The frequency characteristics of the red beam are monitored using the weak reflected beams from a thick glass plate which intersects the main beam just after

coming out of the laser. The laser polarization is vertical (perpendicular to the laser table, and also nominally perpendicular to the magnetic field, though the 2s→3s transition is not polarization sensitive) and this weak beam splitter is oriented close to Brewster's angle. The front surface reflection is deflected by a mirror through a half-wave plate (really a broadband retarder) which prepares the red laser polarization for the wavemeter. This beam is deflected by another mirror into another dichroic beam splitter which sends the red beam toward the wavemeter. The back surface reflection of the weak beam splitter is scanned by a 1.5 GHz free spectral range spectrum analyzer. This device monitors ring laser performance by displaying the laser's spectral characteristics.

The main beam of the yellow laser has a slightly more complicated path. After deflection by two mirrors, the beam traverses a half-wave plate used for polarization rotation and then enters a telescope with -7.5 magnification, made with lenses of 20 mm and 150 mm focal lengths. The second lens is on a linear translator so that the exit beam can be made nearly parallel. Unlike the "red telescope", the "yellow telescope" is inverting and has an internal focus. Occasionally we chop the yellow laser for phase-sensitive detection; placing the chopping wheel at a focus minimizes the time that the blade edge is moving through the beam thus reducing the dead time in this detection method. The beam then passes through a neutral density filter holder (not shown in Fig. 4.3.4) which permits attenuation of the laser. We found that filters

which are volume absorbing are more useful than those which are partially reflecting because the latter act like a low-finesse etalon with a free-spectral range of about 0.5 cm^{-1}. The filter holder is followed by a linear polarizer which removes most of the ellipticity produced by the retarding plate, telescope lenses, and neutral density filters. Elements further down the beam path can also degrade the polarization quality; one of the worst is the prisms inside of the interaction region. Therefore, a dichroic sheet polarizer is completely adequate, although the transmission through this element is only about 50%. However, we usually attenuate the laser anyway. After deflection by two mirrors, the yellow beam traverses a thick wedge beam splitter. The reflection is used for power monitoring by focusing the beam onto an EG&G SGD-040-A photodiode with a 18 mm focal length lens. The focusing reduces the photodiode's sensitivity to the small motion of the laser beam which occurs while scanning the laser. The associated electronics are shown in Fig. 4.3.5. The wedge geometry removes the etalon effect. Next the beam is deflected by two more mirrors, the second of which is held in a precision Aerotech mount. The beam passes through the dichroic mirror beam splitter mentioned in the description of the red laser beam path. The two laser beams are combined here. This element transmits about 70% of the yellow beam – the best CVI could do. Finally, the yellow beam follows the red beam through the final focusing lens into the interaction region, via the entrance window. The beam waist is 64(3) μ. The yellow system is not as efficient as the red. With no neutral density filters, the power entering the cryostat is 33% of the power just after the first

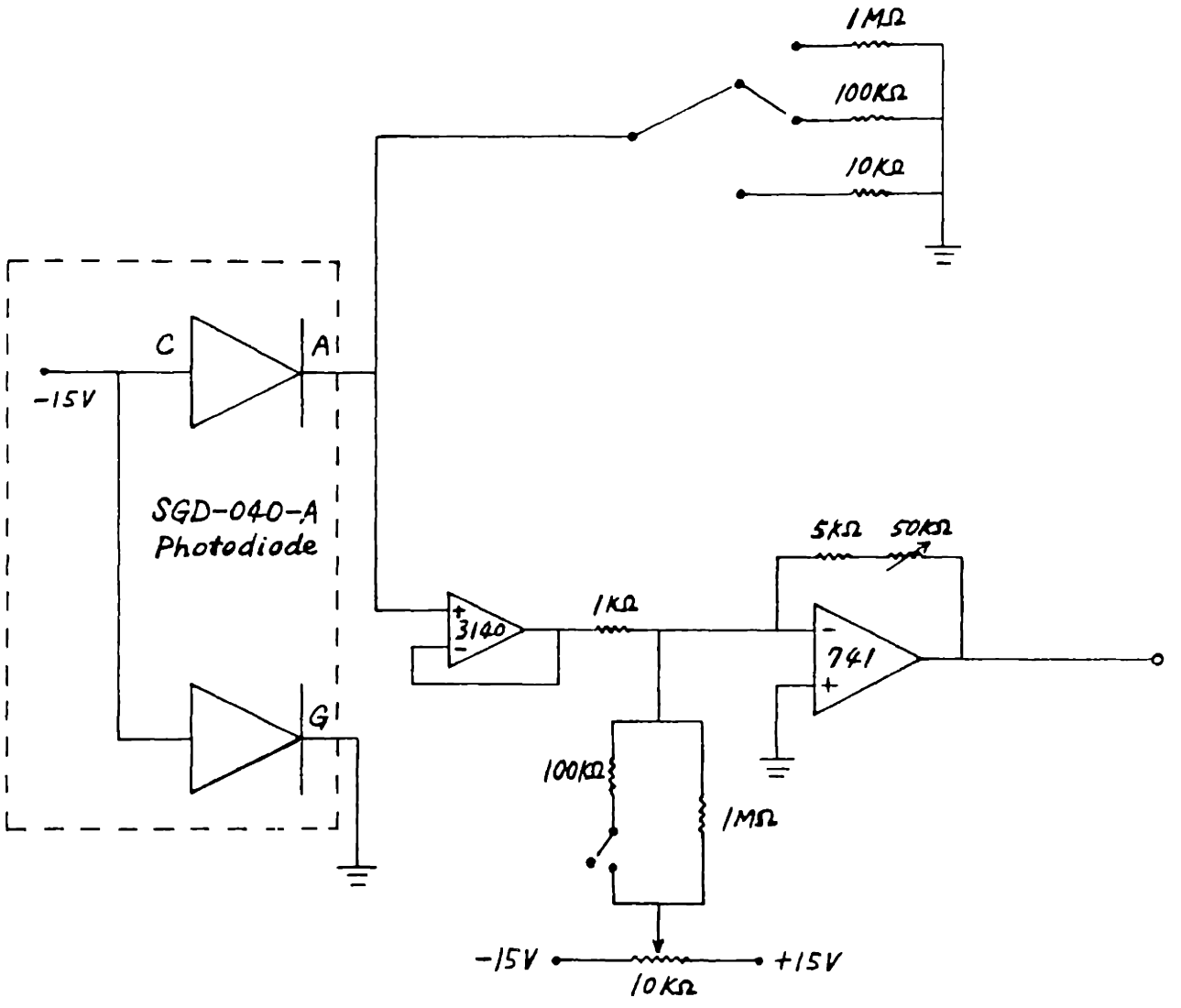

Figure 4.3.5 Electrical Schematic of the photodiode circuitry.

beam splitter past the laser. It is, however, quite adaptable: the polarization can be changed, the power is properly monitored and can be changed over many orders of magnitude without major misalignment.

Frequency characteristics of the yellow beam are found from weak beams produced by a thick glass plate just after the laser. Mirrors deflect these beams in such a way that the polarization is horizontal (parallel to the laser table) – appropriate for the wavemeter. One beam passes through the dichroic mirror mentioned in the red beam path description, toward the wavemeter. (Note: Either the red beam or the yellow beam entering the dichroic mirror must be blocked in order to use the wavemeter.) Before reaching the wavemeter, the beam is again divided. One of these two new beams passes through a 48 cm long iodine cell and is focussed on a photodiode; the other beam goes to another photodiode and provides power normalization. The other beam is divided and each beam excites a spectrum analyzer. One has a free spectral range of 1.5 GHz; the other, 300 MHz.

The red and yellow laser beams must be overlapped at their foci inside of the interaction region. As mentioned above, the focus of the final lens is set by maximizing the cascade fluorescence produced in the lithium atoms by the red laser. The beam is temporarily deflected by a plane mirror placed in the beam past the final lens but before the window. A 100(4) μ diam pinhole, laser drilled in thin stainless steel by National Aperture, is placed at the focus using an $x-y-z$ translator and a

power meter. The Rayleigh length (distance over which the intensity drops to half the maximum value) of these beams is ~1 cm. The position of the focus can be located within several millimeters. Now the yellow laser beam is made to go through this pinhole using the differential screws on the yellow pointing mirror. The yellow telescope is adjusted to get the yellow beam focus at the pinhole location. After removing the temporary plane mirror, the lasers are always well enough overlapped to find a Rydberg state using electric field ionization. The overlap can then be optimized by maximizing the Rydberg state signal.

Actually, laser beam insertion requires several iterations to achieve satisfactory alignment. The photon detection system is more sensitive to yellow light than to red; often the yellow laser must be repositioned to reduce the noise associated with its scattered light. Then the pinhole is positioned according to the yellow beam focus, and the red beam is moved to pass through the pinhole.

Wavelength Selection with the Wavemeter

There are two goals involved with the determination of laser wavelength. The first is the ability to set the laser frequency to within several GHz of a desired resonance so it can be found easily. This is accomplished with a HeNe-based Michelson wavemeter. The second is the precise and accurate measurement of the transition frequency so that energy levels can be assigned. An iodine reference cell and a passively-stabilized Fabry-Perot etalon provide this capability.

Inspired by the design of Hui-Rong, Benson, and Hänsch [HBH81], George Welch and Ishai Nir (a UROP) built a hand-operated wavemeter using a Spectra-Physics Model 155 multimode random-polarization HeNe laser as a wavelength reference. See Fig. 4.3.6 for a schematic diagram. The basic operating principle is to count the number of interference fringes of unknown dye laser light produced by moving one arm of a Michelson interferometer through a known distance. Changing the path difference by one wavelength shifts one interference fringe into the next. The distance is measured by counting the number of fringes of reference HeNe laser light produced over the same path difference. Therefore, over the same path difference,

$$n_u \lambda_u^{air} = n_r \lambda_r^{air} \tag{4.3.1}$$

where n_u and n_r and the number of unknown and reference fringes counted, and λ_u and λ_r are the unknown and reference wavelengths. In the original version of the wavemeter, both lasers were vertically polarized (perpendicular to the plane of the wavemeter) because the central cube beam splitter was ≈50% T/50% R only for s polarization, so the two lasers had to be separated spatially. The fringes are detected with EG&G FND-100 photodiodes with 90 V bias. The signals are increased by a buffered Evans Model 4163 dual wideband (10 MHz) amplifier, and tabulated with a Philips 6673 Model (120 MHz) counter operated in ratio mode. The wavemeter reads

$$x = \frac{n_r}{n_u} = \frac{\lambda_u^{air}}{\lambda_r^{air}} \ . \tag{4.3.2}$$

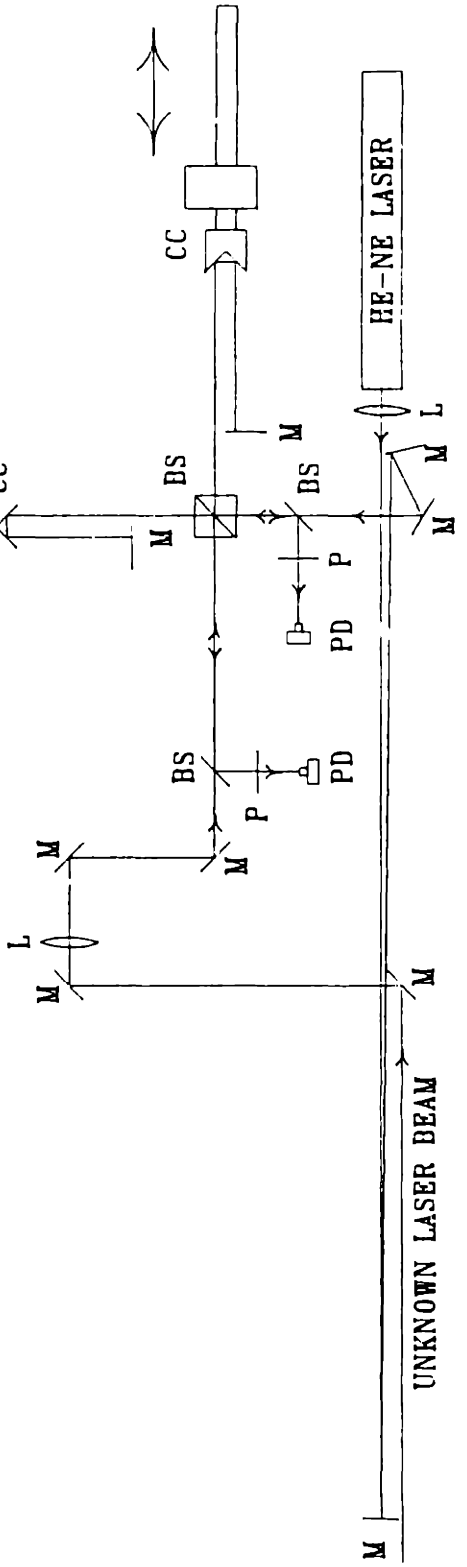

Figure 4.3.6 Wavemeter Diagram. A Michelson interferometer is formed with the cube beam splitter (BS), the corner cube reflectors (CC), and the plane mirrors (M). The length of one arm is varied by moving one of the corner cubes. The corner cubes reduce the deviation of laser beams when the path length is changed. The reference and unknown beams are expanded slightly with lenses (L) and travel over long paths prior to entering the interferometer to give more fringe area. In the interferometer, the beams are overlapped, and separated with polarizers (P) into their proper photodiodes (PD).

The multimode output of the HeNe laser restricted the number of reference fringes with adequate visibility; the precision was 1×10^{-5} or about 0.06 Å.

George Welch upgraded the wavemeter using a new cube beam splitter, a Coherent Model 200 single frequency stabilized HeNe laser, and motorizing the corner cube motion. The new beam splitter is rather polarization insensitive, so the unknown and reference beams can be completely overlapped with orthogonal polarization; the two lasers can be separated with dichroic sheet polarizers. The single-mode HeNe allows visible reference fringes throughout the travel of the corner cube. The path difference changes by four times the distance the corner cube moves; the latter has a travel of about 15 cm, so about 1 million HeNe laser fringes should be present. However, we lose some fringe visibility toward the ends of the travel; only 500,000 fringes are counted. By triggering the counter with the motor drive, most of the travel can be used to determine the wavelength. The motor drive makes reading the wavemeter very easy, although optical alignment is tricky. The precision is $1\text{-}2\times10^{-6}$. Changing the dye laser frequency by tuning the etalon transmission peaks is well resolved by the wavemeter. The following table shows typical operating parameters.

Li transition	Approximate Wavelength (nm)	Wavemeter reading (x)	Change in Reading for One Mode Hop of the Etalons Thin (225 GHz) (Δx)	Thick (10 GHz) (Δx)
2s→3s (^{7}Li)	734.93(1)	1.161,360(1)	0.000,640(3)	0.000,029(3)
3s→21p	623.615(1)	0.985,460(1)	0.000,461(3)	0.000,021(3)
3s→76p	614.759(1)	0.971,463(1)	0.000,448(3)	0.000,020(3)

Table 4.3.3 Useful wavemeter facts. Note that going red increases the wavemeter reading. The air wavelengths are based on Johansson's energy levels [JOH59], Martin's fit [MAR80] and the CRC refractive index [WEA75].

To convert the wavemeter reading to wavelength (or frequency), the reference wavelength must be known. According to the MIT wavelength tables [HAR69], the appropriate transition in neon has an air wavelength of

$$\lambda_r^{air} = 632.8173(20) \text{ nm} \tag{4.3.3}$$

where the uncertainty comes from the room temperature Doppler width of neon, about 1.5 GHz. To find the vacuum frequency, the refractive index of air is needed, which is about

$$n^{air} = 1.000,27(1) \tag{4.3.4}$$

over most visible wavelengths [EDL53], thus the vacuum frequency is

$$\sigma_r = 15,798.1(2) \text{ cm}^{-1} . \tag{4.3.5}$$

With respect to the stability of the reference laser, the Coherent Model 200 HeNe laser is stabilized against thermal drift by making the two active orthogonal

components have equal intensity. The long term drift specification is 5 MHz/°C of ambient temperature change, once the laser is warmed up. (We never turn the laser off.) The 0.2 cm^{-1} uncertainty in the laser frequency (Eq. 4.3.5) is too large for our needs. To find the frequency more accurately than this, we measured 21 iodine absorption lines near 614 nm (3s→21p in Li) with the yellow dye laser and the wavemeter. The iodine atlas [GEL78] lists the vacuum frequencies of these resonances, so the vacuum frequency of the HeNe was determined from (data set 1987: dec 16)

$$\sigma_r = \frac{1}{21} \sum_{i=1}^{21} x_i \sigma_i = 15{,}798.01(1)\ \mathrm{cm}^{-1}\ , \tag{4.3.6}$$

where x_i and σ_i are the wavemeter fringe ratio and the tabulated frequency of each iodine line, respectively. This formula neglects the dispersion of air, an omission which can be justified as follows. The correct conversion from wavemeter reading to reference frequency is given by

$$x = \frac{\lambda_u}{\lambda_r} = \frac{n_r \sigma_r}{n_u \sigma_u} \tag{4.3.7}$$

so

$$\sigma_r = x \cdot \sigma_u \cdot \frac{n_u}{n_r} \tag{4.3.8}$$

or

$$\sigma_u = \frac{1}{x} \cdot \sigma_r \cdot \frac{n_r}{n_u} \,. \tag{4.3.9}$$

The ratio of refractive indices can be estimated from the Cauchy Formula found in the CRC Handbook [WEA75]:

$$(n-1)10^7 = 2589.72 + \frac{12.259}{\lambda^2(10^{-6})} + \frac{0.2576}{\lambda^4(10^{-16})} \tag{4.3.10a}$$

for an environment of dry air, ≈0.05% CO_2, a pressure of 760 torr, and a temperature of 30°C; λ is the air wavelength in angstroms. For λ_u = 6236 Å and λ_r = 6328 Å, we find

$$\frac{n_u}{n_r} \approx 1 + 1.1\times10^{-8} \tag{4.3.10b}$$

which is sufficiently close to unity that the difference can be ignored. We use the wavemeter from 610 to 735 nm; the refractive index decreases by 1×10^{-6}. Changes in the dispersion caused by humidity, and changes in barometric pressure and temperature, have a negligible effect on the wavemeter reading [EDL53].

Wavelength Determination with the Iodine Cell and the Etalon

One of the most difficult tasks in high resolution spectroscopy is the precise and accurate determination of transition frequencies. We use the accurately known absorption lines in an iodine reference cell and a passively stabilized Fabry-Perot etalon as an interpolation reference standard.

The iodine cell optical arrangement is shown in Fig. 4.3.4. The cell is 48 cm long and is mounted with its axis vertical. The cell is used in absorption mode. After leaving the cell, the laser beam is focussed by an 18 mm focal length lens onto an EG&G SGD-040-A photodiode. The lens is mounted on an x-y translation stage so that the diode output can be maximized. Focusing the beam reduces the sensitivity of the photodiode to the small motion of the laser beam that occurs during a laser scan. A second photodiode monitors the laser power, so a normalized spectrum is produced.

The iodine atlas [GEL78] presents an incredibly large (14,800–20,000 cm^{-1}) iodine absorption spectrum in which most of the big peaks are labeled by the frequency of their deepest point. The quoted precision is often several tenths of a milliwavenumber. The accuracy, however, is difficult to assess; a later atlas [GVC82] indicates that the older tabulation is systematically high by about 0.005 cm^{-1}.

A confocal Fabry-Perot etalon is used to transfer the listed frequency of an iodine peak to a lithium transition. It is actually a Coherent Model 216 spectrum analyzer with standard 550-650 nm optics. The nominal free spectral range is 300 MHz, while the finesse is about 200. To produce frequency markers during laser scans, its PZT drive is defeated. The transmission of laser light through the etalon is monitored by a Coherent Model 216PP photodiode.

Changes in the ambient temperature and pressure cause the transmission peaks to shift. The condition for transmission is that an integral number of (air) wavelengths

equals the path perimeter in the cavity. For a non-mode-matched confocal cavity with a distance l between the mirrors, the condition for mode number m is

$$m\lambda_m = 4l \tag{4.3.11a}$$

so that the vacuum frequency of this mode is

$$\nu_m = \frac{c}{n\lambda_m} = \frac{cm}{4nl} \tag{4.3.11b}$$

where n is the refractive index of the medium between the mirrors.

If the coefficient of (linear) thermal expansion of the etalon housing is α, then the shift in transmission frequency caused by a temperature change ΔT is

$$\frac{\Delta\nu_m}{\Delta T} \approx -\frac{\nu_m}{\Delta T}\frac{\Delta l}{l} = -\frac{c}{n\lambda_m}\alpha \approx -170 \text{ MHz/°C} \tag{4.3.12}$$

for $\alpha = 3.5\times10^{-7}$/°C [COH86], $\lambda_m \approx 610$ nm, and $n \approx 1$.

The refractive index of air depends on pressure according to

$$n = 1 + \beta P \ , \tag{4.3.13a}$$

where $\beta \approx 3.6\times10^{-7}$/Torr. The change in transmission frequency caused by a pressure change ΔP is

$$\frac{\Delta\nu_m}{\Delta P} \approx -\frac{\nu_m}{\Delta P}\frac{\Delta n}{n} = -\frac{c}{n^2\lambda_m}\beta \approx -170 \text{ MHz/Torr} \ , \tag{4.3.13b}$$

again using $\lambda_m \approx 610$ nm and $n \approx 1$.

A change in temperature of 1°C or a change in pressure of 1 Torr shifts a transmission peak by about half of the free spectral range. Note, however, that the free spectral range is hardly affected at all, because the free spectral range is the *difference* between adjacent mode frequencies:

$$FSR = \nu_{m+1} - \nu_m = \frac{c}{4nl} . \tag{4.3.14a}$$

The change in FSR with temperature is

$$\frac{\Delta FSR}{\Delta T} \approx - \frac{FSR}{\Delta T} \frac{\Delta l}{l} = -(FSR)\alpha \approx -110 \text{ Hz/°C} , \tag{4.3.14b}$$

while the change with pressure is

$$\frac{\Delta FSR}{\Delta P} \approx - \frac{FSR}{\Delta P} \frac{\Delta n}{n} = - \frac{FSR}{n} \beta \approx -110 \text{ Hz/Torr} . \tag{4.3.14c}$$

Using the spectrum analyzer to measure the frequency of a lithium peak relative to an iodine absorption requires that the spectrum analyzer transmissions not drift more than a few MHz during a scan. We accomplish this by placing the etalon in a sealed can, which is itself put inside a temperature stabilized box. The box is made from thick fiber board, and the temperature is maintained with an RFL Industries Model 70A proportional temperature controller. Theoretically, the refractive index of a gas depends on its *density;* inside of a sealed can, the density is nearly constant. The temperature was measured with a thermistor over a three day period; the temperature remained at 36.4 ± .1°C throughout the study. We also made repeated 1.5 GHz scans

with the yellow laser over an iodine line around 615.704 nm, which is very near 3s→50p in lithium. The relative frequencies of four etalon peaks were measured as a function of time; the shifts were ±20 MHz in 2 hours, in rough agreement with the temperature box's stability and Eq. (4.3.12). (Data sets 1986: jul 14, 16-19)

The value of the free spectral range must be known to assign transition frequencies. The procedure is to measure a long spectrum of iodine absorptions and etalon peaks. A typical 15 GHz scan appears in Fig. 4.3.7. We scan the yellow laser by 15 GHz, hop by 10 GHz, and scan again. Each etalon peak is numbered consecutively, with the reddest one assigned zero. The data analysis program described in Sec. 4.5 assigns an interpolated mode number to each iodine peak. Mode number is plotted as a function of peak frequency. A straight line is fit to the data; the slope is the reciprocal of the free spectral range.

The fitting is complicated by the uncertainties in both the assignment of mode number to the iodine peaks, and the quoted uncertainty of the frequency of the iodine peaks in the atlas. The mode number determination is limited by the uncertainty in locating the absorption minima (~0.0002 cm^{-1} from fitting a polynomial to the peak shape) and by the uncertainty in locating the etalon peaks (~0.0005 cm^{-1}, from the laser step size (15 GHz/1024 points)). The quoted uncertainty in the frequency of the iodine peaks is ~0.0005 cm^{-1}. Because the uncertainty in both variables is comparable, the method of effective variance [ORE82] is used to fit the data. An

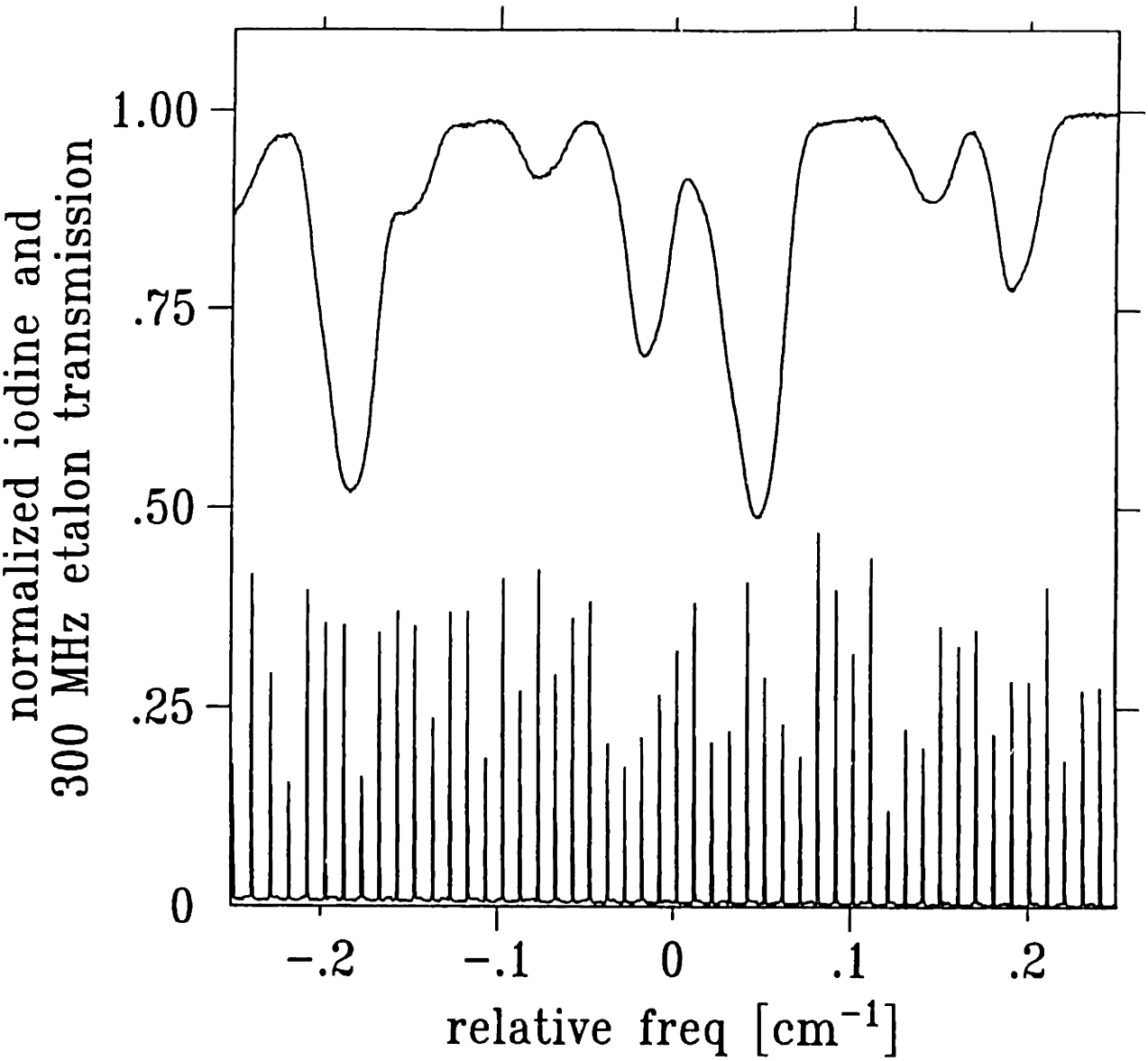

Figure 4.3.7 Yellow laser scan showing the transmission peaks of the ≈300 MHz spectrum analyzer and the corresponding iodine absorptions. (Data file 1987: oct 22.1)

effective (reduced) "chi-squared" is also evaluated.

About 70 iodine lines near 624 nm were studied in an 11 cm^{-1} scan. There were two runs.

Date	Free Spectral Range (MHz)	χ^2 (reduced)
Oct. 22, 1987	298.882(10)	3.3
Nov. 6, 1987	298.922(11)	2.8

Table 4.3.4. The free spectral range of the etalon.

Clearly, the fit isn't too good. The difference in the two results is about 4 times the expected uncertainty, and χ^2 is too big. Examination of the *deviation* from fit as a function of frequency reveals the scatter of points around zero is ~3 times the size of the (effective) error bars, as may be seen in Fig. 4.3.8. The deviation from fit of the same iodine absorption is nearly identical for both data sets. Therefore, though the iodine lines are in the same place both days, it seems that their frequencies are reproducibly inconsistent to a substantially larger extent than their quoted uncertainties would suggest. It is possible that our iodine lines aren't in the same place as those studied by the authors of the atlas, because the cell conditions are not identical. Another possibility is that they were a little too optimistic in their assignment of uncertainty.

For now, the free spectral range of the spectrum analyzer is 298.9(1) MHz. The

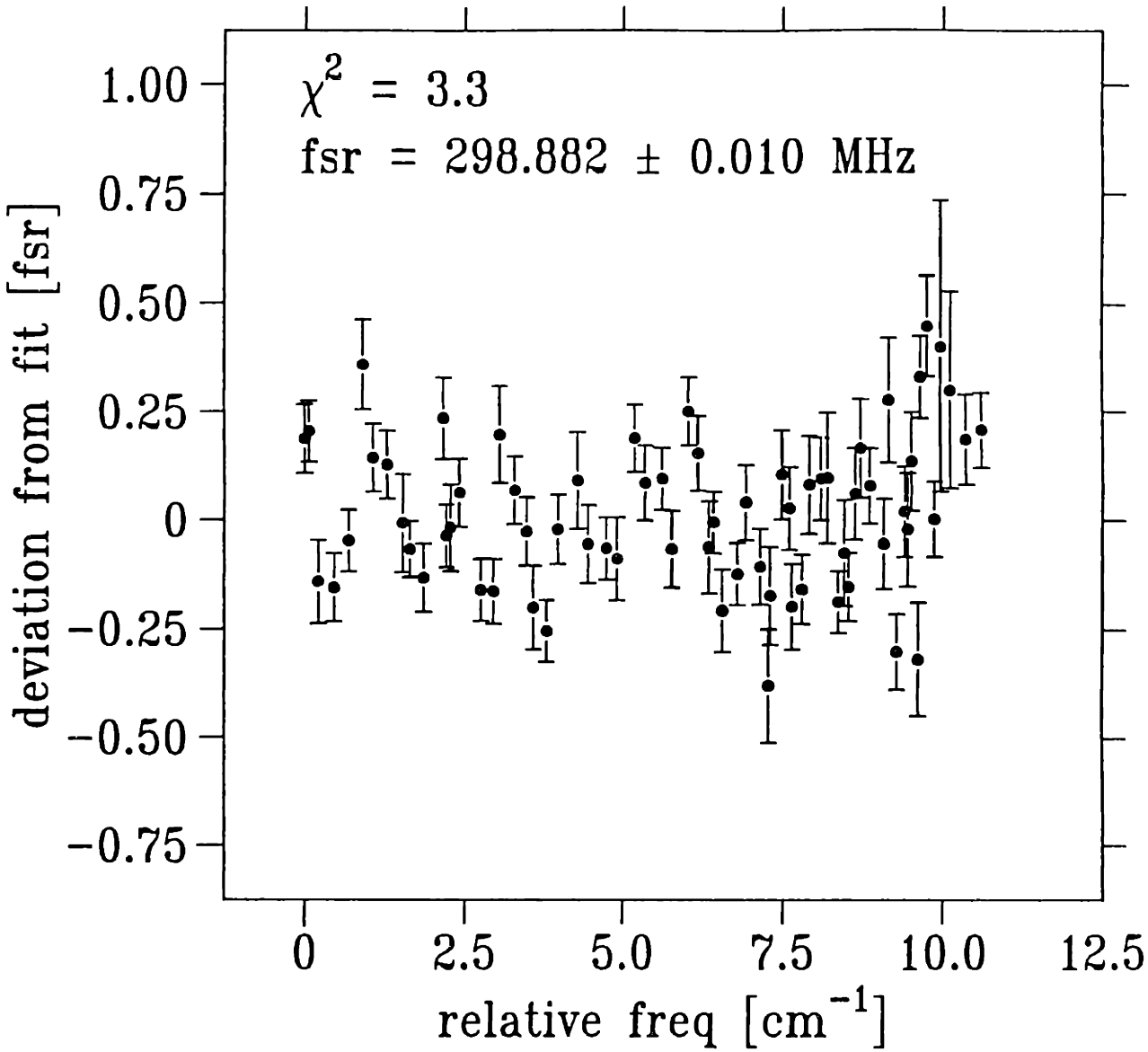

Figure 4.3.8 Deviation from fit to a straight line of mode number as a function of frequency. The error bars are determined from the effective variance method. (Data files 1987: oct 22.1-33)

uncertainty in the frequency of our iodine absorptions is ~0.005 cm^{-1}, which limits the determination of absolute transition frequency.

4.4 Excitation and Detection of Rydberg Atoms

Laser spectroscopy not only requires lasers with well characterized wavelengths, but also some means of detecting that resonance has taken place in the system under study. Since the goal is to determine the energy levels of lithium atoms in a magnetic field, the lasers must probe the atoms inside of the magnet. Each stage of the two-step excitation process must be independently monitored, because both transitions are narrow and both depend on the field size. The first step, 2s $\rightarrow$ 3s, is detected by measuring the accompanying cascade fluorescence. The second step, 3s $\rightarrow$ Rydberg state, is observed by counting the electrons producing during static electric field ionization. Also, the excitation should take place in a region with no electric field, for the sensitivity of Rydberg atoms to electric fields will complicate the spectra.

Interaction Chamber

A great deal of effort went into developing the interaction chamber where the atoms are excited, and a detailed description seems worthwhile. The chamber is made from a cylinder of aluminum approximately 1.6" long and 1.6" in diameter. Aluminum was selected because it is supposed to be a good high voltage material: if a small, sharp region causes a discharge, aluminum will melt into a smoother shape. (The chamber floats at -20 kV.) Also, aluminum is not ferromagnetic, though it is weakly paramagnetic. (Any ferromagnetic hardware could distort the magnetic field at the atoms.) A diagram of the interaction chamber is contained in Fig. 4.4.1. It is

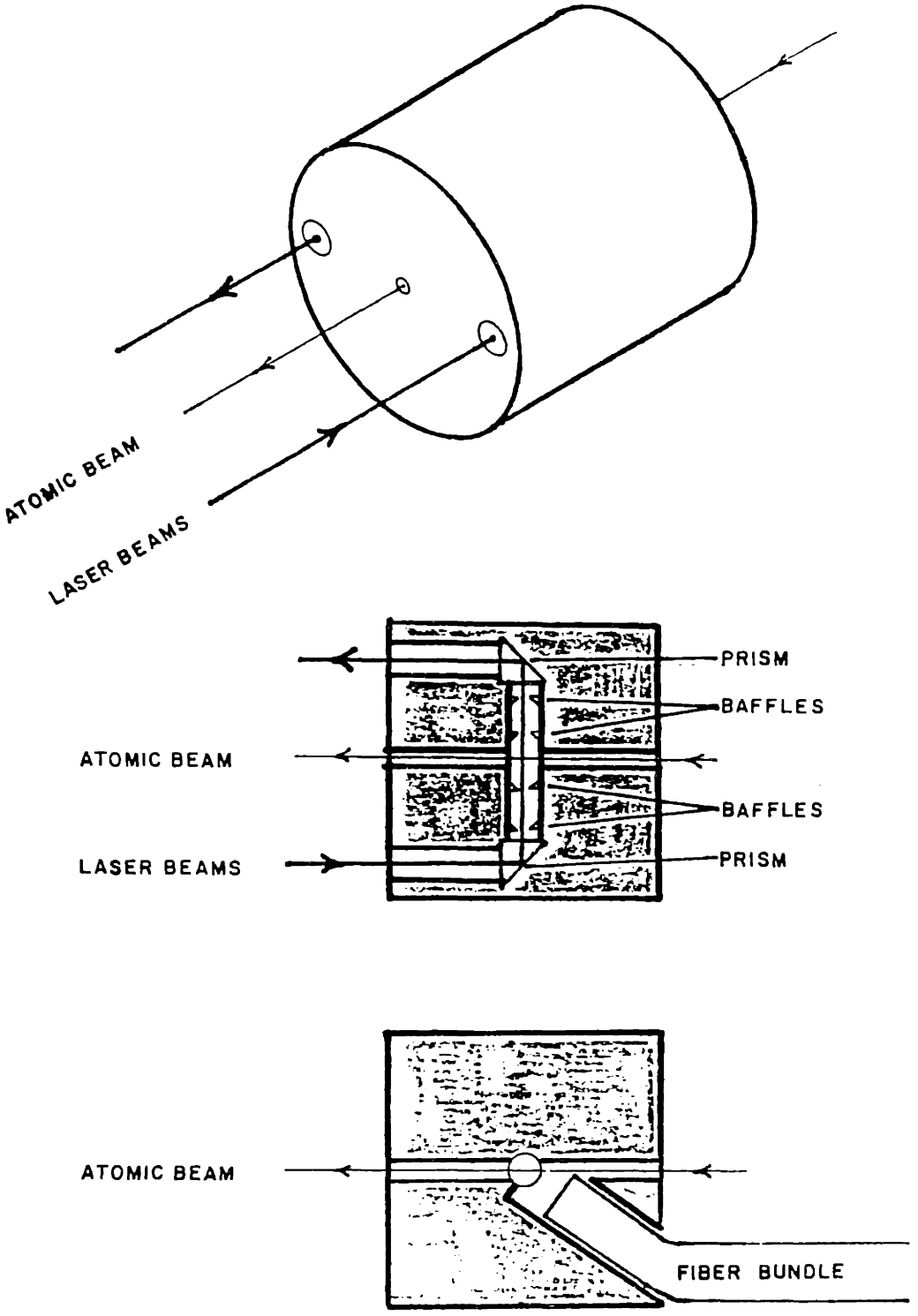

Figure 4.4.1 The Mark IV interaction chamber. It was designed to shield the laser-atom intersection point from external electric fields, and to provide cascade fluorescence and (static) electric field ionization for their respective detectors.

named Mark IV because it is the result of many design principles gleaned from earlier chambers. The main features are the atomic beam hole, the laser beam holes, the prism periscope, fiber bundle hole, the heater and the thermocouple.

The atomic beam hole runs along the axis of the cylinder. Its diameter is 0.150". Electric fields outside of the cylinder do not penetrate significantly down the hole because of the small diameter to length ratio. When used in conjunction with the atomic beam collimating tube, it should not be possible for anything coming out of the oven to hit directly the inside surfaces of the atomic beam hole. The desire is to remove the source of insulating contaminants near where the lasers and atoms intersect.

The laser beam holes are parallel to the atomic beam hole but lie close to the edge of cylinder on the downstream side. They must be large enough to accommodate the converging laser beams without significant scattering.

The laser beams are deflected across the atomic beam by a small prism. A second prism reflects the light away from the interaction region. We find great utility in having the laser beams come back out of the interaction region. First, looking for the apertured transmitted beam is an alignment tool. Second, the unapertured transmitted beam shape can reveal clipping, and therefore usually unacceptably high amounts of scattered light. The prisms are Melles Griot Model 01 PRS 005 right angle glass (BK-7) prisms with square entrance legs (6.4×6.4 mm). The thickness is

also 6.4 mm, and the hypotenuse is not aluminized. We have the legs treated with a CVI Corporation antireflection coating, optimized for 620 and 735 nm. (The CVI coatings have a very high damage threshold, whereas the standard Melles Griot HEBBAR coating was often burned by our focused dye laser beams.) We use prisms because total internal reflection gives very high *broadband* reflectivity as long as the convergence isn't too strong. Dielectric mirrors are generally not good at *both* 735 and 620 nm, while according to Jarbas Castro, aluminum coatings have a magnetic field dependent reflectivity. Also, the aluminum coatings may provide discharge sites.

The prisms are clamped in a tube forming a periscope. The relative angle between the prisms and the periscope axis is fixed by the way the periscope is made; the angle about an axis through the triangular surfaces of the prisms is carefully set with an alignment jig. The periscope has an atomic beam hole, a fiber bundle hole (see below) and four knife-edge baffles along the laser beams (1 mm diam holes) to reduce the scattered light (from the prism surfaces) which gets into the optical fiber bundle. The inside surface is coated with Aqua-dag, from Acheson Corporation. This material is reasonably black, and helps reduce scattered light. It also has good surface conductivity, which helps minimize stray electric fields.

The fiber bundle hole is angled to place the end of the optical fiber bundle close to the laser-atom intersection without blocking the atomic beam. Since the glass fibers are insulators, the end of the hole closest to the periscope contains a Pyrex glass disk

(0.370(5)" diam×1/16" thick, a special order from Esco Products) covered with a conductive, optically transmitting coating (Metavac #7163, which we believe is indium oxide). The disk is cemented in place with Aqua-dag. Again the goal is to reduce stray electric fields. The disk is approximately 0.35" from the laser-atom intersection. Its optical transmission is about 70%.

Stray electric fields are a critical problem. We found that baking the interaction chamber reduces the stray electric field at the start of a run. A 2W, (initially) 100 Ω carbon composition resistor is used as a heater. The temperature is measured with a type T (copper-constantan) thermocouple, monitored by an Omega Model CN310 digital temperature controller. The system has a long time constant (≈6 hours) but reasonably small thermal conductance to the liquid helium dewar (usually filled with LN_2 during baking) so 2-3 W is enough power. A bake of ≈140°C for one day often reduces the stray electric field to less than 0.1 V/cm at the beginning of the run. It takes many hours for the interaction chamber to cool down to near liquid nitrogen temperature. The heater resistance changes with time, usually decreasing before eventually becoming infinite. The lifetime is about 3-4 months.

Collection Optics for Fluorescence

The cascade fluorescence resulting from the two-photon excitation 2s→3s is detected by a sensitive photomultiplier tube. The light travels from the atoms to the PMT via the path indicated in Fig. 4.4.2. Two Edmund Scientific 1/4" diam

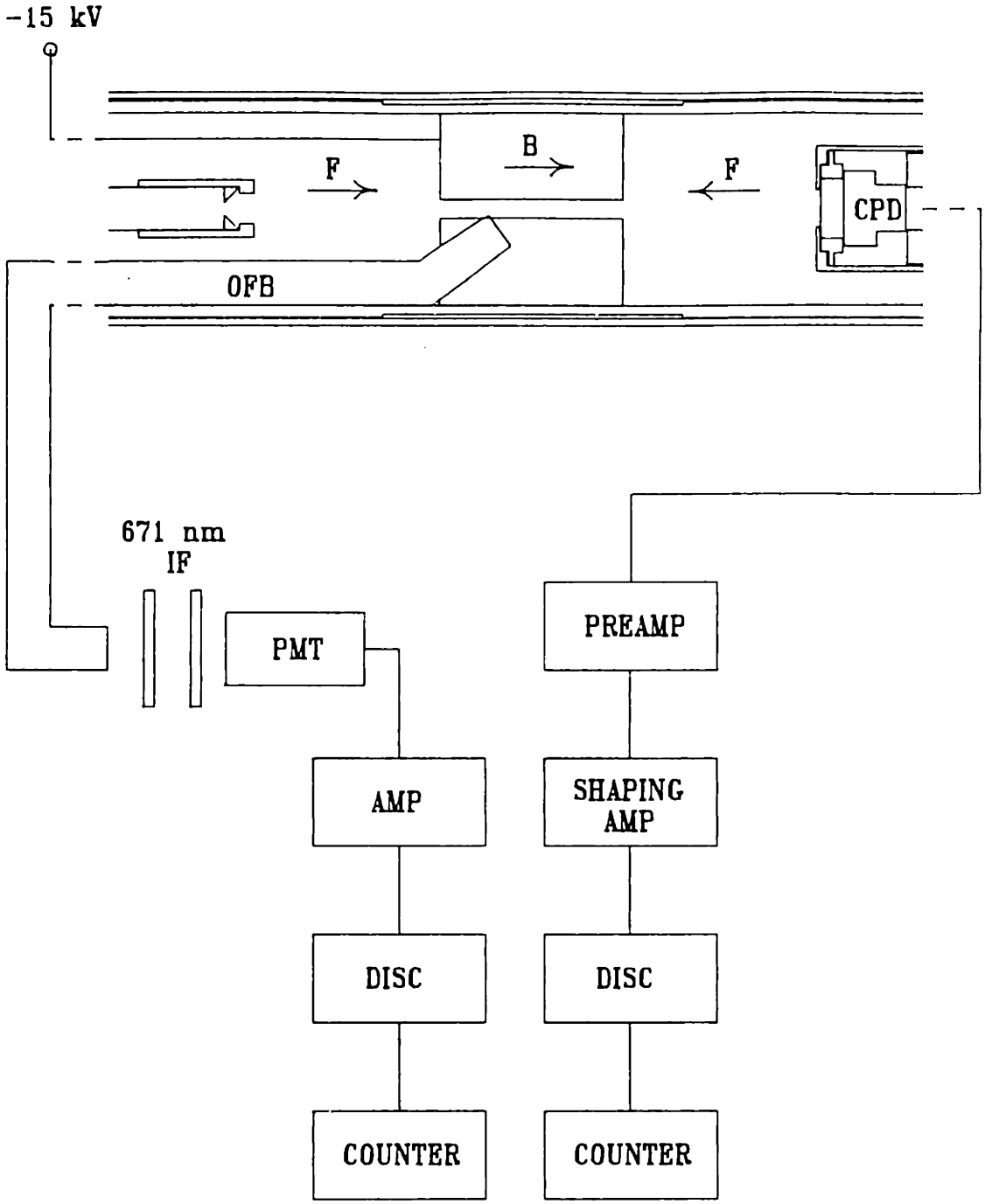

Figure 4.4.2 Detector arrangements. The interaction region is electrically isolated from the magnet bore with a teflon sleeve. The sleeve is thinner around the interaction region to reduce its thermal conduction to the magnet dewar. Cascade fluorescence is collected by the optical fiber bundle (OFB) and transmitted to the PMT via two interference filters (IF). The PMT (photomultiplier tube) is an RCA C31034A-02 with a gallium-arsenide photocathode; the CPD (charged particle detector) is an EG&G/Ortec CR-015-050-100-S surface barrier diode made with cryogenic epoxy.

incoherent fiber bundles, containing 5880 fibers, transmit the light. The bundle between the vacuum window and the photomultiplier tube is a standard 3 foot length. The bundle between the interaction chamber and the vacuum window is modified by removing the steel ferrule and sheath reinforcement. These are magnetic, and the sheath is an electrical conductor which would prevent us from floating Mark IV to high voltage. The ferrule is dissolved with concentrated, boiling hydrochloric acid. The fibers are epoxied together at the appropriate length, and a new aluminum (originally Delrin) ferrule is slipped over the wet epoxy. After drying, the fiber is cut and polished with an aluminum oxide polishing wheel. A new sheath of black heat-shrink tubing protects the fibers. With care, the modified bundle yields 56% transmission, which compares quite favorably the the factory produced 50% transmission. When placed in the fiber bundle hole of the interaction chamber, the end of the bundle subtends about 3×10^{-2} fractional solid angle from the laser-atom intersection point.

The two bundles are joined at a vacuum window, which is made from a microscope slide "torr-sealed" to an aluminum cylindrical fitting. This structure fits over the standard ferrule on the bundle outside of the chamber, and is sealed by a Cajon Ultratorr fitting. The inside standard ferrule fits into a similar brass structure soldered to the flange which also contains the ultratorr fitting. The two bundle ends are separated by only the microscope slide, and the assembly is vacuum and light-tight.

Although there are baffles around the laser beam, the periscope is coated with black Aqua-Dag, and the bundle is at right angles to the laser beam, a substantial amount of laser light still gets into the optical fiber bundle. Interference filters are used to screen out laser light at 735 nm and 610-630 nm, while passing the desired fluorescence: 671 nm (2p→3s). We use two Ealing 671 nm 1" diam, "3 cavity" filters, one after the other. The bandwidth is about 10 nm, the peak transmission is about 50%, and the rejection of light we do not want is about 10^4.

The lore of interference filters has two tales. The first is that any light getting through an interference filter will be at the transmission wavelength because that light is fluorescence of the plastic used in the filter. Therefore, a second filter will not reject anymore background light, but only attenuate signal (and background) light by 50%. However, we found that the signal to background is increased using two filters instead of one, though it decreased using three instead of two. The transmission of 735 nm light through the two filters is probably 10^{-7}-10^{-8}; it's difficult to say. The second tale concerns tuning the transmission peak of interference filters by changing the angle of incidence away from normal: the peak shifts blue. The light exiting the bundle will generally not be normal to the filter, so light blue of 671 nm has much higher transmission than light red of 671 nm. Our two lasers operate at 735 nm and 610-630 nm. The red laser is more powerful; about 1W or 4×10^{18} photon/sec goes through the interaction chamber. The corresponding PMT counting rate is about 50(20) cps. The

yellow laser is less powerful; about 0.1W or 3×10^{17} photon/sec goes through the interaction chamber. The corresponding PMT counting rate is 3(1) kcps. The red rejection is 1000 times higher.

Angle tuning also selects which of the two cascade transitions, 3s→2p (813 nm) or 2p→2s (671 nm), to monitor. If we had used 3s→2p, both lasers would cause strong background, even though deep red interference filters generally have higher specified (normal incidence) rejection. In fact, we have two Corian 810 nm interference filters that we tried and then relegated to a cabinet.

The light coming out of the bundle is imaged on the PMT photocathode with two Melles Griot aspheric lenses, the first 18 mm focal length (24 mm diam) and the second 26.5 mm focal length (30 mm diam). Both are coated with HEBBAR antireflection coating. Although the f numbers are small, the lenses are aspheric and the images are reasonable. We experimented with a HeNe laser, the fiber bundle, and a dead PMT to help us find the appropriate distances between the optics. The lenses and filters are held in a cylindrical chamber, one end of which has a Cajon Ultratorr fitting for the bundle, the other of which is mounted on the gated PMT housing. O-ring seals are used; the system is light-tight.

Photon Detection

The photomultiplier tube is an RCA Model C31034A-02, which uses a reflection

mode photocathode. The photocathode is GaAs:Cs-O, the most red-sensitive type. The photocathode also has a very flat response over a wide wavelength range; the suffix "A" means that it is red enhanced. The specified responsivity is 80-95 mA/W over 350 to 860 nm. The flatness is not very important to us, but we need the high quantum efficiency at 671 nm – around 15%. The "-02" suffice means low dark noise; this also is not very important to us, but it is nice that the dark background is only 4(1) cps. The tube is mounted in a Products for Research Model TE-104-RF cooled, shielded housing, which operates at -30°C. The bias is -1648 V, provided by a Bertan Model 315 high voltage power supply. The pulses are enhanced by a Modern Instrument Technology (MIT) Model F-100T amp-discriminator, whose output is nearly TTL. The computer's counter board tabulates this signal. Please refer to Fig. 4.4.3 for an example of cascade fluorescence.

The overall collection efficiency should be approximately

$$
\begin{aligned}
E_{PMT} = \quad & (\text{fractional solid angle of fluorescence subtended by fiber}) \\
& \times(\text{conducting disk transmission}) \times(\text{inside bundle transmission}) \\
& \times(\text{vacuum window transmission}) \times(\text{outside bundle transmission}) \\
& \times(\text{lens transmission}) \times(\text{filter transmission}) \\
& \times(\text{PMT quantum efficiency}) \\
\approx \quad & (3\times10^{-2})(0.7)(0.56)(0.92)(0.5)(0.96)(0.25)(0.15) \\
\approx \quad & 2\times10^{-4} \, . \qquad (4.4.1)
\end{aligned}
$$

When the oven operates around 700°C, and 1.2 W of red laser power is focussed to a 51(3) μ waist, we see about 2×10^{4} cps of fluorescence (adding up both hyperfine

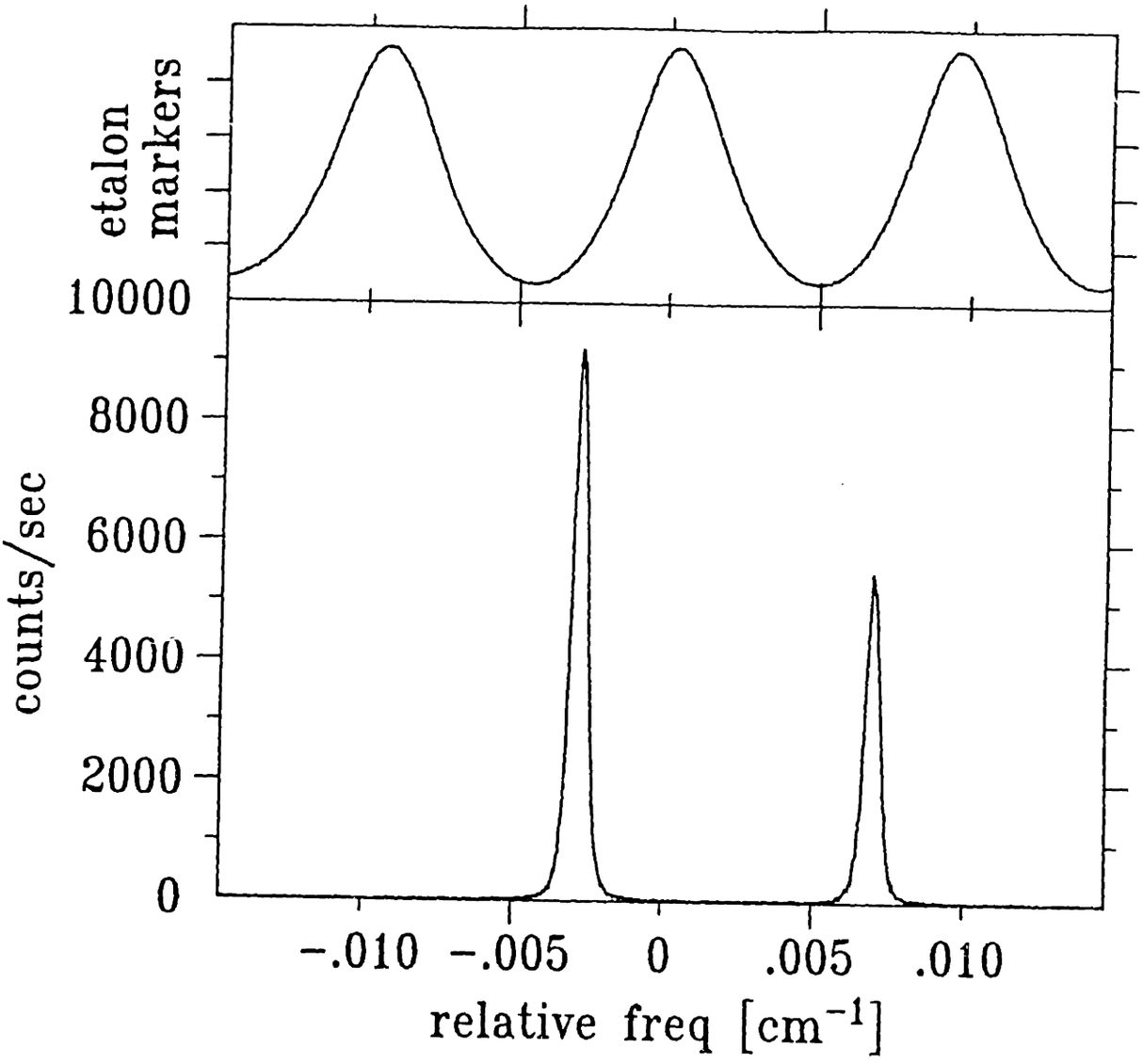

Figure 4.4.3 Cascade fluorescence accompanying the two photon transition in ^{7}Li. The 300 MHz frequency markers are broad because of the low finesse of the spectrum analyzer at this wavelength. The laser power was 1.2 W focused to a 51(3) μ waist, and the tube oven temperature was 735°C. The dichroic mirror was positioned to give symmetric lines, as described in Sec. 4.3 (Data file 1988: apr 19.10).

transitions), so we estimate that the red laser causes the lithium atoms to emit approximately 1×10^{8} cascade photons/sec.

One may obtain a semiclassical derivation of the two-photon excitation probability [KAW87]. The system under consideration is shown in Fig. 4.4.4. The total cascade fluorescence rate from a collimated atomic beam with radius r, density n_I, and speed v, excited by a perpendicular Gaussian laser beam of power P and waist w, is given by

$$S = n_I(2r\pi w^2)\,\frac{\omega_{Reff,0}^2}{\gamma_3}\,\psi(x,\eta) \tag{4.4.2a}$$

where the effective Rabi frequency (on-axis) is

$$\omega_{Reff,0} = \frac{<3\,|\,\vec{d}\cdot\hat{\varepsilon}\,|\,2><2\,|\,\vec{d}\cdot\hat{\varepsilon}\,|\,1>}{4\hbar^2\Delta_o}\,\frac{4P}{\pi w^2 c\,\varepsilon_o}\,, \tag{4.4.2b}$$

and the Voigt function is defined by Davies and Vaughan [DAV63]:

$$\psi(x,\eta) = \frac{1}{\eta\sqrt{\pi}}\int_{-\infty}^{\infty} dy\;\frac{\exp\{-[(x-y)/\eta]^2\}}{1+y^2} \tag{4.4.2c}$$

where

$$x = 4\Delta/\gamma_3\,, \tag{4.4.2d}$$

and

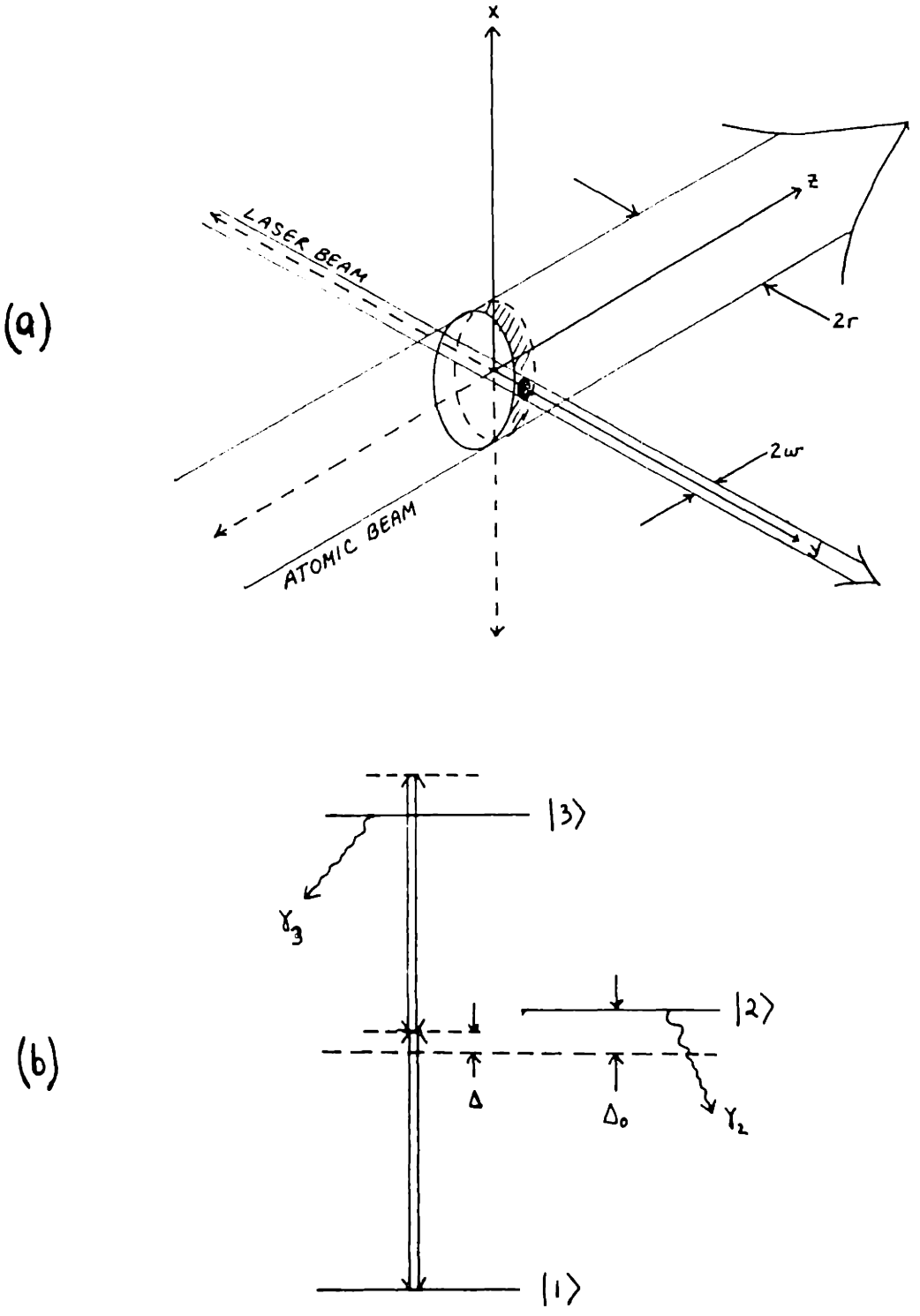

Figure 4.4.4 (a) Schematic representation of the red laser – atomic beam interaction volume. (b) Energy level diagram, defining several symbols used in the text. The "energy defect" is $\Delta_o = \omega_2 - (\omega_3 - \omega_1)/2$; the laser detuning is $\Delta = \omega_L - (\omega_3 - \omega_1)/2$. The spontaneous emissions rates of states $|3\rangle$ and $|2\rangle$ are γ_3 and γ_2.

$$\eta = 4v/\gamma_3 w \ . \qquad (4.4.2e)$$

Other terms are defined in Fig. 4.4.4. Table 4.4.1 presents the relevant parameters for the lithium 2s→3s transition.

Laser field:

$$\vec{E}(\vec{r},t) = E_o \cos(ky - \omega t)\exp[-(x^2+z^2)/w^2]\hat{z} \ .$$

The polarization: $\hat{\epsilon} = \hat{z}$.

Total time-averaged power: $P = \frac{\pi}{4} w^2 c \varepsilon_o E_o^2$

Atomic states of Lithium:

$$|1> = |\, 2s \ \ m=0> \ , \ |2> = |\, 2p \ \ m=0> \ , \ |\, 3> = |3s \ \ m=0>$$

$$< 2 \,|\, \vec{d}\cdot\hat{z} \,|\, 1 > = 4.12(-ea_B)/\sqrt{3}; \ \ \gamma_2 = 3.80\times10^7 \ \text{sec}^{-1}$$

$$< 3 \,|\, \vec{d}\cdot\hat{z} \,|\, 2 > = 3.01(-ea_B)/\sqrt{3}; \ \ \gamma_3 = 3.42\times10^7 \ \text{sec}^{-1}$$

$$\omega_{Reff,0} = (131 \ \text{cm}^2/\text{Wsec})P/w^2$$

$$\Delta_o = 2.45\times10^{14}\text{sec}^{-1}$$

Table 4.4.1 Useful parameters for the two-photon transition of lithium. The radial matrix elements are evaluated with the method of Zimmerman et al. [ZLK79].

Substituting the experimental values for laser beam power (1.2W), waist (51μ), atomic beam speed (2×10^5cm/sec) and radius (1 mm) yields a signal size of

$$S = n_I(5.1\text{cm}^3/\text{sec}) \ . \qquad (4.4.2f)$$

For 700°C, Table 4.1.2 indicates that the density of atoms in the interaction chamber should be $n_I = 9.3\times10^8$atoms/cm^3, so the total signal should be about 5×10^9sec^{-1}: too

high by a factor of 50. As with the absorption measurement discussed in Sec. 5.2, we suspect that the density is not as high as the tube oven thermocouple reading would indicate. Alternatively, the optical collection efficiency may be over-estimated. In either case, we're not too far off as these things go. Clearly a good photomultiplier tube is needed to see the cascade fluorescence from an atomic beam.

Apart from finding the two-photon transition and helping adjust the laser focus, cascade fluorescence also provides the means of stabilizing the red laser on the two-photon transition. Figure 4.4.5 shows a block diagram of the feedback system. The output of the amp-discriminator feeds a frequency-to-voltage converter, which feeds a PAR JB-5 lock-in amplifier. The lock-in output is integrated and run into the external scan input of the red ring laser. The lock-in is operated in internal mode; the reference signal is summed just after the integrator, so the laser is frequency modulated. Thus the derivative signal coming out of the lock-in when the laser is tuned to the resonance is accumulated by the integrator, which holds the laser on the line. Note that when the laser frequency is at line center, the lock-in output is zero, but the laser needs the accumulated error voltage to be at the proper frequency. The dither frequency is 32 Hz and the time constant is 3 sec; it only responds to slow changes in laser frequency. We usually set the modulation amplitude to be about one half of the FWHM of the resonance. The system is quite stable and keeps the laser frequency fixed for $\simeq$6 hours, until the output of the "lock box" pegs at $\pm$15 V.

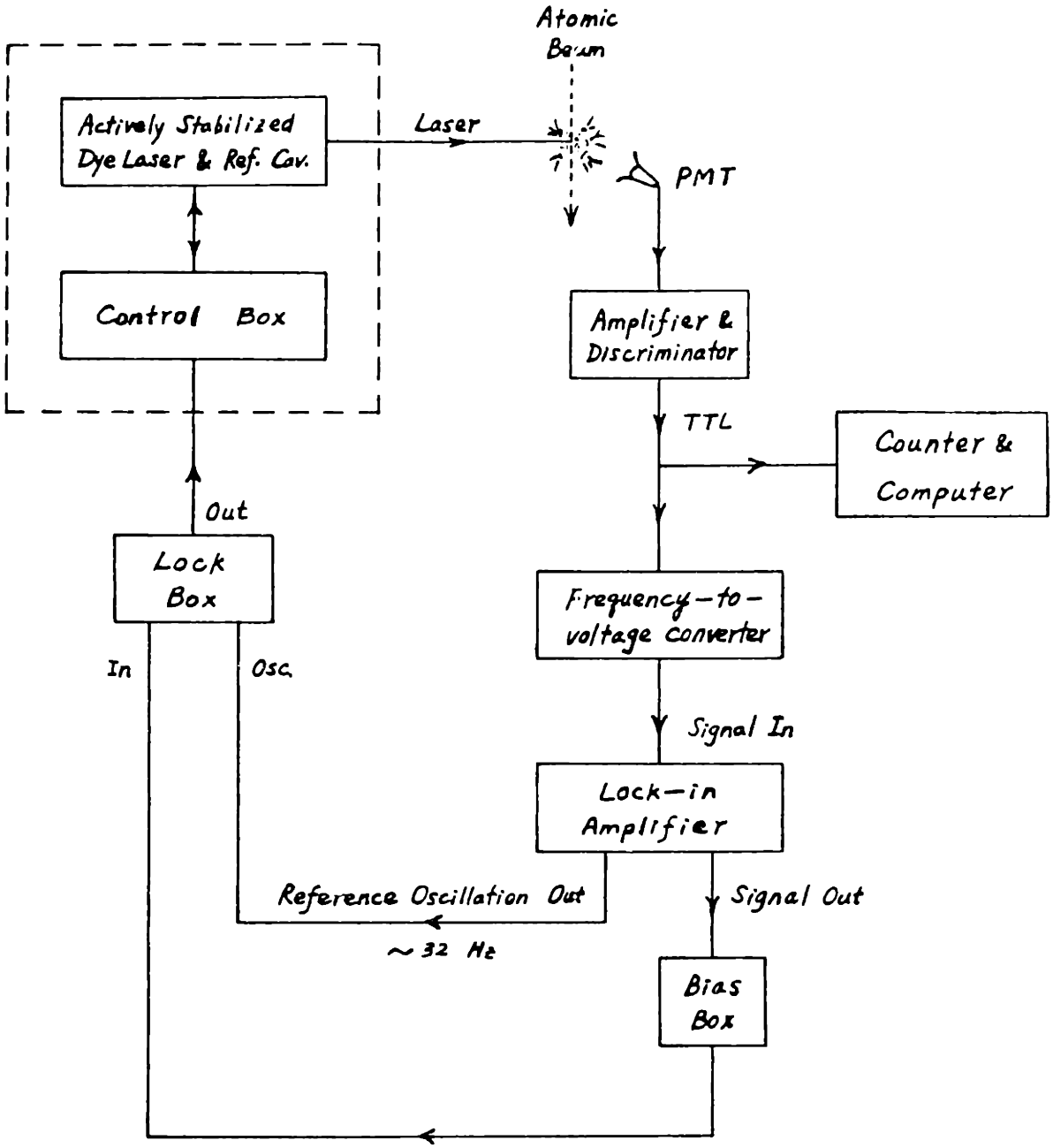

Figure 4.4.5 Block diagram of the slow stabilization system for the red ring laser.

Figures 4.4.6 and 4.4.7 are electrical schematics of the frequency-to-voltage converter, and the lock box.

Field Ionization

One of the most sensitive detection methods for Rydberg atom spectroscopy is (static) electric field ionization. Its basic principle: if an atom is in a Rydberg state, the valence electron is weakly bound to the ionic core, so a relatively small electric field can rip the electron out of the atom. This *doesn't* happen when the atom is in a low energy state. Some of the details of the process are discussed in earlier papers from our group [LKK78]. The simple saddle point model works quite well for alkali metal atoms, where the ionic core mixes the hydrogenic states. The model finds the local minimum in the potential energy of Coulomb plus uniform electric fields:

$$V(\rho, z) = -(\rho^2+z^2)^{-1/2} + Fz \ , \tag{4.4.3a}$$

$$V_{MIN} = V(0, -1/\sqrt{F}) = -2\sqrt{F} \ . \tag{4.4.3b}$$

When the atomic energy is greater than this minimum value, the electron can escape classically so the atom ionizes rapidly; if the atomic energy is lower, ionization is quite slow. (A more refined model uses the effective atomic potential, including the centrifugal contribution. For $m=0$ states, there is no difference.) The simplest application of this model just equates the unperturbed atomic energy to this minimum value, and finds the characteristic critical field:

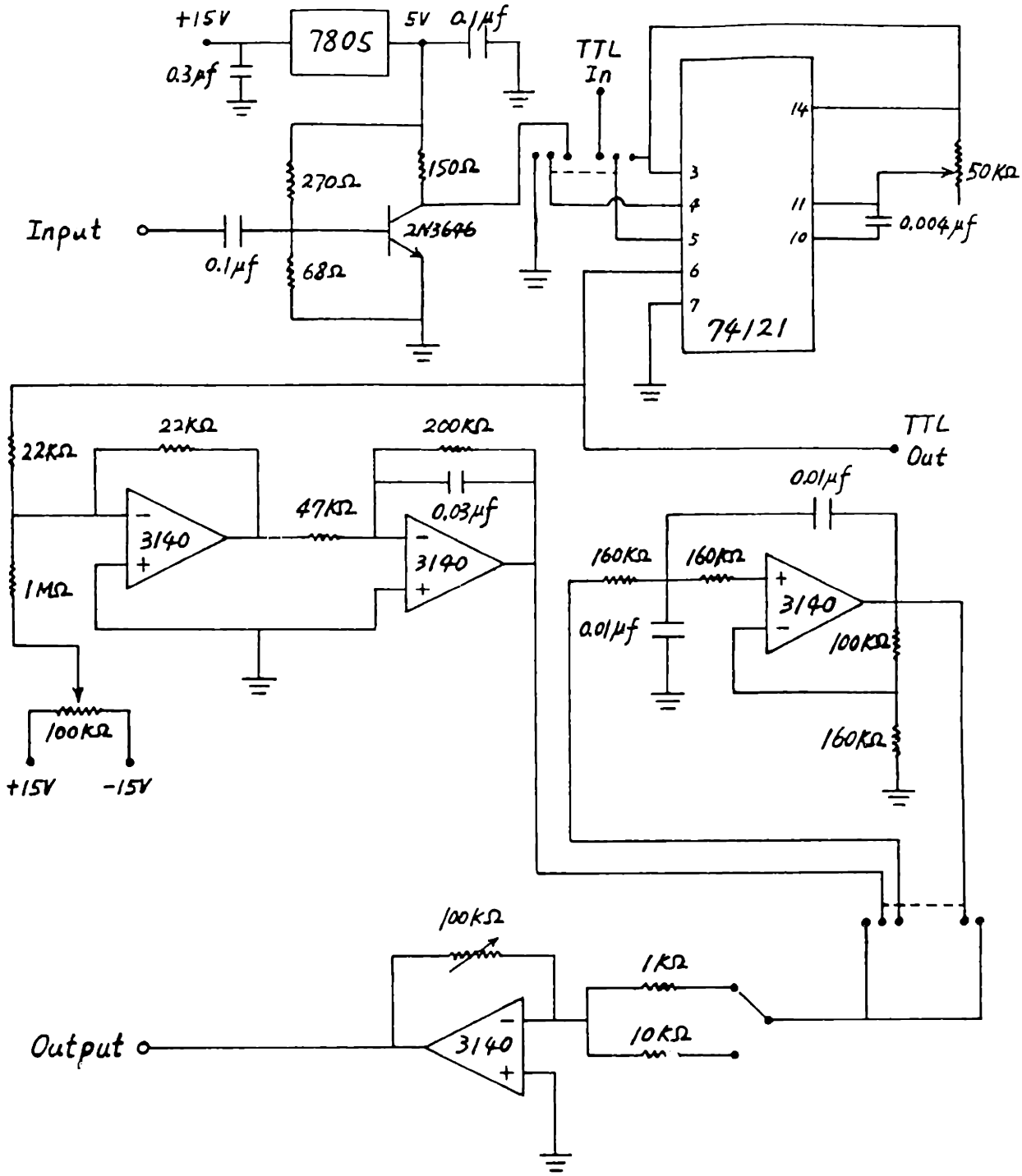

Figure 4.4.6 Schematic diagram of the frequency-to-voltage converter. The analog output also drives an analog meter for convenient signal optization. The TTL output goes to a secondary counter for visual display.

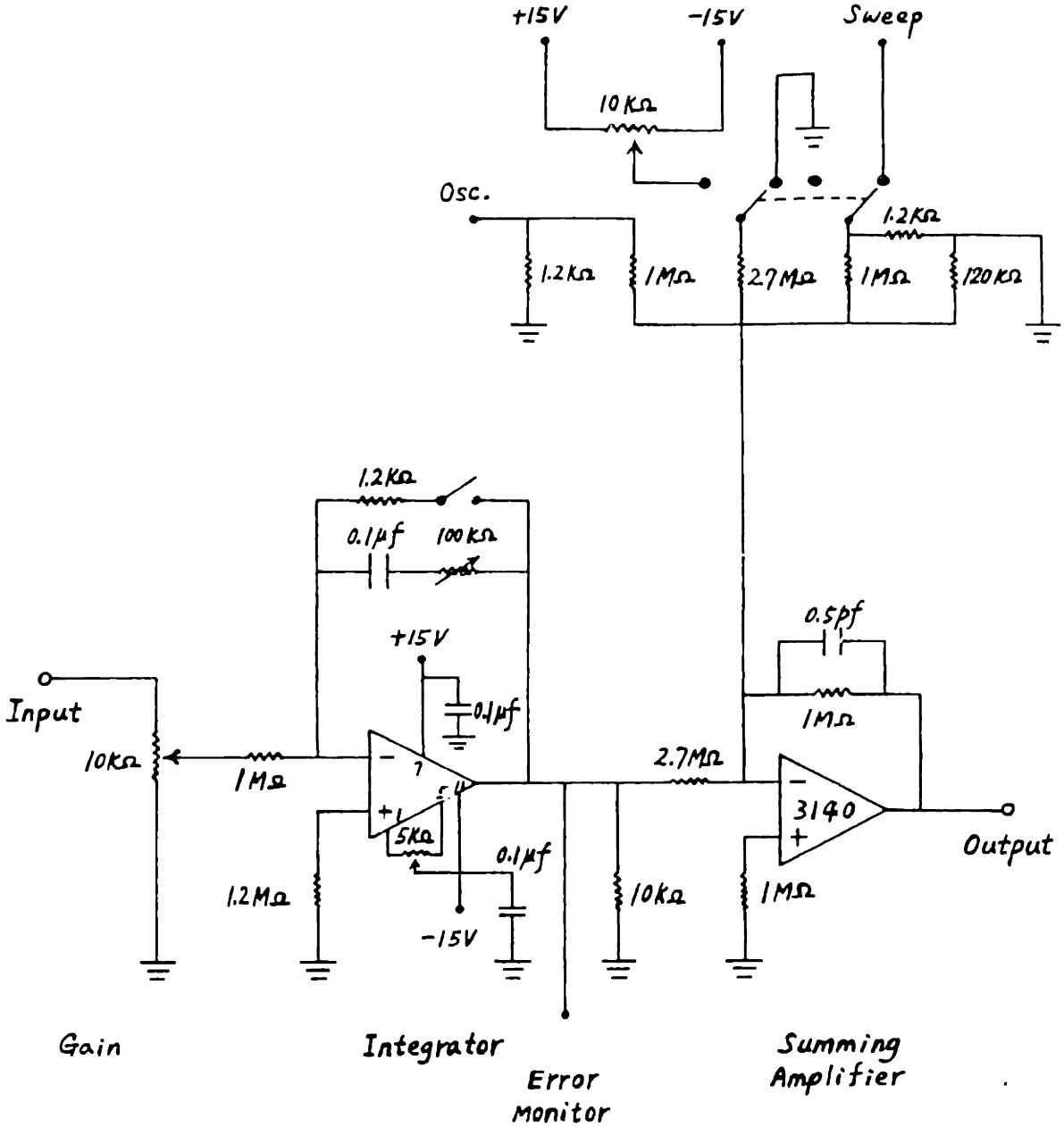

Figure 4.4.7 Schematic diagram of the lock-box. It was designed by Prof. John Thomas of Duke University. The bias control is used to set the laser to the desired frequency. The gain and damping controls have somewhat mysterious behavior, but the basic idea is to turn up the gain with zero damping until the laser frequency begins to oscillate, and then to turn up the damping until the oscillation stops.

$$-\frac{1}{2}(n^*)^{-2} = -2\sqrt{F_c}\ , \tag{4.4.4a}$$

$$F_c = \frac{1}{16}(n^*)^{-4}\ . \tag{4.4.4b}$$

(A better model would incorporate the shift in atomic energy caused by the Stark effect.) The critical field is a sensitive function of n^*, and hence may often be used for state identification. This is called "selective field ionization."

In our experiment, we simply want to detect an atom if it is in a Rydberg state. For the 20p state of Li, the critical field is about 2 kV/cm. Please refer to Fig. 4.4.2. The interaction chamber is electrically isolated from the magnet bore by a teflon sleeve; the interaction chamber is floated to -15 to -20 kV, using a Hipotronics Model R-30-B high voltage power supply, and the charged particle detector is at ground. The distance between the detector and the end of the interaction chamber is about 3.3 cm, so the field is around 4.5 to 6.1 kV/cm. Any Rydberg state higher than $n^* = 18$ will be ionized.

Electron Detection

The very high voltage requirement is due to the type of charged particle detector we use. Charge multiplication devices such as electron multiplier tubes, channeltrons, and microchannel plates do not operate in high magnetic fields. The reason is that electrons spiral tightly around magnetic field lines. Multiplication occurs when the

primary particle impacts on a metal surface and ejects secondary electrons; the motion of the primary and secondary particles cannot be in the same direction, so some aspect of the multiplication will be stopped by the magnetic field.

We detect the electrons with a solid state detector: a surface barrier diode. The diode is reverse biased, and electron-hole pairs are created as the detected particle loses energy in the depletion region (3.6-3.7 eV/pair in silicon [EG&G80]). These electron-hole pairs are separated by the applied electric field in the silicon and are collected by the appropriate electrode. The particle motion is over a very small distance (~1 mm), and in our system, the motion is parallel to the magnetic field. The problems are that there is a certain threshold energy required for the detected electrons to reach the depletion region, and that the energy deposited in the detector must be larger than the equivalent detector noise.

To assure that nearly every electron is detected, we need to operate the accelerating voltage at about -22 kV. We spent many years learning how to float Mark IV to this level without having discharge or substantial electron background. Unfortunately, sometimes high voltage is still a problem. There are some basic principles:

1. Avoid sharp corners. The interaction chamber has rounded edges, and is polished to a mirror finish. It can take weeks to polish the chamber using emery paper, a Dremel motor tool, Carborundum polishing powders, and jewelers rouge to achieve a bright and shiny Mark IV. The finish degrades with time.

2. Avoid insulator edges. Discharges can also start if the insulating material has sharp edges against the floating conductor. Mark IV has a snug fit inside of the teflon sleeve, but the inside is quite smooth.

3. Direct all electrical connections away from the detector. A certain number of sharp edges at cable terminations is unavoidable, and these may have low electron emission rates without actually making discharges. Therefore, putting all connections on the end of Mark IV *not* facing the detector reduces the electron background. We have four wires which connect Mark IV to a feedthrough. Two are bare 18 gauge wires insulated with 1/4" OD, 1/8" ID teflon tubes; these wires operate the heater during baking, and one provides HV while detecting Rydberg states. The other two wires are teflon coated thermocouple wires, also insulated with the same kind of heavy teflon tubing. When HV is applied, all the leads are at high potential; the feed through need only stand off HV to ground. We use a black plexiglass flange with steel rods torr-sealed in place. The rods are surrounded by a large diameter PVC pipe for additional discharge prevention, on both sides of the flange. Note that we cannot bake or read the thermocouple when HV is applied.

4. Operate at low pressure. Generally -12 kV is the maximum HV when the system is at room temperature and the pressure is $\approx 2\times10^{-5}$ torr. Under these conditions, the background events observed with a scope on the detector amps are "big"; multiple electrons hitting the detector at the same time. We believe that gas molecules are ionized, and produce a small shower. When the dewars are cooled with LN_2, the pressure drops to $1\text{-}2\times10^{-6}$ torr, and the high voltage can be set to -20 to -22 kV with a background that appears to be mostly small, single electron events at a rate of 10-30 cps.

The detector itself is an EG&G/Ortec Model CR-015-050-100-S surface barrier diode. The "C" means that the connector is BNC; while the "R" means "ruggedized" which implies for us that the detector is rather insensitive to the scattered laser light. The "-015-" is the specified resolution of alpha particles in keV. A more important figure for us is the noise width, which decreases with the alpha resolution. For this

detector the noise width is specified to be 7 keV, and that's the best available from EG&G/Ortec. The next number, "-050-", indicates that the active area is 50 mm^2. This is bigger than we need, but it is the smallest standard value for the ruggedized series. The last number says the depletion depth, or the minimum sensitive depth of the detector, is 100 μ. Since we just count low energy electrons, this parameter isn't particularly relevant. These detectors are designed for nuclear physics experiments where the energies are >0.1 MeV (and the counting rates are <0.1 Mcps) so a large depth may be needed to collect all of the energy. It's all we can do to get the electrons into the depletion region. Finally, the suffix "-S" indicates that the detector is made with cryoepoxy, so that it can be repeatedly cycled between room and LN_2 temperatures. Cooling reduces the detector background noise caused by thermal fluctuations, and slightly improves the collection efficiency.

Recently, we purchased a Model E50-20-100B surface barrier diode from Paul Downey and Company. Its package size, connector, active area, and depletion depth are the same as the EG&G/Ortec detector; the specified alpha resolution is 20 keV, so the detector could be noiser, but in fact isn't. It is NOT constructed for cryogenic operation, but we've cycled it several times to LN_2 without noticeably degrading its performance. (Also, the EG&G/Ortec detector costs $730, whereas the Downey detector costs only $180.)

Signals from the surface barrier diode are amplified by the system shown

schematically is Fig. 4.4.2. The first stage is a Canberra Model 2004 charge sensitive preamp. The background noise of this device depends on its input FET and the input capacitance. Minimizing the cable length and using RG-62/U air-spaced coax (13.5 pF/ft) helps reduce the capacitance. The detector must be biased to sweep effectively the electrons or holes toward the active electrode, and to reduce the detector capacitance [EGG80]. For the EG&G/Ortec instrument, the bias is -100V; for the Paul Downey detector, the bias is +100V. The leakage current of the reverse-biased diode is typically 0.15(5) μA. The preamp has a bias resistor of 110 MΩ (nominal), so its voltage drop is appreciable. The bias comes from a Bertan Model 315 high voltage power supply.

For pulse counting, the preamp is followed by an amplifier and then by a discriminator. We use an EG&G/Ortec Model 440 Selectable Active Filter Amplifier (SAFA), which is designed to work with charge sensitive preamplifiers by shaping the pulses to have short tails. The discriminator is an EG&G/Ortec Model T105/N Dual Discriminator, which has a threshold value of -0.050 to -5.000 volts. The preamp is inverting, so when the EG&G/Ortec (Paul Downey) detector is used, the preamp output pulses are negative (positive). Since the discriminator only responds to negative pulses, the output of the preamp is connected to the positive (negative) input of the SAFA. The discriminator input is connected to the prompt output of the SAFA, in unipolar mode. The detector data sheet suggests a shaping time of 0.5 μsec. When

the gain is set to ×16, the discriminator threshold is set to -0.070V (-0.065V). This setting is somewhat of a compromise; it reduces much of the background, but also misses some single electron events if the magnitude of the accelerating potential is less than 22 kV. The discriminator output is a fast negative pulse, which is lengthed to 31 nsec with an EG&G/Ortec Model 425 delay line. This pulse is converted to TTL (for counting by the computer) and an analog voltage (for on-line signal optimization) by another frequency-to-voltage converter. (See Fig. 4.4.6) As an example, Fig. 4.4.8 shows the field ionization signal as the yellow laser is tuned near the 3s(F=2) to 40p transition. Also recorded are iodine reference absorptions, and 300 MHz frequency markers.

The system dead time is nearly 1 μsec. This was measured by sending a train of two short pulses into the preamp's test input. The delay between the two pulses is decreased until the output counting rate drops to one-half of the true pulse rate. (Data set 1985: mar 12). Therefore the system saturates: when the output counting rate is 100 kcps, we miss about 10% of the events.

"Antisaturation" also occurs when the magnitude of the accelerating potential is too low. Then, many single-electron events are missed because the pulse size is smaller than the discriminator setting. Double-electron events (two electrons entering the detector within the charge collection time, ≈10 nsec [EG&G80]) have pulse heights twice that of single-electron events, and are more likely at higher counting rates.

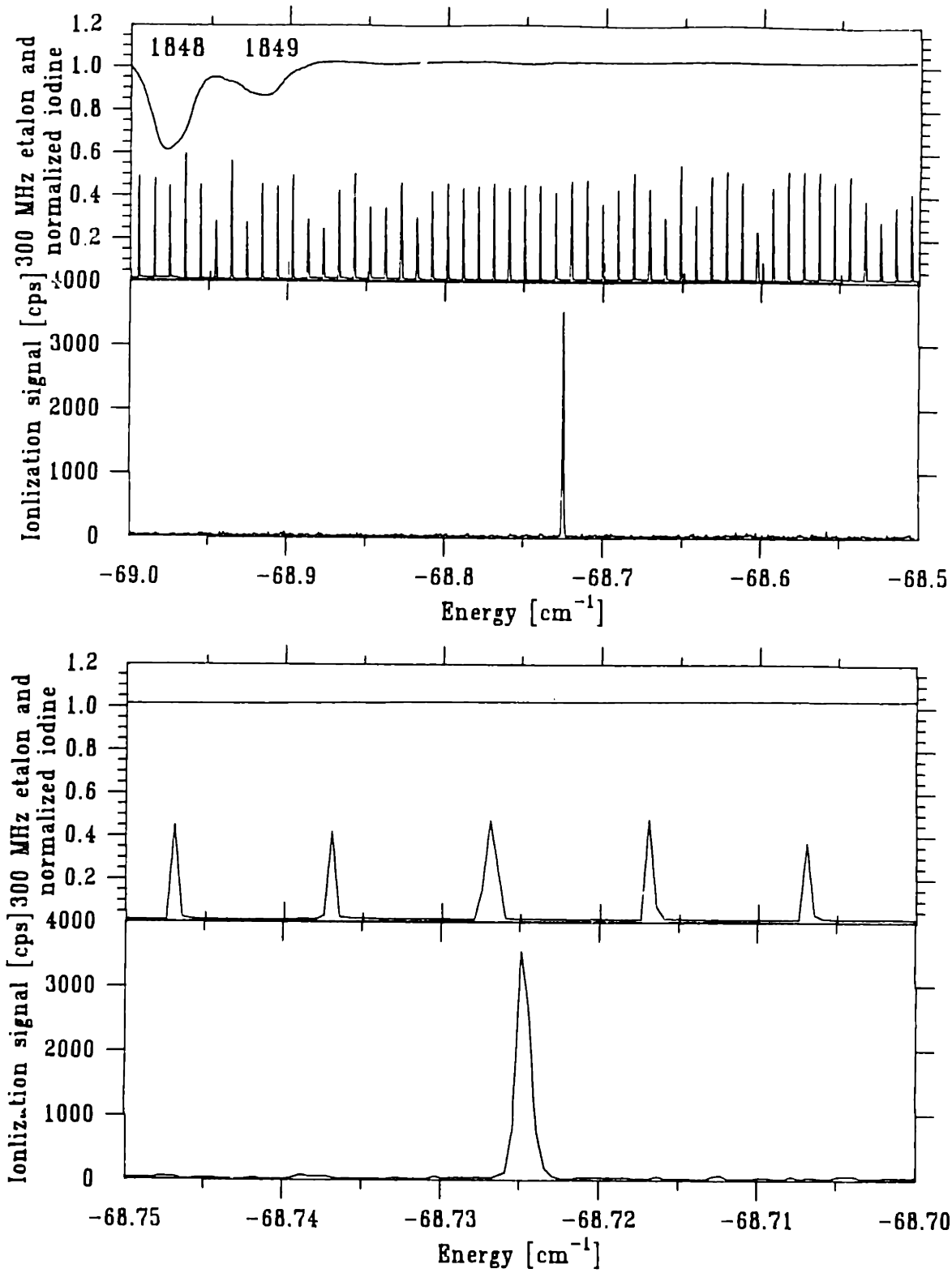

Figure 4.4.8 Field ionization signal showing the 3s to 40p transition. Also displayed are the iodine absorptions [GEL78] and the etalon frequency markers. Two frequency scales are shown. The laser yellow power was 40 mW focussed to a 64(3) μ waist; the oven temperature was 690 °C. The FWHM of the transition is about 25 MHz. (Data file 1986: apr 23.26)

Since we simply count pulses which are bigger than the discriminator threshold setting, the system is not exactly linear with the excitation rate of Rydberg atoms.

The collection efficiency of the charged particle detection system, E_{CPD}, is difficult to assess. We think that all Rydberg atoms which get into the accelerating field will be ionized and that all of the resulting electrons will hit the detector, but the quantum efficiency of the surface barrier diode is questionable. Certainly it depends on the accelerating potential. We measured the efficiency using a technique that involves decreased cascade fluorescence. First the cascade fluorescence rate is measured when the second laser is off resonance. Then the 3s→25p transition is driven strongly enough that we can see a decrease in the cascade fluorescence rate. This is compared with the counting rate on the charged particle detector. Let $r(x)$ mean the rate of x.

yellow laser off resonance: $r(PMT) = E_{PMT}\, r(3s)$ (4.4.5a)

yellow laser on resonance: $r'(PMT) = E_{PMT}\, r'(3s)$ (4.4.5b)

$$r(CPD) = E_{CPD}\, r(25p) \tag{4.4.5c}$$

$$r(25p) = r(3s) - r'(3s) \tag{4.4.5d}$$

$$E_{CPD} = E_{PMT}\, \frac{r(CPD)}{r(PMT) - r'(PMT)} \tag{4.4.5e}$$

We had only -13 kV for the accelerating potential, and measured (Data set 1986: mar 26)

$$r(PMT) = 11.4 \text{ kcps} \tag{4.4.5f}$$

$$r'(PMT) = 9.9 \text{ kcps} \tag{4.4.5g}$$

$$r(CPD) = 97 \text{ kcps}\,, \tag{4.4.5h}$$

so

$$E_{CPD} \approx 65 E_{PMT} \approx 1\times 10^{-2}\,. \tag{4.4.5i}$$

where E_{PMT} is taken to be 2×10^{-4} (see Eq. (4.4.1)). Increasing the accelerating potential increases the counting rate of Rydberg atoms, but then saturation becomes appreciable. Normally, we attenuate the yellow laser so that the counting rate is around 20-50 kcps.

Stray Electric Field

The most significant problem in this experiment is the presence of a stray electric field in the interaction chamber. It has been mentioned many times throughout this chapter. The field ultimately limits the usefulness of the experiment.

Rydberg atoms are strongly affected by external fields – that fact is both their strength and weakness. On the strength side, the interaction between an atom and a magnetic field can be pushed into untested regimes. On the weakness side, a small

electric field drastically changes the overall character of a spectrum by causing twice as many levels to appear, shifting isolated levels, and changing anticrossing sizes. The charm and curse of high resolution laser spectroscopy are that we see all of these.

Most devastating is that we can't get rid of the stray electric field. While we have made progress in reducing it, we cannot control it. We don't really understand its origin.

The stray electric field is most evident when the magnetic field is zero. Figure 4.4.9 shows the field ionization signal near the 3s(F=2) to 76p transition. The peak is not simply the 76p state, but rather it involves the projection of the 76p state onto the entire n=76 "Stark manifold". Individual states are not resolved because the stray field is inhomogeneous. The width of the manifold is proportional to the stray field magnitude. From the first order Stark effect in hydrogen, the width is (see Eq. (3.3.3))

$$\Delta\nu \simeq (3.84\ \text{MHz/V/cm}) n^2 F \ . \qquad (4.4.6)$$

This applies when the states are "well-mixed", so that the first-order Stark effect dominates. Note that the 76s state is visible, although far removed from the manifold. The direction of the stray field can be determined by rotating the yellow laser polarization until the 76s state is minimized; then the laser polarization is perpendicular to the stray field. Ever since we installed the conducting-disc over the optical fiber bundle, the field direction has been horizontal, essentially parallel to the atomic beam and the magnetic field.

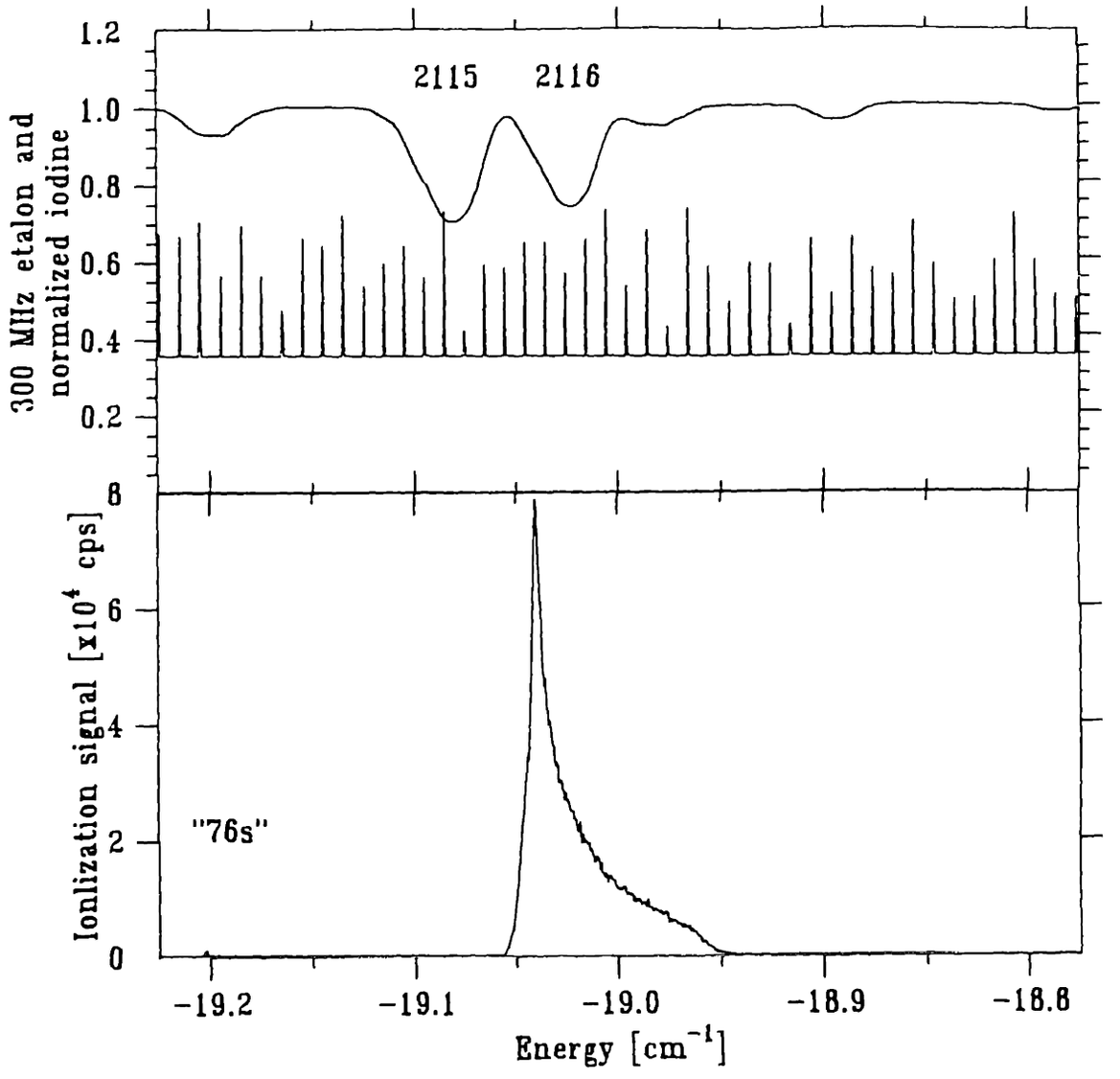

Figure 4.4.9 Field ionization signal of the n=76 manifold. The stray electric field is about 0.138(3) V/cm for this scan. Note the presence of the "76s" state. (Data file 1987: nov 29.10)

The field magnitude is not constant. After baking the interaction chamber, the field starts out small and builds up as the atomic beam passes through it. A history of stray electric field appears in Fig. 4.4.10. This particular set of data involved misaligning the tube oven with respect to the beam collimator tube. (See Sec. 4.1) With constant temperature, the beam *flux* stays constant, but the beam *current* is smaller when it is clipped by the apertures. The rate of field increase seems to be related to the current.

The rate of field increase doesn't seem to be depend on the rate of ionization. Again referring to Fig. 4.4.10, the field increase rate is independent of whether or not Rydberg atoms are made in between scans.

The fact that a low temperature (150°C) bake reduces the initial electric field suggests that some surface effect is the source of the field. Perhaps water is carried in by the atomic beam and forms an insulating layer which holds charge. Using lithium which was never in mineral oil, cryotrapping the oven manifold, and installing the beam collimate tube seem to have no effect on the field build-up rate. The best we've done is to bake long enough so that the initial field is low, and run the oven at low temperature so that the rate of increase is low. Perhaps a Mark V interaction chamber will have all of its surfaces far away from the laser-atom intersection point: that might help reduce the stray electric field.

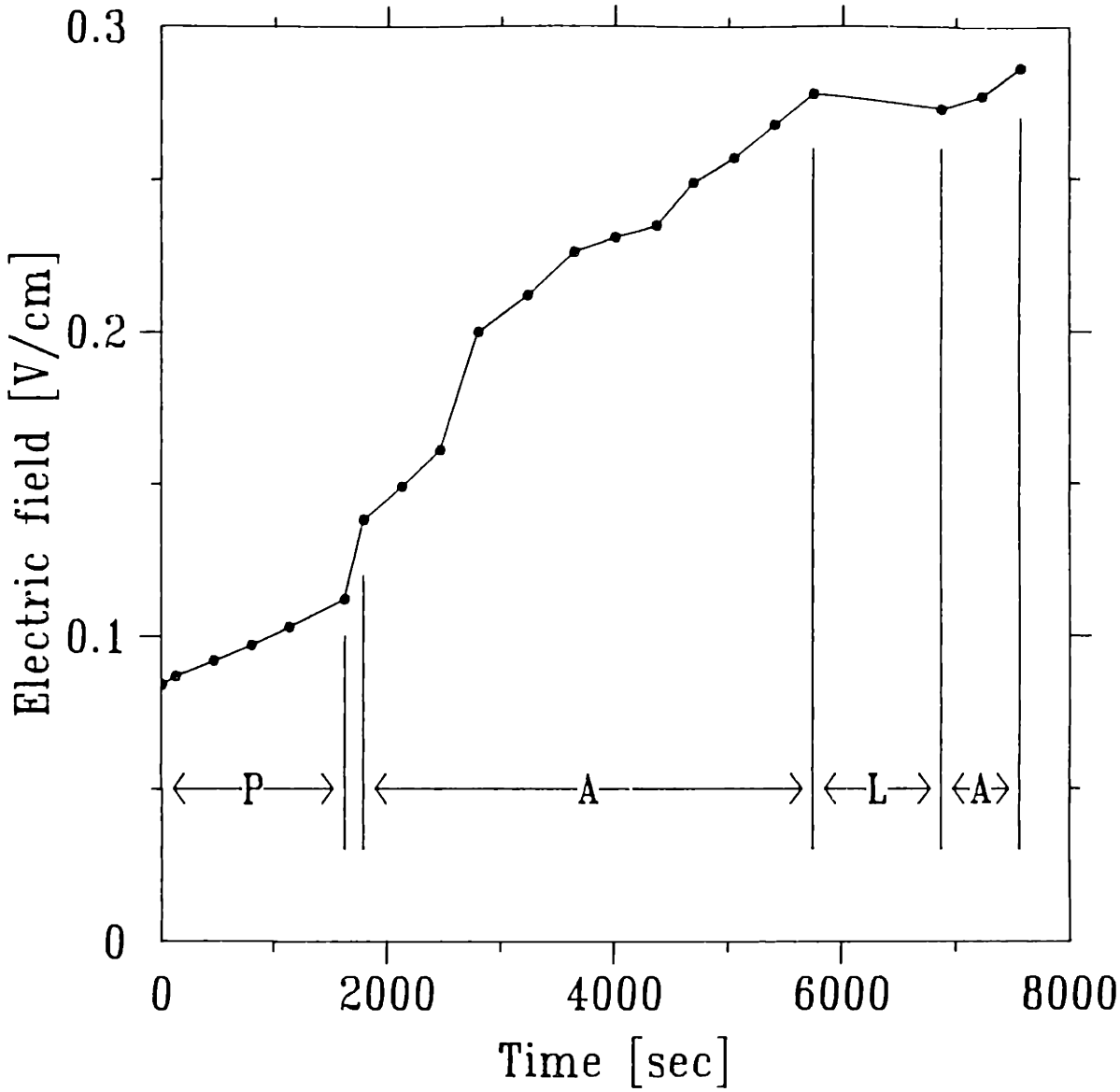

Figure 4.4.10 Stray electric field history. The tube oven was partially misaligned (P), aligned (A), completely misaligned (L), and finally aligned (A) with respect to the beam collimator tube. (Data files 1987: nov 29.2-26)

4.5 Data Acquisition

Data acquisition is under the control of a DEC 11/73 microcomputer. We've gone through several stages, starting with a DEC 11/02 acting as a satellite computer to the lab's old DEC 11/34, and later a Charles River Data Systems 11/23. Over the years, George Welch has developed wonderfully useful and elaborate data-taking software. Here only a few features are noted.

Recorded Information

The computer scans the yellow (3s to Rydberg p) laser by applying a D/A voltage to the laser's external scan input. The state of various detectors are recorded as the laser is tuned. Cascade fluorescence and field ionization are tabulated by counters. Yellow laser power, iodine cell transmission and normalization, and spectrum analyzer transmission are monitored by photodiodes whose outputs are read by A/D's. The field ionization signal may be divided by the cascade fluorescence and the yellow laser power so that relative transition strengths may be observed without the complication of fluctuations in the atomic beam current or either laser's power.

At the beginning and end of a scan, several parameters are recorded. A GPIB (IEEE-488) interface reads the Philips counter in the wavemeter (giving the yellow laser frequency to $1\text{-}2\times10^{-6}$), and the Keithley 197 DMM on the Hall generator (giving a local value of the magnetic field). The magnet current is also measured with

A/D's by reading the voltage across a (0.0096 ohm) resistor in the GE magnet supply, and the voltage across a resistor in the Kikusui trimming circuit. These parameters help assess the magnet's short term stability.

During a scan, the computer halts the 300 MHz spectrum analyzer sweep (so that the frequency markers are fixed), and the wavemeter (whose motor makes a little noise on the charged particle detector).

Resolution versus Scan Width

Both the A/D and D/A's have twelve-bit resolution. This means that the laser can be set to 4096 different frequencies, or laser points. However, accumulating five channels of data at 4096 points for each scan is somewhat impractical. Most scans have 1024 data points. At each data point, the laser spends 1/4 of the measurement time at the four corresponding laser points. To determine the channel value at each data point, the counters are summed; the A/D's are averaged. The averaging helps display very narrow features such as the spectrum analyzer transmission peaks. Usually the laser scan width is 15 GHz; the laser points are 3.7 MHz apart. The laser frequency jitter is about 1 MHz, so the frequency domain is not covered completely. Many spectral features are sufficiently narrow that only a few data points form the peak. It is unlikely that one of the data points will be at the peak center, so narrow etalon transmissions often have a spread of heights. Basically the resolution is limited to the data point spacing, about 15 MHz. Of course, if a particular peak needs to be

studied in detail, the laser scan width can be decreased. When we study the cascade fluorescence of the two-photon transition, for example, the scan width is 1 or 2 GHz; the data point spacing is 1-2 MHz. (See Figs. 4.4.3, 5.4.4, and 5.4.5.)

All of this points out a problem in the experimental design: the desire is to take long scans with high resolution. Normally, these two goals are contradictory, but in some experiments such as ours, both are needed. The 1024 data points fit reasonably on a single sheet of paper; 15 GHz is a reasonable scan width which won't miss any features. But if we want to scan 10 cm^{-1} (300 GHz), we take 30-15 GHz scans and overlap them. Sometimes we'll produce a scroll that's 20 feet long. Though crude, this is the best way we have found to display a lot of high resolution data – much of which is empty space, because the resonances are far apart.

This problem is not unique to us. Coherent, Inc. makes a version of the ring dye laser called an Autoscan (Model 699-29), which automatically produces high-resolution scans over a width of ~100 cm^{-1}. Each scan's data almost fills a floppy disk. The data may be plotted on a scroll. Robert Field, MIT Professor of Chemistry, justified the expense of his 699-29 by estimating how many inches/year of the *Journal of Molecular Spectroscopy* could be published.

Perhaps a future data acquisition program will proceed in two steps. The first would be a coarse scan, which would roughly locate spectral peaks. Then the program would automatically perform a high resolution scan around each peak. This might

solve the data storage problem, but not the display problem.

The major goal of data analysis is the assignment or location of unknown peaks relative to the location of known peaks. A computer program assigns the index point to the center of a peak by fitting an eighth-order polynomial to the data, and then finding the position of zero derivative. By counting the 300 MHz frequency markers between a known (iodine) peak and an unknown (atomic) peak, the absolute frequency of a transition is determined, minimizing the effect of scan non-linearity. Thus a long scan may be reduced to a set of numbers: the location of line centers in absolute frequency. At present, the absolute frequency can be assigned to ≈150 MHz (0.005 cm^{-1}); the relative uncertainty in the location of peaks within one 15 GHz scan is ≈30 MHz (0.0001 cm^{-1}).

As described in Sec. 4.2, we use the n=21, k=19, m=±1 states of lithium to measure the magnetic field. The procedure is to set the magnet to some fixed value, scan over the m=+1 state, and then over the m=−1 state. (See Sec 6.1.) The energy difference is due solely to the paramagnetic interaction; the splitting is about 1 cm^{-1}/T. (See Table 3.1.1 for more accurate conversions.) For B>0.5 T, the m=±1 states are too far apart to be recorded in one scan. Therefore, we must rely on the iodine cell to provide the absolute frequencies, and then subtract those values. As explained above, the uncertainty in the absolute frequency determination is about 0.005 cm^{-1}, so the uncertainty in the difference frequency is about 0.007 cm^{-1}, which would lead to an

uncertainty in field of about 70 gauss. To reduce this uncertainty, we scanned the yellow laser continuously, with overlapping 0.5 cm^{-1} scans, (see Sec. 4.3) from 16,029 to 16,039 cm^{-1} while recording iodine absorptions and etalon frequency markers. (Data files 1988: jan 21.22-55) This allows us to assign the *relative* frequencies of the iodine peaks in the vicinity of the 3s $\rightarrow$ 21p transition to about 0.0005 cm^{-1}, and thus find the frequency difference between the $m=\pm 1$ states to about 0.001 cm^{-1}. That corresponds to a field determination of around 10 gauss. The stability of the magnetic between the two required scans limits the determination slightly, so we report the total uncertainty as about 20 gauss.

Normalization of Field Ionization Signals

The field ionization signal magnitude depends on the transition strength, the red and yellow laser powers, the atomic beam flux, and the dimensions of the interaction volume, as determined by collimation of the atomic beam and the foci of the laser beams. We want our data to show only the first factor. The atomic beam collimation and the laser focusing are generally constant. To reduce the effect of fluctuations in the other parameters, we normalize the signal with the following procedure.

Let

A = PMT background: red and yellow lasers, and room and oven light,
B = PMT background: red laser, and room and oven light,
C = PD voltage: yellow laser, corresponding to the power used in A,
a = averaged PMT signal at each data point,
c = averaged PD voltage at each data point,
m = measured ionization signal at each data point,
n = normalized ionization signal at each data point.

Then the normalized ionization signal is

$$n = \frac{m}{\left[\frac{a-[B-(A-B)(\frac{c}{C})]}{10^4 \text{ cps}}\right]\left[\frac{c}{10 \text{ volts}}\right]} . \qquad (4.5.1)$$

The dimensions of A, B, a, m, and n are cps; those of C and c are volts.

The first factor in the denominator divides out the population of the 3s state, by correcting the PMT signal for the background light. This removes the effect of fluctuations in the red laser power and the atomic beam flux. The factor is relative to 10^4 cps, the order of magnitude of the PMT signal.

The second factor in the denominator divides out the yellow laser power. Assuming the transition is not saturated, this removes the effect of changes in the yellow laser power which occur during laser scans. The factor is relative to 10 volts, the order of magnitude of the output of the photodiode amplifier, as set by the gain switches (see Fig. 4.3.5) for a given yellow laser attenuation.

The PMT signal, m, is smoothed at each data point by taking the arithmetic mean of the PMT signal at the nearest 20 data points. Roughly speaking, this corresponds to increasing the measurement time by a factor of 20, typically from 50 msec to 1 sec. This reduces the statistical noise. The factors A, B, and C are taken with 10 sec measurement times at the beginning or end of a data set.

Chapter 5. LITHIUM SPECTROSCOPY

The preceding chapters have set the stage for performing high-resolution laser spectroscopy on an atomic beam of lithium in a magnetic field. The present chapter contains the specific details about the lithium spectrum in zero magnetic field which are needed to predict the behavior of lithium in a large magnetic field. After a brief note on the discovery of lithium, the literature of lithium's electronic structure is discussed and evaluated. Then the parameters of fine and hyperfine structure are compiled. Finally, the paramagnetism of electronic and nuclear magnetism is presented, including its impact on our spectra.

5.1 Historical Note

Lithium (from the Greek work *lithos*, meaning stone) was discovered by the Swedish chemist Johann August Arfvedson (or Johan Arfwedson) (1792-1841) in 1817. He was a student in the laboratory of the well known Swedish chemist John J. Berzelius, and began his scientific apprenticeship determining the composition of the minerals manganous oxide (MnO) and manganosic-oxide (Mn_3O_4). Arfvedson's next assignment was to determine the structure of petalite, a mineral which had been discovered near Utö, Sweden in 1800 by the Brazilian scientist and statesman Jozé Bonifai'cio de Andrada e Silva. Chemical analysis revealed the presence of an element which was similar to sodium and potassium (discovered in 1807 by Humphrey Davy), but with lower atomic weight. Apparently Prof. Berzelius deserves much of the credit for the discovery of lithium, but he allowed the research to be published by Arfvedson alone [WEL68, pp. 457-471].

The fundamental atomic properties of lithium are that the atomic number is 3 and the ground state configuration is $(1s)^2 2s$. The optical spectra are determined by the states available to the (outer) valence electron. Hydrogen and lithium energy levels are compared in Fig. 5.1.1.

The lithium principal transition $2p \rightarrow 2s$ reveals a striking crimson color, apparently first seen in the flame tests of lithium salts by C.G. Gmelin in 1818 [WEL68, p. 463]. Johan Balmer's last publication (1897) contained some of the

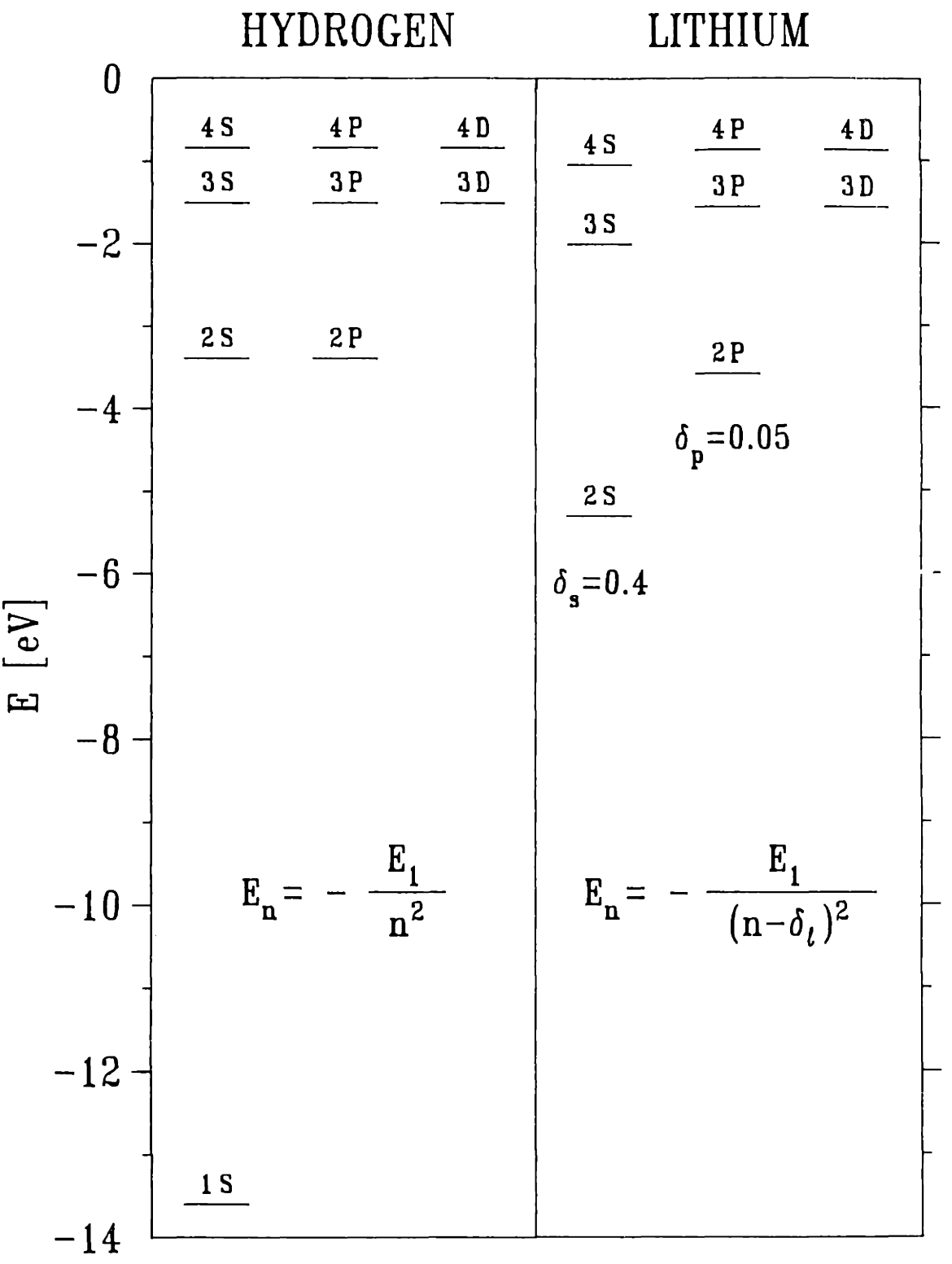

Figure 5.1.1 Comparison of hydrogen and lithium energy levels. Here, E_1 is 13.6 eV.

lithium spectrum and an empirical formula to predict it [ABB84, p. 17].

5.2 Electronic Structure

A detailed knowledge of the atomic energy levels is a prerequisite for undertaking precision laser spectroscopy. Without this, precise comparison with theory would be impossible. Experimentally, there is little hope of even finding the desired level without an accurate data base. As discussed below, an error of 0.02 cm^{-1} can make a troublesome difference.

The Literature

The reference for lithium electronic states which has been most useful is that of Johansson [JOH59]. Johansson measured 23 red and infrared lines in the fluorescence of a hollow cathode discharge. Meissner, Mundie, and Stelson [MMS48] measured 19 (mostly) visible lines in the fluorescence of an atomic beam excited by electron bombardment. After applying the correction pointed out by Edlén and Lidén [EDL49, MMS49], Johansson assigned energies to 30 levels relative to the ground state (for a total of 31 levels), with an overall uncertainty of ± 0.005 cm^{-1}. After averaging over fine structure intervals, the remaining 26 levels (including the ground state) were used to determine quantum defects in a Ritz formula (see Sec. 3.1) for each of the ^2S, ^2P, ^2D, and ^2F series. Of course, the series limit must first be determined in order to assign the binding energy of the levels. Johansson found this limit using the ^2D series because it is so hydrogenic that a two-term Ritz formula is adequate:

$$^2D:\ \delta = \delta^{(0)} + \delta^{(1)}t \tag{5.2.1}$$

where

$$\delta = n - n^*,\ t = (n^*)^{-2} = T(n,l)/R_{Li}\ . \tag{5.2.2a,b,c}$$

Here δ is the (total) quantum defect, T is the (positive) binding energy, n is the principal quantum number, n^* is the effective principal quantum number, and R_{Li} is the reduced mass Rydberg *apparently* calculated using the naturally occurring (abundance weighted) nuclear mass known at the time. Specifically, Johansson took

$$R_{Li} = 109{,}728.64\ \text{cm}^{-1} \tag{5.2.3}$$

The constants $\delta^{(0)}$, $\delta^{(1)}$, and the series limit (see Fig. 5.3.1)

$$L = T(2,0) = W(n,l) + T(n,l)\ , \tag{5.2.4a,b}$$

where W is the energy relative to the ground state, were determined from the 3d, 4d, 5d, and 6d levels. There are four equations (that is one W for each d-level) and 3 unknowns; the unknowns were selected in such a way that the differences in calculated and measured energies are zero for the 3d and 4d levels and of equal magnitude and opposite sign for the 5d and 6d levels. This results in the following series limit:

$$L = 43{,}487.150(5)\ \text{cm}^{-1}\ . \tag{5.2.5}$$

Using this result, Johansson found the following quantum defects:

$$^2S:\ \delta = 0.399{,}491{,}74 + 0.029{,}483t + 0.002{,}24t^2 \tag{5.2.6a}$$

$$^2P:\ \delta = 0.047,160,1 - 0.022,816t - 0.007,82t^2 \qquad (5.2.6b)$$

$$^2D:\ \delta = 0.001,932,0 - 0.004,11t \qquad (5.2.6c)$$

$$^2F:\ \delta = 0.000,310,3 - 0.001,27t \qquad (5.2.6d)$$

Here, the coefficients in the ^2S and ^2P series expansions are chosen so as to make the n = 2, 3, and 4 levels match the observed values exactly. Overall, these formulae reproduce the observed energies to within $\pm 0.05\ cm^{-1}$.

It is not necessary to know the Rydberg constant or the quantum defects to very high accuracy when predicting the binding energy of Rydberg states. For example, knowing R_{Li} to $\pm 0.6\ cm^{-1}$ and δ_s to ± 0.002 is sufficient to calculate the binding energy of the 30s state to $\pm 0.001\ cm^{-1}$. The required accuracy of the Rydberg constant scales as $(n^*)^{-2}$; that of δ scales as $(n^*)^{-3}$. Recently, Goy *et al.* [GLG86] have performed high resolution millimeter-wave measurements among Rydberg state energy levels. These measurements yield s and p series quantum defects with fractional uncertainties of 3×10^{-6} for $n \sim$ 20-40. Goy's quantum defects lie within the uncertainties of Johansson's quantum defects in this region.

The 3s Level

In our experiment, we determine the binding energy of Rydberg states by measuring the wavelength of the yellow laser that drives the transition 3s → Rydberg state. This requires knowing the binding energy of the 3s level. Johansson reports this value as

$$T(3s) = 16{,}281.050(5)\ \text{cm}^{-1} \tag{5.2.7}$$

As is discussed below, we are suspicious about this number; in fact we think it is about 0.02 cm^{-1} too small. We have studied many levels at both zero and non-zero magnetic field, and the levels all seem to be consistently about 0.02 cm^{-1} less tightly bound than the predictions of quantum defect theory. For Rydberg states, it seems unlikely that quantum defect theory should be off by that much. So either $T(3s)$ or the iodine atlas [GEL78], which is our wavelength standard, is in error. We believe that the iodine atlas is reliable; it is modern and many people use it. That leaves $T(3s)$, which relies on Meissner's wavelengths for 3s→2p and 2p→2s to determine $W(3s)$, and Johansson's determination of the series limit. It's difficult to say where the error might lie.

One possibility is that Johansson was not careful about isotopic purity. Meissner clearly states that his own work is with ^{7}Li, but Johansson makes no mention of this. Johansson's value of the Rydberg constant lies between modern values for the two isotopes (see Table 5.3.1 below). Perhaps this affected the determination of the series limit.

Another possibility is suggested when an alternative fitting scheme is used with Johansson's (and Meissner's) data. Martin [MAR80] used the following form to reduce recent measurements in sodium to quantum defects:

$$\delta = a + bm^{-2} + cm^{-4} \tag{5.2.8}$$

where $m = n - \delta_o$, and δ_o is the quantum defect of the lowest term rounded to the most significant figure. Note that this expression is *not* iterative and therefore is much easier to use than Johansson's. Using Johansson's binding energies and

$$R_{^7Li} = 109{,}728.7336(1)\ \text{cm}^{-1} \tag{5.2.9}$$

we have found a, b, and c in the formula. For s states, the deviation between the tabulated and calculated binding energies is shown in the following table.

State	Tabulated − Calculated (cm^{-1})
2s	0.031
3s	-0.071
4s	0.013
5s	0.017
6s	0.004
7s	0.012
8s	-0.012

Table 5.2.1 Difference between measured and fitted binding energies for Johansson's s states.

The 3s state has the largest deviation, implying that $W(3s)$ is in error. It is in the "correct" direction, but looks too large.

Extrapolating the s-series quantum defect of Goy *et al.* [GLG86] formula to n = 3 is completely unsatisfactory. Their measurements are fitted to an expansion which simply isn't designed for low n. The result, explicitly calculated for the ^{7}Li isotope is

$$T(3s) = 16{,}279.6(9)\ \mathrm{cm}^{-1}\ . \qquad (5.2.10)$$

It is way too small.

One might wonder if *ab initio* theory could be used to predict the binding energy of the 3s state. The most accurate reference found is that of Sims & Hagstrom [SIH75]. They use 150 Hylleraas-type terms to calculate the *total* atomic energy. Their results for s states are

$$E(2s\ ^2S) = -14.9561\ R \qquad (5.1.11a)$$

$$E(3s\ ^2S) = -14.7080\ R\ . \qquad (5.1.11b)$$

We subtract these two to get the energy of the 3s state relative to the ground state:

$$W(3s) = 0.2841\ R\ . \qquad (5.2.12)$$

Comparison with experiment requires conversion to wavenumbers. Should R_∞ or R_{Li} be used? It doesn't really matter since an assumed uncertainty of $\pm 5\times10^{-5}\ R$ leads to

$$W(3s, R_{Li}) = 27{,}224(6)\ \mathrm{cm}^{-1} \qquad (5.2.13a)$$

$$W(3s, R_\infty) = 27{,}226(6)\ \mathrm{cm}^{-1}\ . \qquad (5.2.13b)$$

Both of these numbers are about 19 cm^{-1} larger than the experimental value. This sort of calculation can not resolve our problem.

Can we measure $W(3s)$ ourselves? The direct approach has failed. The first (red) laser drives 2s→3s by a two-photon transition, so measuring the wavelength should determine $W(3s)$ accurately. Unfortunately the (air) wavelength, about 7349Å,

is too red to show much absorption in iodine at room temperature. Heating the iodine reference cell does produce some absorption lines, but they do not correspond to known peaks in the "red" iodine atlas [GVC82]. The wavelength can also be determined directly in terms of the wavelength of the HeNe reference laser in our wavemeter, discussed in Sec. 4.3. However, our wavemeter simply is not designed to give enough precision or accuracy. We have found that the laser (air) wavelength (for ^7Li) is 1.161,360(1) HeNe wavelengths. Converting this to state energy yields

$$W(3s) = 27{,}206.05(2)\ \text{cm}^{-1}\ , \tag{5.2.14a}$$

whereas Johansson reports

$$W(3s) = 27{,}206.100(5)\ \text{cm}^{-1} \tag{5.2.14b}$$

based on Meissner's wavelengths. Assuming Johansson's series limit is correct, we get

$$T(3s) = 16{,}281.10(2)\ \text{cm}^{-1}\ , \tag{5.2.15}$$

which is 0.05(2) cm^{-1} larger than Johansson's value. Again, this difference is in the correct direction, but perhaps is too large. In any case, the precision is too low to be convincing.

It is possible to determine $T(3s)$ by measuring many adjacent Rydberg p states

(in zero field). The idea is to assume that the iodine atlas and quantum defect theory for Rydberg states are correct, and to average the derived value of $T(3s)$ for each Rydberg transition. That removes any random errors in the procedure, but if there is a *systematic* error in either assumption, we do not know it. Our recent measurements (Data files 1988: may 31.24-59) suggest a global shift of 0.0167(2) cm^{-1}. This is added to Johansson's 3s binding energy to produce an effective binding energy of

$$T^*(3s) = 16{,}281.067(5)\ cm^{-1} \tag{5.2.16}$$

where the asterisk indicates that this is our best estimate of $T(3s)$. (See Secs. 5.3 and 5.4.)

Another possibility is to measure the red laser wavelength with a uranium hollow cathode ray tube using optogalvanic spectroscopy and the appropriate atlas [PKE80]. Of course that would depend on the atlas' accuracy. Measuring optical wavelengths accurately is hard.

5.3 Fine Structure Parameters

Atomic fine structure plays an important role in the experiment. As will be discussed in Sec. 5.4, the effect of the magnetic field on the electronic and nuclear spins is significant and calculable. For most of our data, the field is high enough so that the spins are essentially decoupled. The red laser selects the nuclear orientation, so scanning the yellow laser results in excited states of definite $|m_I|$ and $m_S \cdot m_I$. In addition, the isotope of lithium is selected by the red laser: the isotope shift for the 2s→3s transition is much larger than our resolution.

Along the way to the "ultimate" experimental goal, we determined the hyperfine constants and isotope shift of the 3s level. These can be added to the literature of lithium properties. The hyperfine constants are determined from the splitting size in several scans such as that shown in Fig. 4.4.3. The isotope shift is determined from continuous scans over both transitions. Relative frequency measurements employ the Fabry-Perot etalon discussed in Sec. 4.3. Although the reflectivity finesse is low at this wavelength, the precision is limited to several MHz by "backlash", a form of non-linearity in the laser's scanning mechanism. The following table summarizes many useful lithium fine structure characteristics. For completeness, both isotopes are included, although only ^7Li is used in the diamagnetism experiment. Information on the 2p state is also presented. Background information on fine structure is outlined in Sec. 5.4. Recall that the relation between magnetic moments and g-factors is given by

$$\vec{\mu}_s = \mu_s \vec{S}/S = g_s \mu_B \vec{S};\ \vec{\mu}_I = \mu_I \vec{I}/I = g_I \mu_N \vec{I} = g_I' \mu_B \vec{I}\ .$$

Property (units)	Lithium-6	Lithium-7	Reference
Nucleus			
m (gm)	$9.985,62(1)\times10^{-24}$	$1.164,762(1)\times10^{-23}$	MTW65, COG87
I	1	3/2	LES78
g_I'(*)	$-4.476,540(3)\times10^{-4}$	$-1.182,2130(6)\times10^{-3}$	AIV77
μ_I/μ_N(**)	0.822,0467(6)	3.256,424(2)	LES78
Q (barn)	-0.000,644(7)	-0.0366(3)	"
Rydberg (reduced-mass corrected R_∞)			
R_{Li} (cm^{-1}) $m(Li^{+++})$	109,727.3054(1)	109,728.7336(1)	MTW65, COG87
R_{Li} (cm^{-1}) $m(Li^{+})$	109,727.3076(2)	109,728.7353(2)	GLG86
Fine Structure ($\Delta E(n,l) = ha(n,l)\,(2l+1)/2$)			
a(2p) (MHz)	6701.84(15)	6702.16(15)	BEW67
Hyperfine Structure ($\Delta E(nS_{1/2}) = hA(nS_{1/2})\,(2I+1)/2$)			
$A(2S_{1/2})$ (MHz)	152.136,8407(20)	401.752,0433(5)	AIV77
$A(2P_{1/2})$ (MHz)	17.375(18)	45.914(25)	"
$A(2P_{3/2})$ (MHz)	-1.155(8)	-3.055(14)	"
$B(2P_{3/2})$ (MHz)	-0.10(14)	-0.221(29)	"
$A(3S_{1/2})$ (MHz)	40(3)	92(3)	KWI88
$A(4S_{1/2})$ (MHz)	13.1(1.3)	36.4(4.0)	KNS78
Other Information			
μ_B/h = -13.996,241,8(42) GHz/T			COG87
μ_N/h = 7.622,591,4(23) MHz/T			"
$\mu_N/\mu_B = -m_p/m_e$ = -1836.152,701(37)			"
g_e = 2.002,319,304,386(20)			"
g_s(Li 2s) = 2.002,3010(7)			BBE74
Isotope shift, ^{7}Li-^{6}Li			
2S-3S: 11.44(3) GHz			KWI88
2S-3D: 13.312(4) GHz			KNS78
2S-4S: 14.661(14) GHz			"

*"Uncorrected for atomic diamagnetism"
**"Corrected for [atomic] diamagnetism when possible"

Table 5.3.1 Atomic fine structure properties of lithium.

A few comments are in order. First, relativistic effects make the g-factor of the bound electron (g_s) different from the g-factor of the free electron (g_e). This could have an impact on our study of paramagnetism, as mentioned in Sec. 5.4. The table shows that the *largest* possible shift because of this effect is

$$(g_e - g_s(2s))(-\mu_B/h) = 0.25 \text{ MHz/T} , \tag{5.3.1}$$

which is smaller than our resolution. Second, the s-state hyperfine constants agree reasonably well with the semi-empirical Fermi-Segrè formula [SOB72, p. 214].

$$A(nS_{1/2}) = \frac{8}{3}\frac{\alpha^2 g_I Z}{n_*^3}\left[\frac{m_e}{m_p}\right]\left[1 + \left|\frac{\partial \delta_s}{\partial n}\right|\right] cR . \tag{5.3.2}$$

The results of the theory are contained in Table 5.3.2.

Hyperfine Constant (MHz)	Lithium-6	Lithium-7
$A(2S_{1/2})$	157.93	417.07
$A(3S_{1/2})$	35.93	94.90
$A(4S_{1/2})$	13.48	35.61

Table 5.3.2 Hyperfine constants from the Fermi-Segrè formula.

Third, the isotope shift can be estimated using the "normal mass shift" [SOB72, pp. 222-223]:

$$\Delta E = \left[\left[1 + \frac{m_e}{m(^7Li)}\right]^{-1} - \left[1 + \frac{m_e}{m(^6Li)}\right]^{-1}\right] E(2s \rightarrow 3s) \tag{5.3.3}$$

The normal mass shift and the derived specific mass shift are displayed in Table 5.3.3.

Transition	Normal Mass Shift (GHz)	Specific Mass Shift (GHz)
2S-3S	10.615	0.82(3) GHz
2S-3D	12.206	1.104(4)
2S-4S	13.661	0.998(14)

Table 5.3.3 Isotope shifts in lithium transition.

The reason for discussing these fine structure features is that they are resolved in the experiment, and so must be taken into account when assigning the energy of the states. For instance, $W(3s)$ must be determined from a transition-strength weighted average over the allowed hyperfine transitions. (There are two allowed 2s→3s hyperfine transitions, separated by about 300 MHz in ^{7}Li and about 85 MHz in ^{6}Li). Clearly the particular isotope used affects the determination of $W(3s)$. See Fig. 5.3.1 for a summary of these ideas for the 2s→3s transition.

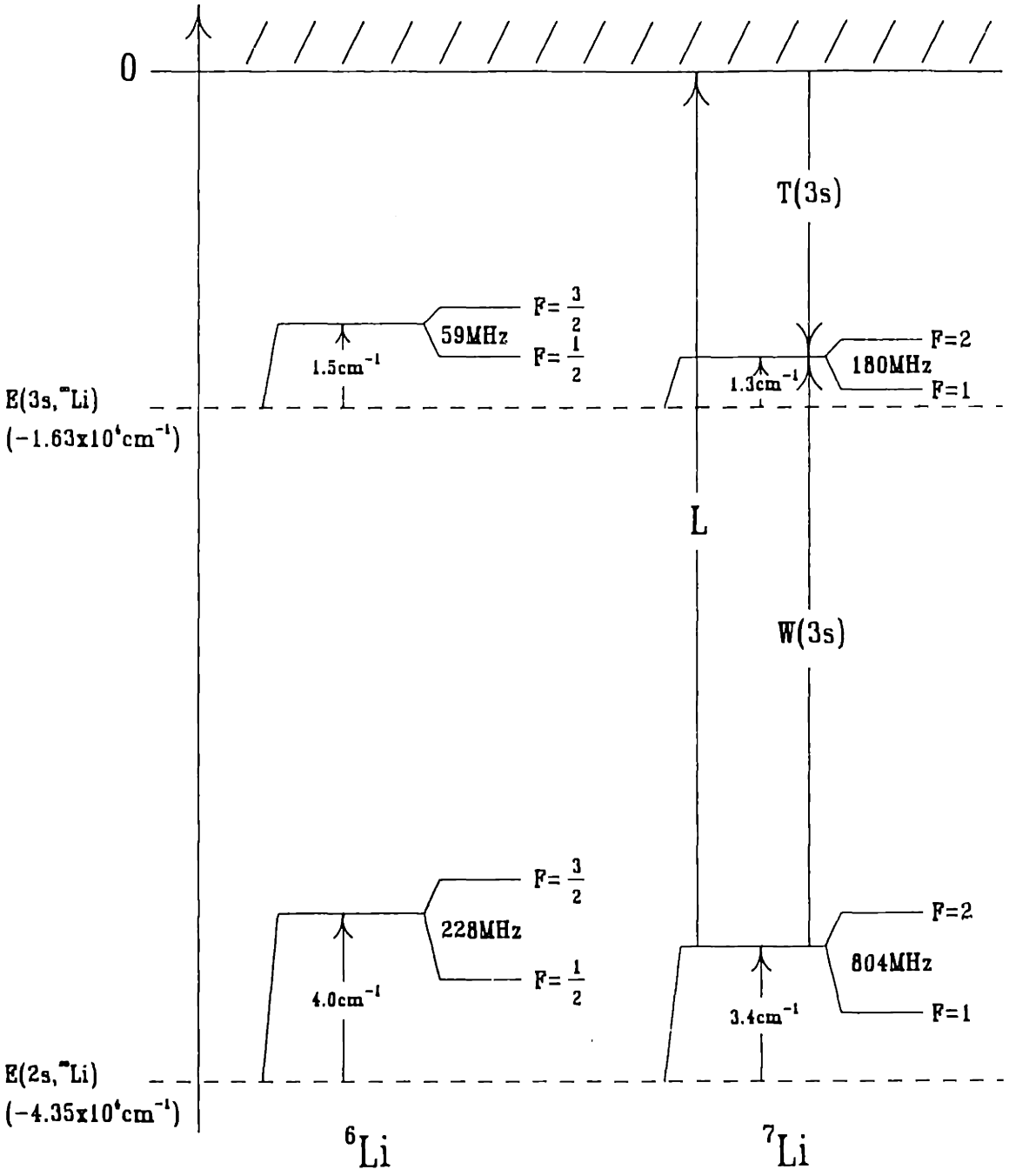

Figure 5.3.1 Schematic representation of the 2s and 3s states of lithium. The diagram shows the (normal mass) isotope shifts and hyperfine splittings, and explains the meaning of L, T(3s) and W(3s).

5.4 Effects Arising from Electronic and Nuclear Moments

In Chap. 3, we ignored the magnetic dipole moments of the electron and the nucleus. These moments produce the fine and hyperfine structure of atoms and also interact with an external magnetic field. This *interaction* is linearly proportional to the field, and therefore comes under the heading of paramagnetism. There are intermediate ranges of magnetic field where the energy shifts are quadratic in field because of changes in the way in which the angular momenta couple. We feel this is properly the "quadratic Zeeman effect", because the Zeeman effect is associated with the paramagnetic Hamiltonian. Diamagnetism results from another interaction, which is itself quadratic in field.

In our experiment, the magnetic field is large in the sense that the field-spin interaction is much larger than the spin-orbit interaction: we are in the Paschen-Back regime [WEI78, pp. 346-355]. This means that all of the angular momenta are decoupled. The magnetic moments associated with the electronic spin and the orbital angular momenta are of the same order of magnitude, so the shift is *not* negligible. However, electric dipole transitions do not change the (decoupled) state of the electron or nucleus. Thus, the paramagnetic shift caused by these magnetic moments is the same for all states, and our transitions are virtually insensitive to it.

In our experiment, the red laser drives the 2s→3s transition, and the yellow laser drives the 3s→Rydberg state transition. This section contains a discussion of the fine

structure of alkali-metal atoms and the effect of fine structure on lithium diamagnetic Rydberg states. Then the s-state hyperfine structure is considered, along with its effect on the spectra in our experiment.

Fine Structure of Alkali-Metal Atoms

We begin by considering the Pauli equation for a single electron with electromagnetic coupling. This is an approximation to the Dirac equation to order $(v/c)^2$. The result is [WEI78, pp. 316-321] (in standard atomic units, that is, the units of hydrogen with infinite nuclear mass),

$$\left[\frac{1}{2}(\vec{p}+\vec{A})^2 + V(r) + \frac{\vec{\sigma}}{2}\cdot\vec{\nabla}\times\vec{A} - \frac{\alpha^2}{8}p^4 - \frac{\alpha^2}{8}\nabla^2 V - \frac{\alpha^2}{4}\vec{\sigma}\cdot\vec{\nabla}V\times\vec{p}\right]|\psi> = E|\psi>. \quad (5.4.1)$$

The first two terms are the usual non-relativistic kinetic and potential energies of the electron, with the vector potential included in the kinetic energy. The potential energy is $-1/r$ for hydrogen. The third term is $\vec{S}\cdot\vec{B}$, and represents the interaction of the electronic magnetic moment with the external magnetic field. The fourth term is the lowest order difference between the relativistic and non-relativistic kinetic energies. The fifth term is the Darwin term, $-\alpha^2(4\pi\delta^{(3)}(\vec{r}))/8$, which expresses the average shift caused by "Zitterbewegung", the relativistic vibration of the electron, in a Coulomb potential [SAK67]. It is non-zero only for s-states. The sixth term is $(\alpha^2/2r^3)\vec{S}\cdot\vec{L}$ for

the Coulomb potential and is the manifestation of the spin-orbit coupling between the electronic magnetic moment and the Coulomb field transformed into the electron's rest frame. It is zero for s-states. The parameter E represents the difference between the eigenvalue of the Dirac equation and the electron rest energy, mc^2. Finally, the state $|\psi>$ generally contains both space and spin specifications. In the (static) symmetric Coulomb gauge, $\vec{A} = (\vec{B}\times\vec{r})/2$, the Hamiltonian for hydrogen in a magnetic field is

$$H_o'(B) = H_o + H_p' + H_d + H_{FS} \tag{5.4.2a}$$

where

$$H_o = \frac{1}{2}p^2 - \frac{1}{r} \tag{5.4.2b}$$

$$H_p' = (\frac{1}{2}\vec{L} + \vec{S})\cdot\vec{B} \tag{5.4.2c}$$

$$H_d = \frac{1}{8}(\vec{B}\times\vec{r})^2 \tag{5.4.2d}$$

$$H_{FS} = -\frac{\alpha^2}{8}p^4 - \frac{\alpha^2}{8}(4\pi\delta^{(3)}(\vec{r})) + \frac{\alpha^2}{2r^3}\vec{L}\cdot\vec{S} \tag{5.4.2e}$$

For multi-electron atoms in zero magnetic field, the relativistic kinetic energy correction and the Darwin terms add for each electron and simply shift the level. This may be considered as part of the electronic structure, or the "center of gravity" of fine structure intervals which is used to determine quantum defects. (See Secs. 3.1 and

5.1.) The spin-orbit coupling terms also add for each electron and vanish when summed over a closed shell [WEI78, pp. 465-468]. For alkali-metal atoms, there is just one electron outside of a closed shell. Therefore, with respect to the center-of-gravity of a level, the fine structure of the atom is determined by that of the valence electron.

The Hamiltonian for light alkali-metals is given by

$$H_A' = H_A + a(n,l)\vec{L}\cdot\vec{S} \tag{5.4.3a}$$

where H_A is given by Eqs. (3.1.2). For neutral alkali-metal atoms, $a(n,l)$ is given by [SOB72, p. 166]

$$a(n,l) = \frac{\alpha^2}{2}\,\frac{(Z_{eff})^2}{(n^*)^3 l(l+1)(l+1/2)}\ ,\quad l \geq 1\ . \tag{5.4.3b}$$

where $Z_{eff} \approx 0.94$ for lithium and n^* is the effective principal quantum number given in Eqs. (3.1.4). The spin-orbit coupling allows the total angular momentum, $\vec{J} = \vec{L} + \vec{S}$, to remain constant, but not the individual orbital or spin angular momenta. The fine structure parameter $a(n,l)$ may be determined experimentally from the fine structure interval:

$$\Delta E(n,l) = a(n,l)[\langle\vec{L}\cdot\vec{S}\rangle_{j=l+1/2} - \langle\vec{L}\cdot\vec{S}\rangle_{j=l-1/2}] = a(n,l)(l+1/2)\ . \tag{5.4.3c}$$

Because the fine-structure parameter scales approximately as $(n^* l)^{-3}$ it is quite small for Rydberg states. For instance, for lithium $a(2p) \approx 6.7$ GHz (see Table 5.3.1), from which it follows $a(25p) \approx 3.2$ MHz, which is below our experimental resolution.

In a magnetic field, the approximate Hamiltonian for lithium is

$$H_A'(B) = H_A' + H_p' + H_d \ , \tag{5.4.4}$$

where H_A', H_p', and H_d are defined by Eqs. (5.4.3a), (5.4.2c), and (5.4.2d) respectively. We assume that the correct reduced units for this expression are given in Table 3.1.1, a questionable assertion given that the fine structure corrections were derived for hydrogen with infinite nuclear mass. A *two-body* relativistic Hamiltonian is quite complicated, and beyond the scope of this discussion. Briefly, the difference in reduced units between hydrogen (with infinite nuclear mass) and lithium is a small difference in the small correction introduced by relativistic effects. This shift is far beyond our resolution. For precision fine-structure spectroscopy, the procedure is to let

$$H_p' = \frac{1}{2}\,(\beta\vec{L} + g_s\vec{S}) \cdot \vec{B} \ , \tag{5.4.5}$$

where β is the reduced mass factor discussed in Sec. 3.1, and g_s is the g-factor for the bound electron. Generally, it differs form the g-factor of the free electron, and depends on the state of the atom. (See Table 5.3.1, and the following discussion.) The data are fit by adjusting g_s.

In our experiment, the field is sufficiently high that in Rydberg states

$$|\langle a(n,l)\vec{L} \cdot \vec{S}\rangle| << |\vec{S} \cdot \vec{B}| \ , \tag{5.4.6}$$

so the spin-orbit term may be considered as a perturbation, and the orbital and spin angular momenta are decoupled. We may rewrite Eq. (5.4.4) as

$$H'_A(B) = H_A(B) + \frac{g_s}{2}(\vec{S}\cdot\vec{B}) + a(n,l)\vec{L}\cdot\vec{S}\,, \tag{5.4.7a}$$

where $H_A(B)$ is the Hamiltonian for non-relativistic lithium in a magnetic field, defined by Eqs. (3.1.6c). If the eigenstates and eigenenergies of $H_A(B)$ are defined by

$$H_A(B)\,|\,nkm_l;\,B\,> = E(nkm_l;\,B)\;|\,nkm_l;\,B\,>\,, \tag{5.4.7b}$$

we may form products of spatial and spin states given by

$$|\,nkm_l m_s;\,B\,> = |\,nkm_l;\,B\,> \times |\,s\,=1/2,\,m_s\,>\,. \tag{5.4.7c}$$

The orbital azimuthal quantum number is now specifically labeled with a subscript, m_l. The energy of such a state is given by first order perturbation theory:

$$E(nkm_l m_s;\,B) = E(nkm_l;\,B) + \frac{g_s}{2}\,m_s B + a(n,l)m_l m_s\,. \tag{5.4.7d}$$

Note that the orbital paramagnetic energy shift $\beta(\vec{L}\cdot\vec{B})/2$ is contained in $E(nkm_l;\,B)$. The effect of spin-orbit coupling is negligible for the Rydberg states in our experiment.

Hyperfine Structure of S-states in Alkali-Metal Atoms

Hyperfine structure arises from the interaction of the nuclear multipole moments with the multipole moments associated with the orbital and spin angular momenta. For the single valence electron in the s-state of an alkali-metal atom, the hyperfine

structure Hamiltonian is given by [WEI78, pp. 358-374, 478-481]

$$H_{HFS} = A\,(n\,\mathrm{s})\vec{I}\cdot\vec{S}\ . \tag{5.4.8a}$$

Here, A is the hyperfine structure parameter for which an approximate expression was presented in Eq. (5.3.2). The spin-spin coupling allows the total angular momentum, $\vec{F} = \vec{S} + \vec{I}$, to remain constant. (Note: for s-states, $\vec{L} = 0$ so $\vec{J} = \vec{S}$.) The parameter may be determined experimentally from the hyperfine structure interval:

$$\Delta E\,(n,\mathrm{s}) = \langle H_{HFS}\rangle_{F=I+1/2} - \langle H_{HFS}\rangle_{F=I-1/2} = A\,(n\,\mathrm{s})(I+1/2)\ . \tag{5.4.8b}$$

The center of gravity is not shifted by this interaction. The parameter scales as $(n^*)^{-3}$. It also depends on the particular isotope under consideration. We primarily study ^{7}Li, which has I=3/2 and A(2s) ≈ 400 MHz (see Table 5.3.1). Then A(25s) ≈ 0.11 MHz, and is much smaller than our experimental resolution.

Although hyperfine coupling is completely negligible in Rydberg states, the hyperfine structure of the 2s and 3s states are resolved in our two-photon transition. As is discussed by Grynberg, Biraben, Giacobino and Cagnac [GRG77], the two-photon transition operator is (approximately) a scalar with respect to the total angular momentum. Therefore, the selection rules are $\Delta F = 0$ and $\Delta m_F = 0$, and each $|\,2\,s\ m_F\,\rangle \rightarrow |\,3\,s\ m_F\,\rangle$ transition has the same strength. Therefore, as the red laser is scanned over the 2s→3s transition, there are two peaks, whose separation is one-half of the difference of the hyperfine structure intervals of the 2s and 3s states. See Figs.

5.3.1 and 4.4.3. For ^{7}Li, this value is 310(3) MHz. The height ratio is simply the ratio of the multiplicities, 5/3. The fluorescence has a spherical distribution, so there is no need for "magic angle" detection [WAL82].

When a magnetic field is applied, the Hamiltonian for the lithium 2s and 3s states is

$$H_A''(B) = H_A + H_d + \frac{g_s}{2}\vec{S}\cdot\vec{B} + \frac{g_I'}{2}\vec{I}\cdot\vec{B} + A(n\,\mathrm{s})\vec{I}\cdot\vec{S} \qquad (5.4.9a)$$

where the diamagnetic interaction is assumed to be small enough that n- and l-mixing are negligible. Here, g_I' is the nuclear g-factor referenced to the Bohr magnetron. See Table 5.3.1 for values of this parameter. The eigenvalues of the last three terms of this Hamiltonian are given by the Breit-Rabi Formula [RAM56, pp. 76-80]. For the 2s and 3s states of ^{7}Li, these values are displayed in Fig. 5.4.1. (The diamagnetic shift is completely invisible for these states in this field range.)

If the magnetic field is large enough so that the electronic and nuclear spins are essentially decoupled, then the energies may be expressed in terms of the quantum numbers of the "high field" states $|n\,s m_s m_I>$ by using perturbation theory:

$$E(n\,s m_s m_I;\, B) = E(n\,s;\, B) + \frac{g_s}{2} m_s B + \frac{g_I'}{2} m_I B + A(n\,s) m_s m_I \qquad (5.4.9b)$$

where $E(n\,s;\, B)$ is the eigenvalue of $H_A + H_d$. Because the two-photon transition operator is a scalar, we must have $\Delta m_s = 0$ and $\Delta m_I = 0$. The transition frequencies

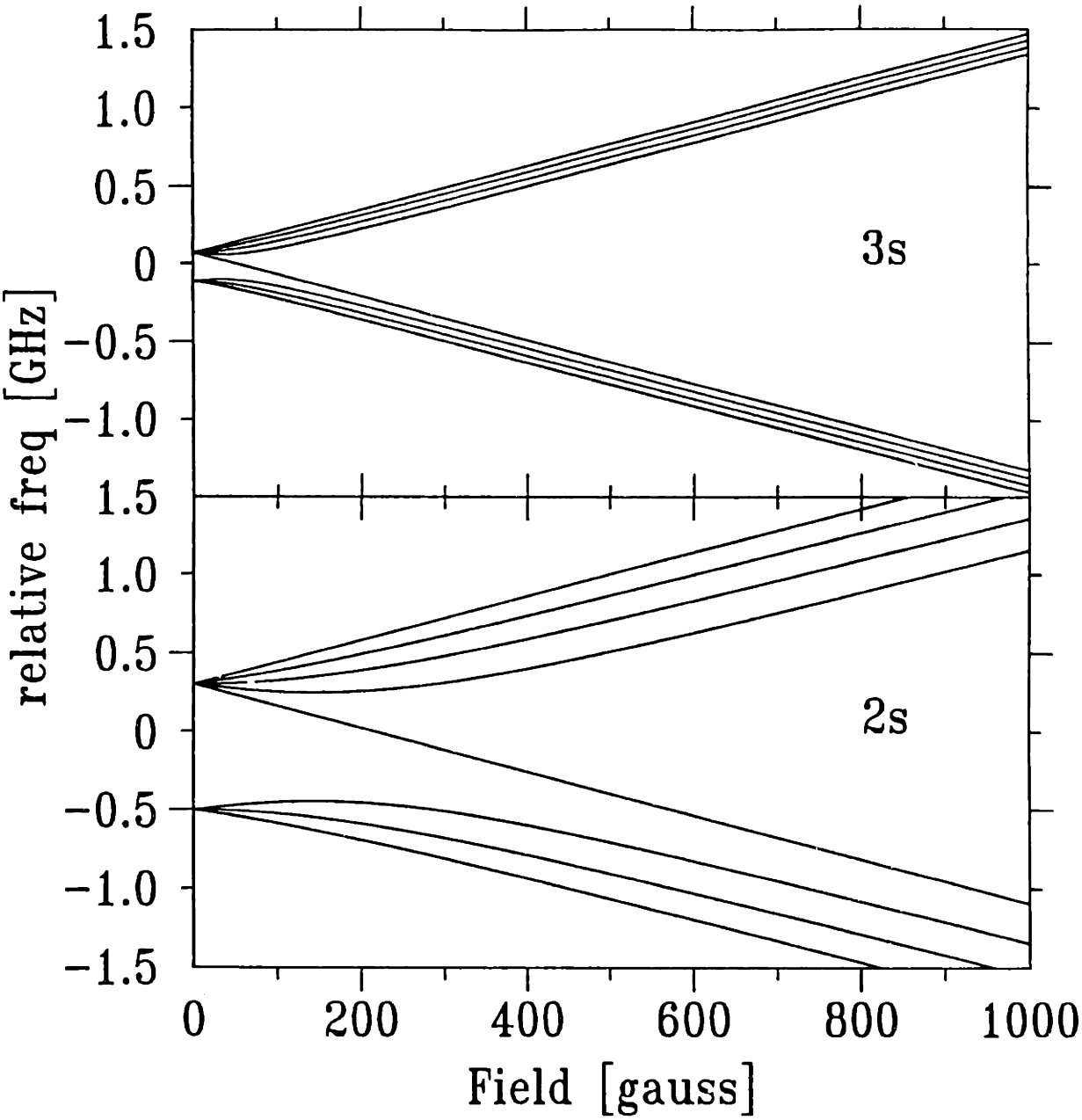

Figure 5.4.1 Energies of the ^7Li hyperfine states in a magnetic field. The curves are generated from the Breit-Rabi formula [RAM56, pp. 76-80], using the data of Table 5.3.1.

are then

$$\nu = \frac{1}{2}\{E(3s;\, B) - E(2s;\, B) + [A(3s) - A(2s)]m_s m_I\}\ . \tag{5.4.9c}$$

In practical units, using Eq. (3.1.16), the shift from the center-of-gravity frequency is

$$\Delta\nu = (500\ \text{MHz/T}^2)B^2 - (155(2)\ \text{MHz})m_s m_I \tag{5.4.9d}$$

There are eight transitions, but because this expression takes on only four different values, there are only four different transitions frequencies observed. These are separated by $[A(2s) - A(3s)]/4 = 77(1)$ MHz. The product of the nuclear and electronic spin quantum numbers is selected by the particular transition used, as listed in the following table:

Shift in Transition Frequency (MHz)	Large Field Quantum Numbers (m_s, m_I)	Total Quantum Numbers m_F
−116(1)	(1/2, 3/2)	2
	(−1/2, −3/2)	−2
−39(1)	(1/2, 1/2)	1
	(−1/2, −1/2)	−1
+39(1)	(1/2, −1/2)	0
	(−1/2, 1/2)	0
+116(1)	(1/2, −3/2)	−1
	(−1/2, 3/2)	1

Table 5.4.1 Quantum numbers selected in the two-photon transition.

Because the two-photon transition operator is a scalar, the transition strengths each equal 2/8 of the total. At zero magnetic field, the 2s $F=2 \rightarrow 3s$ $F=2$ transition strength is 5/8 of the total. Therefore, the fluorescence signal in a strong field will be 40% of the maximum fluorescence signal at zero field.

Because the 2s and 3s states have different hyperfine intervals, these two states also have different "critical fields", where the eigenstates are not well approximated by either $| n s F m_F >$ nor $| n s m_s m_I >$. This field is defined by

$$| A(ns) | = B_c \tag{5.4.10}$$

so $B_c(3s) = 70$ gauss, and $B_c(2s) = 300$ gauss. Referring to Fig. 5.4.1, these are the fields at which states with $| m_F | < 2$ clearly change shape. There are three regimes to consider. When the field is much less than $B_c(3s)$, F is a good quantum number for both the 2s and 3s states and the selection rules $\Delta F = 0$, $\Delta m_F = 0$ hold. When the field is much greater than $B_c(2s)$, m_s and m_I are good quantum numbers for both the 2s and 3s states, and the selection rules $\Delta m_s = 0$, $\Delta m_I = 0$ hold. Between these regions, the red laser can drive transitions between states which would be forbidden at small or large field.

Figure 5.4.2 shows all possible transitions consistent with $\Delta m_F = 0$. It is made by taking half of the difference between states with the same m_F in Fig. 5.4.1. The eight "allowed" transitions are between states with $\Delta F = 0$, $\Delta m_F = 0$ at small fields, or

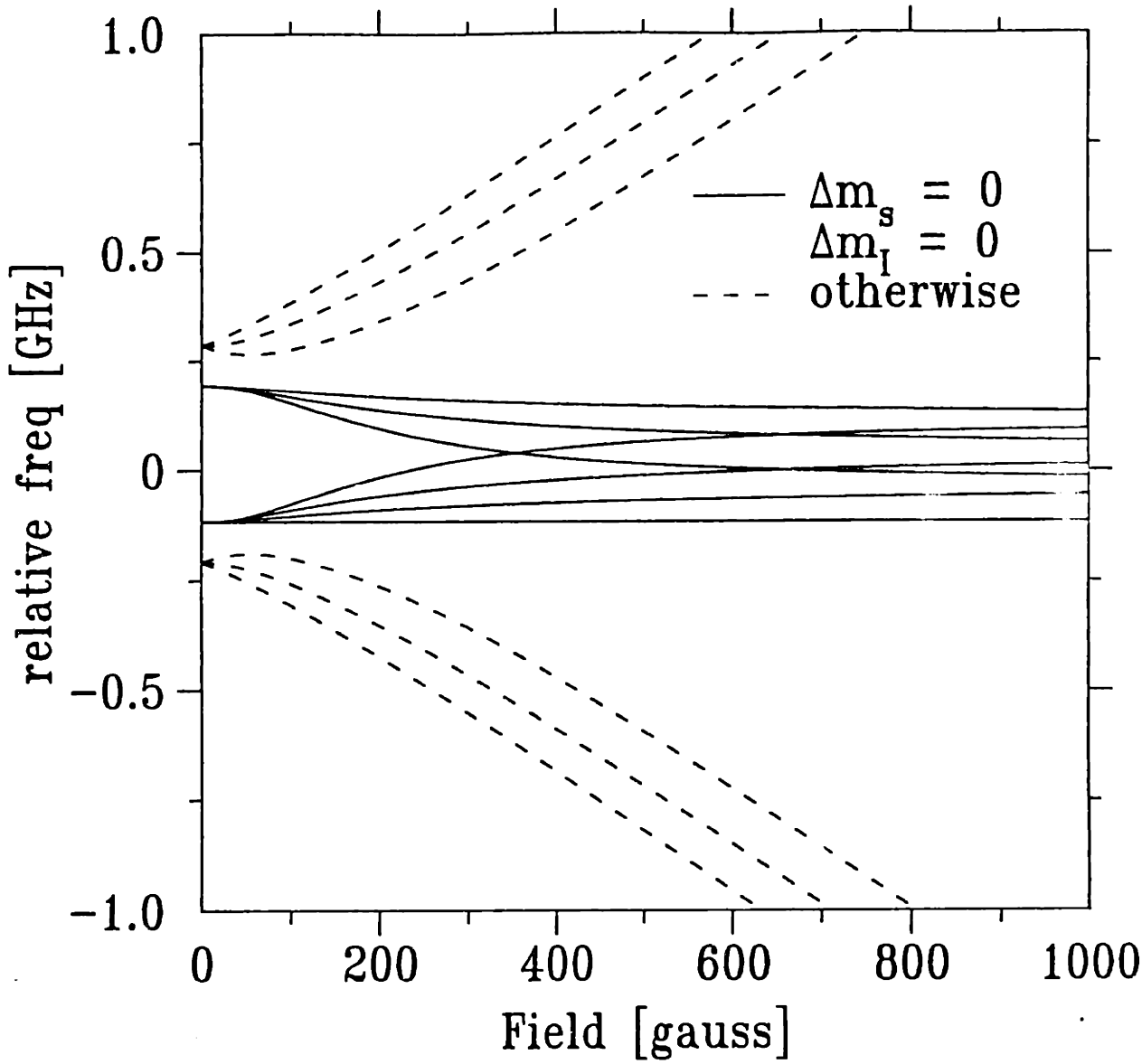

Figure 5.4.2 Possible two-photon transitions between the 2s and 3s states of ^7Li. Each line is one-half the difference between the levels of Fig. 5.4.1 with the same m_F. "Allowed" transitions are shown solid; "forbidden" transitions are shown dashed. There are 14 transitions, though only 13 show here, because the transitions with $m_F = \pm 2$ have the same frequency.

$\Delta m_s = 0$, $\Delta m_l = 0$ at high fields. The six "forbidden" transitions are between states which violate these rules at small or high fields.

At all fields, the states can be written as linear combinations of just two $|n\,sFm_F>$ states. The formalism used in the two-state model of Sec. 3.2 provides the mixing coefficients. Then the selection rules $\Delta F = 0$, $\Delta m_F = 0$ may be applied at all fields. Rather than write out all the fourteen strengths, we present the results graphically in Fig. 5.4.3. Since there are eight allowed transitions at small and large field, each transition strength is normalized to 1/8. Six "forbidden" transitions become visible in the 70-400 gauss field range.

An experimental map of the two-photon cascade fluorescence as a function of red laser frequency for a sequence of magnetic fields is shown in Fig. 5.4.4. The "forbidden" transitions are clearly visible in Fig. 5.4.5, where the signal scale of Fig. 5.4.4 has been magnified. Note the "forbidden" peaks are large only in the expected field range. A scan of the fluorescence in high field ($B \simeq 5.5$ T) is presented in Fig. 5.4.6, which verifies the predictions of Eq. (5.4.9d).

Optical Transitions to Rydberg States

The approximate Hamiltonian which describes the valence electron and the nucleus of a Rydberg state of lithium in a magnetic field is given by

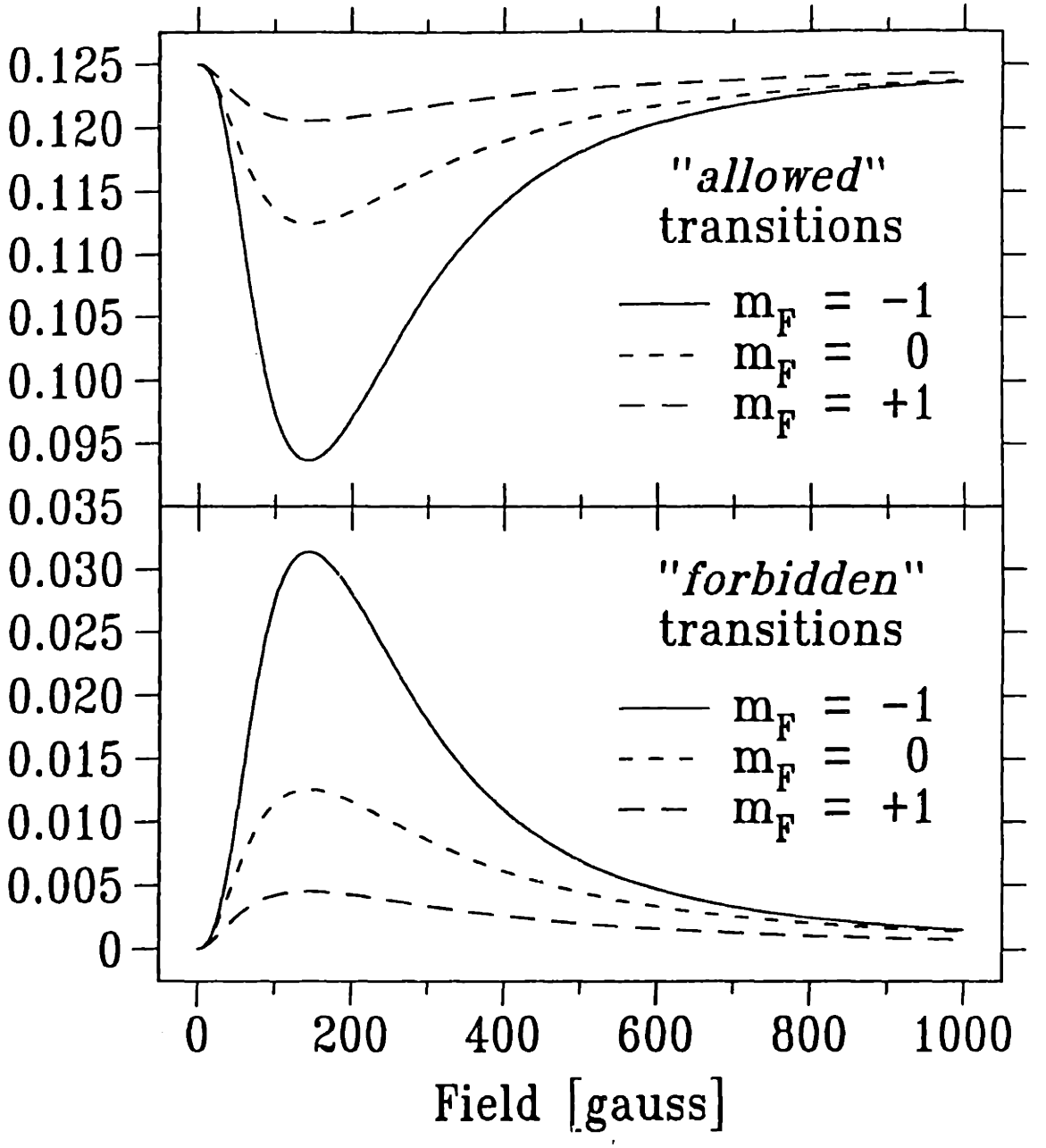

Figure 5.4.3 Normalized transition strengths. Of the 14 transitions shown in Fig. 5.4.2, those originating with a given m_F and (in high field) m_s = +1/2 have the same strength as the corresponding m_F and m_s =-1/2. Therefore only 7 strengths need be considered. The transition from m_F = 2 is a constant 1/8 and is not displayed.

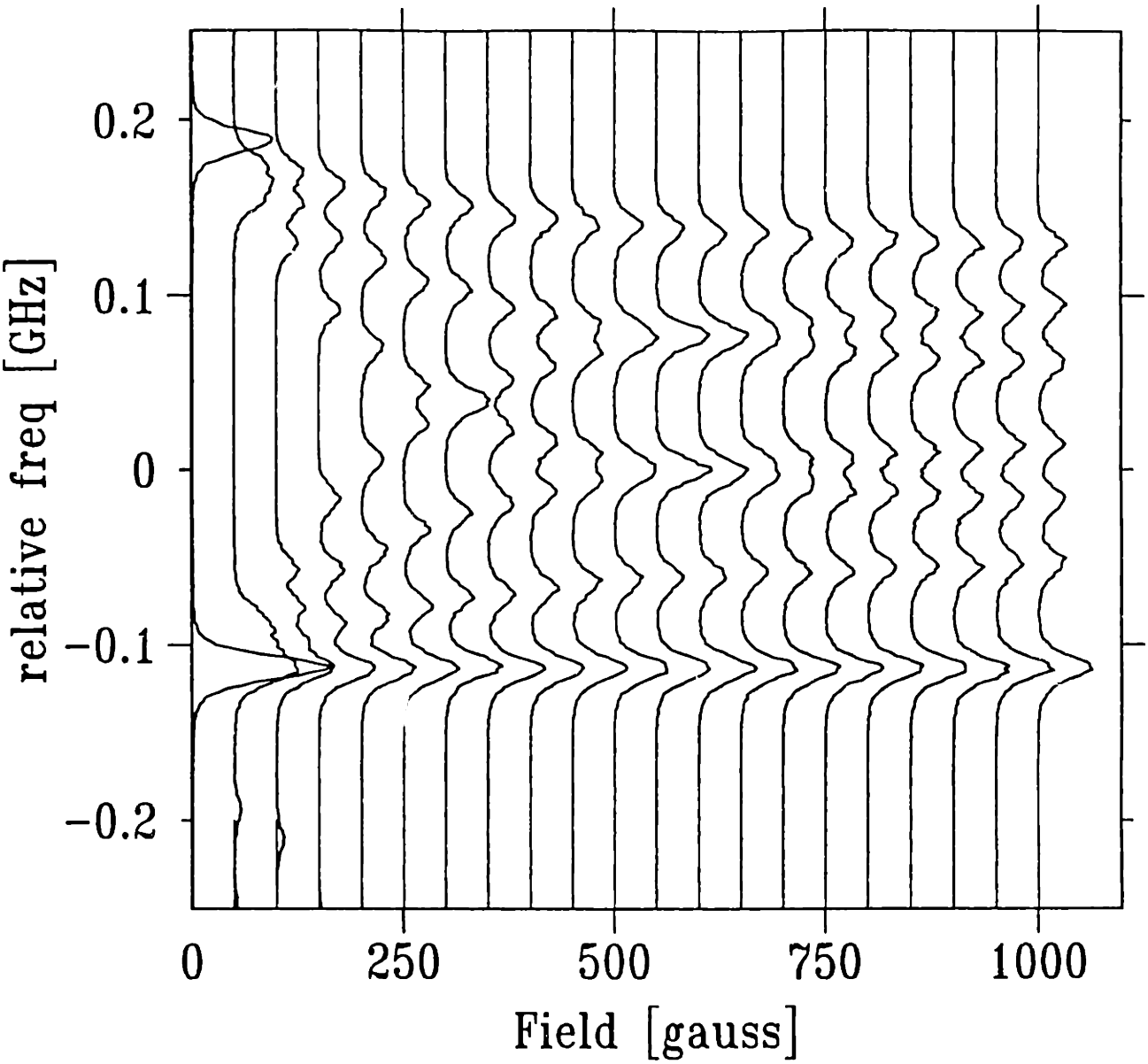

Figure 5.4.4 Map of Cascade Fluorescence. The magnetic field is given by the base line of each scan, and the red laser is tuned over a range of approximately 2 GHz. The signal scale is constant. (Data files 1987: dec 3.19-39)

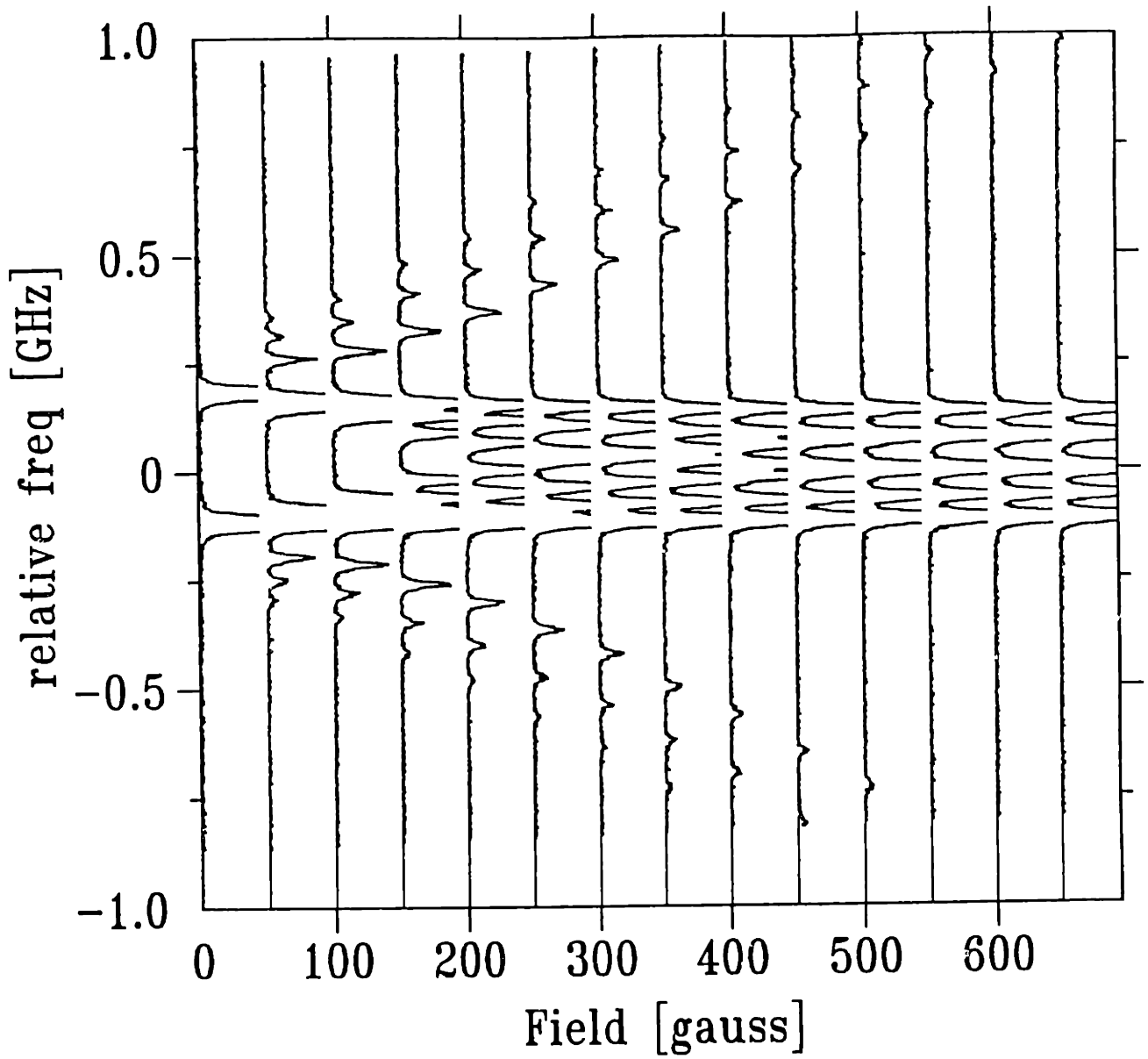

Figure 5.4.5 Map of Cascade Fluorescence. The magnetic field is given by the base line of each scan, and the red laser is tuned over a range of approximately 2 GHz. The signal scale is constant (about 0.28 Mcps/T) but magnified so that the "forbidden" transitions are visible, and the "allowed" transitions are truncated. (Data files 1987: dec 3.19-32)

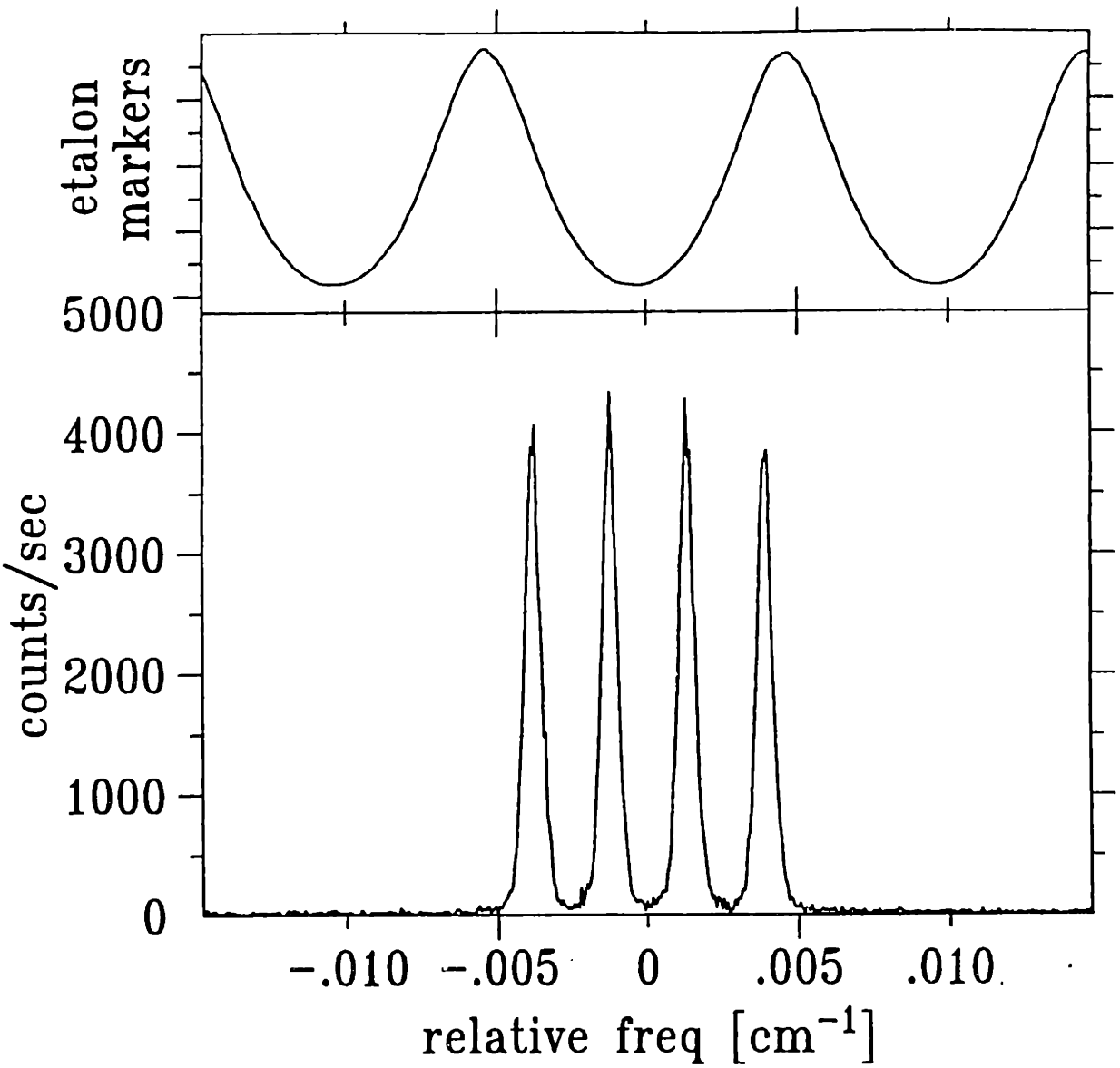

Figure 5.4.6 Cascade fluorescence in high field. The magnetic field is approximately 5.5 T, and the red laser was scanned approximately 2 GHz. The 300 MHz frequency markers are also shown. The slight variation in the signal peak height is caused by the 0.5 MHz step size of the laser. (Data file 1987: dec 3.50)

$$H_A'''(B) = H_A(B) + \frac{1}{2}(g_s\vec{S} + g_I\vec{I}) \cdot \vec{B} \qquad (5.4.11a)$$

where $H_A(B)$ is defined by Eq. (3.1.6c). We assume that fine and hyperfine coupling are negligible for Rydberg states, as argued earlier in this section. The eigenstates of $H_A'''(B)$ are simple product states:

$$| nkm_l m_s m_I; B > = | nkm_l; B > \times | s = 1/2\ m_s > \times | I\ m_I > \qquad (5.4.11b)$$

where the eigenstates and eigenvalues of $H_A(B)$ are defined by Eq. (5.4.7b). Then the eigenvalues of $H_A'''(B)$ are given by

$$E(nkm_l m_s m_I; B) = E(nkm_l; B) + \frac{1}{2}(g_s m_s + g_I' m_I)B \ . \qquad (5.4.11c)$$

For fields greater than 1 T, the energy of the 3s state is given by Eq. (5.4.9b). Then the yellow laser transition frequency is

$$\nu = E(nkm_l; B) - E(3s; B) - A(3s)m_s m_I \qquad (5.4.12a)$$

For $m_F = \pm 2$, or $m_s m_I = 3/4$, then Eq. (5.4.12a) is valid at all fields. Now

$$E(3s; B) = E(3s) + \frac{1}{8}\langle\rho^2\rangle_{3s}B^2 + \frac{1}{4}\langle\rho^2\rangle_{1s}B^2, \qquad (5.4.12b)$$

where, from Eq. (5.2.16),

$$E(3s) = -T(3s) \ . \qquad (5.4.12c)$$

The diamagnetic shift of the 3s state was presented in Eq. (3.1.15). Therefore, the energy of a diamagnetic Rydberg state is determined by measuring the yellow laser

frequency and evaluating

$$E(nkm_l; B) = \nu - T(3s) + \frac{1}{8}\langle\rho^2\rangle_{3s}B^2 + \frac{1}{4}\langle\rho^2\rangle_{1s}B^2 + A(3s)m_s m_l \ . \quad (5.4.12d)$$

The paramagnetism of the spins has canceled out, but the particular value of $m_s m_l$ makes a measurable difference in the determination of Rydberg state diamagnetic energies. We always lock the red laser to the reddest of the four two-photon transitions, so from Table 5.4.1 we have $m_s m_l = 3/4$. In practical units, we have finally,

$$E(nkm_l; B) = \nu - 16{,}281.065(5)\ \text{cm}^{-1} + (4.0\times10^{-5}\ \text{cm}^{-1}/\text{T}^2)B^2 \ . \quad (5.4.12e)$$

The 3s diamagnetic shift is negligible in determining the Rydberg state energies.

Chapter 6. RESULTS AND CONCLUSIONS

This chapter contains the major experimental results on Rydberg Atom Diamagnetism. Previous chapters presented the theoretical and experimental techniques that we employ to understand and to demonstrate the behavior of atoms in magnetic fields. This chapter is considerably shorter than others, which reflects the way experiments really are: It took four years to force the apparatus to yield results, and a few days to collect the desired data.

The experiment may be classified as the laser spectroscopy of Rydberg states of lithium in a magnetic field. Our achievement has been the accurate determination of laser wavelength and magnetic field, which allows stringent comparison of theory and experiment. The data of this thesis are in a regime of energy and field where we have reasonable confidence in the theory. This allows us to assess the effect of systematic problems, such as the stray electric field.

We begin with the n=21 manifold, which we use to measure the magnetic field. Then several anticrossings are displayed and compared with numerical diagonalization calculations. The last section presents an evaluation of the results, and some speculations about the future.

6.1 The n=21 manifold.

As discussed in Sec. 4.2, we use the n=21, k=19, m=±1 states of lithium to measure the magnetic field. The basic idea is that the *difference* in energy of these two states is solely from the paramagnetic interaction. Theoretical odd parity levels are displayed in Fig. 4.2.1. Here we present an experimental study of the n=21 manifold in a magnetic field.

The results are displayed in Fig. 6.1.1. Each laser scan is 0.5 cm^{-1} long. At $B \approx 3.4$ T, 19 scans are overlapped. The experimental curves are taken directly from the data; the linewidth is too small to see on this scale.

The raw data include iodine absorptions and etalon frequency markers (see Fig. 4.4.8) to make accurate wavelength measurements. As described in Secs. 4.2 and 4.5, the field is determined with an uncertainty of 20 gauss. As discussed in Secs. 4.4, 4.5, 5.2, 5.3, and 5.4, the absolute energy (relative to the zero-field ionization limit of lithium) is determined with an uncertainty of 0.005 cm^{-1}.

In Fig. 6.1.2, theory and experiment are compared by overlaying Figs. 6.1.1 and 4.2.1. There is an experimental peak corresponding to each eigenstate in the experimental range at a given field, though some peaks are quite small. The extended scan at $B \approx 3.4$ T was taken with the laser polarization oriented roughly 45° to the magnetic field, so that m=0 and m=±1 states were excited. All other scans were taken with the laser polarization set perpendicular to the field, producing only m=±1 states.

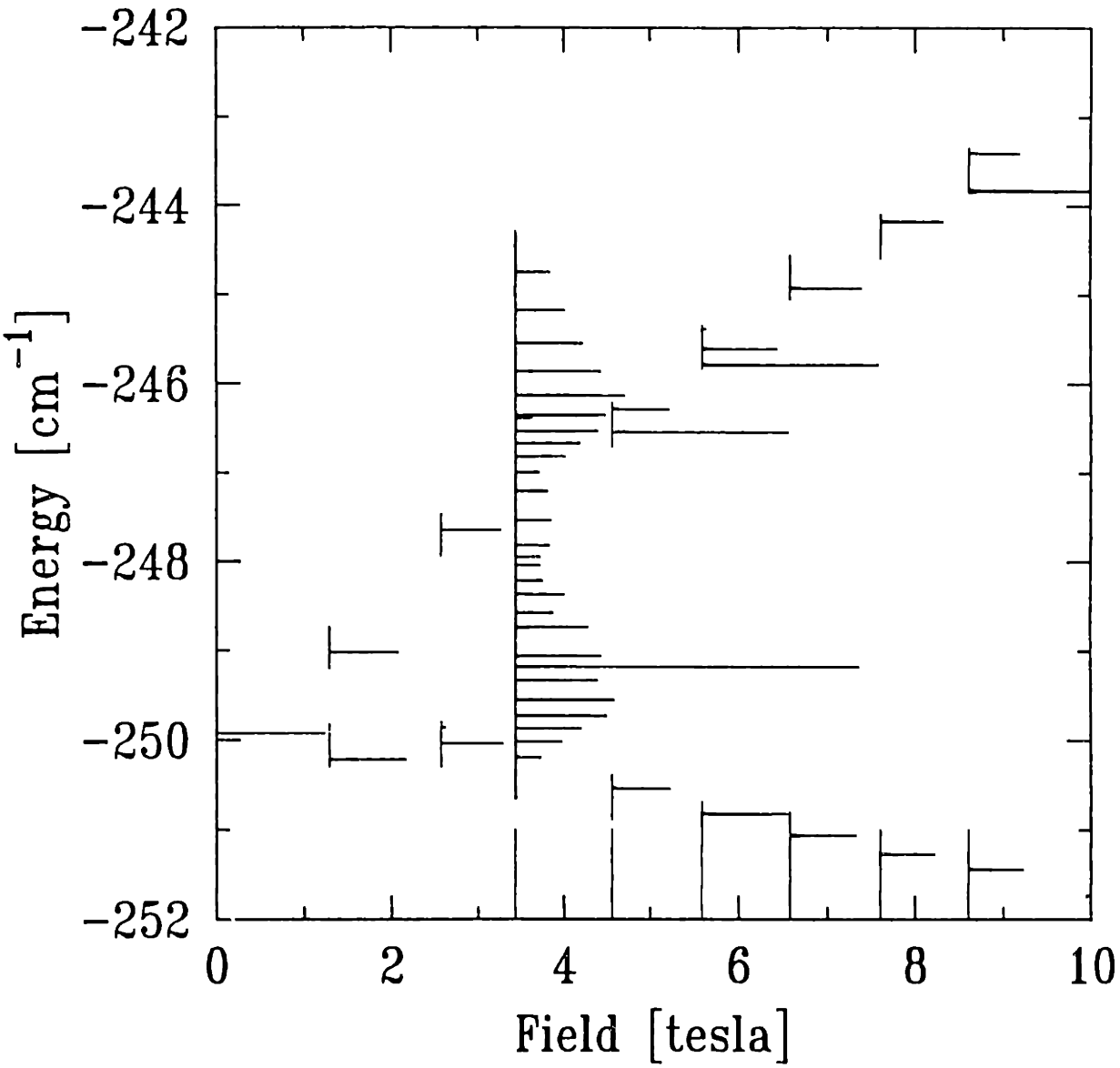

Figure 6.1.1 Measured spectra for m=0, ±1 states of lithium. The spectral lines appear as horizontal peaks pointing to the right. The magnetic field at which the data were taken is indicated by the location of the base line of each scan. The signal scale is constant for each scan, but varies between scans. (Data files 1988: jan 21.7, 19-37, 53, 55-66, 69-72)

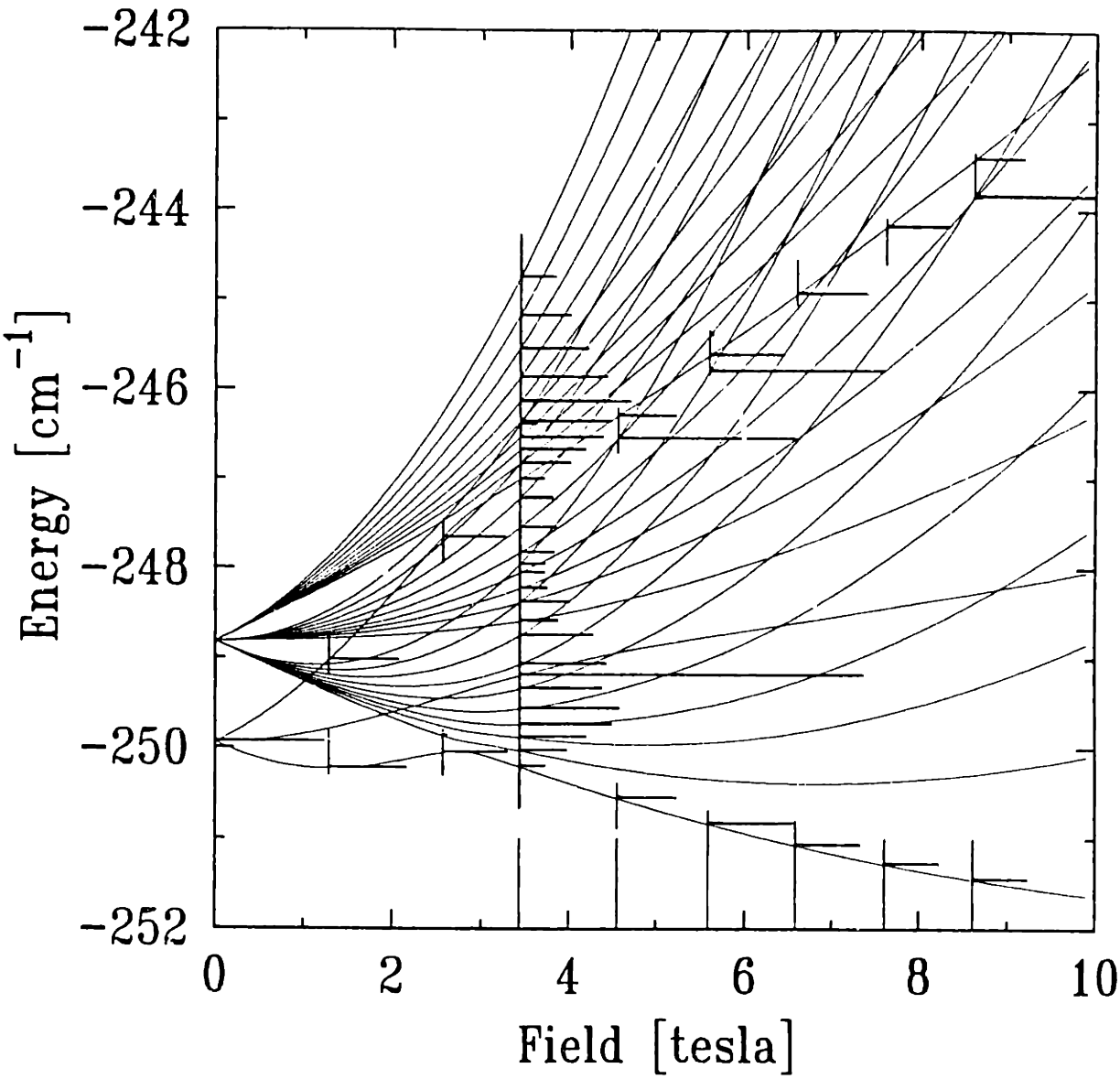

Figure 6.1.2 Overlay of Figs. 6.1.1 and 4.2.1. The laser polarization for the long scan at $B \approx 3.4$ T was oriented to excite $m=0$ and $m=\pm 1$ states, while in all other scans, the polarization was set to produce only $m=\pm 1$ states.

The agreement appears quite satisfactory.

A more stringent test is shown in Fig. 6.1.3. Here we consider the scan at $B \approx 3.4$ T shown in Fig. 6.1.1, and plot the difference between theory and experiment as a function of the energy of each state. The agreement appears better than the expected 0.005 cm^{-1} uncertainty. The reason is that we used the relative energy scale discussed in Sec. 4.5. Essentially we used the etalon and measured the frequency difference from the $B=0$ 21p state. Thus, we are really comparing theoretical and experimental diamagnetic *shifts*. This measurement has an uncertainty of about 0.001 cm^{-1}. The systematic trend in the deviations may indicate an error in the free spectral range of the reference etalon (see Sec. 4.3).

The mean deviation between experiment and theory is 0.001 cm^{-1}, indicating that the theoretical values are accurate to within the experimental resolution. The statistical errors are consistent with the spectral linewidth, 0.001 cm^{-1}, and with the fluctuations expected from the step size of the laser scan, about 0.0005 cm^{-1}.

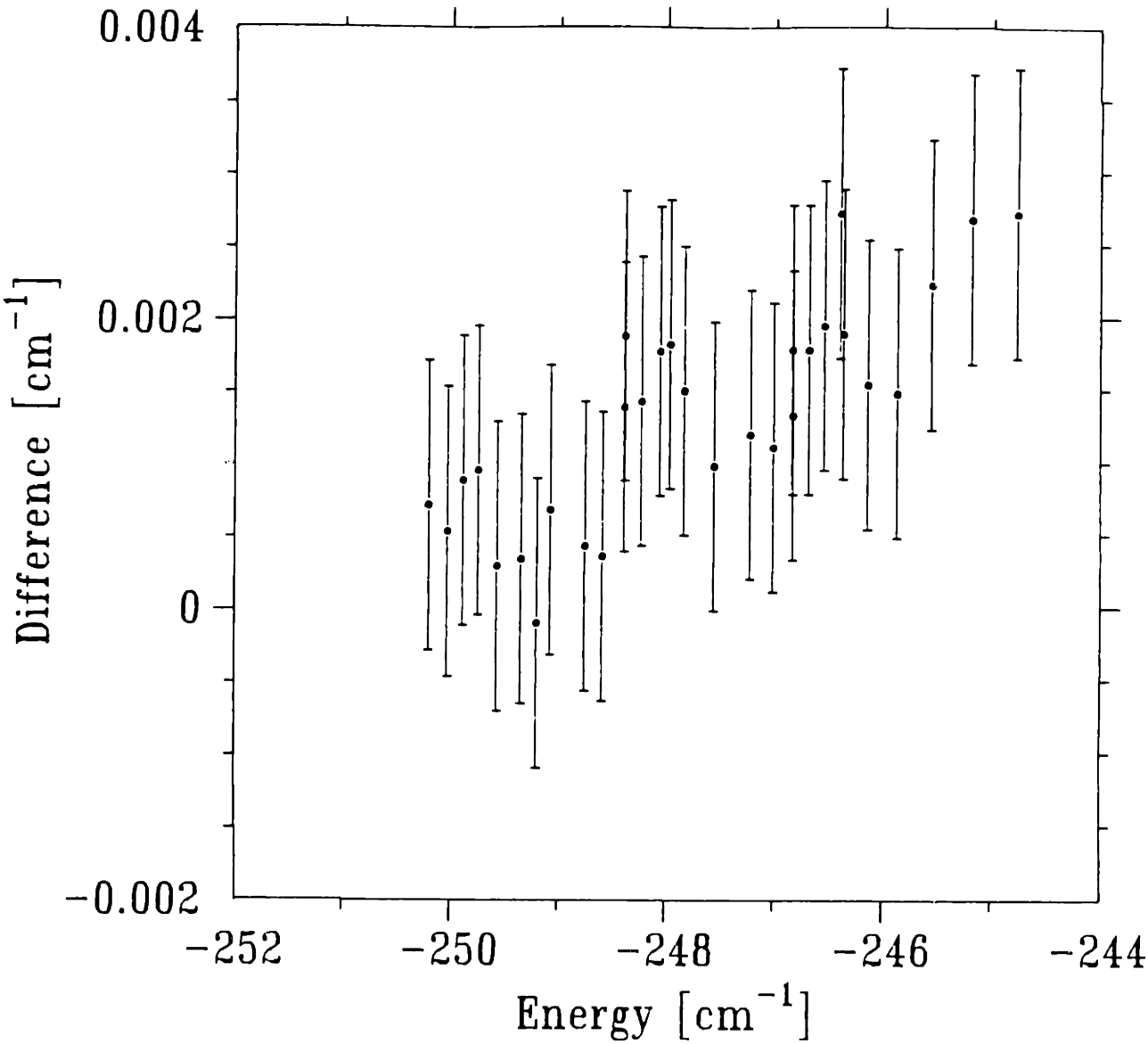

Figure 6.1.3 Theory-experiment for n=21, m=1,0,−1, π=−1. All 30 states are compared. The small uncertainty results from comparing the theoretical and experimental shifts, rather than the absolute energies.

6.2 Anticrossings of Lithium Diamagnetic Levels

In this section we present some anticrossings in the lithium diamagnetic spectrum around n = 24 and 25. The measurements are compared with theory. We discuss the possible cause of discrepancies.

Core Anticrossings

Figure 6.2.1 shows the three anticrossings which are investigated. In light of the discourse in Sec. 3.2, these anticrossings are caused by the lithium core.

The data are taken in the usual manner: set the field, and sweep the laser; then increment the field, and sweep the laser. Iodine absorptions and etalon frequency markers are part of the raw data. The magnetic field value is determined as described in Sec. 4.2: The first and last fields are measured using the n=21, k=19, and m=±1 states, and the Hall probe provides the intermediate fields by linear interpolation. Finding a *particular* anticrossing can be difficult because the Hall probe determines the absolute field only to about 0.1 T (see Fig. 4.2.4). We obtain an accurate value of the field during data analysis.

Figure 6.2.2 contains the experimental map of the anticrossing of states $|\,25\ 23\ 0\,>$ and $|\,24\ 1\ 0\,>$. It is the first anticrossing of Fig. 6.2.1. The structure looks hyperbolic, and the upper state transition strength vanishes while that of the lower state increases. This supports the two-state model of Sec. 3.2. Theory and experiment are

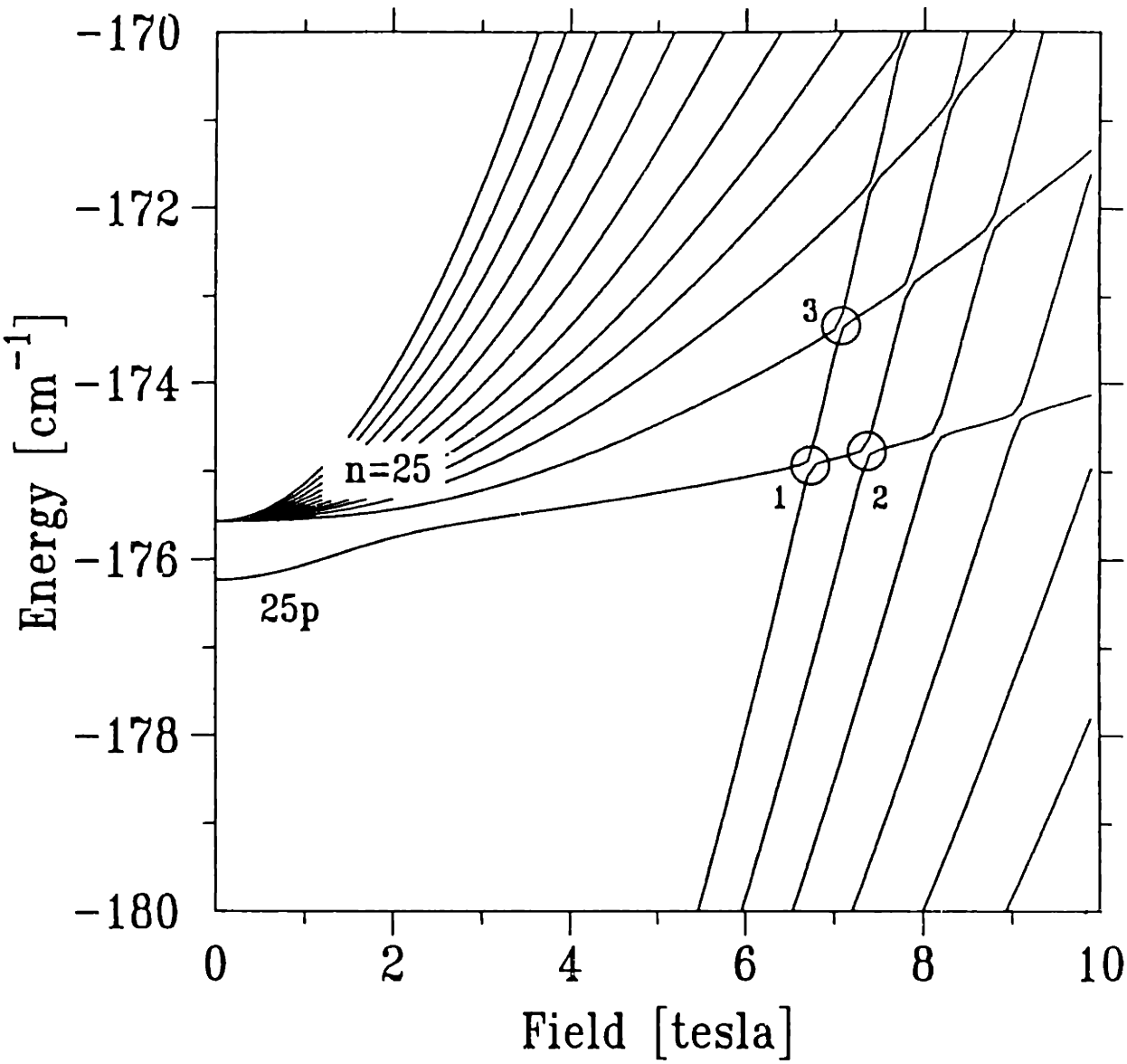

Figure 6.2.1 Lithium energy levels as a function of magnetic field, with m=0, π=-1, and n's near 25. This is quite similar to Fig. 3.1.1, here with three anticrossings circled. These are experimentally investigated in Figs. 6.2.2, 6.2.6, and 6.2.7.

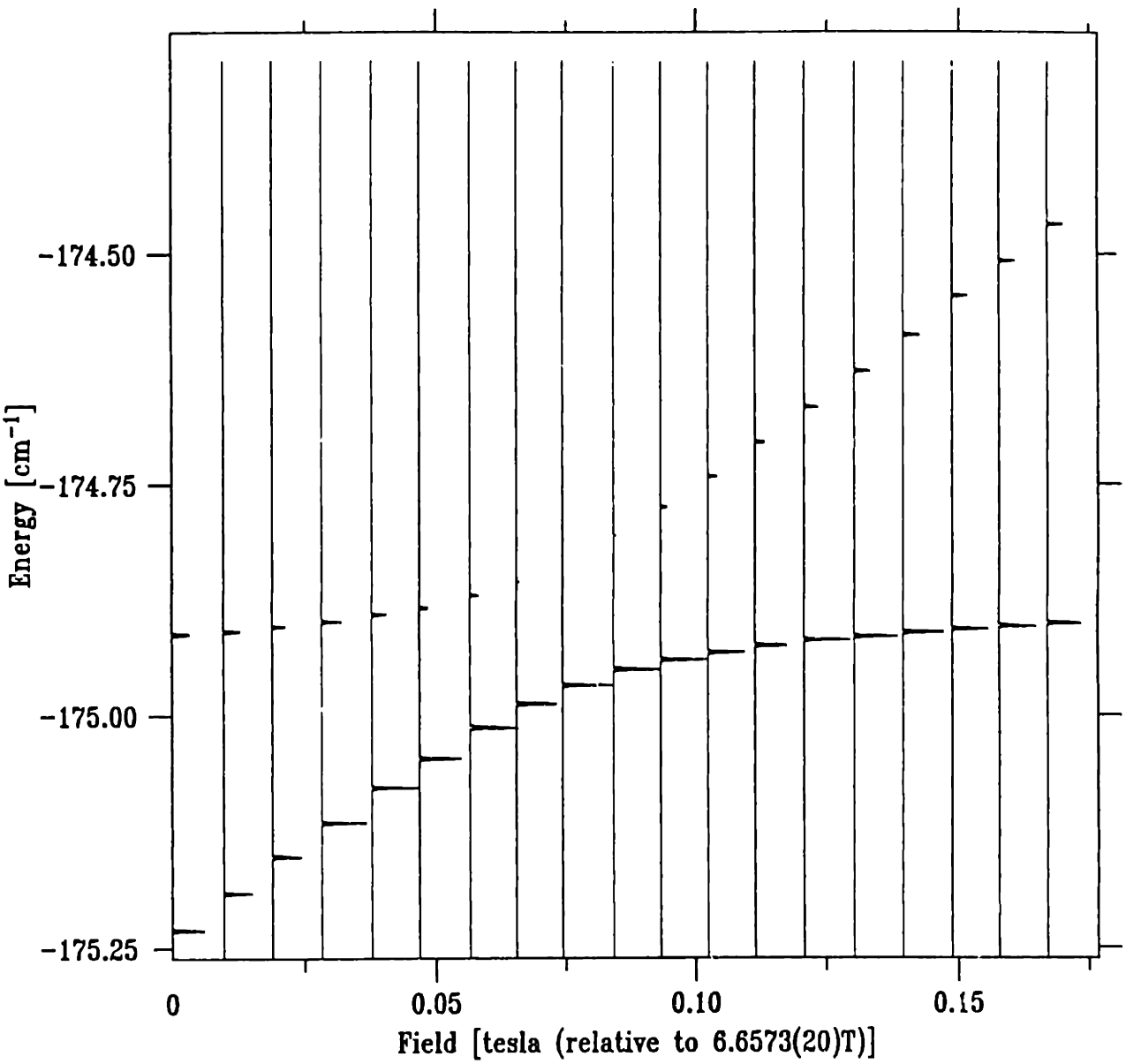

Figure 6.2.2 Anticrossing of the states | 25 23 0 > and | 24 1 0 >. This is anticrossing 1 in Fig. 6.2.1. (Data files 1988: jan 21.107-125)

overlaid in Fig. 6.2.3, and compared critically in Fig. 6.2.4. The latter is the result of fitting Eq. (3.2.16a) to the experiment and theory. The uncertainty in the theoretical values comes from the finite number of diagonalizations performed in the vicinity of the anticrossing.

The discrepancy is probably not caused by the finite basis size used in the calculation. Figure 6.2.5 shows the anticrossing size and the field location as a function of basis size. Both parameters are constant for bases containing more than 50 states.

The stray electric field is probably responsible for the small difference between theory and experiment. As shown in Fig. 3.3.4, such a field can change the anticrossing size by this magnitude. We do not have a measurement of the electric field during the time these data were accumulated, because the field changes with time. Therefore a detailed calculation of the effect of the electric field is not possible. However, we estimate that the field was about 0.5 V/cm.

Figures 6.2.6 and 6.2.7 are the second and third anticrossings of Fig. 6.2.1, with their theoretical comparisons. The data of Fig. 6.2.6 were taken in 1986, when only the magneto-resistor probe was available for the determination of the magnetic field. Consequently, the accuracy was lower. The effect of the stray electric field is evident:

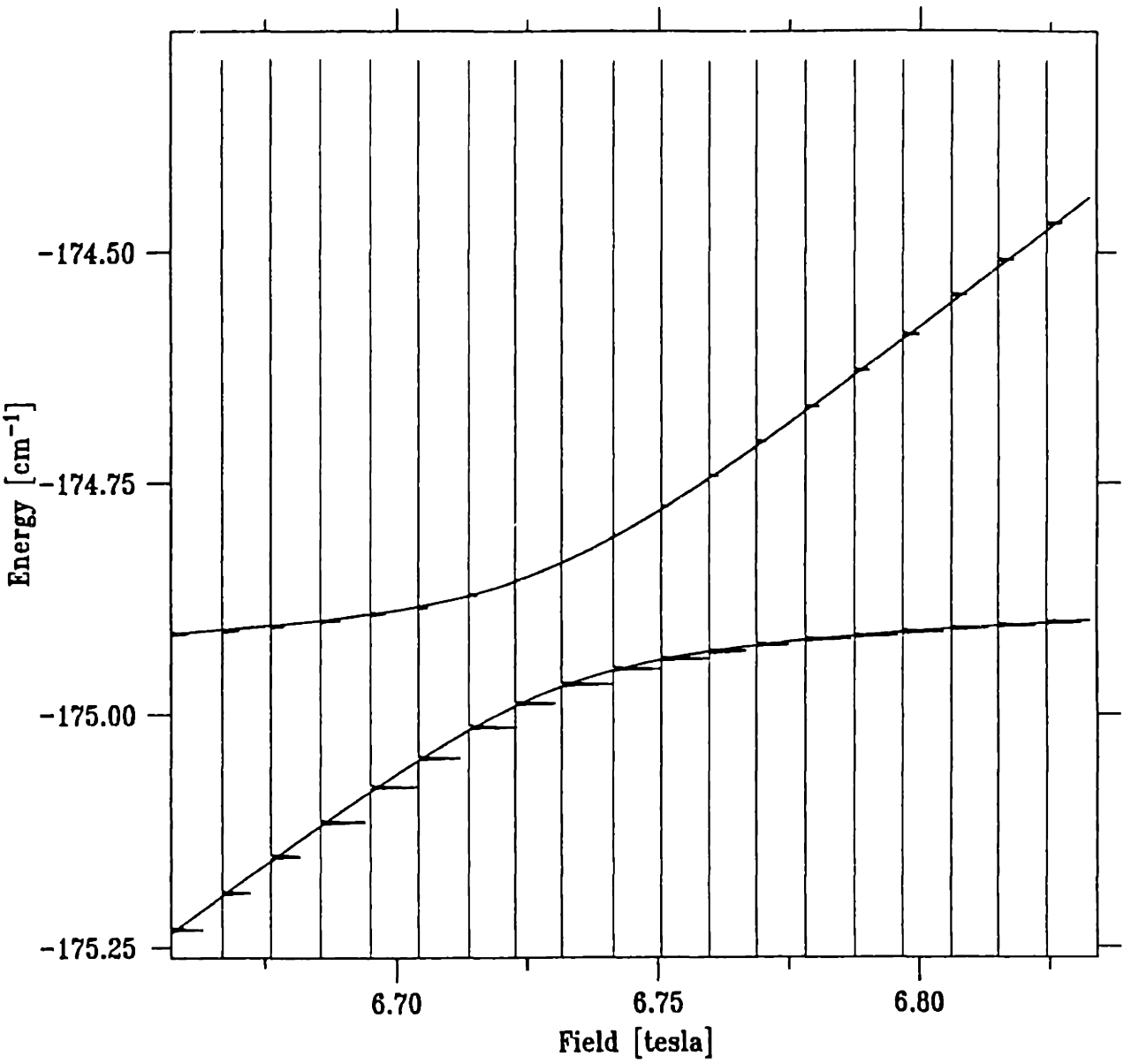

Figure 6.2.3 Overlay of Figs. 6.2.2 and 3.2.1.

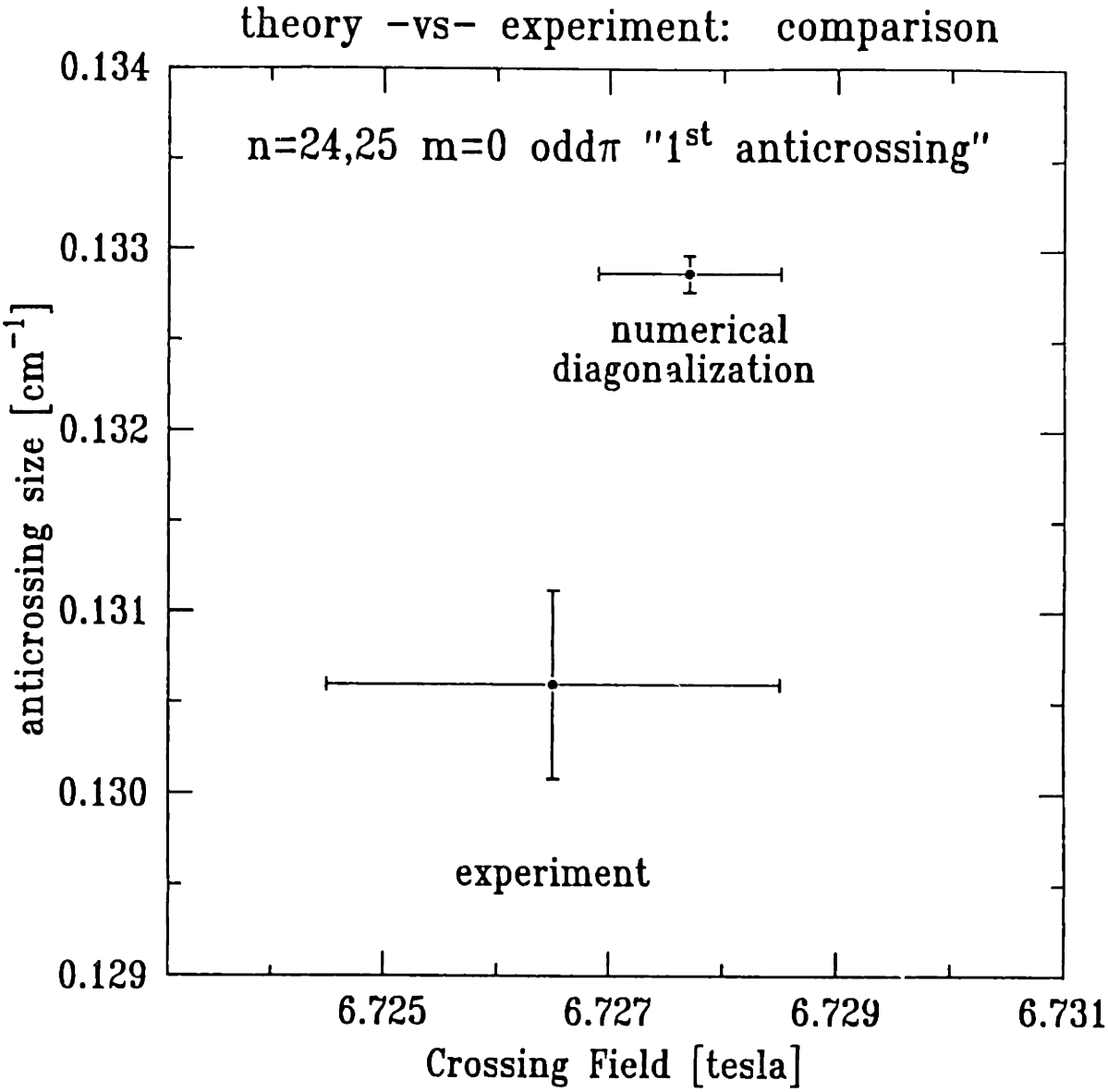

Figure 6.2.4 Comparison of theoretical and experimental anticrossing size and field location in Figs. 6.2.2 and 3.2.1. These parameters were determined by fitting Eq. (3.2.16a) to the calculations and the data.

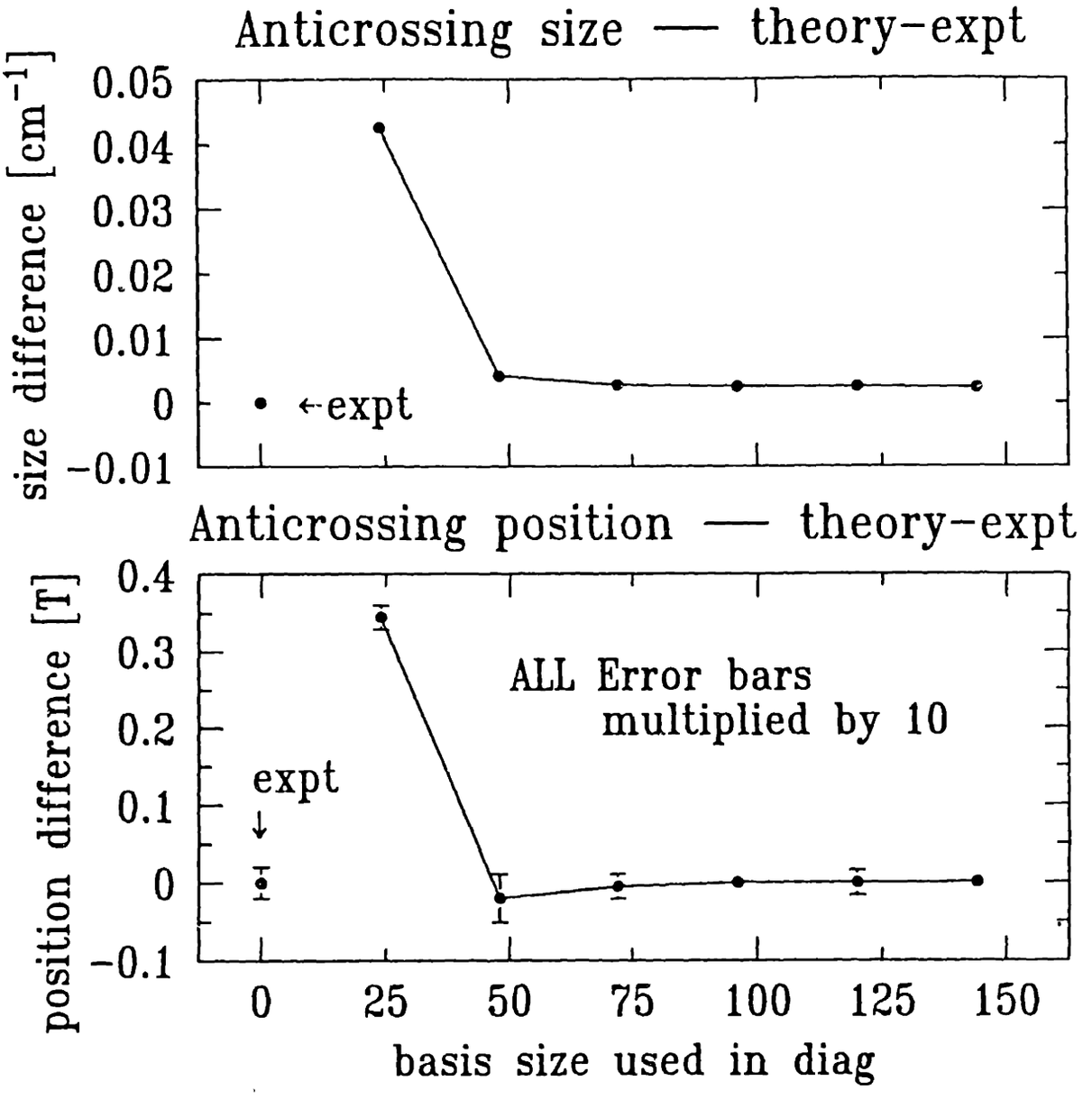

Figure 6.2.5 Theoretical anticrossing size and field location as a function of basis size, for the anticrossing of Fig. 6.2.2.

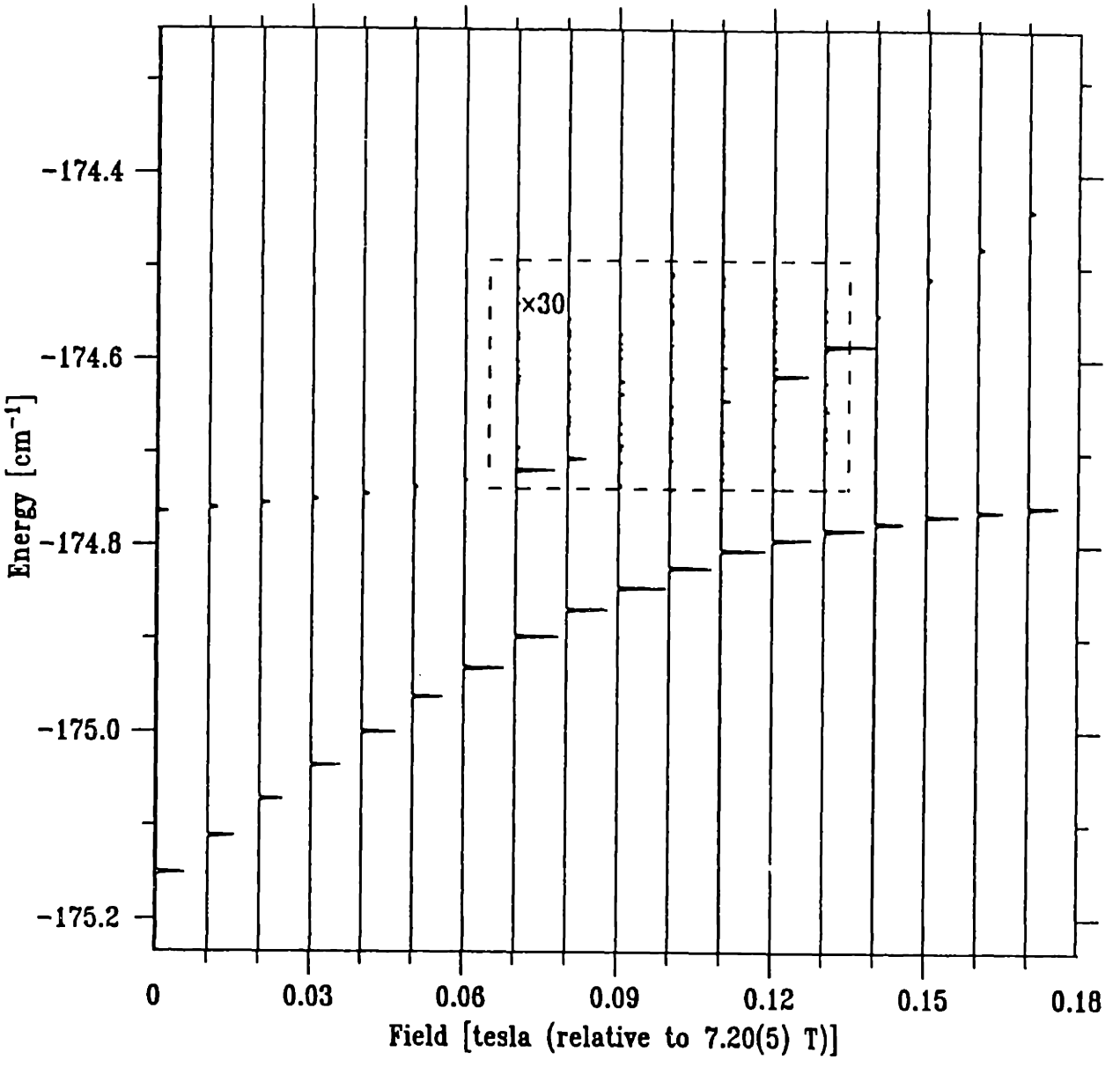

Figure 6.2.6a Anticrossing of states | 25 23 0 > and | 24 3 0 >. This is anticrossing 2 in Fig. 6.2.1. The field measurement has a large uncertainty because this measurement predates the installation of the Hall probe. (Data files 1986: dec 16.47-69)

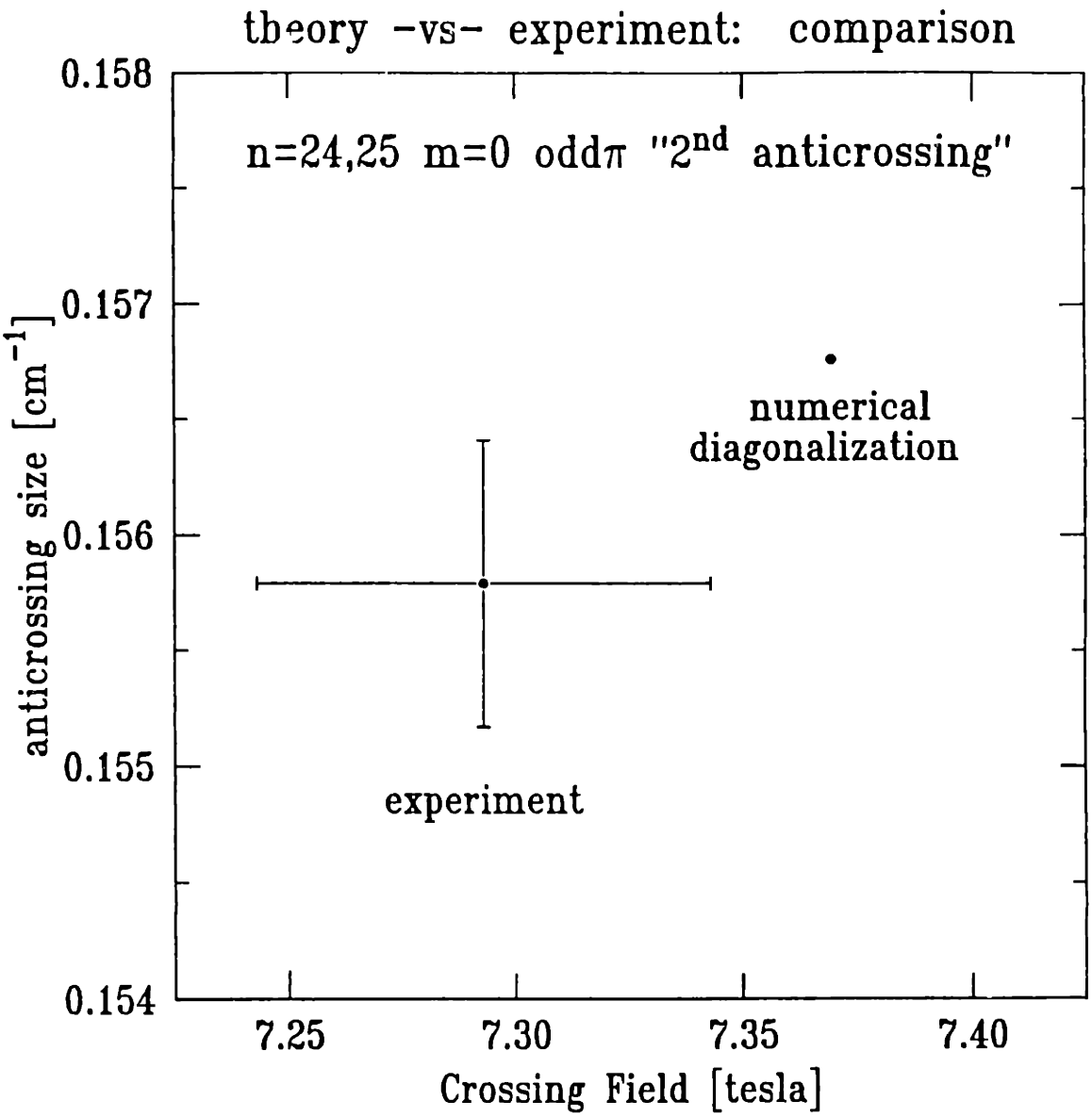

Figure 6.2.6b Anticrossing of states | 25 23 0 > and | 24 3 0 >: comparison of experiment and theory. This is anticrossing 2 in Fig. 6.2.1. The field measurement has a large uncertainty because this measurement predates the installation of the Hall probe. (Data files 1986: dec 16.47-69)

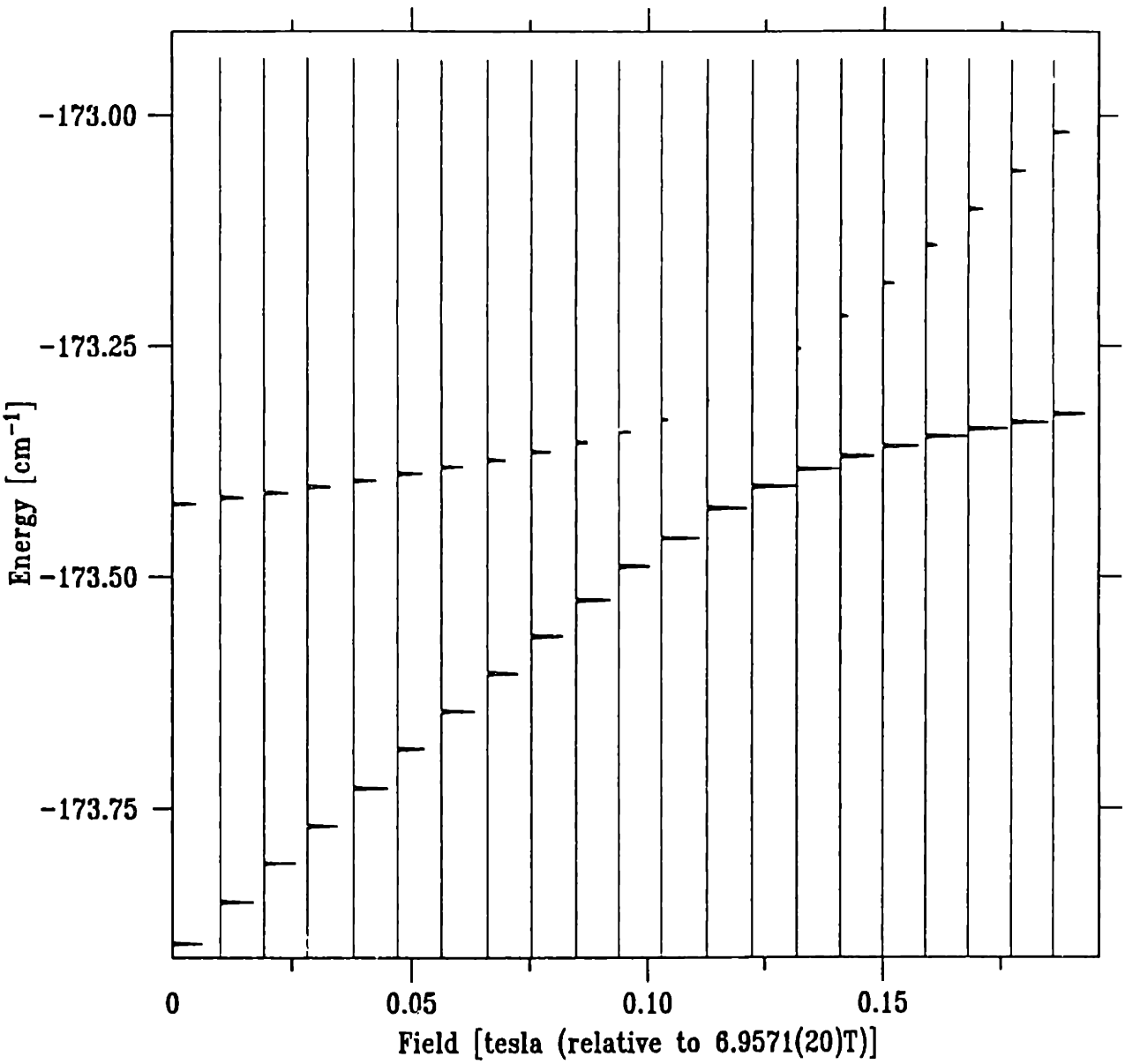

Figure 6.2.7a Anticrossing of states | 25 21 0 > and | 24 1 0 >. This is anticrossing 3 in Fig. 6.2.1. (Data files 1988: jan 21.128-148)

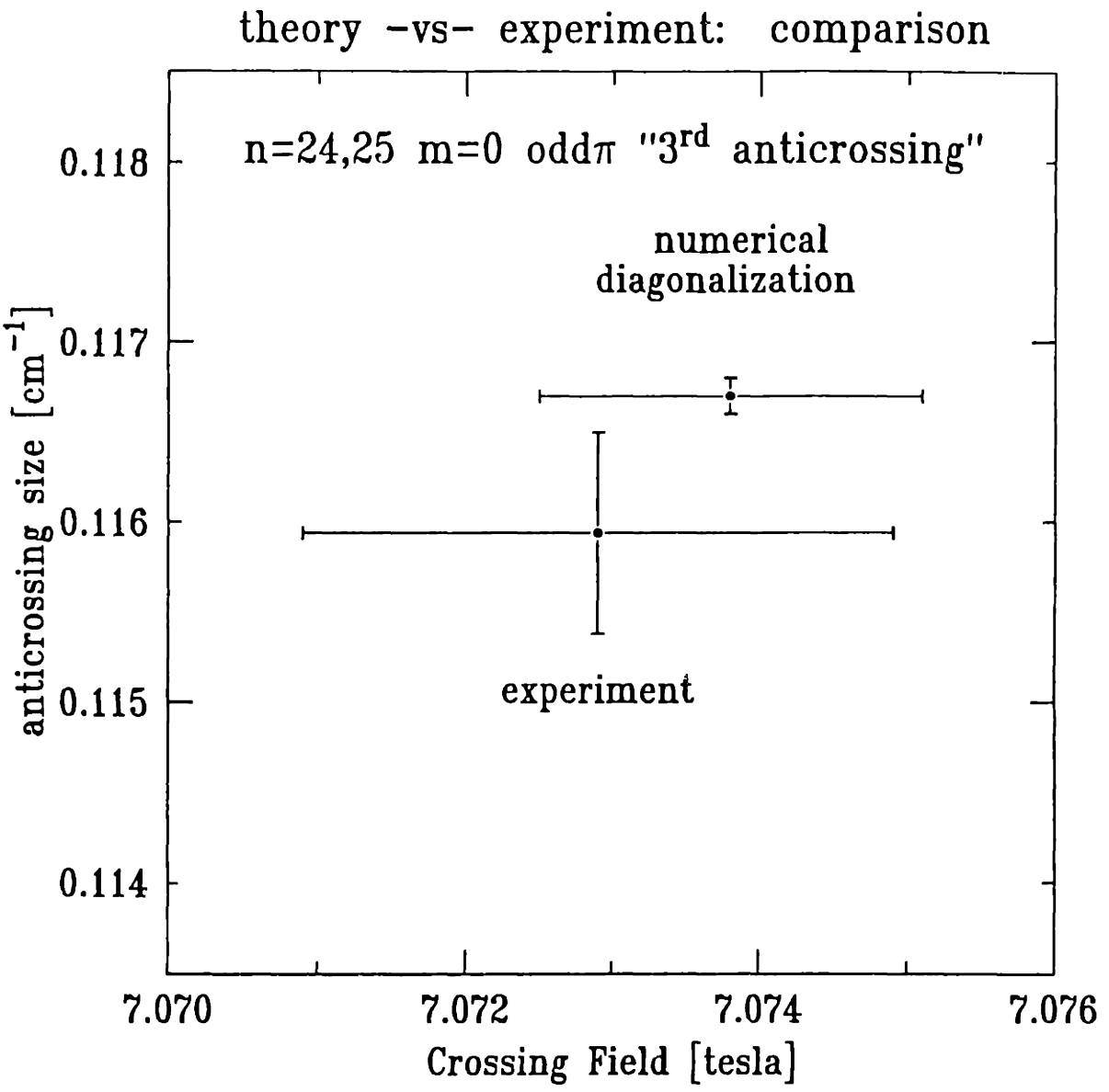

Figure 6.2.7b Anticrossing of states | 25 21 0 > and | 24 1 0 >: comparison of theory and experiment. This is anticrossing 3 in Fig. 6.2.1. (Data files 1988: jan 21.128-148)

for Fig. 6.2.6, the field was probably around 0.2 V/cm, and for Fig. 6.2.7, about 0.5 V/cm.

Electric Field Anticrossings

Figure 6.2.8 shows the anticrossing of odd and even parity states | 25 23 0 > and | 25 24 0 >. (See Fig. 3.1.2 at E=−175 cm^{-1} and B=6.9 T.) As discussed in Sec. 3.2, excitation of the even parity state is not possible; this is mixing induced by the stray electric field. The size is 492(1) MHz; a numerical calculation using second-order perturbation theory (see Eq. (3.3.7)) predicts a z-matrix element of 1536 au. Therefore, the field was about 0.13 V/cm (see Eq. (3.3.10)).

The danger of this phenomenon is that unwanted states appear in the spectrum. In this regime we have accurate calculations available and we are able to assign each state. However, in higher energy ranges, this luxury is absent.

Sometimes the stray electric field is very inhomogeneous. Then the states which are coupled by this field are unusually broad. Figure 6.2.9 shows an example. The odd-parity core-anticrossing states are | 25 23 −1 > and | 24 1 −1 >. The electric field couples in the even parity state | 25 22 −1 >. Note how the transition strength changes between these three levels, and how the broadening increases toward the center of the anticrossing, where the mixing is greatest. Also note that the state | 24 7 1 > goes right through the other states: it is degenerate, but no interaction couples it to the

other states.

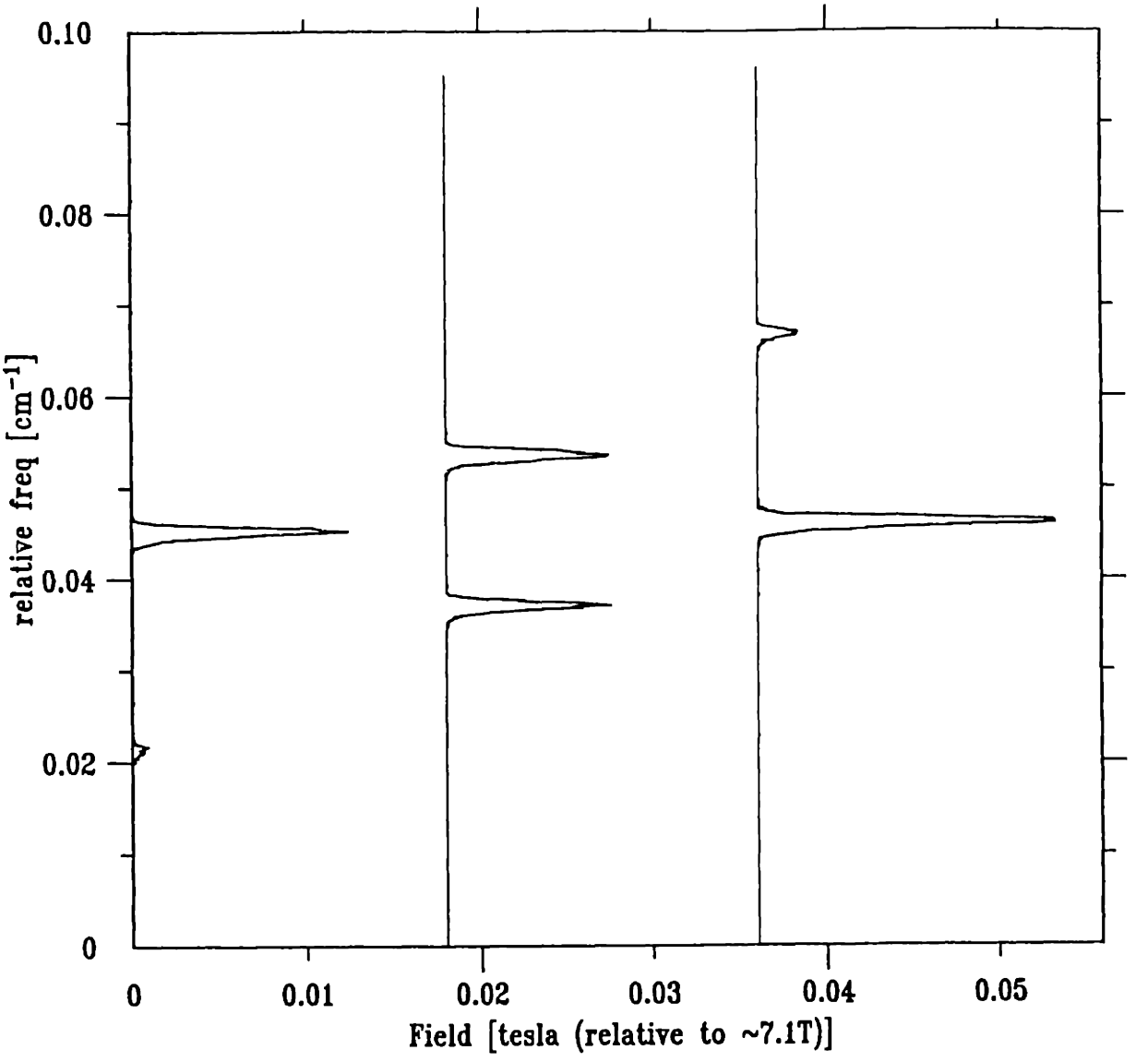

Figure 6.2.8 Anticrossing of the states | 25 23 0 > and | 25 24 0 >. These states are of opposite parity and are coupled by the stray electric field. See Fig. 3.1.2 at E=−175 cm^{-1} and B=6.9 T. (Data files 1986: dec 16.44-46)

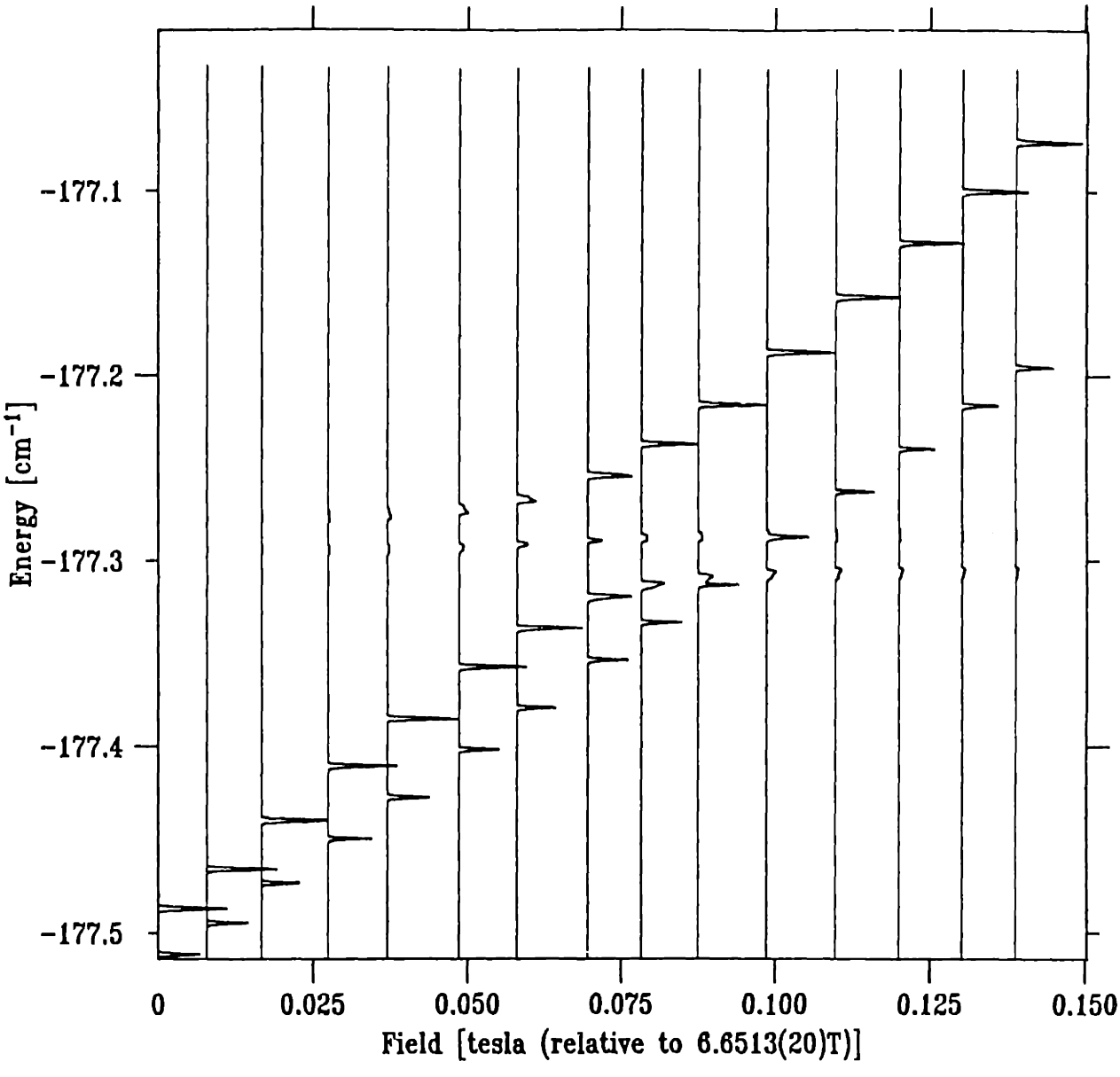

Figure 6.2.9 Anticrossing of states | 25 23 −1 > and | 24 1 −1 >. Also appearing are state | 25 22 −1 >, which is coupled in by the stray electric field, and state | 24 7 1 >, which does not interact with the other states. (Data files 1988: jan 21.86-100)

6.3 Summary

This thesis dealt with the diamagnetism of free atoms in Rydberg states. Theoretical predictions about the energy levels of lithium atoms in a magnetic field were compared carefully with experiment. Those data were the $n=21$ manifold and three core anticrossings near $n=25$. Although the experiment is affected by the presence of a stray electric field, the general level of agreement between experiment and theory is excellent and gives us confidence in both.

The calculations and data presented here are in the regime of weak n-mixing. There is much interest in higher energy ranges, where satisfactory methods for solving Schroedinger's equation do not yet exist. The most straightforward approach would be to increase the number of spherical states in the basis set, but computer memory and computation speed set severe limits. New techniques are needed to handle the contribution of the continuum to the shift of bound states and to predict the energies of states above the zero-field ionization limit. Possibly the coupled-oscillator representation discussed in Sec. 2.3 can be carried forward and also adapted to lithium by a core perturbation such as described in Sec. 3.2. Perhaps a direct numerical solution of the time-independent Schroedinger equation, viewed as two-dimensional boundary-value problem, will become feasible.

The major impact of this work, however, is to provide a firm foundation for investigating the high energy regime with the goal of gaining the physical insight

needed to generate new theoretical approaches. Sometimes it is easier to solve a problem if the answer if known. The role of symmetry is currently obscure in the range $n^3B \gg 1$, though "understanding" a system often means recognizing its symmetries. Perhaps in the future levels and states will be calculated for all energy and field ranges, but a description of the gross structure in simple terms will not be possible. The reverse might also be true. The excitement is in finding out.

Our experiment can be pushed into the higher energy regimes. During a recent run, for example, spectra were taken from 10 cm^{-1} below to 10 cm^{-1} above the zero-field ionization limit, at fields of 3 and 6 T. Qualitatively new features were observed, such as sharp resonances embedded in the continuum. These data will be the subject of future theses.

Appendix. A RECENT HISTORY OF IMPORTANT EVENTS

A difficult experiment is more that just planning, taking data, and interpreting it. George Welch and I spent most of our time trying things that didn't work. Here is a summary of major events that dominated our lives after we inherited the magnet from former Kleppner Group members Myron Zimmerman, Jarbas Castro, and Randy Hulet.

- September 3, 1977: *The History of Atomic Physics*

My advisor said that hydrogen was really discovered at Harvard University in 1959 by Daniel Kleppner (1932-). This discovery generated widespread interest, because prior to that time there was no element with atomic number one. This system revealed so many important phenomena that Kleppner dubbed hydrogen as "the proper study of man."

- November, 1982: *Move into the MIT Spectroscopy Laboratory*

We received operating instructions for dye and ion lasers from Dan Heinzen, Peter Pappas, and LeRoy Bartman.

- January, 1983: *Develop the Mark I interaction chamber*

The original plan was to adapt the design of the interaction chamber which had been used on earlier Kleppner Group pulsed laser experiments. We tried to see Rydberg states by electric field ionization but there was no way to set the wavelength of *both* lasers accurately and to be sure that the lasers were overlapped. We never saw any signal. To convince ourselves that cw lasers really could excite atoms, Mark I was

built. It was placed adjacent to the atomic beam oven, and had Brewster windows and a detection port (all made from microscope slides) arranged so the lasers could cross the atomic beam at right angles. The fluorescence detector was one of George's eyes. I tuned the laser around the 2s→2p wavelength until he screamed that he could see threads of light inside.

- February, 1983: *Adjustable Oven Manifold*

George and I designed the new oven manifold. It used a large diameter bellows to allow on-line oven position adjustment. The fundamental concept was Dan Kleppner's, and it was a good one.

- March, 1983: *Develop the Mark II interaction chamber*

Mark II was also just for fluorescence detection, and was mounted next to the oven. A fiber optic bundle and a photomultiplier tube replaced George's eyes. We carefully studied the laser induced fluorescence from the principal transition, resolving the 2p fine structure, the $2S_{1/2}$ and $2P_{1/2}$ hyperfine structure, and the ^{6}Li-^{7}Li isotope shift. An interesting secret was revealed: the isotope shift of this transition is very nearly equal to the 2p fine structure splitting, and ^{6}Li, $2S_{1/2}$ (F=1/2) → $2P_{3/2}$ (F=3/2, 1/2) lies (almost) on top of ^{7}Li, $2S_{1/2}$ (F=2) → $2P_{1/2}$ (F=1). This probably confused earlier, lower resolution studies.

- April 15, 1983: *Detect cascade fluorescence in Mark II*

The two-photon transition 2s→3s was first observed. We obtained a highly red-

sensitive photomultiplier tube, which we operated in current mode. The output of a Keithley electrometer drove the y-input of an xy-recorder, while the laser internal scan moved the x-position. Interference filters screened out the laser light at 735 nm while passing the 2p→2s cascade fluorescence at 671 nm. Our advisor bought us beer.

- February 1, 1984: *See cascade fluorescence with Mark III*

We learned to do photon counting, and Ishai Nir built Mark III to collect cascade fluorescence inside of the magnet bore. We also kept Mark II to allow us to set the red laser wavelength for the 2s→3s transition. We used two fiber bundles, one inside the vacuum and the other the outside, joined at a window in a Mark II flange. Atoms *really* could be excited inside of the magnet using prisms to bend the laser beam.

- February 16, 1984: *Overlap of laser beams*

Dan Kelleher of NBS Gaithersburg had a terrific plan for overlapping two laser beams. After setting the laser beams to go through the system, deflect the beams with a plane mirror (past the final focusing lens) so as to go through a small pinhole at the desired location. If both lasers get through the pinhole, they are overlapped.

- March 14, 1984: *Detect a Rydberg state in Mark II*

Cascade fluorescence was very useful. Calculations indicated that if enough spectral intensity was applied to the 3s→15p transition, the cascade fluorescence should decrease. While the red laser was producing about 10,000 cps of detected cascade fluorescence, we chopped the yellow laser while scanning near the 3s→15p transition.

Phase sensitive detection revealed a 3-4% dip in the fluorescence with a time constant of 10 seconds. The point was that we could detect Rydberg atoms with no new technology.

- March 23, 1984: *Use a computer to scan and record*

A DEC 11/2 was used as a satellite computer to the laboratory DEC 11/34, via a phone line. (No one could call us while we were taking data.) The ability to scan the laser over subsets of its range and to record many channels of data was a huge advantage. George developed (and continues to develop) phenomenal data acquisition programs. Tom Scott wrote the operating system.

- July, 1984: *A New Spec Lab Drain*

The Spec Lab was built in 1932 with drains which were never meant to carry the cooling water from so many ion lasers. That summer, if more than about three lasers were running simultaneously anywhere in the building, the sink in our pump room would overflow. George suggested sealing our drain so that the sinks upstairs would overflow instead. Deputy Director Ramachandra Dasari contacted Jim Gardner, an *absolutely great* guy from Physical Plant. Jim knew exactly how the Spec Lab drains left the building via a large central drain in the courtyard of buildings 4, 6, and 8, and then connected to "the river line," a huge culvert which lies between and parallel to buildings 4 and 6, and runs directly into the Charles River, terminating equidistant from the Harvard Bridge and the Wood sailing pavilion. Jim reasoned that there was

an obstruction in the pipe between the Spec Lab and the central courtyard drain, and "because research gets top priority," decided to add a new drain immediately. Two days after our first meeting, a 4" diam PVC pipe connected room 6A-160 directly to the river line. Soon all lasers on the south side of the building were attached to this drain and the problem was solved. This was by far our best experience with Physical Plant.

- August 23, 1984: *Get a wavemeter*

A manually operated Michelson wavemeter was constructed by Ishai and George. This made the Heath monochromator obsolete: the laser frequency could now be set reproducibly to 10 GHz with the wavemeter. The number 1.16136 became etched in our brains, as the number of HeNe wavelengths in the two-photon transition.

- November 5, 1984: *Install Mark IV*

Mark IV was designed to be the ultimate in interaction chambers. George made it to go inside of the magnet, to have good optical collection for cascade fluorescence, and to be floated to high voltage for electric field ionization. However, the first month of operation was devoted to reducing laser light scattered into the fiber bundle.

- December 4, 1984: *Rydberg states inside of the magnet*

Decreased cascade fluorescence was used to detect the 15p state inside of Mark IV. The inner surfaces of Mark IV were made black with incompletely burned acetylene to reduce light scattering.

- March 3, 1985: *Rydberg states seen with field ionization*

We found that the "un-ruggedized" surface barrier diode electron detectors are light sensitive; ruggedized types must be used. After polishing Mark IV to a mirrored finish, it could be floated to 10-20 kV. We set the lasers to produce 25p states as detected by decreased cascade fluorescence and then turned up the HV. The electron signal was huge. But it was all rather anticlimatic: we had *forced* it to work.

- April 21, 1985: *Install an iodine reference cell*

Jeff Norman "lent" us a 1-1/2 foot long iodine cell. We used it in absorption mode and in combination with our 300 MHz spectrum analyzer and the appropriate atlas, the cell allowed accurate laser wavelength determination. George proclaimed the cell "the most useful thing per unit effort in our experiment."

- June 6, 1985: *First operation of the magnet*

We learned to handle liquid helium. Calibration of the magneto-resistor probe was attempted by measuring the 2s→2p transition in a magnetic field. Rydberg states were not investigated because the krypton-ion laser had died on May 20, 1985, so we couldn't drive 2s→3s.

- September 3, 1985: *Chun-ho Iu arrives*

John Iu, George and I became the $\vec{B}$ team. Among John Iu's many contributions was the development of a data analysis program which assigned the absolute frequency of Rydberg atom resonances.

- December 12, 1985: *New krypton-ion tube*

LeRoy Bartman installed the new plasma tube. It looked marvelous. Now we could study Rydberg atoms. Shortly thereafter, we found that there was a large electric field inside of our interaction chamber. We put iso-dag inside of Mark IV instead of acetylene black to increase the surface conductivity. That reduced the field to about 1 volt/cm.

- February 16, 1986: *Protect the detector*

Our surface barrier diode electron detectors were being destroyed by the lithium atomic beam. A material which passed electrons and stopped lithium atoms was needed. Dan Kleppner suggested a company which made carbon foils. Nuclear physicist E.J. Beise indicated that a sufficiently thin foil should not scatter electrons significantly. The foil was mounted on a copper mesh and did effectively protect the detector without seriously reducing the electron counting rate.

- April 21, 1986: *Atmospheric pressure affects the spectrum analyzer*

Using the iodine reference cell, we investigate the stability of the transmission peaks of the 300 MHz spectrum analyzer. Although the etalon was in a temperature box stabilized to about 0.1°C, the peaks shift with changes in atmospheric pressure. The drift was correlated with the barometric pressure recorded at the Meteorology and Physical Oceanography Center. Later, (July 10, 1986) the etalon was placed in a pressure sealed can.

- August 4, 1986: *Bake Mark IV*

After much study it was found that the stray electric field could be reduced if prior to the run, Mark IV was baked for ~1 day @ 150°C. But the field increased while running the atomic beam through the interaction chamber.

- December 16, 1986: *Rydberg atoms in a magnetic field*

The goal was achieved. Our advisor bought us champagne. We found that our magnetic field calibration was inadequate and that the electric field produced substantial parity mixing. Much more work was needed to reduce the electric field, to stop high voltage breakdowns, to measure laser wavelengths, and to determine the magnetic field at the atom-laser intersection.

REFERENCES

ABB84 D. Abbott, *The Biographical Dictionary of Scientists: Physicists,* (Peter Bedrick Books, New York, 1984).

ABS70 M. Abramowitz and I.A. Stegen, eds., *Handbook of Mathematical Functions,* (Dover, New York, 1970), p. 506, #13.3.7.

AIV77 E. Arimondo, M. Ingucio, and P. Violino, Rev. Mod. Phys. *49,* 31 (1977). "Experimental determinations of the hyperfine structure in the alkali atoms."

AMI81 American Magnetics, Inc., *Selection Guide,* (P.O. Box 2501, Oak Ridge TN 37831), pp. 1-4.

BAY73 G. Baym, *Lectures on Quantum Mechanics,* (Addison-Wesley, Reading MA, 1973), p. 179. The reference is to problem #3.

BBE74 A. Beckmann, K.D. Böklen, and D. Elke, Z. Phys. *270,* 173 (1974). "Precisions Measurements of the Nuclear Magnetic Dipole Moments of ^{6}Li, ^{7}Li, ^{23}Na, ^{39}K, and ^{41}K."

BES57 H.A. Bethe and E.E. Salpeter, *Quantum Mechanics of One- and Two-Electron Atoms,* (Springer-Verlag, Berlin, 1957), p. 227. This discusses the ground state diamagnetism of helium.

BEW67 K.C. Brog, T.G. Eck, and H. Wieder, Phys. Rev. *153,* 91 (1967). "Fine and Hyperfine Structure of the 2^2P Term of Li^6 and Li^7."

CAS81 J.C. Castro, Ph.D. Thesis, MIT, 1981. "Highly Excited Magnetic Atoms."

CDL77 C. Cohen-Tannoudji, B. Diu, and F. Laloë, *Quantum Mechanics,* (Wiley, New York, 1977).

CFF77 C.F. Fischer, *The Hartree-Fock Method for Atoms,* (Wiley-Interscience, New York, 1977), p. 28.

CIV82 J. Cizek and E.R. Vrscay, Int. J. Quant. Chem. *21,* 27 (1982). "Large Order Perturbation Theory in the Context of Atomic and Molecular Physics — Interdisciplinary Aspects.

CLA81 C.W. Clark, Phys. Rev. A *24,* 605 (1981). "Case of broken symmetry in the

quadratic Zeeman effect."

CLP86a P. Cacciani, E. Luc-Koenig, J. Pinard, C. Thomas, and S. Liberman, J. Phys. B: At. Mol. Phys. *19*, L519 (1986). "Anticrossing effects in odd Rydberg states of Li in the presence of a magnetic field."

CLP86b P. Cacciani, E. Luc-Koenig, J. Pinard, C. Thomas, and S. Liberman, Phys. Rev. Lett. *56*, 1124 (1986). "Experimental Studies of a Diamagnetic Multiplet in Odd Rydberg States of Lithium."

COG87 E.R. Cohen and P. Giacomo, Physica *146A*, 1 (1987). "Symbols, Units, Nomenclature and Fundamental Constants in Physics."

COH82 Coherent, *CR-699 Ring Lasers*, (Coherent Inc., Palo Alto CA, 1982).

COH84 Coherent, *CR-599 Dye Laser Systems*, (Coherent Inc., Palo Alto CA, 1984), p. 2.

COH86 Coherent, *Innova 100 Series Ion Laser Manual*, (Coherent Inc., Palo Alto CA, 1986), p. 5-3.

COS51 E.U. Condon and G.H. Shortley, *The Theory of Atomic Spectra*, (Cambridge University, London, 1951).

CZH80 J.C. Castro, M.L. Zimmerman, R.G. Hulet, D. Kleppner, and R.R. Freeman, Phys. Rev. Lett. *45*, 1780 (1980). "Origin and Structure of the Quasi-Landau Resonances."

DAL55 A. Dalgarno and J.T. Lewis, Proc. Roy. Soc. (London) *A233*, 70 (1955). "The exact calculation of long-range forces between atoms by perturbation theory."

DAV63 J.T. Davies and J.M. Vaughan, Astrophys. Journ. *137*, 1302 (1963). "A New Tabulation of the Voigt Profile."

DEG84 D. Delande and J.C. Gay, J. Phys. B: At. Mol. Phys. *17*, L335 (1984). "Group theory applied to the hydrogen atom in a strong magnetic field. Derivation of the effective diamagnetic Hamiltonian."

DEG86 D. Delande and J.C. Gay, J. Phys. B: At. Mol. Phys. *19*, L173 (1986). "The hydrogen atom in a magnetic field. Spectrum from the Coulomb

dynamical group approach."

DMO69 Y.N. Demkov, B.S. Monozon, and V.N. Ostrovskii, Zh. Eksp. Teor. Fiz. *57*, 1431 (1969). [JETP *30*, 775 (1970).] "Energy Levels of a Hydrogen Atom in Crossed Electric and Magnetic Fields."

EDL49 B. Edlén and K. Lidén, Phys. Rev. *75*, 890 (1949). "A Note on the Arc Spectrum of Lithium."

EDL53 B. Edlén, Journ. Opt. Soc. Am. *43*, 339 (1953). "The Dispersion of Standard Air."

EGG80 EG&G/Ortec, *Condensed Product and Application Information*, (EG&G/Ortec, Oak Ridge TN, 1980), pp. 10-20.

EIS48 L.P. Eisenhart, Phys. Rev. *74*, 87 (1948). "Enumeration of Potentials for Which One-Particle Schroedinger Equations are Separable."

ENG72 M.J. Englefield, *Group Theory and the Coulomb Problem*, (Wiley-Interscience, New York, 1972).

FLU74 S. Flügge, *Practical Quantum Mechanics*, (Springer-Verlag, Berlin, 1974), Vol. II, pp. 257-258.

FOC35 V. Fock, Z. Phys. *98*, 145 (1935). "Contributions to the Theory of the Hydrogen Atom." Fritz Buchinger translated this article for us.

GAD87 J.C. Gay and D. Delande, Few-Body Systems, Suppl. 2, 280 (1987). "Probing the quantum theory of chaos with atoms in external fields."

GAP76 A. Galindo and P. Pascual, Il Nuovo Cimento *34B*, 155 (1976). "Hydrogen Atom in a Strong Magnetic Field."

GAR77 R.H. Garstang, Rep. Prog. Phys. *40*, 105 (1977). "Atoms in high magnetic fields."

GAT69 W.R.S. Garton and F.S. Tomkins, Astrophys. Journ. *158*, 839 (1969). "Diamagnetic Zeeman effect and magnetic configuration mixing in long spectral series of Ba I."

GAY84 J.C. Gay, in *Progress in Atomic Spectroscopy, Part C*, edited by H.J. Beyer

and H. Kleinpoppen (Plenum, New York, 1984), pp. 177-246. "High-Magnetic-Field Atomic Physics." The references contained in this paper are extensive.

GAY86 J.C. Gay in *Atoms in Unusual Situations*, ed. J.P. Briand (Plenum, New York, 1986), pp. 107-152. "The Structure of Rydberg Atoms in Strong Static Fields."

GBG77 G. Grynberg, F. Biraben, E. Giacobino, and B. Cagnac, Journ. de Phys., *38*, 629 (1977). "Doppler-Free Two-Photon Spectroscopy of Neon. II. Line Intensities."

GEL78 S. Gerstenkorn and P. Luc, *Atlas of the Absorption Spectra of Molecular Iodine for 14,800 to 20,000 cm^{-1}*, (C.N.R.S., Paris, 1978). We subtract 0.005 cm^{-1} from all entries, as per instructions in GVC82.

GIL74 C.C. Gillispie, *Dictionary of Scientific Biography*, (Charles Scribner's & Sons, New York, 1974).

GLG86 P. Goy, J. Liang, M. Gross, and S. Haroche, Phys. Rev. A *34*, 2889 (1986). "Quantum defects and specific-isotope-shift measurements in ns and np highly excited states of lithium: Exchange effects between Rydberg and core electrons."

GVC82 S. Gerstenkorn, J. Verges, and J. Chevillard, *Atlas of the Absorption Spectra of Molecules Iodine for 11,000 to 14,000 cm^{-1}*, (C.N.R.S. II, Aime Cotton, 1982).

HAM75 C.R. Hammond in *CRC Handbook of Chemistry and Physics*, 56th ed. (Chemical Rubber, Cleveland OH, 1975), p. B-22. "The Elements."

HAR28 D.R. Hartree, Proc. Camb. Phil. Soc. *24*, 426 (1928). "The Wave Mechanics of an Atom with a non-Coulomb Central Field. Part III. Term Values and Intensities in Series in Optical Spectra."

HAR58 D.R. Hartree, *Numerical Analysis*, 2nd ed. (Oxford University, London, 1958), pp. 142-143. The reported formula actually solves $y'' = f(x)y + g(x)$.

HAR69 G.R. Harrison, *MIT Wavelength Tables*, 1969 ed. (MIT Press, Cambridge MA, 1969).

HBH81 X. Hui-Rong, S.V. Benson, and T.W. Hänsch, Laser Focus, 55 (March, 1981.) "A 'toy-train' wavemeter."

HER82 D. Herrick, Phys. Rev. A *26*, 323 (1982). "Symmetry of the quadratic Zeeman Effect for Hydrogen."

HOH80 P. Horowitz and W. Hill, *The Art of Electronics*, (Cambridge University, Cambridge, 1980), pp. 216-218.

HRW81 H. Herold, H. Ruder, and G. Wunner, J. Phys. B: At. Mol. Phys. *14*, 751 (1981). "The two-body problem in the presence of a homogeneous magnetic field." They actually present a more general generalized momentum which applies to an n particle system in a uniform, constant magnetic field. Interestingly, the components all commute only for charge neutral systems.

HUK83 R.G. Hulet and D. Kleppner, Phys. Rev. Lett. *51*, 1430 (1983). "Rydberg Atoms in 'Circular' States."

HWM86 A. Holle, G. Wiebusch, J. Main, B. Hager, H. Rottke, and K. H. Welge, Phys. Rev. Lett. *56*, 2594 (1986). "Diamagnetism of the Hydrogen Atom in the Quasi-Landau Regime."

JBP82 T.F. Johnston, Jr., R.H. Brady, and W. Proffitt, Appl. Opt. *21*, 2307 (1982). "Powerful single-frequency ring dye laser spanning the visible spectrum."

JES39 F.A. Jenkins and E. Segrè, Phys. Rev. *55*, 52 (1939). "The Quadratic Zeeman Effect."

JHR79 T.F. Johnston, Jr., J.L. Hobart, R.C. Rempel, and G.H. Williams, U.S. Patent 4,150,342 (1979).

JIR87 M. Jirmanus, Janis Research Company, October 6, 1987 (private communication).

JOH59 I. Johansson, Arkiv för Fysik *15*, 169 (1959). "The infrared spectrum of Li I."

KAW87 M.M. Kash and G.R. Welch, *Rules of Resonance*, unpublished notes, MIT, 1987.

KGJ80 I.V. Komarov, J.P. Grozdanov, and R.K. Janev, J. Phys. B: At. Mol. Phys.

13, L573 (1980). "Influence of the atomic core on the Stark structure of alkali atom Rydberg states."

KOC78 P.M. Koch, Phys. Rev. Lett. *41*, 99 (1978). "Resonant States in the Nonperturbative Regime: The Hydrogen Atom in an Intense Electric Field."

KNS78 J. Kowalski, R. Neuman, H. Suhr, K. Winkler, and G. zu Putlitz, Z. Phys. A *287*, 247 (1978). "Two-Photon Intracavity Dye Laser Spectroscopy of the 4S and 3D Terms in ^{6,7}Li." The authors incorrectly evaluated the Fermi-Segrè formula and the normal mass shifts. The correct calculations are actually much closer to their data.

KWI88 M.M. Kash, G.R. Welch, and C. Iu, unpublished data. (Data files 1988: apr 19.6-10).

LAB81 J.J. Labarthe, J. Phys. B: At. Mol. Phys. *14*, L467 (1981). "A basis for the study of the quadratic Zeeman effect in atomic hydrogen."

LAL77 L.D. Landau and E.M. Lifshitz, *Quantum Mechanics (non-relativistic theory)*, 3rd ed. (Pergamon, Oxford, 1977).

LES78 C.M. Lederer and V.S. Shirley, *Table of Isotopes*, 7th ed. (Wiley-Interscience, New York, 1977).

LIT70 U. Litzén, Phys. Scrip. *1*, 253 (1970). "The 5g Levels of the Alkali Metals."

LKK78 M.G. Littman, M.M. Kash, and D. Kleppner, Phys. Rev. Lett. *41*, 103 (1978). "Field-Ionization Processes in Excited Atoms."

MAR80 W.C. Martin, J. Opt. Soc. Am. *70*, 784 (1980). "Series formulas for the spectrum of atomic sodium (Na I)."

MER70 E. Merzbacher, *Quantum Mechanics*, 2nd ed. (Wiley, New York, 1970), pp. 428-429.

MMS48 K.W. Meissner, L.G. Mundie, and P.H. Stelson, Phys. Rev. *74*, 932 (1948). "Structure of the ^{2}D Terms of the Arc Spectrum of Lithium."

MMS49 K.W. Meissner, L.G. Mundie, and P.H. Stelson, Phys. Rev. *75*, 891 (1949). "Erratum: Structure of the ^{2}D Terms of the Arc Spectrum of Lithium."

MTW65 J.H.E. Mattauch, W. Thiele, and A.H. Wapstra, Nucl. Phys. *67*, 1 (1965). "1964 Atomic Mass Table."

NES63 A.N. Nesmeyanov, *Vapor Pressure of the Chemical Elements*, (Elsevier, New York, 1963), p. 423.

NUM33 B. Numerov, Publ. de l'Observ. astrophysique Central de Russie *2*, 188 (1933).

ORE82 J. Orear, Am. J. Phys. *50*, 912 (1982). "Least squares when both variables have uncertainties."

ORT67 J. Ortega in *Mathematical Methods for Digital Computers*, edited by A. Ralston and H.S. Wilf (Wiley, New York, 1967), Vol. II, pp. 94-115. "The Givens-Householder method for symmetric matrices."

PAR60 D. Park, Z. Phys. *159*, 155 (1960). "Relation Between the Parabolic and Spherical Eigenfunctions of Hydrogen."

PAU26 W. Pauli, Z. Phys. *36*, 336 (1926). English translation in *Sources of Quantum Mechanics*, ed. B.L. van der Waerden (Dover, New York, 1968), pp. 387-415. "On the Hydrogen Spectrum from the Standpoint of the new Quantum Mechanics."

PFT88 W.H. Press, B.P. Flannery, S.A. Teukolsky, and W.T. Vetterling, *Numerical Recipes in C*, (Cambridge University, Cambridge, 1988).

PIK74 C.T. Pike, Opt. Commun. *10*, 14 (1974). "Spatial Hole Burning in cw Dye Lasers."

PKE80 B.A. Palmer, R.A. Keller, and R. Engleman, Los Alamos Informal Report #LA-8251-MS, 1980. "An Atlas of Uranium Emission Intensities in a Hollow Cathode Discharge."

RAM56 N. Ramsey, *Molecular Beams*, (Oxford University, Oxford, 1956).

RIC83 D. Richards, J. Phys. B: At. Mol. Phys. *16*, 749 (1983). "The quadratic Zeeman effect for weak fields on hydrogen."

RNS75 L.G. Rubin, D.R. Nelson, H.H. Sample, Rev. Sci. Instrum. *46*, 1624 (1975). "Characterization of two commercially available Hall effect sensors for high

magnetic fields and low temperatures."

ROS73 A.C. Rose-Innes, *Low Temperature Laboratory Techniques,* 2nd ed. (English University Press, Ltd., London, 1973), pp. 19-20.

SAK67 J.J. Sakurai, *Advanced Quantum Mechanics,* (Addison-Wesley, Reading MA, 1967), p. 119.

SCH68 L.I. Schiff, *Quantum Mechanics,* 3rd ed. (McGraw-Hill, New York, 1968), pp. 245-248.

SCS39 L.I. Schiff and H. Snyder, Phys. Rev. *55,* 59 (1939). "Theory of the Quadratic Zeeman Effect."

SIH75 J.S. Sims and S.A. Hagstrom, Phys. Rev. A *11,* 418 (1975). "Combined configuration-interaction-Hylleras studies of atomic states. III. The four lowest ^{2}S and four lowest ^{2}P states of lithium."

SIL78 H.J. Silverstone, Phys. Rev. A *18,* 1853 (1978). "Perturbation theory of the Stark effect in hydrogen to arbitrarily high order."

SIM81 H.J. Silverstone and R.K. Moats, Phys. Rev. A *23,* 1645 (1981). "Practical recursive solution of degenerate Rayleigh-Schroedinger perturbation theory and application to high-order calculations of the Zeeman effect in hydrogen."

SOB72 I.I. Sobel'man, *Introduction to the Theory of Atomic Spectra,* (Pergamon, Oxford, 1972).

WAL82 R.E. Walkup, Ph.D. Thesis, MIT, 1982.

WEA75 R.C. Weast, *CRC Handbook of Chemistry and Physics,* 56th ed. (Chemical Rubber Company, Cleveland, 1975), p. E-224.

WEI78 M. Weissbluth, *Atoms and Molecules,* (Academic Press, New York, 1978).

WEL68 M.E. Weeks and H.M. Leicester, *Discovery of the Elements,* 7th ed. (Journ. Chem. Ed., Easton PA, 1968).

WIL83 M.N. Wilson, *Superconducting Magnets,* (Oxford University, Oxford, 1983).

WUR82 G. Wunner and H. Ruder, Journ. de Phys. C2, *43,* 137 (1982). "Energy

levels and electromagnetic transitions of atoms in superstrong magnetic fields." See Fig. 2.

WWZ86 G. Wunner, U. Woelk, I. Zech, G. Zeller, T. Ertl, F. Geyer, W. Schweitzer, and H. Ruder, Phys. Rev. Lett. *57*, 3261 (1986). "Rydberg Atoms in Uniform Magnetic Fields: Uncovering the Transition from Regularity to Irregularity in a Quantum System." See Fig. 3(a).

WZW87 G. Wunner, G. Zeller, U. Woelk, W. Schweizer, R. Niemeier, F. Geyer, H. Friedrich, and H. Ruder in *Physics of Atoms and Molecules*, edited by K.T. Taylor (Plenum, Oxford, 1987). "Strongly Magnetized Atoms - In the Laboratory and in the Cosmos."

ZCK78 M.L. Zimmerman, J.C. Castro, and D. Kleppner, Phys. Rev. Lett. *40*, 1083 (1978). "Diamagnetic Structure of Na Rydberg States."

ZKK80 M.L. Zimmerman, M.M. Kash, and D. Kleppner, Phys. Rev. Lett. *45*, 1092 (1980). "Evidence of an Approximate Symmetry for Hydrogen in a Uniform Magnetic Field."

ZKW82 M.L. Zimmerman, M.M. Kash, and G.R. Welch, Journ. de Phys. C2, *43*, 113 (1982). "Avoided Crossings and Autoionization Widths of Hydrogen and Alkali Metals in a Magnetic Field."

ZLK79 M.L. Zimmerman, M.G. Littman, M.M. Kash, and D. Kleppner, Phys. Rev. A *20*, 2251 (1979). "Stark Structure of the Rydberg states of alkali-metal atoms."

ACKNOWLEDGEMENTS

Many people helped me throughout my graduate student career. Some provided financial support or professional guidance, while others improved the quality of life. Everyone in the Kleppner Group contributed time and effort to produce this document.

George Robert Welch began working with me on his arrival here in June of 1979. Together, we survived the "triple Michelson mode selector," a device for making a high power, standing wave cw dye laser. We think it worked one afternoon. His practical approach to everything profoundly increased the speed at which things were accomplished, and his clear view of many aspects of physics and mathematics kept me from going too far astray. He miraculously made Mark IV, deftly sends the laser beams through it, mysteriously aligns the wavemeter, and avidly programs many computers. He is the "Son of Unix Man." His good nature generally elevates laboratory conditions. George often assumes the most literal meaning in what is said to him. He plays with things until he understands them thoroughly, or until they break or he hurts himself. He produced 38 of the figures in this thesis, and read chapters 3, 4, and 5.

Chun-ho Iu joined our subgroup in September of 1985, and immediately began developing data analysis programs. He is experienced with many numerical algorithms, and "can integrate anything." He has a theory to explain all phenomena,

real or imagined. He understands physics quite well. Using C-PLOT, Chun-ho created the drawings of the apparatus, and contributed 21 figures in all. He also knows when things "look marvelous."

Long Hsu left electrical engineering to become a physicist. He has created many useful circuits which help the experiment, is learning about ring dye lasers, and has the best handwriting in the history of civilization. He made 6 of the figures in this document, including all of the circuit diagrams.

Barbara Joan Hughey (Beckwitt) brought classical music and high energy into the environment. She is skilled in both experiment and theory, and knows more than anyone about microwave cavities that are resonant with the 46s $\rightarrow$ 46p transition in calcium. She typed much of the reference section, and proofread chapters 3 and 5.

Thomas Richard Gregory Gentile introduced me to pizza, ice cream, and his wife, Elizabeth Jane Beise. All of these are *very* good things. His lab is extremely well organized. Tom is so neat that Paramount Pictures consulted him as technical advisor for Felix Unger in "The Odd Couple." He is extremely careful and thorough on all things, and I am confident that his efforts will be rewarded with experimental success, and also with recognition for his substantial contributions to the laboratory. He read chapters 2 and 4 of this thesis. Betsy and Tom drew Fig. 4.4.4 (a) and (b), respectively.

Scott Nelson Paine is the only Laker's fan in the lab. Also known as "Mr. UHV," Scott's proudest moment was reaching the 10^{-10} Torr scale on the ionization gauge in his apparatus. He carefully plans everything he does, and rarely has to do anything twice. He is a gifted experimentalist. He checked chapters 1 and 6, and the appendix. He also made 4 figures, and mounted most of the others.

Pin Peter Chang kept my spirits high with his constant impersonation of Rodney Dangerfield. Peter is an extremely perceptive physicist, who is able to define clearly problems and solve them. His favorite pastimes are drinking strong tea and searching for his cup.

Andrea Leigh Gelinas expertly typed most of the thesis, though she had to leave before it was complete. She is the undisputed Master of Troff, and was always willing and able to take my meaningless scratchings and instantly turn them into respectable documents. Andrea recently married Thomas Patrick Scott III, "Unix Man." Tom helped me see MIT in a special light.

Professor Theodore William Ducas often provided insight into whatever problem was under consideration. He is the fastest man alive. Ted has been known to tell a joke, align a dye laser, drink half-a-cup of coffee, and go to France, all before people begin to laugh at his joke. He knows much about laser spectroscopy.

To the current members of my group, I express sincere gratitude and best wishes for the future.

I benefited greatly from interactions with former group members Bill Phillips, Mike Littman, Myron Zimmerman ("Father of Unix Man"), Jan Rubbmark, Fritz Buchinger, Bill Spencer, Ganesh Vaidyanathan, Jarbas Castro, Randy Hulet, Larry Brewer, Zhong Xubin, Ted Schadler, Eric Hilfer, Ishai Nir, Mark Finlay, Karen Plonty, Subir Sachdev, and Sandra Vianna. They have all gone on to do great things. Thanks also go to Phil Gould, Phil and Warren Moskowitz, Brian Stewart, Robert Weisskoff, Eric Raab, Peter Martin, Neil Smith, Alex Martin, Pete Magill, Greg Lafyatis, Bob Flanagan, Eric Cornell, Bruce Oldaker, Rick Stoner, Vanderlei Bagnato, and Prof. Dave Pritchard for many useful conversations. My friends Jeff Norman, Ken Jacobs, and Bob Tench gave me different points of view about physics and life in general. Bob Walkup is an exceptional person from whom I learned a great deal. He's the person I still call if I can't figure out something.

The Research Laboratory of Electronics offered many useful facilities, notably those of George Leach and Dave Taylor. Moving the experiment to the G.R. Harrison Spectroscopy Laboratory not only provided excellent equipment, but also the skills of John Thomas, Peter Pappas, Ramachandra Dasari, Carter Kitrell, Jim Childs, Stewart Cameron, Bob Quinn, Tony Willis, Kim Tseko, and Carol Campbell. The legendary Daniel Joseph Heinzen taught me all about dye lasers, and illustrated many other useful laboratory skills. We also tried to understand other things.

I thank the thesis readers, Prof. Michael S. Feld and Prof. George F. Koster for

their interest, enthusiasm, and insights. They made me feel that the effort was worthwhile. Prof. Feld offered advice throughout my stay in the Spec Lab.

Peggy Berkovitz demonstrated concern and kindness all of the time she has been here, and especially during the last hectic days of thesis preparation.

Prof. Daniel Kleppner provided guidance and moral support. He's the one who generated interest in Rydberg Atom Diamagnetism in the physics community, and thereby was able to finance the effort. He tried as often as possible to help solve the technical problems that we faced. He also firmly believed that the experiment would eventually work. He was right, and I thank him for his confidence. Dan has wide experience in the real world of physics. He knows how overhead and Congress work. One of his most enviable traits is the ability to understand things in a simple way, which I sometimes find difficult to emulate. I think he feels that I am a quantum man stuck in a classical world, whereas I feel the opposite about him. We do share a reverence for good data. I hope that I have gained some of his wisdom.